Universidade do Porto
Faculdade de Engenharia
FEUP

Shape and Vibration Control of Composite Structures with Piezoelectric Elements Using Genetic Algorithms

Suzana da Mota Silva

Dissertação submetida à Universidade do Porto
para obtenção do grau de Doutor em
Engenharia Mecânica

Fevereiro 2003

Shape and Vibration Control of Composite Structures with Piezoelectric Elements Using Genetic Algorithms

Suzana da Mota Silva

Faculdade de Engenharia da Universidade do Porto
Departamento de Engenharia Mecânica e Gestão Industrial

Supervisors: *Professor José Dias Rodrigues*
Professor Mário Vaz

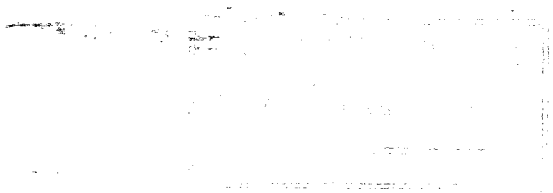

Thesis submitted in February 2003

Acknowledgements

I would like to acknowledge my supervisors Professor José Dias Rodrigues and Professor Mário Vaz from the Faculdade de Engenharia da Universidade do Porto, Portugal and Dr. Rui Ribeiro that supervised the work done at the European Laboratory for Particle Physics (CERN), Geneva, Switzerland.

This thesis represents three and a half years of work essentially done at CERN in the TA1 Group. My gratitude goes to the entire group and in special to the TA1 group leader, Alfredo Placci, for giving me excellent working conditions, to Mike Price, always available to discuss any problem, and to the technicians André Domeniconi and Michel Delattre.

This work was funded by the Fundação para a Ciência e a Tecnologia, Portugal and by the European Social Fund (III Quadro Comunitário de Apoio). I'm most grateful for their financing during the last 42 months of work.

A special thanks to Marco.

Abstract

The European Laboratory for Particle Physics (CERN) in Geneva foresees in the year 2005 the construction of a new particle's accelerator, the Large Hadron Collider (LHC). Two general purpose High Energy Physics Experiments, CMS and ATLAS, will study the LHC collisions and will try to explore nature's most fundamental questions. Typically with several tens of meter long, these experiments are both huge in size and complexity and can not be compared with any particle physics experiment done so far. Catching 800 million collisions each second these detectors impose stability requirements in the order of tens of a micron in structures with several meters length.

Therefore, future High Energy Physics experiments require the use of light and stable structures to support their most precise radiation detection elements. These large structures must be light, highly stable, stiff and radiation tolerant in an environment where external vibrations, high radiation levels, material ageing, temperature and humidity gradients are not negligible [1]. Unforeseen factors and the unknown result of the coupling of environmental conditions, together with external vibrations, may affect the position stability of the detectors and their support structures, thus compromising their physics performance [2]. Shape control of the supporting structures and alignment systems, as well as, effective damping of vibrations are engineering design problems that should be considered and which support and justify the approach presented in this work [3]. The need of an optimisation algorithm able to solve efficiently these problems without imposing a high number of requirements and restrictions lead us to opt for Genetic Algorithms. Based in the natural evolutionary process of human beings and on the survival-of-the-fittest, Genetic Algorithms are stochastic optimisation techniques mainly used when the search space is large and when a near-optimal solution is sufficient. By exploiting the knowledge contained in old solutions (reproduction and crossover) and by changing information in a random way (mutation), these methods are quite powerful and easy to implement.

In this work, a new methodology, based in Genetic Algorithms, is applied to the solution of two different classes of optimisation problems: shape control and vibration control of adaptive structures. After a general overview of the most commonly used materials for sensing and actuating and of the mathematical formulation and optimisation methodology used, two main applications will be presented and discussed.

The first application consists in finding the best set of actuation voltages applied to piezoelectric patches placed on a structure in order to achieve a certain pre-defined shape. Different boundary conditions and different structures were considered. The initial algorithm was also slightly modified in order to accommodate the determination of the optimal location of the piezoelectric actuators for shape control purposes. The model was investigated numerically and experimentally verified. Measurements were carried out using a non-contact capacitive displacement sensor, as well as, Electronic Speckle Pattern Interferometry (ESPI). The second application is related with the optimal placement of collocated sensors/actuators for the purpose of free vibration's damping. The weighted sum of the closed loop damping ratios is used as a measure of the performance of the system and a constant gain feedback control methodology is assumed. The proposed procedure, based on genetic algorithms and on the finite element method, is quite flexible since it allows the optimisation of the piezoelectric placement considering one single vibration mode or a combination of several modes. Collocated sensors and actuators were adopted. This collocation enhances robustness and stability in feedback resulting in an easier controller design. The strain energy fraction distribution within the structure was used for cross checking the results. The validation of the developed methodology is finally completed with some experimental tests.

The two methodologies previously described, and concerning the optimal placement of piezoelectric elements for shape and vibration control, are then applied to a real structure: a 2.5 meter sandwich disk supporting the alignment system of one of the future particle detectors. Main conclusions and considerations about future work finalise this thesis.

Keywords: Genetic Algorithms, Shape Control, Vibration Control, PZT

Resumo

O Laboratório Europeu de Fisica das Partículas (CERN), em Genebra, projectou construir em 2005 um novo acelerador: o Large Hadron Collider (LHC). Duas grandes experiências, CMS e ATLAS, irão estudar as colisões que se produzirão no LHC com o objectivo de responder a questões fundamentais relativas à natureza das partículas. Ambas as experiências, quer em dimensão, quer em complexidade, não se assemelham a nenhuma outra existente presentemente. Capazes de detectar 800 milhões de colisões por segundo estes novos detectores impõem requisitos de estabilidade na ordem dos micron em estruturas com alguns metros de dimensão.

Assim sendo, o uso de estruturas leves, estáveis, rígidas e tolerantes à radiação, para suporte dos diversos elementos sensíveis às partículas em ambientes com grandes variações de temperatura e humidade e na presença de vibrações, é indispensável [1], [2].

O controlo da forma e das vibrações destas estruturas é um problema de engenharia actual que motiva e suporta o trabalho desenvolvido nesta tese [3]. A necessidade de um processo de optimização capaz de resolver eficazmente este problema sem impor grande número de restrições levou-nos a optar pelos Algoritmos Genéticos. Baseados na teoria evolucionista das espécies e na sobrevivência do mais forte, os Algoritmos Genéticos constituem técnicas de optimização estocástica usadas essencialmente quando o domínio é vasto e quando uma solução aproximada é suficiente. Baseando-se na informação de soluções anteriores e trocando informação aleatoriamente estes algoritmos são muito funcionais e fáceis de implementar.

Uma nova metodologia, baseada nos Algoritmos Genéticos, é aplicada na resolução de dois tipos de problemas de optimização: controlo da forma e das vibrações livres das estruturas adaptativas. Após a apresentação dos materiais mais comuns utilizados em estruturas inteligentes, da formulação matemática e do processo de optimização usados, as duas aplicações serão discutidas em pormenor.

A primeira aplicação consiste em determinar a posição e a voltagem a aplicar a um número máximo de actuadores piezocerâmicos, colados numa estrutura, de modo a deformá-la de uma maneira pré-definida. A validação experimental da metodologia foi feita utilizando duas técnicas distintas: medição localizada dos deslocamentos com um sensor capacitivo sem contacto e medição no espaço através de uma técnica de interferometria óptica (ESPI).

A segunda aplicação está relacionada com o controlo das vibrações livres usando sensores e actuadores piezocerâmicos. A soma ponderada dos coeficientes de amortecimento dos diversos modos de vibração é utilizada como a função de optimização a maximizar. A metodologia desenvolvida para a determinação da localização dos sensores e actuadores piezoeléctricos é bastante flexível na medida em que a optimização do posicionamento pode ser feita considerando um único modo ou uma combinação ponderada dos diversos modos de vibração. Os resultados obtidos foram comparados com a distribuição da energia de deformação interna modal. A validação da metodologia foi completada com alguns testes experimentais suplementares.

As duas metodologias desenvolvidas e anteriormente descritas foram aplicadas a uma estrutura real: o disco de suporte, com um diâmetro de 2,5 metros, do sistema de alinhamento de um dos futuros detectores de partículas. O trabalho realizado termina com a apresentação das conclusões principais e algumas considerações sobre desenvolvimentos futuros.

Palavras Chave : Algoritmos Genéticos, Controlo da Forma, Controlo de Vibrações, PZT.

Contents

List Of Symbols

$[]$	matrix
$[]^T$	transposed matrix
$\{\}$	vector
$\{\}^T$	transposed vector
∇	gradient operator
$\dot{\eta}, \ddot{\eta}$	first and second time derivatives
$\partial/\partial x$	spatial derivative with respect to x
δ_{ij}	*Kronecker* delta function
δ	variation operator
ϱ	mass density
ϕ	electrical potential energy
$[\epsilon^s]$	dielectric constants matrix evaluated at constant strain
η	modal co-ordinates
$\{\phi_i\}$	potential generalised co-ordinates
$[\Psi]$	mass-normalised eigenvectors
ω	natural frequency
ω_d	frequency of damped vibration
ξ_i	modal damping ratios
θ	orientation angle between the material axes of layer k and the global axes
σ^2	variance associated with the noise process
A_{ij}	extensional stiffness matrix
$\widehat{A}$	estimate of the system's matrix of dynamics
$[A]$	system's matrix of dynamics
B_{ij}	bending-extensional coupling stiffness matrix
$\widehat{B}$	estimate of the system's input matrix
$[B]$	system's input matrix
$[B_q]$, $[B_\phi]$	shape functions derivatives
$[C]$	system's output matrix
$[C^E]$	matrix of elastic coefficients at constant electric field
$[C_{mm}]$	damping matrix
d_{ij}	piezoelectric charge coefficient
D_{ij}	the bending stiffness matrix

$\{D\}$	vector of electrical displacements
$[D]$	system's feedthrough matrix
$[\bar{D}]$	transformed stiffness matrix
e	error between the system's state vector and its estimate
$[e]$	piezoelectric moduli matrix
$\{E\}$	electrical field vector
$E\{\}$	denotes mathematical expectation
$[F]$	disturbance matrix of the state vector
$\{F_c\}_i$	external force vector
g	problem co-ordinates
g_{ij}	piezoelectric voltage coefficient
G	constant feedback gain
h_k	thickness of the k^{th} layer
$[I]$	identity matrix
$\{\kappa\}$	bending (curvature) strains
K	shear correction coefficient
$\widehat{K}$	optimum matrix gain
$[K]$	global stiffness matrix
$[K_{mm}]$	mechanical stiffness matrix
$[K_{me}]$	coupled electrical/mechanical stiffness matrix
$[K_{ee}]$	piezoelectric stiffness matrix
$[L]$	differential operator matrix
m	material co-ordinates
$[M]$	global mass matrix
nf	number of applied external forces
np	number of piezoelectric layers
$\{\bar{N}\}$	in-plane loads and moment resultant vector
$[N_q]$, $[N_\phi]$	shape functions matrices
$pdf[x;t]$	probability density functions
$\{q_i\}$	mechanical generalised co-ordinates
[Q]	state weighting matrix
$\{\bar{Q}^{(k)}\}_{ij}$	lamina stiffness
[R]	control weighting matrix
$\{S\}$	strain vector

$\{\bar{S}\}$	generalised strain vector
$\{S^0\}$	mid-plane membrane strains
$\{S^s\}$	transverse shear strains
T_i	stress components of the stress vector
$\{T\}$	stress vector
$\mathcal{T}$	kinetic energy
$\{u\}$	control input vector
u, v, w	displacements relatives to the x, y, z axes
u_0, v_0, w_0	mid-plane displacement vector
$\mathcal{U}$	potential energy
$\{v\}$	system's input noise vector
V	volume
V_a	actuation voltage
V_s	sensor voltage
$V^{(k)}$	electric voltage applied across the k^{th} layer
$[V]$	correlation matrix of system's noise
w	measurement's disturbance vector
$[W]$	correlation matrix of system's noise
W_{ext}	work done by external forces
$\{x\}$	system's state vector
$\widehat{x}(t)$	estimate of the system's state vector
$\{y\}$	control output vector
z_k	coordinate of layer k relative to the mid-plane

Chapter 1

Introduction

During the evolution of materials science different material's characteristics and aspects have been explored. Starting from the use of structural materials, followed by functional materials and more recently by smart or intelligent materials, the whole process has provided the theoretical basis for the implementation of multi-functionality into materials (Figure 1.1).

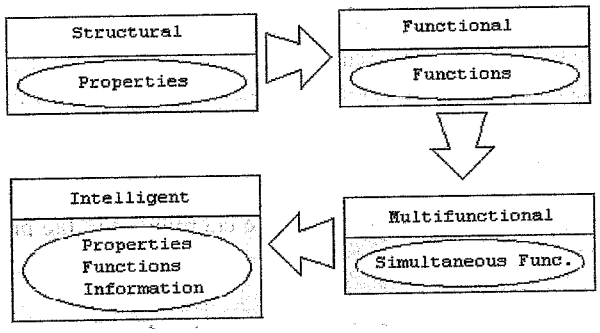

Figure 1.1: *Evolution of materials science [4].*

Structural materials are mainly characterised by their strength and are generally employed in loading-bearing situations. Examples include steel, wood, iron, etc. During the past two centuries one has assisted to the development of *functional materials* - materials whose principal functional characteristic is exploited in the fields of science and technology rather the inherent structural properties of the material. Presently, one of the most known examples is the use of silicon in computer hardware. In the last decades the research and development towards *multifunctional materials* was a first step in the evolution of smart materials and structures. These materials, characterised by several functional properties, include lead-magnesium niobate and the thermo-electrostrictive properties, lead zirconate titanates and the piezoelectric effect, etc.

The field of smart materials and structures is growing rapidly, presenting technological innovations in the area of materials engineering, sensing and actuation techniques, control algorithms and architectures, and presently, provides an high economical potential in a variety of applications and industries such as automotive, aerospace, defence, biomedical devices, advanced manufacturing, sporting goods, high-precision instruments, buildings, bridges, etc.

The concept of *smart structures* is based in the existence of a network of sensors and actuators, signal processing, computational capabilities and control algorithms (Figure 1.2) that enable these structures to respond autonomously to external stimuli (such as loads or shape change), as well as, to internal stimuli (such as damage or failure).

Sensors may be embedded, without causing any significant changes in the structural stiffness of the

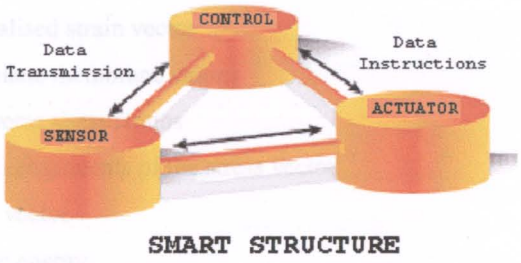

Figure 1.2: *Components of a smart structure [5].*

system, or bonded on the surface of the structure. Sensing may be performed by a functional material whose objective is to measure stress, strain, electrical, thermal or chemical phenomena. *Actuators*, embedded or surface bonded in the structural material, are typically excited by an external stimulus, such as electricity, which results in a controlled change of its geometrical, stiffness, or energy dissipation properties. Alternatively, this function may be performed by an hybrid material which is at the same time a structural and a functional material. *Control capabilities* permit the material to respond to external stimulus according to a predefined control algorithm. These systems possess an inherent adaptive capacity which contributes to their better performance.

Specific projects and applications in the area include shape control for aircraft wings, engine inlets and marine propulsion systems; noise and vibration control for helicopter rotor blades; health and usage monitoring for identification and validation of damage in structures. However, as in any emerging technology, the commercial impact of smart structures will depend on the relation cost/benefit. Expectations and solutions for new engineering applications are enormous and the prospects of smart technologies achieving them are very promising.

1.1 Smart materials

Smart materials must fulfil some specific requirements at different levels: technical properties and mechanical behaviour; technological properties encompassing manufacturing and workability; economic criteria related to raw material, production costs and availability; environmental characteristics including features such as pollution and toxicity and sustainable development criteria implying reuse and recycling capabilities [6].

This new class of smart materials is being typically fabricated by using materials with already known material properties instead of new materials synthesised at the microscopic level. Widely reported in literature smart materials can be grouped in the following main categories: piezoelectric, shape memory alloys, electrostrictive, magnetostrictive, electro-rheological fluids and optical fibres.

The next sections will present the advantages and disadvantages of the most common smart materials currently used for actuating and sensing.

1.1.1 Actuator materials

Actuator materials are typically used to tune dynamically the mechanical properties of the structure or to tailor its shape. The characteristics of the main actuator candidates are summarised in Table 1.1.

- *Piezoelectric materials* are solids which generate an electrical charge in response to a mechanical deformation, or alternatively, develop mechanical deformations when subjected to an electrical field. Consequently can be used either as actuators or sensors. Piezoelectric actuators

Table 1.1: *Actuator candidates for smart materials [4], [7].*

	Electrostrictive Materials	Electro-rheological Materials	Magnetostrictive Materials	Nitinol Shape Memory Alloy	Piezoelectric Ceramic
Cost	Moderate	Moderate	Moderate	Low	Moderate
Technical Maturity	Fair	Fair	Fair	Good	Good
Embedability	Good	Fair	Fair	Excellent	Excellent
Linearity	Fair	Fair	Fair	Good	Good

present high stiffness, good linearity, generally are insensitive to temperature, are easy to implement and are best suited for high frequency applications, demanding small to medium power requirements. Mainly, are used for shape, vibration and acoustic control. Piezoelectric materials normally come in the form of piezoceramics - the most common type is Lead-Zirconate-Titanate (PZT) or piezopolymers - e.g. Polyvinylidene fluoride (PVDF). PZT crystals are generally difficult to manufacture since they are brittle. PVDF represent an attractive option due to the easiness of incorporation during the manufacturing process, however these polymers are difficult to produce in long enough lengths [8].

When connecting electrically several thin wafers of piezoelectric material, typically PZT, one obtains a stack actuator (Figure 1.3).

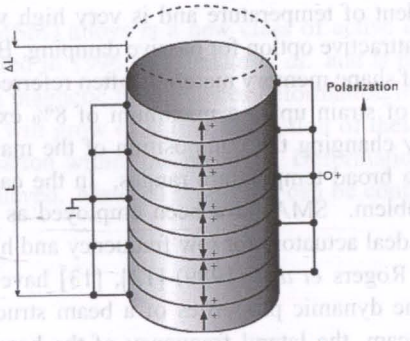

Figure 1.3: *Design of a PZT stack actuator [9].*

This arrangement allows the mechanical displacement to sum in series while the electric properties remain in parallel. Therefore larger displacements can be obtained with lower applied voltages. Applications for stack actuators include micro-positioning, vibration isolation, truss structural control, etc.

In spite of a good technical maturity, some issues still remain unanswered concerning the general and broad use of piezoelectric materials. Research on modelling is needed, namely to include non linear strains and to predict the response for a high voltage and a lower frequency. On the materials engineering side, investigation for enhancing material properties of piezoelectrics is also necessary [7]. Previous research performed on PZT-actuated beam and plate structures has lead to the development of mathematical models describing their response. However, much less research has been performed on structures with curvatures (shells). Piezoelectric materials will be further discussed in Section 1.1.2.

- *Electro-rheological fluids* (ER) are typically suspensions of micron-sized particles in suitable carrier liquids, that undergo significant instantaneous reversible changes in their rheological properties

such as viscosity, plasticity and elasticity when subjected to electric fields. These changes, which exhibit complex characteristics and non linear effects, are due to controllable interaction between the micron-sized dielectric particles and the ER suspension. The voltages required to activate the phase-change in ER fluids are typically in the order of 1-4 KV/mm of fluid thickness and current densities in the order of 100 A/m^2, thus the total power required to change the properties of the fluid is quite low [4]. The most common ER fluids are composed of silicon oil and corn starch [8]. ER applications can be divided in two classes: controllable devices and adaptive structures. The former include devices such as valves, mounts, brakes and dampers. In the second case, ER are embedded in the voids of the structural material. By imposing an appropriate electric field the properties of the ER fluid change thus enabling the tuning and the control of the mechanical properties of the host material. ER fluids present low time responses and weight penalties associated with introducing fluid into the structure.

- *Shape-memory alloys* (SMA) are metals which, when plastically deformed at one temperature, will completely recover their original non deformed state upon raising their temperature above their transition temperature. The thermo-mechanical behaviour of SMA material depends upon the internal crystalline structure (phase), stress, temperature and history of the material. When an SMA is below its phase transition temperature, it possesses a low yield strength crystallography referred to as martensite. While in this state, the material can be deformed into other shapes with relatively little force. The new shape is retained provided the material is kept below its transition temperature. When heated above this temperature, the material reverts to its parent structure known as austenite causing it to return to its original shape. The damping coefficient of SMA is dependent of temperature and is very high when compared to that of steel making these materials an attractive option for passive damping. Buehler and Wiley (1965) [10] received a patent on a series of shape memory materials often referred to as Nitinol (Nickel-Titanium alloys). A 100% recovery of strain up to a maximum of 8% extensional pre-strain was achieved with this alloy [11]. By changing the composition of the material the transition temperature can be selectively tuned to broad temperature ranges. In the case of high strain configurations fatigue may become a problem. SMA have been employed as actuators and sensors: these materials have proven to be ideal actuators for low frequency and high stroke applications, with low power requirements [8]. Rogers *et al.* (1989) [12], [13] have used the properties of shape memory alloys to change the dynamic properties of a beam structure: by embedding eight SMA wires into a composite beam, the lateral frequency of the beam ranged from 18% heating two SMA wires, to 73% heating six SMA wires. Additional theoretical work show that mode shapes of a composite plate can be changed by distributing SMA wires in a grid fashion and by adjusting the strain energy distribution through controlled actuation of the wires [14]. After significant research on development, modelling, manufacturing, and utilisation of shape memory alloys, many issues remain to be addressed such as the influence in the degradation of the host material in the presence of SMA wires. A systematic validation of the constitutive models of SMA for different temperatures and strains is not available and represent a major barrier for design development. Shape memory phenomena is not only limited to metals: shape-memory-plastics have also been developed under the name of Norsorex ®.

- *Electrostrictive materials* develop mechanical deformations when subjected to an external electrical field. This effect results from the rotation of the electrical domains present in the material when an electrical field is imposed. The ceramic compound lead-magnesium-niobate, PMN, exhibits a thermo-electrostrictive effect dependent on the ambient temperature. The advantages of these materials over piezoelectrics are related to the fact that the former ones have higher density charge thus producing bigger forces when activated, hysteresis appears to be less significant and they can potentially achieve larger displacements [8]. The strain effect in these materials is quadratic with voltage and decreases with temperature. However a linear relationship over a limited range of

excitation may be obtained after some biasing. Electrostrictive materials have been widely used in shape control of mirrors and other optical surfaces (Ealey and Wellman, 1989) [15]. The absence of hysteresis and creep at low frequencies and moderate temperatures make electrostrictive actuators ideal for low frequency precision positioning applications.

- *Magnetostrictive materials* are solids which when subjected to a magnetic field develop large mechanical strains. Conversely, a magnetic field, proportional to the material's strain rate, is generated when the material is stressed. This magnetostriction phenomena results from the interaction forces between applied magnetic fields and the magnetic dipoles in the material. When compared to electrostrictive and piezoelectric materials, magnetostrictive materials offer lower strain and forces while consuming more power, justifying their use in fewer applications [7]. Apart from the power requirements, other disadvantages include the technological challenge in the application of a magnetic field to a magnetostrictive actuator embedded within the host structural material, the fact that the materials generates a much greater response when subjected to compressive loads, the existence of hysteresis, non-linearity and temperature dependence. Because of the coil and magnetic return path, these actuators are often bulky. Therfenol-D, an alloy of iron and the rare earth elements, Terbium and Dysprosium, is a commercially available magnetostrictive material. Therfenol-D transducers have been successfully used as positioners, sonar projectors (500-2000 Hz), isolators (15-20 Hz), shock absorbing mounts, and to mimic the vibrations of artificial hearts. Magnetostrictive materials can act as distributed sensors in multifunctional composites or as actuators for vibration suppression, micro-positioning and shape control.

- *Magnetic shape memory* (MSM) alloys is a new class of active materials. The magnetic shape memory effect was discovered in 1996 by Ullakko *et al.* and is present in Ni-Mn-Ga and Fe-Pd alloys. The application of a magnetic field induces deformation in the material. In this deformation, variants of martensite will grow or shrink by motion of their twin boundaries with little or no rotation of the magnetisation within the material. Deformations of the material in the order of a few percent can be achieved. Material properties can be controlled by composition and heat treatment [16].

1.1.2 Sensing materials

Generally the response of a material can be mechanical, electrical, magnetic, thermal or chemical. In terms of mechanical structures monitoring the electrical response is the more suitable one due to the easiness of integration in a control algorithm. Several sensing technologies are available. Typical sensors consist of strain gauges, accelerometers, fibre optics, piezoelectric films, piezoceramics and SMA. However while piezoceramic and strain gauge sensors can only provide local information, fibre optic or SMA sensors may provide global measurement of the deformation field. Key factors for sensors are their sensitivity to strain or displacement, bandwidth and size. Table 1.2 presents information about the most common sensors: fibre optic, SMA, piezoelectric and strain gauge sensors.

Table 1.2: *Sensor candidates for strain measurement [4].*

	Fibre-Optic Interferometer	Nitinol Shape Memory Alloy	Piezoelectric Ceramic	Strain Gauge
Cost	Moderate	Low	Moderate	Low
Technical Maturity	Good	Good	Good	Good
Embedability	Excellent	Excellent	Excellent	Good
Linearity	Good	Good	Good	Good

- *Fibre optic sensors* are excellent sensors since they are immune to electromagnetic interference, are very sensitive, light weight and highly flexible. Due to their high melting point and inherent strength of the glass, these sensors are able to perform in very hostile environments [8]. Fibre optics provide, in smart structures, a sensing capability and a transmission medium for the light signal. The light signal, modified by an external stimulus, is transmitted to a receiver system which infers the information concerning the characteristics of the stimulus. In the case of surface bonded optical fibres, the strain field in the structure is directly coupled to the optical fibre by an adhesive film, while in the case of polymeric composite materials, when the fibre is embedded, this coupling is given by the adhesive properties of the matrix material. Fibre optic sensors respond to a change in intensity, phase, frequency, polarisation, wavelength or mode. The most simple ones respond to any form of perturbation, such as bending or twisting, that changes the intensity of the transmitted light. Interferometric sensors, such as the *Mach-Zehnder interferometer* responds to changes in phase and spectrometry. In this case two coherent beams, coming from the same light beam and divided by a beam-splitter, are coupled into two single-mode fibres. One of the fibres is protected from the strain field and external stimuli, while the other is subjected to mechanical deformations. This later one will experience a change in length of the transmission medium, and hence a change in the optical path length of the light beam. The difference in the optical path length of the two beams results in a relative phase shift between them which is detected by observing the shift in the fringe pattern upon recombining the two beams. The maximum range is in the order of a wavelength (a few microns) and the sensitivity is limited by detector noise. The elimination of unwanted signals requires great care in the design of these sensors.

  Another type are the multiplexed sensors such as the *Fibre Bragg Grating* sensors (FBGs). With applications in vibration and health monitoring, providing quasi-static and dynamic strain measurements, these sensors are an enabling technology. FBG elements can be either surface bonded or embedded. The main advantages of FBGs in mechanical sensing are the direct transformation of the sensed parameter to an optical wavelength and the potential for highly multiplexed operation [17]. FBG consists in a periodic modulation of the index of refraction in the core of the optical fibre. When light travelling down the fibre comes in contact with the Bragg grating, a narrow band of wavelengths centred at one particular wavelength known as the Bragg resonance wavelength, is reflected back in the opposite direction. The Bragg resonance wavelength in the fibre is twice the period of the grating spacing (Bragg condition). If the fibre grating is strained, ε, the Bragg wavelength, λ, of the reflected light changes slightly ($\delta\lambda/\lambda \cong 0.74\delta\varepsilon$) [18]. By detecting the frequency shifts in the reflected power spectrum, strains can be inferred in the grating region. Detectable resolutions are approximately in the order of 6 nano-strains. Multiple FBGs can be connected in series, and each of which reflects a different wavelength of light. By scanning the return signals with a fibre optic Fabry-Perot interferometer filter allows the reading of the multiple sensors.

  In general, fibre optic sensors are no longer just a research topic and several commercial devices are already available. Networking is possible, for example, by imprinting different Bragg grating frequencies. However, thermo-optic effects have not been completely solved and a complex processing electronics is still required for interpreting the results. A desirable use for these sensors is the monitoring of the development of cracks, delaminations and debonding, as well as, damage detection.

- *Piezoelectric sensors* are ideal due to their high strain sensitivity and low noise. Typically, present excellent linearity and dynamic range, a low temperature sensitivity and are easy to implement. Table 1.3 presents a comparison between two piezoelectric materials: a piezoceramic (PZT) and a piezofilm (PVDF).

  Piezofilms are robust and flexible but low modulus. In comparison, piezoceramics are rigid and brittle, but less durable and with higher densities. The high rigidity of piezoceramic ensures that electrical energy is efficiently converted into mechanical energy which ensures good actuation

Table 1.3: *Comparison of the mechanical properties of PZT and PVDF materials. Indicative properties [18], [19].*

Mechanical Properties	Piezoceramic	Piezofilm
Lateral Strain Coefficient d_{31} [m/V]	$1.8x10^{-10}$	$23x10^{-12}$
Axial Strain Coefficient d_{33} [m/V]	$3.6x10^{-10}$	$33x10^{-12}$
Shear Strain Coefficient d_{15} [m/V]	$5.4x10^{-10}$	-
Young's Modulus [Pa]	$6.3x10^{10}$	$2.0x10^{9}$
Density [Kgm^{-3}]	7500	1780
Relative Permittivity	1700	12
Resistivity [Ω-m]	$1.0x10^{10}$	$1.0x10^{13}$
Coef. Thermal Expansion [μ-strain/^{o}K]	1.4	30-40
Max. Electrical Field [10^{6}V/m]	0.6	40
Max. Operating Temp. [^{o}C]	140	90

capabilities. Having higher dielectric strength, piezofilms can be exposed to much higher electric fields than piezoceramics. PVDF elements are more sensitive to mechanical loads over a wider range of loading conditions, responding to higher frequencies than PZT. Therefore making them good candidates for sensor applications. In practice, PZT sensors have less noise and are used universally for accelerometers. On the other hand, PVDF sensors are inexpensive and easy to use, and are typically applied in musical pickups and touch sensors.

- *Strain Gauges* are simple to operate, low cost and practical sensors presenting a good technical maturity. The most common type used nowadays is the bonded resistance strain gauge. Consisting of a grid of fine wires, strain gauges, can be glued to the structure with a thin layer of epoxy. The epoxy will transfer the strain in the specimen to the strain gauge. Upon a tensile or compressive state of stress in the specimen, the cross-sectional area of the conducting wires will change. Because the electrical resistance is proportional to the inverse of the cross-section, by measuring and calibrating the change in resistance, the strain gauge can determine the degree of strain in the material. Sensitivity of the sensor is defined by the gauge factor, equal to the ratio of the fractional change in resistance divided by the fractional change in length along the axis of the gauge. Common gauge factors are in the range of 2.0-4.0 [18]. In order to reduce length, common strain gages use a grid pattern instead of a straight wire. This grid pattern allows the gauge to be sensitive also to deformations transverse to the gauge length. Therefore, corrections for transverse strains may be computed and applied to the strain data [20]. Higher sensitivity can be obtained with a wheatstone bridge circuit [21]. The gauge is placed in a bridge with balanced nominal resistance such that zero strain gives zero differential voltage. For a constant current source, voltage changes produce indications of resistance and hence strain. In order to obtain accurate strain measurements, temperature must be compensated. This can be done by matching the coefficient of thermal expansion of the gauge with the specimen material. Strain gauges only provide strain measurement's at the immediate point of connection, however are able to provide useful reference points for comparison with other less proven sensors.

1.2 Applications and *state-of-the-art*

The technology of smart materials and structures is a highly interdisciplinary field which may explain the small number of practical applications. Despite this delay, envisaged applications may be, in a near future, expanded in a global way to the aeronautical, automotive, civil/construction, military and medical industries. According to [19] some applications could include smart skins for aircraft's external surfaces with the ability of detecting surface impact/damage and strain monitoring during flight manoeuvres;

noise reduction in vehicles including neutralisation of shaking in helicopter rotor blades [22] and noise suppression in aircraft's cockpit; modification of aerodynamics in rotor blades [23]; etc.

Presently, there are still some key barriers to the extensive use and to the application of smart materials technology to current engineering needs [19] [24]. Namely, there is a need of further research and development in the following domains

- Smart materials characterisation: design and development of smart structures implies the knowledge of the material's main characteristics and properties. At the moment a complete database is non existent. For example, basic mechanical properties such as Young Modulus and yield stress for Nitinol at different temperatures and stresses are still not available.

- Modelling of piezoelectrics: concerning beam modelling, most analysis assume linear actuation strain with electrical field and hence do not include non linear effects, important to predict the response for higher voltages and lower frequencies. In plate modelling there is a lack of experimental studies and detailed analysis. Several theories were proposed for the analysis of laminated composite plates with integrated piezoelectric sensors and actuators. The majority of the models were based in the classical laminate plate theory (Crawley and de Luis (1987) [25], Lee (1990) [26]) and in the first order shear deformation theory. In the prediction of stresses of highly anisotropic plates and/or moderately thick composite plates these theories may lead to significant errors. More accurate mathematical models can be based either in 3D finite elements with an high computational cost or in single layer models based on higher order displacement fields [27]. The development of 3-D finite elements including non linear actuation strain could be used to validate and check the limitations of the current analysis.

- Large stroke smart actuators: the most current available smart actuators are piezoceramics, electrostrictive and magnetostrictors which present, in general, low stroke and low force capabilities for present needs. Current investigations try to respond to a need for compact, high force and large displacement actuators [28]. An increase of 300% to 500% displacement capabilities of smart materials actuators is envisaged.

- Constitutive relations: contrary to piezoceramics and SMA actuators there are few studies on simplified constitutive relations for magnetostrictive and electrostrictive actuators [29]. To promote the use of these smart materials in special applications the development of simplified constitutive relations and their validation with experimental data is important.

- Shape memory alloys: systematic validation of SMA mathematical models for different temperature and strains, efficient manufacturing procedures for embedding SMA in composites, correlation of predicted results with measured data should be carried out in order to develop and improve the design of smart structures using these materials. SMA have good strain characteristics but their bandwidth response time needs improving.

- Design and application to current systems: a proper assessment of smart materials technology relies in its application to realistic structures. Testing and evaluation of the performance of control algorithms and actuators under different operating conditions on scaled models, the use of experimental data to validate analysis and carry out optimisation studies will push forward the necessity of development of smart structures. Power conditioning and switching must be optimise in order to minimise local heat loads and avoid thermal damage of the host material.

- Structural health monitoring: only a number of limited experimental studies and analytical tools are available in the domain of structural health monitoring. Frequent inspection of systems lead to high operating and maintenance costs and justify a bigger investment in this field. Present applications are related with civil engineering structures or marine applications and fibre optics. The

Taylor bridge in Headingley, Canada, was instrumented in order to actively monitor the behaviour of the bridge structure and of the new advanced materials, over time. Another example, in Canada, is the Confederation Bridge, the longest bridge over iced-water spanning 12.9 km, which was also instrumented to monitor the long-term effects of wind, ice and traffic loads [30]. The viability of fibre optics distributed sensors for hundreds of point measurements has already yet been proven in theory, but not in practice due to the high complexity of signal processing.

- Manufacturing: cost-effective manufacture and fabrication of smart materials and structures, as well as, processing and embedding smart materials in the host structures are generally neglected issues. Some of the existing studies are on the fabrication and mechanical performance of smart composites incorporating fibre optics [31], on the fabrication of active PZT fibres [32] and in the influence of the presence of embedded sensors/actuators on material's behaviour [33], [34], [35].

- Durability and longevity: sensor and actuator integrity depend on their location and exposure to external environment. There is little evidence of the effect on smart materials of irradiation, outgassing, thermal cycling corrosion, humidity, ageing, and cycling mechanical loading [36].

In general, much of the current research is focused on the application of piezoelectric technology to aerospace and aeronautical related systems. By far, the most investigated application for smart structures is the vibration control. The earliest works on this area are from Bailey and Hubbard (1985) [37] and Tzou and Tseng (1990) [38]. In the first case the vibrations, of a Euler-Bernoulli cantilever beam, were controlled by using distributed PVDF films and negative velocity feedback control algorithm. Tzou and Tseng proposed a methodology to evaluate the dynamic characteristics of integrated piezoelectric sensors/actuators on plates and shells. Constant gain negative velocity feedback and constant amplitude negative velocity feedback were used to suppress and control the vibrations of the plate. Some of the most common and current applications are presented next, with a strong emphasis on the use of piezoelectric materials.

Shape control Shape control can improve the aerodynamic and hydrodynamic performances of lifting surfaces, correct the shape of antennas or mirrors, as well as, compensate quasi-static displacements due to temperature or humidity variations. The most common methods to control the shape of a structure consists in embedding piezoelectric materials on it. Crawley and De Luis (1987) [25] developed static and dynamic analytical models for structures with distributed sensors and actuators, glued or embedded in the structure. These models lead to the ability to predict, a priori, the response of the structure. Koconis, Kollar and Springer (1994) [39] [40] addressed the shape control problem: calculation of the shape of the structure due to specified voltages and calculation of the required voltages to produced a pre-defined shape. The model developed had a general applicability: it could be solved for structures and actuators with different shapes, different support configurations and different laminar arrangements. Optimisation techniques such as genetic algorithms and simulated annealing have also been used to determine optimal actuator locations in truss structures for the correction of static deformations (Onoda *et al.*, 1992) [41]. Chandrashekhara and Varadarajan (1997) [42] used the Lagrange multiplier approach to determine the optimal actuator voltages needed to attain the pre-defined shape of a composite beam while S. da Mota Silva *et al.* (2001) [43] used genetic algorithms for determining the optimal position and the optimal actuation voltages of collocated sensors/actuators in composite beams and plates. The employed methodology was also experimentally validated.

Buckling control The main objective in buckling control is to maximise the compressive axial load before buckling occurs. In 1993 Meressi and Paden [44], using the LQR methodology, controlled the buckling of an horizontal simply-supported column with PVDF film actuators and subjected to axial compressive loads. Thompson and Loughlan (1995) [45] investigated the active control of buckling, of a composite column with PZT actuators surface bonded on the both sides of the mid-span, by using

a proportional control algorithm. Pai and Chamis (1992) [46], based in finite element techniques and probabilistic analysis methods, were able to determine buckling loads, as well as, vibration frequencies and axial member forces in truss space structures.

Acoustic control Research has been conducted on the use of surface-bonded piezoelectric actuators to attenuate noise in aircraft fuselages. Active noise suppression methods include the control of either the acoustic field or the structural vibration. One of the early research on acoustic modelling was reported by Foxwell and Francklin (1959) [47]. Since then, several techniques of noise suppression, combining passive and active control, have been used. Waterman *et al.* (1989) [48] used narrow-band damping. Elliot *et al.* (1990) [49] used active control obtaining a reduction in the order of 10 dB in the cockpit. Brama (1991) [50] used optimisation techniques in the design of the fuselage and its interior in order to reduce the transmission of vibrations.

Inspection methods Piezoelectric materials can be used to monitor the structural integrity of civil, industrial and aerospace structures. Sun *et al.* (1995) [51] monitored the structural integrity of a truss structure with piezoelectric sensors and actuators based in the impedance concept - any damage in the structure provokes the change of its impedance. By monitoring the natural frequencies of a structure with piezoceramic patches it is possible to determine if the structure has suffered delamination [52] or damage [53]. In the last decade optical fibre technologies dominate the monitorisation of the structural integrity in structures. These fibres, like piezoelectric elements, can be embedded or glued in the structure and may be used to detect heat, strain or damage.

Vibrations control Piezoelectric sensors/actuators have been widely used in structural vibration control. A proper selection of the number and position of sensors/actuators is critical in an efficient control methodology and consequently is one of the key issues that should be addressed. Several objective functions and optimisation methods have been used. Liang, Sun and Rogers (1997) [54] used the actuator power factor concept to determine the optimal actuator location, length and thickness. Chattopadhyay and Seely (1994) [55] used a multi-objective formulation technique (Minimum Sum Beta) considering the energy dissipated by the actuators and the fundamental frequency as the objective function. The manufacturing of high performance structures requires an efficient control design methodology. Conventional methodologies are based in a priori development of the system model. The LQG/LTR control design methodology is an easy-to-use method for feedback control [56], applied by Agarwal *et al.* (1998) in the active vibration control of laminated doubly curved shells with piezoelectric sensors and actuators [57]. In the case of complex vibration control problems the definition of the dynamical characteristics of the system may be impossible or prohibitively expensive. By using neural networks the existence of an explicit model of the system is avoided. Several researchers have used the potential of neural networks for structural vibration control [58] [59].

1.3 Overview of the present investigation

As already seen, smart (active, adaptive or intelligent) structures are complex systems with inherent characteristics that allow them to achieve an optimum functionality. In spite of not always involving recent material technologies, smart structures represent a new and different project philosophy that integrates a network of actuators, sensors and control methodologies in a unique and global system, able to respond efficiently to environmental changes. Needs for different and efficient methodologies able to deal with multidisciplinary and complex systems, such as smart structures motivate and support the current work.

The modelisation of mechanical structures with integrated piezoelectric elements is done using standard techniques such as the finite element analysis. The equations governing the equilibrium of the

structure, and their respective boundary conditions, were determined using the Hamilton's principle and Mindlin's plate theory. All the formulation is based in linear piezoelectricity. Two different applications for piezoelectric materials, shape control and vibration damping, are considered. For both applications, the location of sensors and actuators is one of the most important factors affecting the performance of the system. The large set of candidate solutions, results in a substantially large number of combinations that must be evaluated, and consequently the need of an effective and robust optimisation method.

An innovative optimisation methodology using Genetic Algorithms is developed and validated, and applied to these two classes of problems. Concerning the shape control application, optimal placement of piezoelectric actuators and optimal actuation voltages are determined in order to achieve a certain predefined shape. Experimental validation on beam and plate structures is done. However the methodology is general and can be applied to any other structure.

The control of vibrations is done by using a simple control methodology: constant gain feedback. The weighted sum of the closed loop damping ratios was assumed as the performance index for optimising the location of collocated sensors/actuators. The obtained results are compared with the modal strain energy.

In both applications, the developed methodologies, based on Genetic Algorithms, reduce the computational effort in large scale problems and eliminate a large number of restrictions common to most optimisation methods. Namely, any kind of objective functions and any kind of constraints (linear or non-linear) defined on discrete, continuous, or mixed search spaces can be easily integrated; the implementation of a specific problem is highly flexible; the susceptibility of the method of focusing on local optimum is reduced and little knowledge of the problem itself is required.

Key points of the modelisation and of the global methodology were experimentally verified and the extension to real applications is straightforward. The biggest effort was put in the optimisation process and not in high-performance control techniques.

The work presented in the next sections is organized as follows. Chapter 2 (Mathematical formulation) is dedicated to the determination of the equations of motion governing the static/dynamic characteristics of orthotropic plates with piezoelectric elements glued or embedded in it. The finite element code used is described.

Chapter 3 (Control theory) introduces several control methodologies that can be employed to damp vibrations. Experimental results using constant amplitude/gain feedback control are presented. Simulations using more robust techniques like the linear quadratic regulator are also introduced.

Chapter 4 (Optimisation procedure) presents the optimisation method applied to the two classes of problems treated in this thesis: the genetic algorithms. After describing the main concepts, the genetic operators are introduced. The general structure of the algorithm and the particularities related to each problem type: shape control and optimal location of collocated sensors/actuators for vibration control are presented.

Chapter 5 (Shape control) presents the first application: the use of piezoelectric actuators for correcting/modifying the shape of mechanical structures. Both the determination of the optimal voltages, as well as, the determination of the optimal position of the actuators are addressed. Several beam and plate structures are studied. Experimental results obtained using simple set-ups and sophisticated optical methods are compared with simulations enabling the validation of the whole methodology.

Chapter 6 (Optimal placement) introduces the second application: the use of genetic algorithms to determine the optimal location, within a discretised domain of the structure, of collocated sensors/actuators for vibration control. The weighted sum of the closed loop damping ratios is used as a measure of the performance of the system. The simulations are compared with results available on the literature and with the modal strain distribution within the structure. Experimental results are also available for the first two vibration modes of a beam structure.

Chapter 7 (Applications) contains the description of the application of the methodologies developed in the two last chapters to a real structure: the alignment disk. The modal testing of this 2.5 meter structure is first presented followed by the simulation results concerning the determination of the actuation

voltages for shape control and of the optimal placement of piezoelectric actuators for both shape and vibration control.

Chapter 8 (Conclusions) summarises the principal conclusions of the last chapters, together with some considerations about future work.

Chapter 2

Mathematical Formulation

The word *piezo* is derived from the Greek word for pressure. In 1880 Jacques and Pierre Curie first demonstrated the piezoelectric effect - a pressure applied to a quartz crystal created an electrical charge in the crystal. After the discovery it took several decades before starting to use the piezoelectric phenomenon. The first application appeared in 1918 when Langevin proposed the piezoelectric transducer. However, it was not until 1946 (Cady, 1946) that scientists discovered that polycrystalline ferroelectric ceramics, such as barium titanate ($BaTiO_3$) and Lead Zirconate Titanate (PZT), could be made piezoelectric by the application of an electrical field. In 1969 Kawai discovered the piezoelectric properties of polyvinylidene fluoride materials commonly named as PVDF, but only on the early 80's these materials were made commercially available [60].

Piezoelectricity is the property of certain materials of becoming electrically charged when submitted to a deformation field. This behaviour, widely used in transducers design, is due to the crystal structure of the material: a mechanical deformation produces an electric dipole as consequence of the displacement of positive and negative charges of the atomic structure. In this case the electrostatic equilibrium is destroyed and a polarisation appears within the material: the direct piezoelectric effect. The inverse piezoelectric effect, applied in actuators design, consists in the mechanical deformation of the material when an electric field is applied. Piezoelectricity can be exhibited either by natural materials such quartz, tourmaline, Rochelle salt, etc or by synthetic materials. For the former ones the effect is very small. The principal commercially available piezoelectric materials and widely used for sensor and actuator applications are PZT. PZT are centro-symmetric cubic (isotropic) before poling, exhibiting tetragonal symmetry (anisotropic structure) after poling and below the Curie temperature (see Figure 2.1).

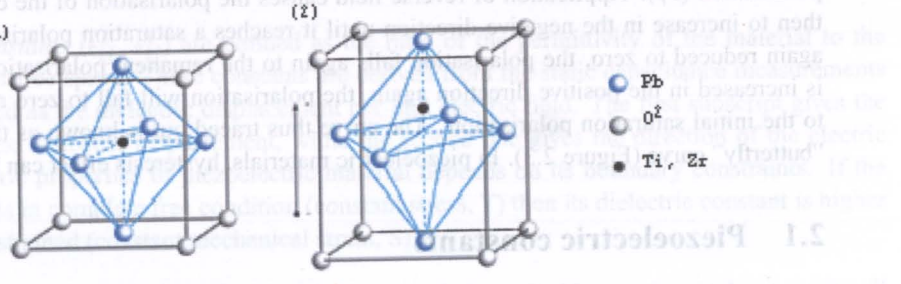

Figure 2.1: *Piezoelectric elementary cell. (1) before poling (2) after poling [9].*

Above the Curie temperature, piezoelectric properties are lost and the material exhibits simple cubic symmetry (Figure 2.1 (1)). In this case the positive and negative charges sites are coincident, so there are no dipoles present in the material. One of the advantages of piezoelectric ceramics relative to

piezoelectric crystals is their higher Curie temperature.

In ferroelectric ceramics dipoles are randomly oriented throughout the material. However neighbouring dipoles align each other to form regions of local alignment known as Weiss domains. The direction of polarisation between these domains can differ by 90° or 180° and owing to this random distribution no overall polarisation is exhibited. The manufacture of commercial piezoelectric materials involves exposing the material to a very strong electric field (≥2000 V/mm) [4] at a temperature slightly below the Curie point. Poling causes the ceramic to grow in the field direction and to shrink laterally, roughly according to Poisson's ratio. Domains mostly nearly aligned with the field will grow at the expense of the other domains. After poling, the dipoles remain locked in approximate alignment giving the material a remanent polarisation and remanent strain (Figure 2.2).

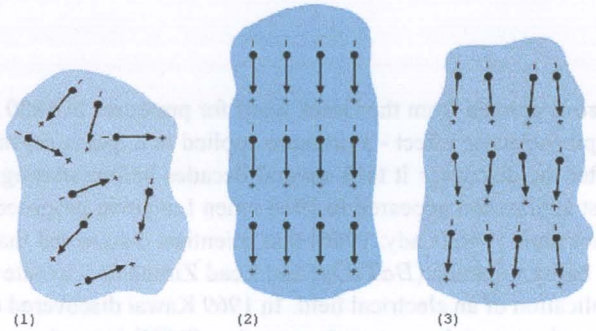

Figure 2.2: *Electric dipoles in Weiss domains. (1) unpoled ferroelectric ceramic (2) during and (3) after poling [9].*

The orientation of the dipoles in the direction of the polarisation field is followed by mechanical stresses whose relaxation during time provoke a depoling process. Piezoelectric material's ageing is a logarithmic function of time. However this effect is negligible with actuator applications because repoling occurs whenever an high electric field is applied, in the poling direction, to the material.

Polarisation in a ferroelectric material is hysteretic. As the electric field increases, more and more dipole domains are switched over in the direction along the field, until saturation is attained. The material is then said to have reached its saturation polarisation (P_s). When the field is reduced to zero, the dipoles become less strongly aligned. However they do not return to their original alignment since there are still several preferred directions within the material and therefore the crystal still exhibits a remanent polarisation (P_r). Application of reverse field causes the polarisation of the ceramic to fall to zero and then to increase in the negative direction until it reaches a saturation polarisation ($-P_s$). If the field is again reduced to zero, the polarisation falls again to the remanent polarisation, and finally, if the field is increased in the positive direction again, the polarisation will fall to zero and then eventually return to the initial saturation polarisation. The curve thus traced out is known as the hysteresis curve or the "butterfly" curve (Figure 2.3). In piezoelectric materials, hysteresis effect can be as high as 20%.

2.1 Piezoelectric constants

Piezoelectric materials are anisotropic by nature while presenting a privileged polarisation axis. Therefore these materials are orthotropic at the piezoelectric and mechanical levels, and in some cases can be considered transverse isotropes. Their mechanical and electrical properties are dependent on the direction. Figure 2.4 presents the 3 axis of orthotropy of a piezoelectric material volume. These axes - the polarisation direction established during the manufacturing process, z, the laminate process elongation, x, and the third direction, y - form an orthonormade co-ordinate system.

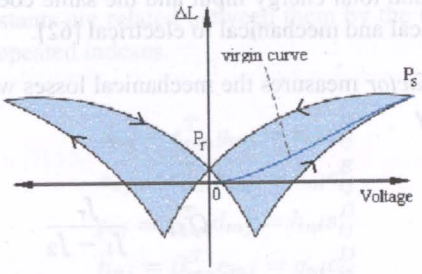

Figure 2.3: *Response of a PZT actuator to a bipolar drive voltage. When certain threshold voltage (negative to the polarisation direction) is exceeded, reversion of polarisation can occur [9].*

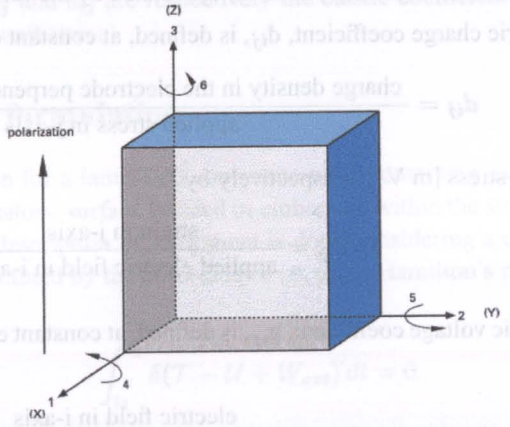

Figure 2.4: *Orthogonal system describing the properties of a poled piezoelectric ceramic. Axis 3 is the poling direction [9].*

The interaction between the electrical and mechanical behaviour in piezoelectric materials can be characterised by several constants. The piezoelectric constants are not independent but vary with temperature, pressure, electric field, mechanical and electrical boundary conditions. The main piezoelectric constants are:

- *Dielectric constants* (ϵ_{ij}^T, ϵ_{ij}^S) are defined as the ratio of the permittivity of the material to the permittivity of free space. These constants are derived from the static capacitance measurements and are defined as the dielectric displacement per unit electric field. The first subscript gives the direction of the dielectric displacement, while the second one gives the direction of the electric field. Dielectric properties of piezoelectric material depends on its boundary constraints. If the piezoelectric is in complete free condition (constant stress, T) then its dielectric constant is higher than if it is restrained (constant mechanical strain, S).

- *Resonance / anti-resonance frequencies*: when a ceramic is excited by an electrical source, it will oppose to that source an impedance, Z, which can be calculated by the piezoelectric equations. From this value, valid for a ceramic without losses, one can determine the resonance frequency, f_r, for which $Z = 0$ and the anti-resonance frequency, f_a, for which Z is infinite [61].

- *Coupling coefficients* (K_{ij}^T) characterise the capability of the material to convert electric energy into mechanical energy and vice-versa. The square of the coupling coefficient is defined as the ratio of

transformed energy and total energy input and the same coefficient is used for both conversions, electrical to mechanical and mechanical to electrical [62].

- *Mechanical quality factor* measures the mechanical losses within the piezoelectric ceramic and it can be determined by

$$Q_M = \frac{f_r}{f_1 - f_2} \tag{2.1}$$

with f_1 and f_2 being -3dB frequencies, corresponding to a decrease in amplitude by a factor of $1/\sqrt{2}$ when compared to the amplitude at the resonance frequency, f_r.

- *Piezoelectric coefficients:* the mechanical variables (stress and strain) and the electrical variables (electrical displacement and electric field) are related by the following piezoelectric coefficients.

The piezoelectric charge coefficient, d_{ij}, is defined, at constant electric field [C N^{-1}], by

$$d_{ij} = \frac{\text{charge density in the electrode perpendicular to i-axis}}{\text{applied stress in j-axis}} \tag{2.2}$$

and at constant stress [m V^{-1}] respectively by

$$d_{ij} = \frac{\text{strain in j-axis}}{\text{applied electric field in i-axis}} \tag{2.3}$$

The piezoelectric voltage coefficient, g_{ij}, is defined, at constant electrical displacement [V m N^{-1}], by

$$g_{ij} = \frac{\text{electric field in i-axis}}{\text{applied stress in j-axis}} \tag{2.4}$$

and at constant stress [m^2 C^{-1}] respectively by

$$g_{ij} = \frac{\text{strain in j-axis}}{\text{applied charge density in the electrode perpendicular to i-axis}} \tag{2.5}$$

The piezoelectric coefficient, e_{ij}, is defined, at constant electric field [C m^{-2}], by

$$e_{ij} = \frac{\text{charge density in the electrode perpendicular to i-axis}}{\text{applied strain in j-axis}} \tag{2.6}$$

and at constant strain [N m^{-1} V^{-1}] respectively by

$$e_{ij} = \frac{\text{stress in j-axis}}{\text{applied electric field in i-axis}} \tag{2.7}$$

The piezoelectric coefficient, h_{ij}, is defined, at constant electrical displacement [V m^{-1}], by

$$h_{ij} = \frac{\text{electric field in i-axis}}{\text{applied strain in j-axis}} \tag{2.8}$$

and at constant strain [N C^{-1}] respectively by

$$h_{ij} = \frac{\text{stress in j-axis}}{\text{applied charge density in the electrode perpendicular to i-axis}} \tag{2.9}$$

The four piezoelectric constants are related between them by the following relations, where it was assumed the summation over repeated indexes.

$$\begin{aligned} d_{nj} &= \varepsilon^{T}_{mn} g_{mj} = e_{ni} s^{E}_{ij} \\ e_{nj} &= \varepsilon^{S}_{mn} h_{mj} = d_{ni} c^{E}_{ij} \\ g_{nj} &= \beta^{T}_{mn} d_{mj} = h_{ni} s^{D}_{ij} \\ h_{nj} &= \beta^{S}_{mn} e_{mj} = g_{ni} c^{D}_{ij} \end{aligned} \tag{2.10}$$

The index m and n are electrical indexes and the index i and j are mechanical ones. The superscripts E stands for constant electric field (short-circuit electrodes), D for constant electrical displacement (open circuit electrodes), T for constant stress (material specimen free) and S for constant strain (clamped specimen). The matrices c_{ij} and s_{ij} are respectively the elastic coefficient matrix and the compliance matrix (strain produced per unit stress).

2.2 Finite element formulation

The equations of motion for a laminated composite plate containing piezoelectric elements, acting either as sensors or/and actuators, surface bonded or embedded within the structure, can be derived using Hamilton's principle. The description of movement is done considering a cartesian co-ordinate system and each point in space is defined by the co-ordinates (x, y, z). Hamilton's principle can be written as

$$\int_{t_1}^{t_2} \delta(\mathcal{T} - \mathcal{U} + W_{ext})\, dt = 0 \tag{2.11}$$

where t_1 and t_2 are arbitrary instants, $\mathcal{T}$ is the kinetic energy, $\mathcal{U}$ the potential energy (including strain and electrical energies) and W_{ext} the work done by external forces. For coupled electro-mechanical systems the kinetic, $\mathcal{T}$, and potential energy, $\mathcal{U}$, terms are defined as [38]

$$\mathcal{T} = \int_V \frac{1}{2} \varrho \{\dot{q}\}^T \{\dot{q}\}\, dV \qquad \mathcal{U} = \int_V \frac{1}{2} [\,\{S\}^T \{T\} - \{E\}^T \{D\}]\; dV \tag{2.12}$$

where $\{\dot{q}\} = \partial q / \partial t$ is the velocity vector of any generic point (x, y, z) in space, ϱ the mass density, $\{S\}$ the strain vector, $\{T\}$ the stress vector, $\{E\}$ the electrical field vector and $\{D\}$ the vector of electrical displacements. The integration is done over the volume V of the structure.

Considering only discrete applied external forces, W_{ext}, can be defined as

$$W_{ext} = \sum_{i=1}^{nf} \{q\}_i^T \{F_c\}_i \tag{2.13}$$

with $\{F_c\}_i$ and $\{q\}_i$ being, respectively, the external force vector and the displacement vector acting at $(x, y, z)_i$ and nf the number of applied external forces.

2.2.1 Constitutive equations

The linear theory of piezoelectricity assumes that the deformations are infinitesimal and the electric field is quasi-static, which means that it can be described only by the gradient of the electric potential [63]. Under these assumptions, the linear piezoelectric constitutive equations coupling the elastic field and the electric field vector can be expressed by the direct and the converse piezoelectric equations [38]

$$\{D\} = [e]^T\{S\} + [\epsilon^s]\{E\} \tag{2.14}$$

$$\{T\} = [C^E]\{S\} - [e]\{E\} \tag{2.15}$$

with $[e]$ being the piezoelectric moduli matrix, $[\epsilon^s]$ the dielectric constants matrix evaluated at constant strain and $[C^E]$ the matrix of elastic coefficients of the piezoelectric material at constant electric field. Figure 2.5 shows the components, T_i, of the stress vector $\{T\}$. The last two equations together with Hamilton's principle will be used to derive the equations of motion.

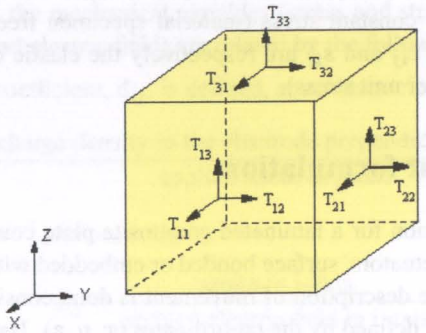

Figure 2.5: *Stress tensor components.*

Normally one can consider piezoelectric materials as transverse isotrope in the plane normal to the polarisation axis, z. In this case, Equations (2.14) and (2.15) can be simplified. Expanding all the terms one obtains

$$\begin{bmatrix} D_1 \\ D_2 \\ D_3 \end{bmatrix} = \begin{bmatrix} 0 & 0 & 0 & 0 & e_{15} & 0 \\ 0 & 0 & 0 & e_{15} & 0 & 0 \\ e_{31} & e_{31} & e_{33} & 0 & 0 & 0 \end{bmatrix} \begin{bmatrix} S_1 \\ S_2 \\ S_3 \\ S_4 \\ S_5 \\ S_6 \end{bmatrix} + \begin{bmatrix} \epsilon^s_{11} & 0 & 0 \\ 0 & \epsilon^s_{11} & 0 \\ 0 & 0 & \epsilon^s_{33} \end{bmatrix} \begin{bmatrix} E_1 \\ E_2 \\ E_3 \end{bmatrix} \tag{2.16}$$

$$\begin{bmatrix} T_1 \\ T_2 \\ T_3 \\ T_4 \\ T_5 \\ T_6 \end{bmatrix} = \begin{bmatrix} C^E_{11} & C^E_{12} & C^E_{13} & 0 & 0 & 0 \\ C^E_{12} & C^E_{11} & C^E_{13} & 0 & 0 & 0 \\ C^E_{13} & C^E_{13} & C^E_{33} & 0 & 0 & 0 \\ 0 & 0 & 0 & C^E_{55} & 0 & 0 \\ 0 & 0 & 0 & 0 & C^E_{55} & 0 \\ 0 & 0 & 0 & 0 & 0 & C^E_{66} \end{bmatrix} \begin{bmatrix} S_1 \\ S_2 \\ S_3 \\ S_4 \\ S_5 \\ S_6 \end{bmatrix} - \begin{bmatrix} 0 & 0 & e_{31} \\ 0 & 0 & e_{31} \\ 0 & 0 & e_{33} \\ 0 & e_{15} & 0 \\ e_{15} & 0 & 0 \\ 0 & 0 & 0 \end{bmatrix} \begin{bmatrix} E_1 \\ E_2 \\ E_3 \end{bmatrix} \tag{2.17}$$

where the notation of Voigt-Kelvin was used, i.e.,

$$\begin{array}{llllll} T_1 = T_{11} & T_2 = T_{22} & T_3 = T_{33} & T_4 = T_{23} & T_5 = T_{13} & T_6 = T_{12} \\ S_1 = S_{11} & S_2 = S_{22} & S_3 = S_{33} & S_4 = S_{23} & S_5 = S_{13} & S_6 = S_{12} \end{array} \tag{2.18}$$

Given this isotropy, the coefficients e_{34}, e_{35} and e_{36} are null, and the actuation and/or sensing of torsion movements can not be done. If the material studied is not isotrope transverse in the reference plane the coefficient e_{36} is non zero and can be used to measure or control torsion movements.

The electric field vector, $\{E\}$, is defined by the electrical potential energy, ϕ, by means of the gradient operator

$$\{E\} = -\nabla\phi \tag{2.19}$$

In the case of non-isotropic materials and when the piezoelectric is cut in other directions different from its orthotropy axes, the stress and strain relations in the material co-ordinate system are related to the global co-ordinate system by the following expressions

$$\{T\}_m = [R]\{T\}_g \tag{2.20}$$

$$\{S\}_m = [R]^{-T}\{S\}_g \tag{2.21}$$

where m stands for material co-ordinates and g for problem co-ordinates. The transformation matrix between the two co-ordinate systems, $[R]$, is given by

$$[R] = \begin{bmatrix} m^2 & n^2 & 0 & 0 & 0 & 2mn \\ n^2 & m^2 & 0 & 0 & 0 & -2mn \\ 0 & 0 & 1 & 0 & 0 & 0 \\ 0 & 0 & 0 & m & n & 0 \\ 0 & 0 & 0 & -n & m & 0 \\ -mn & mn & 0 & 0 & 0 & m^2 - n^2 \end{bmatrix} \tag{2.22}$$

with $m = \cos(\theta_k)$, $n = \sin(\theta_k)$ and θ_k the angle between the two systems.

2.2.2 Strain-displacement relations

The displacement field is based on the Mindlin theory of plates and can be written as (Figure 2.6)

$$\begin{aligned} u(x,y,z,t) &= u_0(x,y,t) + z\theta_y(x,y,t) \\ v(x,y,z,t) &= v_0(x,y,t) - z\theta_x(x,y,t) \\ w(x,y,z,t) &= w_0(x,y,t) \end{aligned} \tag{2.23}$$

where u_0, v_0 and w_0 are the in-plane and transverse displacements of a point (x, y) in the midplane of the laminate ($z = 0$), and θ_x and θ_y are the rotations of a transverse normal about the x and y axes respectively.

This displacement field is equivalent to the one of the first-order shear deformation theory for single-layer laminates [64] and accommodates the transverse shear strains. In the Mindlin formulation it is assumed that a section originally straight and perpendicular to the mid surface of the plate remains straight, but no longer orthogonal, when the plate is extended or bent.

Considering small deformations, the total strain vector can be obtained by substituting Equation (2.23) into the infinitesimal strain tensor, $S_{ij} = \frac{1}{2}(\frac{\partial u_i}{\partial x_j} + \frac{\partial u_j}{\partial x_i})$

$$\{S\} = \{S^0\} + z\{\kappa\} + \{S^s\} \tag{2.24}$$

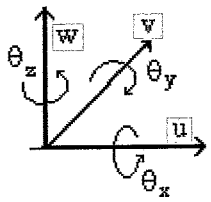

Figure 2.6: *Degrees of freedom in the Mindlin formulation.*

where $\{S^0\} = \{S_x^0, S_y^0, 0, \gamma_{yz}^0, \gamma_{xz}^0, \gamma_{xy}^0\}^T$ are the mid-plane membrane strains, $\{\kappa\} = \{\kappa_x, \kappa_y, 0, 0, 0, \kappa_{xy}\}^T$ the bending (curvature) strains and $\{S^s\} = \{0, 0, 0, \gamma_{yz}^s, \gamma_{xz}^s, 0\}^T$ the transverse shear strains. The strain relations are not function of the material variations through the laminate thickness and consequently the same expressions are valid in any point of the structure. Equation (2.24) can be rewritten as

$$\begin{bmatrix} S_x \\ S_y \\ S_z \\ \gamma_{yz} \\ \gamma_{xz} \\ \gamma_{xy} \end{bmatrix} = \begin{bmatrix} \frac{\partial u_0}{\partial x} \\ \frac{\partial v_0}{\partial y} \\ 0 \\ \frac{\partial w_0}{\partial y} \\ \frac{\partial w_0}{\partial x} \\ \frac{\partial u_0}{\partial y} + \frac{\partial v_0}{\partial x} \end{bmatrix} + z \begin{bmatrix} \frac{\partial \theta_y}{\partial x} \\ -\frac{\partial \theta_x}{\partial y} \\ 0 \\ 0 \\ 0 \\ -\frac{\partial \theta_x}{\partial x} + \frac{\partial \theta_y}{\partial y} \end{bmatrix} + \begin{bmatrix} 0 \\ 0 \\ 0 \\ -\theta_x \\ \theta_y \\ 0 \end{bmatrix} \tag{2.25}$$

It is worth to remark that by choosing the displacement field of Equation (2.23) the strain $S_z = 0$.

The generalised strain vector, $\{\bar{S}\} = \{S_x^0, S_y^0, \gamma_{xy}^0, \kappa_x, \kappa_y, \kappa_{xy}, \gamma_{xz}^t, \gamma_{yz}^t\}^T$, can be defined in terms of the generalised displacement vector, $\{q\}$, and in terms of the differential operator matrix, $[L]$, as follows

$$\{\bar{S}\} = [L]\{q\} \tag{2.26}$$

Expanding all the terms one obtains

$$\begin{bmatrix} S_x^0 \\ S_y^0 \\ \gamma_{xy}^0 \\ \kappa_x \\ \kappa_y \\ \kappa_{xy} \\ \gamma_{xz}^t \\ \gamma_{yz}^t \end{bmatrix} = \begin{bmatrix} \frac{\partial}{\partial x} & 0 & 0 & 0 & 0 & 0 \\ 0 & \frac{\partial}{\partial y} & 0 & 0 & 0 & 0 \\ \frac{\partial}{\partial y} & \frac{\partial}{\partial x} & 0 & 0 & 0 & 0 \\ 0 & 0 & 0 & 0 & z\frac{\partial}{\partial x} & 0 \\ 0 & 0 & 0 & -z\frac{\partial}{\partial y} & 0 & 0 \\ 0 & 0 & 0 & -z\frac{\partial}{\partial x} & z\frac{\partial}{\partial y} & 0 \\ 0 & 0 & \frac{\partial}{\partial x} & 0 & 1 & 0 \\ 0 & 0 & \frac{\partial}{\partial y} & -1 & 0 & 0 \end{bmatrix} \begin{bmatrix} u_0 \\ v_0 \\ w_0 \\ \theta_x \\ \theta_y \\ \theta_z \end{bmatrix} \tag{2.27}$$

2.2.3 Stress-strain relations

The in-plane loads and moment resultant vector, $\{\bar{N}\}$, can be obtained by integrating the stresses over the thickness of the multilayer material

$$\{\bar{N}\} = \{N_x, N_y, N_{xy}, M_x, M_y, M_{xy}, Q_x, Q_y\}^T \tag{2.28}$$

with

$$\{N_x, N_y, N_{xy}, Q_x, Q_y\} = \sum_{k=1}^{N} \int_{-h/2}^{h/2} (T_x, T_y, T_{xy}, T_{xz}, T_{yz})\, dz$$
$$\{M_x, M_y, M_{xy}\} = \sum_{k=1}^{N} \int_{-h/2}^{h/2} (T_x, T_y, T_{xy}) z\, dz \tag{2.29}$$

Taking into account Equation (2.15), Equation (2.28) can be written as the result of two components

$$\{\bar{N}\} = [\bar{D}]\{\bar{S}\} - \{X_p\} \tag{2.30}$$

The first term, $[\bar{D}]\{\bar{S}\}$, represents the resultant of the mechanical stresses while, $\{X_p\}$, the equivalent stress created by the piezoelectrics as a consequence of the actuation strains. The matrix $[\bar{D}]$ is the transformed stiffness matrix of the plate, or one of its plies, in the plate axis system, and is defined in terms of the extensional stiffness matrix, A_{ij}, the bending stiffness matrix, D_{ij}, and the bending-extensional coupling stiffness matrix, B_{ij}.

$$[\bar{D}] = \begin{bmatrix} A_{11} & A_{12} & A_{16} & B_{11} & B_{12} & B_{16} & 0 & 0 \\ A_{12} & A_{22} & A_{26} & B_{12} & B_{22} & B_{26} & 0 & 0 \\ A_{16} & A_{26} & A_{66} & B_{16} & B_{26} & B_{66} & 0 & 0 \\ B_{11} & B_{12} & B_{16} & D_{11} & D_{12} & D_{16} & 0 & 0 \\ B_{12} & B_{22} & B_{26} & D_{12} & D_{22} & D_{26} & 0 & 0 \\ B_{16} & B_{26} & B_{66} & D_{16} & D_{26} & D_{66} & 0 & 0 \\ 0 & 0 & 0 & 0 & 0 & 0 & A_{55} & A_{45} \\ 0 & 0 & 0 & 0 & 0 & 0 & A_{45} & A_{44} \end{bmatrix} \tag{2.31}$$

A_{ij}, D_{ij}, B_{ij} are defined in terms of the lamina stiffness $\{\bar{Q}\}_{ij}^{(k)}$ by

$$(A_{ij}, B_{ij}, D_{ij}) = \sum_{k=1}^{N} \int_{z_{k-1}}^{z_k} \{\bar{Q}\}_{ij}^{(k)} (1, z, z^2)\, dz \qquad (i,j = 1,2,6) \tag{2.32}$$

$$(A_{ij}) = \sum_{k=1}^{N} K \int_{z_{k-1}}^{z_k} \{\bar{Q}\}_{ij}^{(k)} \qquad (i,j = 4,5) \tag{2.33}$$

The transverse shear strains are pre-multiplied by the shear correction coefficient, K. The factor K is computed such that the strain energy due to transverse shear stresses equals the strain energy due to the true transverse stresses predicted by the three-dimensional elasticity theory. It was assumed $K = 5/6$ (Reddy, 1984) [64], [65].

The piezoelectric resultant for the laminate is defined by

$$\{X_p\} = \begin{bmatrix} \{N^P\} \\ \{M^P\} \\ 0 \end{bmatrix} = \begin{bmatrix} \sum_{k=1}^{N} \int_{z_{k-1}}^{z_k} [\bar{e}]^{(k)} \{E\}^{(k)}\, dz \\ \sum_{k=1}^{N} \int_{z_{k-1}}^{z_k} [\bar{e}]^{(k)} \{E\}^{(k)} z\, dz \\ 0 \end{bmatrix} = \begin{bmatrix} \sum_{k=1}^{N} [\bar{e}]^{(k)} V^{(k)} \\ \sum_{k=1}^{N} [\bar{e}]^{(k)} V^{(k)} z_k^0 \\ 0 \end{bmatrix} \tag{2.34}$$

where $\bar{[e]}^{(k)}$ is transformed piezoelectric moduli and $\{E\}^{(k)} = V^{(k)}/h_k$. $V^{(k)}$ is the electric voltage applied across the k^{th} layer, h_k is the thickness of the k^{th} layer, and z_k^0 is the z distance of the lamina mid-plane from the laminate mid-plane, defined by [66]

$$z_k^0 = \frac{1}{2}(z_k + z_{k-1}) \tag{2.35}$$

2.2.4 Finite element discretisation

The displacement field and the electrical potential over an element can be defined in terms of i nodal variables via the shape functions matrices $[N_q]$ and $[N_\phi]$

$$\{q\} = [N_q]\{q_i\} \qquad \{\phi\} = [N_\phi]\{\phi_i\} \tag{2.36}$$

where $\{q_i\}$ is the mechanical generalised co-ordinates and $\{\phi_i\}$ the potential generalised co-ordinates.

Considering Equations (2.19) and (2.26), the electrical and the strain fields can be rewritten function of the potential and of the nodal displacements via the shape functions derivatives, $[B_\phi]$ and $[B_q]$

$$\{E\} = -\nabla\{\phi\} = [B_\phi]\{\phi_i\} \quad , \quad [B_\phi] = -\nabla[N_\phi] \tag{2.37}$$

$$\{S\} = [L]\{q\} = [B_q]\{q_i\} \quad , \quad [B_q] = [L][N_q] \tag{2.38}$$

2.2.5 Finite element code

In this work the structure plus sensor/actuator system are modelled using a four node, bilinear displacement element based on the Mindlin theory of plates (Mindlin, 1951) [8], [65]. This element exhibits good accuracy when dealing with both thick and thin plates in the case that uniform reduced (one point) numerical integration is used to evaluate the element matrices. Since single point integration is not able to capture bilinear contributions to the displacement field, the resulting element is rank deficient and therefore the assembled stiffness may exhibit singularities. Hourglass stabilisation technique has been introduced to control this behavior (Brockman, 1986). The main advantages of the element stems from its simplicity, computational efficiency and high accuracy.

The equations of motion were discretised using quadrilateral shell elements with four nodes. Each node has six degrees of freedom for the elastic behaviour, $q = \{u, v, w, \theta_x, \theta_y, \theta_z\}_i$, and there is one potential degree of freedom (voltage across the thickness) per piezoelectric layer, $\phi = \{\phi_1, ..., \phi_{np}\}$, with np being the number of piezoelectric layers. Figure 2.7 shows the mechanical and the electrical degrees of freedom for a finite element of a composite plate.

It is assumed that the potential degrees of freedom are constant along the piezoelectric layer and vary linearly through the thickness. Consequently, and as widely assumed, the electrical degrees of freedom only receive a contribution from the prescribed potentials, while the induced potential is neglected. Each lamina in the composite plate is presumed to be perfectly bonded, as well as, the bond are presumed to be infinitesimally thin. In the model the thin bonding layer between the piezoelectric and the laminate was neglected [25].

For this bilinear 4-node element the following shape functions were considered

$$N = \frac{1}{4}(\bar{C} + \bar{\xi}\xi + \bar{\eta}\eta + \bar{H}\xi\eta) \tag{2.39}$$

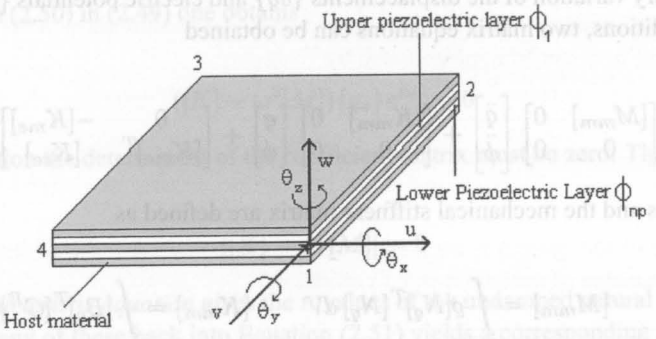

Figure 2.7: *Mechanical and electrical degrees of freedom of a finite element of a composite plate [65].*

with

$$\begin{aligned} C^T &= [1,1,1,1] \\ \xi^T &= [-1,1,1,-1] \\ \eta^T &= [-1,-1,1,1] \\ H^T &= [1,-1,1,-1] \end{aligned} \tag{2.40}$$

As it is defined, each shape function at node i assumes a unit value and vanishes at all other nodes of the element and along all sides of the element that do not contain node i.

2.3 Equations of motion

The equations of motion are derived by substituting the kinetic and the potential energies, Equation (2.12), and the term of virtual work, Equation (2.13), into Hamilton's principle. Integrating the variation of the kinetic energy term, $\varrho\{\delta q\}^T\{\ddot{q}\}$, by parts over the time integral and taking into account the constitutive equations, yields

$$\int_{t_1}^{t_2}\{\int_V (-\varrho\{\delta q\}^T\{\ddot{q}\} - \{\delta S\}^T[C^E]\{S\} + \{\delta E\}^T[\epsilon^s]\{E\} + \{\delta E\}^T[e]^T\{S\} + \{\delta S\}^T[e]\{E\})\,dV + \sum_{i=1}^{N}\{\delta q\}^T\{F_c\}\}\,dt = 0 \tag{2.41}$$

Substituting Equations (2.36), (2.37) and (2.38) into the variational principle (2.41) one obtains

$$\begin{aligned} 0 = &-\int_V \varrho\{\delta q_i\}^T[N_q]^T[N_q]\{\ddot{q_i}\}\,dV - \int_V \{\delta q_i\}^T[B_q]^T[C^E][B_q]\{q_i\}\,dV \\ &+ \int_V \{\delta q_i\}^T[B_q]^T[e][B_\phi]\{\phi_i\}\,dV + \int_V \{\delta\phi_i\}^T[B_\phi]^T[e]^T[B_q]\{q_i\}\,dV \\ &+ \int_V \{\delta\phi_i\}^T[B_\phi]^T[\epsilon^s][B_\phi]\{\phi_i\}\,dV + \sum_{i=1}^{N}\{\delta q_i\}^T[N_q]^T\{F_c\} \end{aligned} \tag{2.42}$$

For any arbitrary variation of the displacements $\{\delta q\}$ and electric potentials $\{\delta\phi\}$, verifying the essential boundary conditions, two matrix equations can be obtained

$$\begin{bmatrix} [M_{mm}] & 0 \\ 0 & 0 \end{bmatrix} \begin{bmatrix} \ddot{q} \\ \ddot{\phi} \end{bmatrix} + \begin{bmatrix} [K_{mm}] & 0 \\ 0 & 0 \end{bmatrix} \begin{bmatrix} q \\ \phi \end{bmatrix} + \begin{bmatrix} 0 & -[K_{me}] \\ [K_{me}]^T & [K_{ee}] \end{bmatrix} \begin{bmatrix} q \\ \phi \end{bmatrix} = \begin{bmatrix} F \\ 0 \end{bmatrix} \tag{2.43}$$

where the mass and the mechanical stiffness matrix are defined as

$$[M_{mm}] = \int_V \varrho [N_q]^T [N_q]\, dV \qquad [K_{mm}] = \int_V [B_q]^T [C^E] [B_q]\, dV \tag{2.44}$$

the coupled electrical/mechanical stiffness and the piezoelectric stiffness matrix as

$$[K_{me}] = \int_V [B_q]^T [e] [B_\phi]\, dV \qquad [K_{ee}] = \int_V [B_\phi]^T [\epsilon^s] [B_\phi]\, dV \tag{2.45}$$

and the forcing matrix as

$$\{F\} = \sum_{i=1}^{nf} [N_q]^T \{F_c\} \tag{2.46}$$

Assembling the matrices obtained for each element and considering the boundary conditions, the global matrices that define the dynamics of our system can be calculated. Equation (2.43) can be rewritten in two separated equations, one referring to the actuation and the other to the sensing

$$[M_{mm}]\{\ddot{q}\} + [K_{mm}]\{q\} - [K_{me^a}]\{\phi^a\} = \{F\} \tag{2.47}$$

$$[K_{me^s}]^T \{q\} + [K_{e^s e^s}]\{\phi^s\} = 0 \tag{2.48}$$

where $[K_{me^a}]$ is formed by the columns of $[K_{me}]$ referring to the actuation patches, $[K_{me^s}]$ by the columns of $[K_{me}]$ referring to the sensing patches and $[K_{e^s e^s}]$ by the lines and by the columns of $[K_{ee}]$ referring to the sensing patches.

2.3.1 Modal analysis

The undamped natural frequencies and the natural modes of a generic multi-degree of freedom system are obtained by solving the equation

$$[M]\{\ddot{q}\} + [K]\{q\} = 0 \tag{2.49}$$

where $[M]$ and $[K]$ are the global mass and stiffness matrices obtained using the finite element method. If an harmonic solution with frequency ω is assumed for the above equation, and considering that the whole system is capable of vibrating at that single frequency, $\{q(t)\}$ has the form

$$\{q(t)\} = \{q_o\} e^{i\omega t} \tag{2.50}$$

Substituting Equation (2.50) in (2.49) one obtains

$$([K] - \omega^2[M])\{q_o\}e^{i\omega t} = 0 \tag{2.51}$$

For a non trivial solution the determinant of the coefficient matrix must be zero. That is

$$|[K] - \omega^2[M]| = 0 \tag{2.52}$$

The roots of the *characteristic equation* gives the n values of the undamped natural frequencies (ω_1^2, ω_2^2, ..., ω_n^2). Substituting any of these back into Equation (2.51) yields a corresponding set of relative values for $\{q_o\}$, the so-called vibration modes Φ_1, Φ_2, ..., Φ_n. Instead of using the mass and stiffness matrices to fully characterise the system one can use the eigenmatrices: $[\omega_n^2]$ and $[\Phi_1 ... \Phi_n]$.

While the eigenvalue matrix is unique, the eigenvector matrix is subjected to an indeterminate scaling factor which affects not the mode shape but the amplitude of that mode. Therefore, the amplitude is not an intrinsic property of the system but something depending on the initial conditions and on the type of the solicitation.

The matrices $[M]$ and $[K]$ are generally band-diagonal matrices. However, due to the fact that modal shapes are orthogonal with respect to both mass and stiffness matrices, it is possible to choose a co-ordinate system where the equations of motion are decoupled. Among the several scaling or normalisation processes the one which is most relevant to modal testing is the normalisation with respect to the mass matrix [67]. The mass-normalised eigenvectors are written as $[\Psi]$ and have the particular property that

$$[\Psi]^T[M][\Psi] = [I] \tag{2.53}$$

where $[I]$ is the identity matrix. Consequently one obtains the following relation

$$[\Psi]^T[K][\Psi] = [\omega_n^2] \tag{2.54}$$

The eigenvectors are linearly independent due to their property of orthogonality. Hence, they form a basis in the n-dimensional space. This means that any possible and arbitrary configuration of the system may be represented by a linear combination of the eigenvectors

$$q(t) = \sum_{i=1}^{n} c_i[\Psi]_i \tag{2.55}$$

where c_i are constants. Each of these constants is a measurement of the mode participation in the system response.

Modal reduction

Using the orthogonality of the eigenvectors with respect to the mass matrix and the stiffness matrix, the modal co-ordinates, η, are introduced as follows

$$q(t) = [\Psi]\eta(t) \tag{2.56}$$

For controlling the vibrations of a structure one mainly tries to act at the level of the maximum amplitudes of oscillation. The contribution of each mode is, in general, inversely proportional to the square of the

frequency, and therefore, only the first few modes play an important role in the response of the system. Assuming that the final response can be written as a linear combination of the the first r vibration modes, the displacement $q(t)$ can be approximated by

$$q(t) \approx \sum_{i=1}^{r} [\Psi]_i \eta_i(t) \tag{2.57}$$

The dimension of the system is no longer the number of the degrees of freedom of the finite element model but the number of modes chosen to model it.

2.3.2 Analysis with damping included

Damping in composite materials plays an important role in the dynamic problem and in general can not be neglected. In order to include the damping effects in the formulation, Equation (2.43) can be slightly modified

$$[M_{mm}]\{\ddot{q}\} + [C_{mm}]\{\dot{q}\} + [K_{mm}]\{q\} - [K_{me}]\{\phi\} = \{F\} \tag{2.58}$$

The $[C_{mm}]$ matrix is the damping matrix and its purpose is to approximate the energy dissipated during the system response. In general, and contrary to mass and stiffness matrices, the damping matrix can not be constructed from the assemblage of element damping matrices. If Rayleigh or proportional damping is assumed, which is an adequated assumption in most analyses, the modal damping matrix can be written as function of the mass and mechanical stiffness matrices as

$$[C] = \alpha[M_{mm}] + \beta[K_{mm}] \tag{2.59}$$

where α and β are the damping parameters. For Rayleigh damping, the damping matrix has the advantage of possesing the same characteristics as the mass or stiffness matrices. This means that the eigenvectors, $[\Psi_i]$, are also orthogonal to the $[C_{mm}]$ matrix (Bathe, 1982) [68] that becomes, in this case, diagonal

$$[\Psi_i]^T [C_{mm}][\Psi_i] = 2\omega_i \xi_i \delta_{ij} \tag{2.60}$$

with ξ_i being the modal damping ratios and δ_{ij} the Kronecker delta function. By using Equations (2.59) and (2.60) one obtains

$$[\Psi_i]^T (\alpha[M_{mm}] + \beta[K_{mm}])[\Psi_i] = 2\omega_i \xi_i \delta_{ij} \tag{2.61}$$

or

$$\alpha + \beta\omega_i^2 = 2\omega_i \xi_i \tag{2.62}$$

which can be used for determining the damping parameters α and β once two of the damping rations, ξ_i, are known.

A more complicated scheme can be considered to calculate the damping matrix. Namely, given p damping ratios ξ_i, $i = 1, 2, ..., p$, it can be shown that the damping matrix obeying Equation (2.60) can be obtained by using the Caughey series [68]

$$[C_{mm}] = [M_{mm}] \sum_{k=0}^{p-1} a_k [[M_{mm}]^{-1} \quad [K_{mm}]]^k \tag{2.63}$$

where the coefficients a_k, $k = 1, ...p$, are calculated from the p simultaneous equations

$$\xi_i = \frac{1}{2}\left(\frac{a_0}{\omega_i} + a_1\omega_i + a_2\omega_i^3 + ... + a_{p-1}\omega_i^{p-3}\right) \tag{2.64}$$

In the case $p = 2$, Rayleigh damping is obtained. One of the advantages of considering proportional damping is that, the *frequency of damped vibration*, ω_d, can be derived from the undamped frequency, ω_a, only by making a small correction: $\omega_d = \omega_a\sqrt{1-\xi^2}$

2.3.3 Reduced modal equations

Taking into account the mass normalisation process, Equations (2.47) and (2.48) can be rewritten in the modal space by

$$\{\ddot{\eta}\} + [2\xi\omega]\{\dot{\eta}\} + [\omega^2]\{\eta\} - [\Psi]^T[K_{me^a}]\{\phi^a\} = [\Psi]^T\{F\} \tag{2.65}$$

$$[K_{me^s}]^T[\Psi]\{\eta\} + [K_{e^se^s}]\{\phi^s\} = 0 \tag{2.66}$$

The last two equations fully describe the system and will be used throughout this work.

Chapter 3

Control Theory

This chapter presents the use of several control design methodologies for vibration damping in mechanical structures integrated with piezoelectric sensors and actuators. Constant gain feedback control and constant amplitude feedback control are the first two methodologies applied to the vibration control of a clamped-free carbon fibre composite beam. Simulation results and experimental measurements are compared with the objective of validating the mathematical models and the implementation of the control laws.

Modern control methods using Linear Quadratic Gaussian with Loop Transfer Recovery (LQG/LTR) are also discussed and applied to the vibration control of a beam structure. The main characteristic of this method is related with the linear dependence of the control input with the state vector or the observation vector. Only based on a numerical approach (MATLAB & SIMULINK ® software), the several cases that will be presented schematise and apply the concepts behind an active control strategy.

In all experimental measurements and simulations, only collocated sensors/actuators were considered. This property presents several advantages. Namely, all the modes are sensed in the same phase and for lightly damped structures collocated sensors/actuators always lead to alternating poles and zeros contributing to the stability and robustness of a wide class of systems. The main drawback is related with the fact that the sensor is in the local strain field of the actuator, so in addition to modal dynamics, there is a large amount of "quasi-static feedthrough" of local actuated stress. This means that the sensor is also picking the actuation and the signal to noise ratio may be degraded. Near collocated sensors/actuators (placed closed to the actuator but outside its strain field) may be a good compromise that will not be exploited here.

3.1 Feedback control methodologies

Control design processes can be used to enhance the damping properties of a system and thus its performance. The several steps involved in the design of a controlled structure are shown schematically in Figure 3.1. The starting point is the mathematical model of the system, the definition of the performance requirements and the knowledge of the disturbances that will be applied to it. The system's model may be developed using two different approaches: the analytical and the experimental approach. The first method is based in the application of the mathematical and physical laws and on methods such as the finite element method and the Rayleigh Ritz method [64] to solve the governing equations. The second approach consists in experimentally measuring the mathematical relations existent between a group of inputs and outputs of the system. Identification methods, related to the modal analysis, such as ARMA and NARMAX can be used for the purpose. The combination of the two approaches represents in general the best way for describing the system [60].

Once the system model is known, the open loop response can then be evaluated and the necessity of active control can be assessed. The next step consists in defining the type, the number and the position

of a set of actuators and sensors. Once the geometry is known in detail a finite element model of the structure is generally developed. The knowledge of some frequency response functions of the system enhance the validity of the mathematical model.

Generally, these models involve an high number of degrees of freedom, so modal transformation is normally used to reduce the model size. If the presence of sensors and actuators influence the dynamics of the system, they must be taken into account in the model before the controller design. Prior to the digital implementation of the controller, the control methodology is chosen and the closed loop performance of the system tested.

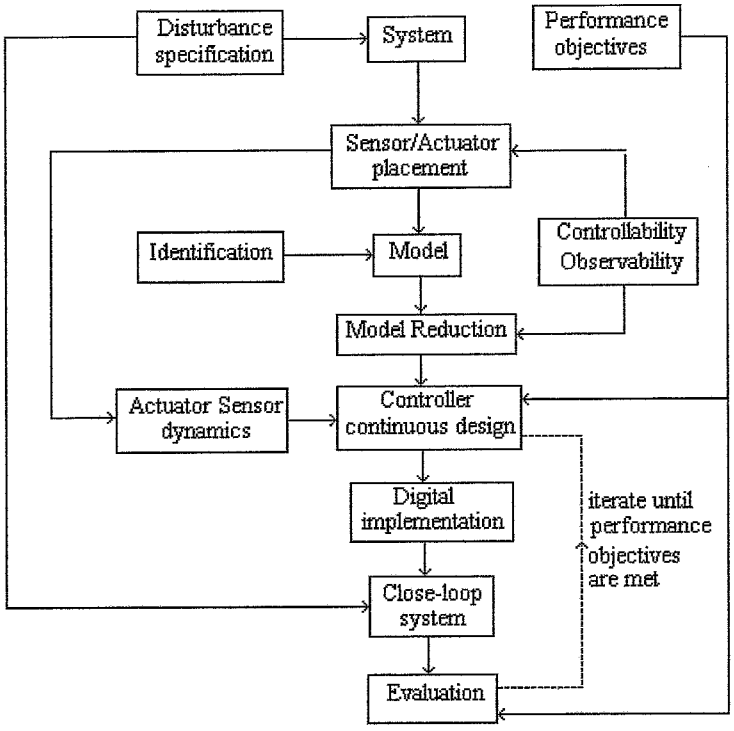

Figure 3.1: *Steps of the design of a controlled structure [69].*

One of the most commonly used control strategies for disturbance rejection, stabilisation and protection against model uncertainties is *feedback control.* It consists in measuring the outputs of the process to control, compare them with a reference input, eventually modify them, and fed back that information to the inputs of the system influencing in this way the control variables.

Next sections, together with some concepts related to modern control theory, will present the results obtained with three different control design methods: constant amplitude feedback control, constant gain feedback control and the robust control design methodology LQG/LTR.

3.2 State-space model

State-space methods are the basis of *modern control theory.* Different factors have contributed to the development of this theory. Namely, the necessity of working with more realistic models, the increase of the computation capabilities, the recent developments concerning optimal control and optimal conception of systems and the use of linear algebra to deal with problems governed by differential equations.

The characterisation of the process is no longer done by transfer functions and the system is described in terms of state variables. This means, on one side, that a larger number of variables can be taken into

consideration by the model and, on the other side, that the model is closer to the reality since it is more susceptible of taking into account the non linearities and the time variations of certain parameters. Therefore, the main advantages of state-space representation are related with the easiness of representing systems with an high number of inputs and outputs, time varying and non linear systems.

The majority of the dynamic systems can be described by Lagrange equations of the form

$$\ddot{q}(t) = f(q(t), \dot{q}(t), Q(t)) \tag{3.1}$$

where $q(t)$ represents the generalised co-ordinated vector, $\dot{q}(t)$ the generalised velocities, $\ddot{q}(t)$ the acceleration vector and $Q(t)$ the generalised force vector (including the control forces). If $x(t)$ is the state vector of the system;

$$x(t) = \begin{bmatrix} \dot{q}(t) \\ q(t) \end{bmatrix} \tag{3.2}$$

the system equations may be rewritten in the following generalised form

$$\dot{x}(t) = a(x(t), Q(t)) \tag{3.3}$$

where

$$a(t) = \begin{bmatrix} \ddot{q}(t) \\ f(q(t), \dot{q}(t), Q(t)) \end{bmatrix} \tag{3.4}$$

Equation (3.3) is the basis of the control of linear systems and when rewritten in the matrix form represents the generalised state-space equations describing the state variation of a continuous system

$$\dot{x} = [A]x + [B]u + [F]v \tag{3.5}$$

$$y = [C]x + [D]u + w \tag{3.6}$$

where $x = [x_1, x_2, ..., x_k]^T$ is the system state vector, $u = [u_1, u_2, ..., u_m]^T$ the control input vector, y the control output vector, v the system input noise vector, $[A]$ the matrix of dynamics, $[B]$ the input matrix, $[C]$ the output matrix, $[D]$ the feedthrough matrix, $[F]$ the disturbance matrix of the state vector and w, the measurement's disturbance vector. The system input noise, v, generally takes into account modelling errors, environmental loads, non modelled dynamics, non linearities and the noise in the input vector. The measurement noise, w, includes the sensor noise and modelling errors. For time-invariant systems the previous matrices are constant matrices, thus, not function of time. The corresponding block diagram is shown in Figure 3.2.

The equations of motion (2.65) and (2.66) written in the modal space and presented in Section 2.3.3 can be rewritten in a state-space form by

$$\begin{bmatrix} \ddot{\eta} \\ \dot{\eta} \end{bmatrix} = \begin{bmatrix} -[2\xi\omega] & -[\omega^2] \\ [I] & 0 \end{bmatrix} \begin{bmatrix} \dot{\eta} \\ \eta \end{bmatrix} + \begin{bmatrix} [\Psi]^T[K_{me^a}] \\ 0 \end{bmatrix} \phi^a \tag{3.7}$$

$$\phi^s = \begin{bmatrix} 0 & -[K_{e^s e^s}]^{-1}[K_{me^s}]^T[\Psi]] \end{bmatrix} \begin{bmatrix} \dot{\eta} \\ \eta \end{bmatrix} \tag{3.8}$$

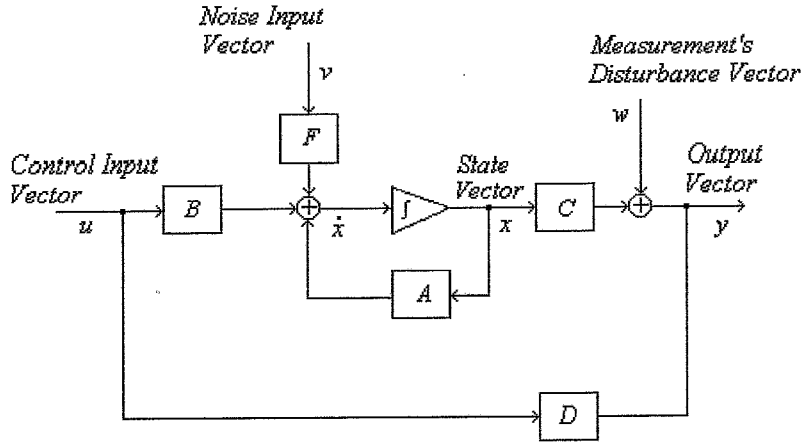

Figure 3.2: *Block-diagram representation of a general linear system in state variable form [70].*

where

$$[A] = \begin{bmatrix} -[2\xi\omega] & -[\omega^2] \\ [I] & 0 \end{bmatrix} \tag{3.9}$$

$$[B] = \begin{bmatrix} [\Psi]^T[K_{me^a}] \\ 0 \end{bmatrix} \tag{3.10}$$

$$[C] = \begin{bmatrix} 0 & -[K_{e^se^s}]^{-1}[K_{me^s}]^T[\Psi] \end{bmatrix} \tag{3.11}$$

$$[D] = [0] \tag{3.12}$$

The terms relative to disturbances, v and w, are not included here since the finite element model does not take them into account. It is only when the controller is being modelled that these terms are included in the simulation. The above equations are used to model the systems dynamics and to design the controller.

3.3 Constant amplitude/gain feedback control - Experimental results

Feedback control may act in the system's outputs. This means that the control input vector, $u(t)$, is function of the measurements (control output vector of the system), $y(t)$, and not directly function of the global state, $x(t)$. This approach will be used in two control methodologies, constant amplitude/constant gain feedback control, and will be presented in detail in the next two sections. Simulations, performed using MATLAB & SIMULINK ®, and experimental measurements will be compared for both cases.

The experimental set-up comprised a graphite T300/epoxy cantilever beam (Figure 3.3) with two symmetrically bonded piezoceramics, the so called collocated sensor/actuator.

The beam, with a stacking sequence of $[0°/45°]_{2s}$, has an Young's Modulus of 59 GPa and a density of 1438 Kg/m^3. The piezoceramic pair is a 0.2 mm thick P1-91 piezoceramic block from Quartz & Silice with 36 mm long and 12 mm wide. Its mechanical properties are shown in Table 3.1.

The piezoelectric patches were sampled and controlled by a 12-bit data acquisition board (National Instruments) with a maximum sampling rate of 500 KHz. The saturation voltage in each piezoelectric

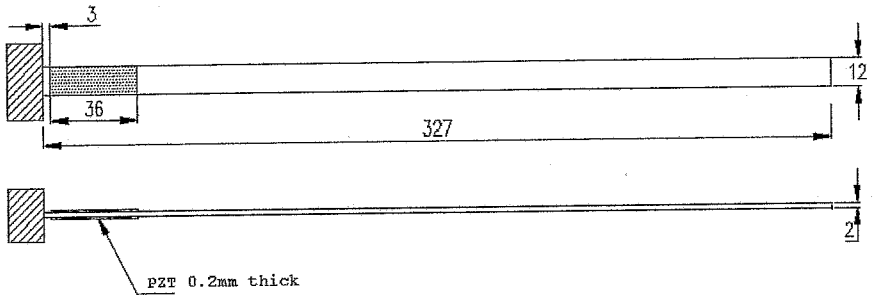

Figure 3.3: *Dimensions [mm] of the T300/Epoxy cantilever beam. One pair of PZT patches attached to a 2 mm thick carbon fibre beam.*

Table 3.1: *Material properties for the P1-91 piezoceramic material (data from the manufacturer).* $[C^E]$ *is the matrix of elastic coefficients at constant electric field,* $[d]$ *the piezoelectric module matrix,* $[\epsilon^s]$ *the dielectric constants matrix evaluated at constant strain and* ϱ *the material density.*

$C_{11}^E\ [N/m^2]$	12.09x10^{10}	$d_{31}\ [m/V]$	-247x10^{-12}
$C_{12}^E\ [N/m^2]$	7.63x10^{10}	$d_{33}\ [m/V]$	600x10^{-12}
$C_{13}^E\ [N/m^2]$	7.31x10^{10}	$d_{15}\ [m/V]$	509x10^{-12}
$C_{33}^E\ [N/m^2]$	11.26x10^{10}	$\epsilon_{11}^s/\epsilon_0$	1820
$C_{44}^E\ [N/m^2]$	3.36x10^{10}	$\epsilon_{33}^s/\epsilon_0$	1461
$C_{66}^E\ [N/m^2]$	2.23x10^{10}	$\varrho\ [Kg/m^3]$	7410

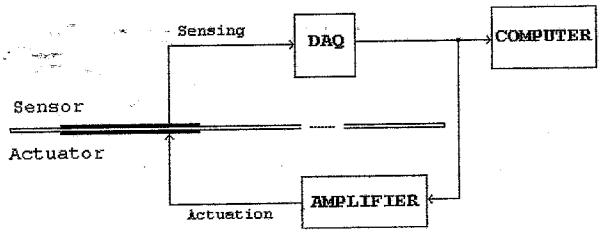

Figure 3.4: *Layout of the general experimental set-up used in the constant amplitude/gain feedback control.*

element was fixed by the voltage limitations of the experimental set up, in this case of the controllable gain power amplifier, at a maximum of $\pm$ 150 Volt (Figure 3.4).

In the simulations the thin bonding layer between the piezoelectric and the composite beam was not taken into account. A finite element model of the composite beam with 2×10 plate elements was considered. A displacement field identical to the first vibration mode (cubic polynomial $ax^3 + bx^2$) was imposed as the initial condition. Namely, a tip displacement of 1.4 mm that corresponds to a modal amplitude of 0.000073 was considered (modal vectors were normalized with respect to the mass matrix). The first four modes of the system were used to obtain the state-space model. The corresponding open loop damping factors of the first four natural frequencies, determined by modal testing, were equal to ξ=[0.0031, 0.00081, 0.00045, 0.00028].

The determination of the modal characteristics of the clamped free beam (Figure 3.3) were performed using an impact hammer in a frequency bandwidth of 0-800 Hz with a frequency resolution of 1 Hz. The

excitation force was measured using a piezoelectric force transducer mounted directly at the head of the hammer, while the response in velocity was measured using a non-contact laser vibrometer. The force and velocity signals, measured in a 6-point mesh, were introduced into a spectrum analyser used to estimate the mobility between the excitation point and the response points.

The response of the system without control, for the first two and four seconds, is presented in Figure 3.5 and Figure 3.6, which respectively show a comparison between experimental and simulated sensing voltage and the correspondent simulated tip displacement. Experimental results are only available for the output or sensing voltage.

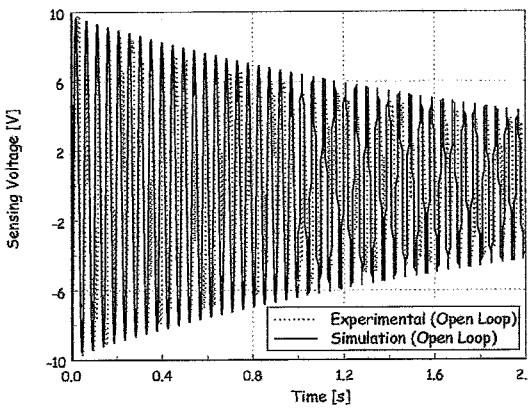

Figure 3.5: *Comparison of the sensing voltage obtained experimentally and by simulation without control.*

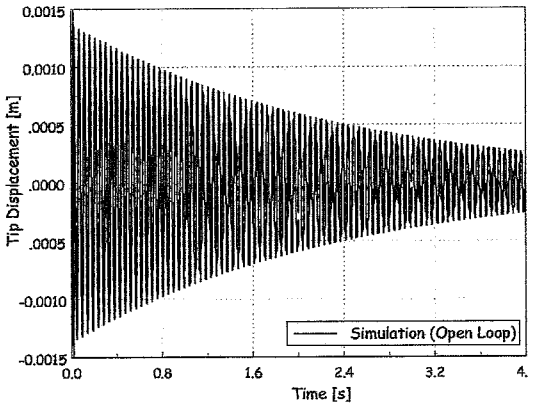

Figure 3.6: *Tip displacement obtained by simulation without control.*

It can be seen that the simulated data presents a slightly lower damping when compared to the data obtained experimentally. The difference between both, and for the sensing voltage, is in the order of 3%. If the experimental first natural frequency, equal to 21.12 Hz, is compared with the one obtained in the simulations a difference less than 1% is found, which means that the time delay existent in the data acquisition of the sensing voltage is not significant and can be ignored in the simulation model. This assumption can not be directly extrapolated to the case of the data acquired in closed loop since that situation involved not only the time delay introduced by the data acquisition board but also the time delay introduced by the power amplifier.

3.3.1 Constant amplitude feedback control

Piezoelectric sensors generate an output voltage when subjected to deformations, for instance, induced by the oscillation of a mechanical structure. This signal, amplified and fed back into the piezoelectric actuator induces opposite strains which result in a counteracting effect that will oppose the deformation of the structure. The feedback force can increase significantly the structure's damping and thus suppress the vibrations of the system. In the case of constant amplitude feedback control the feedback signal amplitude is constant and the sign is opposite to the one of the sensing voltage. Figure 3.7 shows the mathematical model built in MATLAB & SIMULINK ® for this case.

The main block in the diagram - Dynamic model of the plate with piezo sensors/actuators - represents the system dynamics and is defined by the matrices $[A]$, $[B]$, $[C]$ and $[D]$. The input vector is the actuation voltage, while the output vectors are sensor voltages and the state vector, this last one containing the modal displacements and the velocities function of the variable time. A detail of the system dynamics block is shown in Figure 3.8.

The system dynamics block contains the state-space model of the mechanical structure. The implementation was performed in order to have both outputs: sensor voltages and modal state vector available.

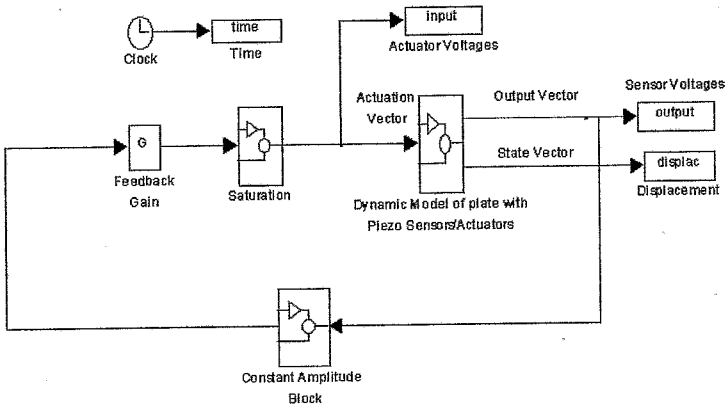

Figure 3.7: *Model of a constant amplitude feedback controller.*

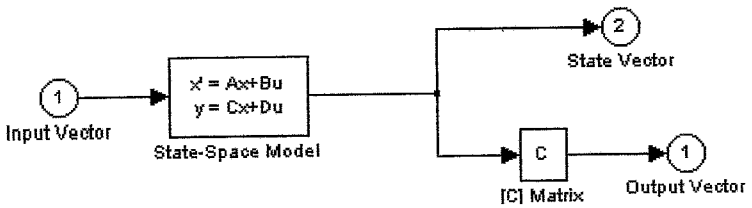

Figure 3.8: *Detail of the system dynamics block.*

This was obtained by introducing separately the matrix $[C]$. Piezoelectric elements acting as actuators have a voltage saturation fixed at ± 150 Volt as already mentioned. A detail of the saturation block together with the constant amplitude block is shown in Figure 3.9 and Figure 3.10, respectively.

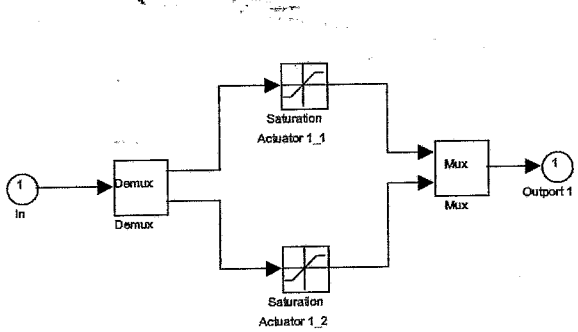

Figure 3.9: *Detail of the saturation block.*

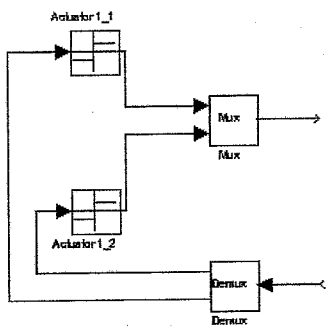

Figure 3.10: *Detail of the constant amplitude block.*

The saturation block guarantees that the voltage in each piezoelectric actuator is less than the saturation voltage. In the case of constant amplitude feedback this block is redundant since the amplitude of the actuation voltage is constant and fixed a priori. The finite element mesh of the structure divided the piezoelectric patch in two elements which explains the existence of two blocks in the saturation and in the constant amplitude blocks. Each function block: Actuator1_1 and Actuator1_2 returns "1" if the sensor voltage is greater than zero, "0" if it equals zero and "-1" if it is less than zero. The amplitude is then fixed by the feedback gain block shown in Figure 3.7.

The response in closed loop was determined experimentally for several amplitude gains ranging from

0 to ±30 Volt [2]. The correspondent damping coefficients of the system, ξ_i, were calculated by means of the logarithmic decrement, δ. For small damping ratios ($\xi \ll 1$) it can be shown that the relation between these two variables is given by [71]

$$\xi = \frac{\delta}{2\pi} = \frac{1}{2\pi n} \log \frac{x_i}{x_{i+n}} \tag{3.13}$$

where n is the number of cycles and x_i the amplitude of the cycle i. Figure 3.11 shows the damping coefficient, calculated with the previous expression using data obtained experimentally, as function of the amplitude gain.

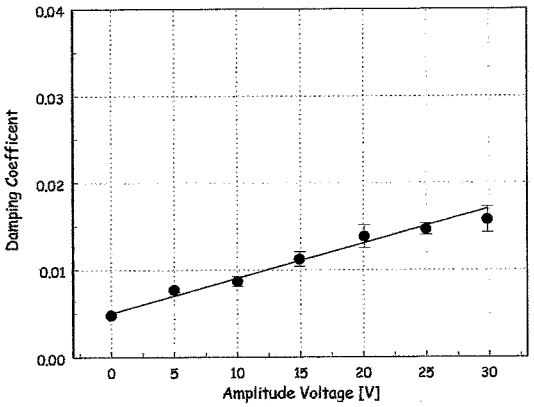

Figure 3.11: *Effect of constant amplitude feedback on the overall damping coefficient of the system. Experimental results.*

As expected, for small oscillations, the overall damping coefficient of the system increases linearly with the constant applied voltage and can be approximated by: $\xi = 0.005 + 0.0004V$. Each point in the graphic represents an average of five values and the error bars the standard deviation associated with the sample.

The performance of the system was simulated for two different amplitudes: $A_1 = \pm 5$ Volt and $A_2 = \pm 10$ Volt and the results were compared to the ones obtained experimentally. For an amplitude gain feedback of ±5 Volt, Figure 3.12 shows the comparison between the experimental and the simulated output voltage at the sensor level and Figure 3.13 and Figure 3.14 show, for the same case, the correspondent actuation voltage and the tip displacement, respectively.

A good agreement between experimental measurements and simulation results was found concerning the sensing voltage. Once again the experimental results present an higher damping when compared to the ones obtained by simulation. Namely the difference between the overall damping is in the order of 8%. Experimentally, it can be verified that the controller induces some instabilities at very small deflections of the beam. These can be related to the time delay between sensing and actuation that exist in practice and which is more important than the one found in open loop. Figure 3.13 shows clearly the relation between the voltage applied to the actuator compared with the one on the sensor. As already mentioned, no time delay was introduced in the simulations between the sensor's reading and the actuation since the agreement between experimental and simulation results is still very good.

The next plots, Figure 3.15, Figure 3.16 and Figure 3.17, show, for a different amplitude gain $A_2 = \pm 10$ Volt, the comparison between the experimental and the simulated sensing voltage, the simulated actuation voltage and the tip displacement of the beam.

The controller induces some instabilities for small deflections of the beam, this time more relevant than the ones observed for $A_1 = \pm 5$ Volt. The approximation to an exponential of the decay, as function

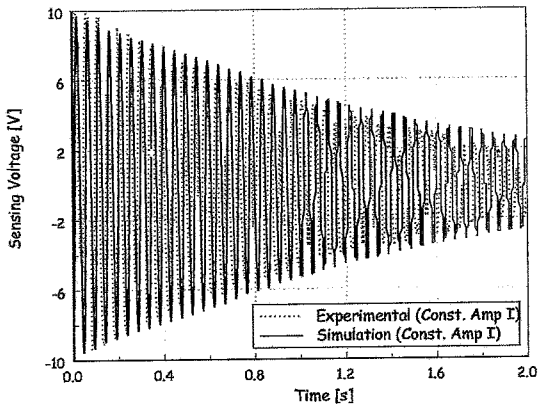

Figure 3.12: *Comparison of the sensor voltage, in closed loop, obtained experimentally and by simulation for a constant amplitude feedback of $A_1 = \pm 5$ Volt.*

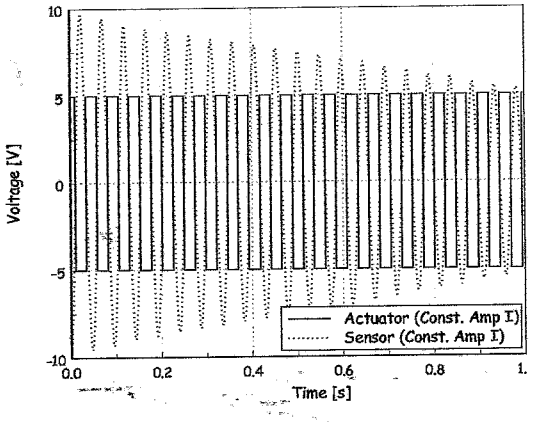

Figure 3.13: *Actuation voltage, in closed loop, obtained by simulation for a constant amplitude feedback of $A_1 = \pm 5$ Volt.*

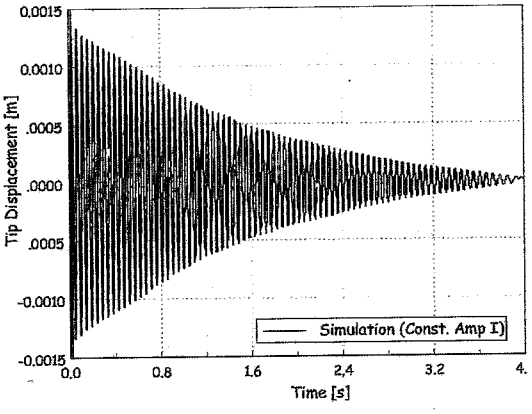

Figure 3.14: *Tip displacement, in closed loop, obtained by simulation for a constant amplitude feedback of $A_1 = \pm 5$ Volt.*

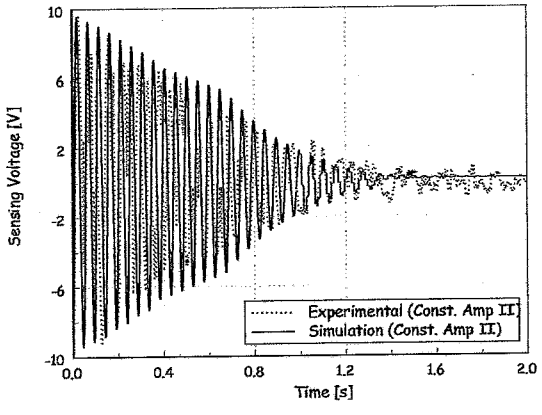

Figure 3.15: *Comparison of the sensor voltage, in closed loop, obtained experimentally and by simulation for a constant amplitude feedback of $A_2 = \pm 10$ Volt.*

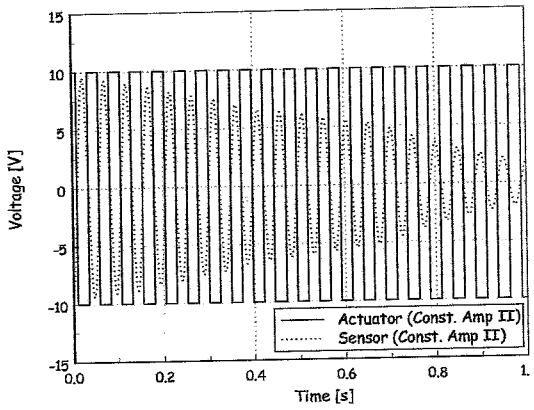

Figure 3.16: *Actuation voltage, in closed loop, obtained by simulation for a constant amplitude feedback of* $A_2 = \pm 10$ *Volt.*

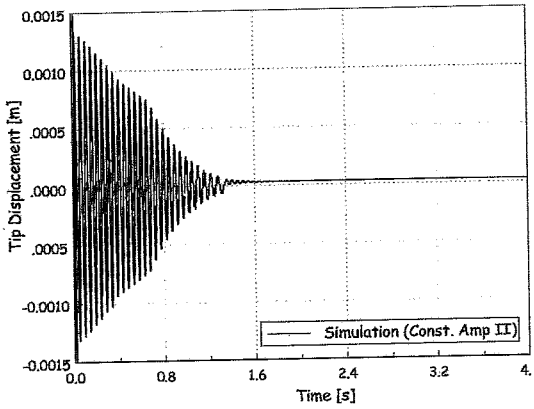

Figure 3.17: *Tip displacement, in closed loop, obtained by simulation for a constant amplitude feedback of* $A_2 = \pm 10$ *Volt.*

of time, of the experimental sensing voltage is relatively bad: R^2 in the order of 0.93. Therefore the difference, of approximately 30%, found between the damping obtained using the experimental data and the simulated one has no conclusive meaning. Thus, the experimental curve in Figure 3.11 can not be correctly reproduced with the available data. Again, no time delay was introduced in the simulations.

3.3.2 Constant gain feedback control

For the case of constant gain feedback control, the feedback gain is kept constant, as before, while the amplitude varies with respect to the sensor voltage. In practice, the sensor voltage, V^s, is fed back to the actuator multiplied by a feedback gain, G, according to

$$V^a = GV^s \tag{3.14}$$

The simulation model for the case of a constant gain controller, built in MATLAB & SIMULINK ®, is presented in Figure 3.18.

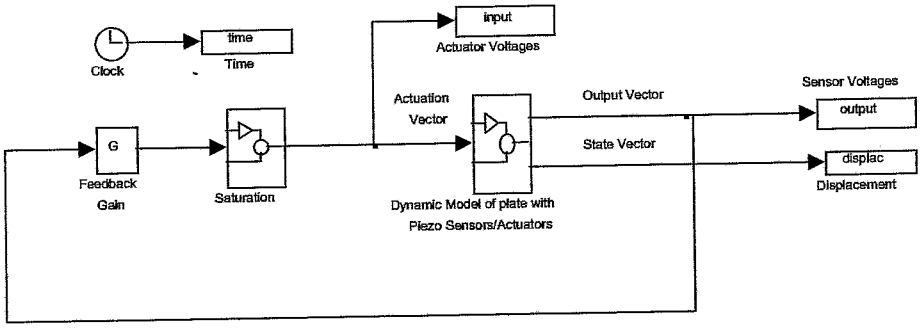

Figure 3.18: *Model of a constant gain feedback controller.*

For the constant gain feedback design, the controller is only defined by a constant gain block since the amplitude is directly given by the sensor. The system's dynamic block and the saturation block are equal to the ones shown in Figure 3.8 and Figure 3.9, respectively.

The response of the system in closed loop was experimentally obtained for several feedback gains. Figure 3.19 shows the overall damping ratio of the system as function of several feedback gains obtained applying Equation (3.13) to the experimental data.

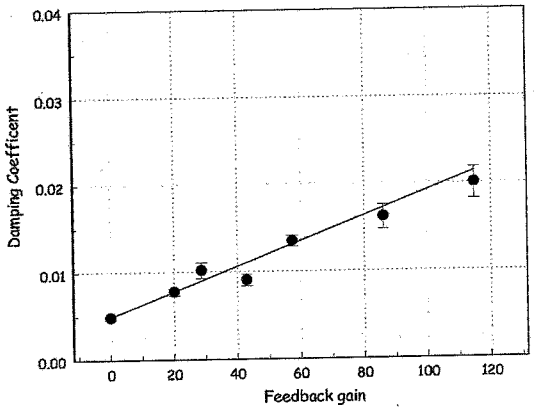

Figure 3.19: *Effect of the feedback gain on the overall damping ratio of the system. Experimental results.*

The relation between the feedback gain and the damping ratio, as expected, is linear and can be fitted by $\xi = 0.005 + 0.00014G$.

The performance of the system was simulated for two different feedback gains, G_1=29 and G_2=59, and the results compared to experimental ones. These gains were chosen arbitrarily among the possible feedback gains of the operational amplifier used in the experimental tests. Figure 3.20 shows the comparison between the experimental and the simulated output voltage when a feedback gain of G_1=29 is considered.

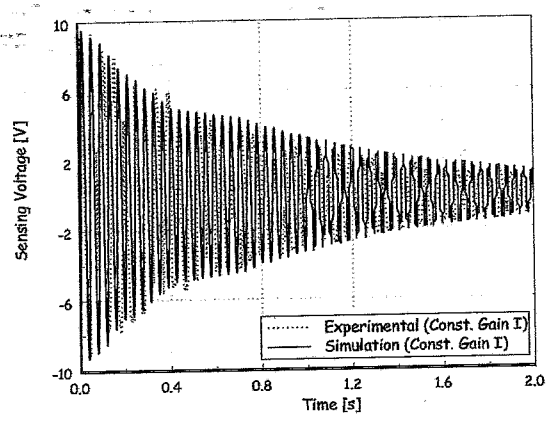

Figure 3.20: *Comparison of the sensor voltage, in closed loop, obtained experimentally and by simulation for a constant gain feedback of G_1=29.*

A good agreement can be found between experimental measurements and simulation results concerning the sensing voltage. Experimental data is slightly more damped than the simulated one; and the difference between the decay of the two functions is approximately 11%. For small voltages it can be observed the existence of an amplification phenomena that prevents the sensing voltage of vanishing, most probably related with time delay effects. Figure 3.21 and Figure 3.22 show, for the same case, the correspondent actuation voltage and the tip displacement, respectively.

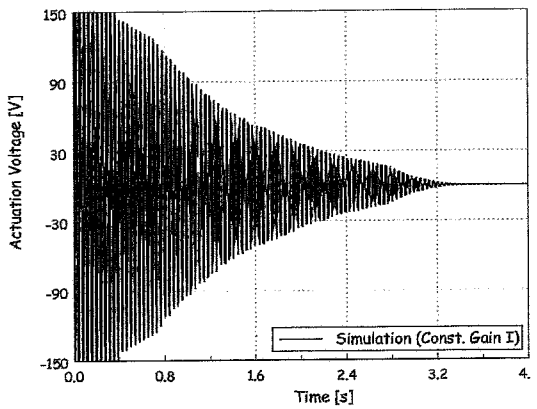

Figure 3.21: *Actuation voltage, in closed loop, obtained by simulation for a constant gain feedback of G_1=29.*

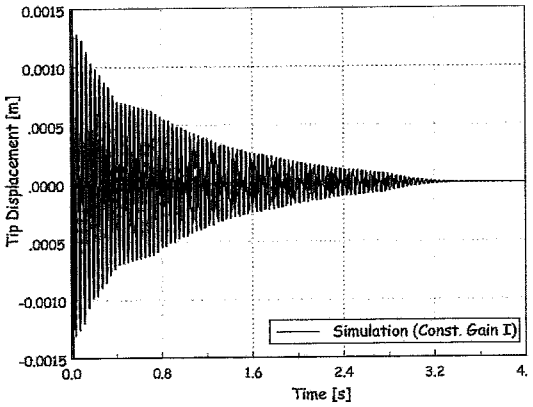

Figure 3.22: *Tip displacement, in closed loop, obtained by simulation for a constant gain feedback of G_1=29.*

In Figure 3.21 the saturation of the power amplifier at ±150 Volt during the first 0.4 seconds can be clearly seen. This effect is again visible in the tip displacement as function of time. Namely, two different decay constants can be associated with the simulated data: one during the saturation of the amplifier and the other after it.

The next three figures, Figure 3.23, Figure 3.24 and Figure 3.25, show the comparison between the experimental and the simulated sensing voltage, the simulated actuation voltage and the tip displacement for a different feedback gain, G_2=59.

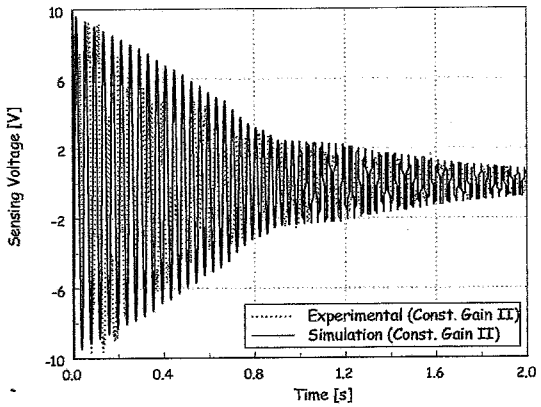

Figure 3.23: *Comparison of the sensor voltage, in closed loop, obtained experimentally and by simulation for a constant gain feedback of G_2=59.*

For this case the saturation zone is longer in time, approximately 0.8 seconds, due to the higher feedback gain. This saturation zone is very clear in all the three figures. Two distinct decay constants can be defined, one correspondent to the amplifier saturation and the other defined after it. The approximation of the full data set, relative to the sensing voltage, by an exponential function is not very satisfactory: R^2=0.97. However a difference of only 8% is found between the decay constant of the simulated and experimental data.

The results presented, concerning constant amplitude and constant gain feedback control methodologies, clearly validate the simulation model of a simple controller built in MATLAB & SIMULINK ®. The differences found are compatible with the simplifications made in the simulations. Even considering

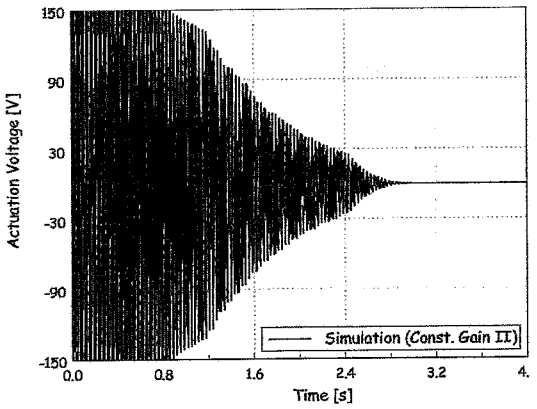

Figure 3.24: *Actuation voltage, in closed loop, obtained by simulation for a constant gain feedback of G_2=59.*

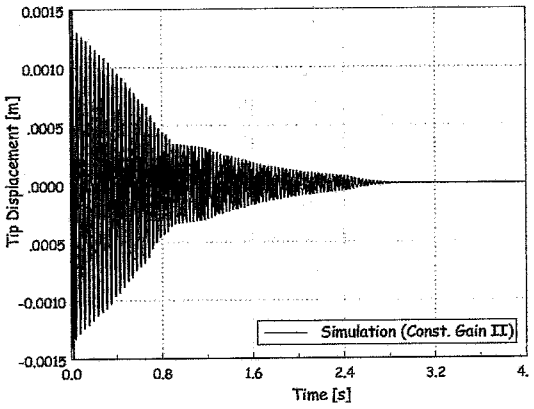

Figure 3.25: *Tip displacement, in closed loop, obtained by simulation for a constant gain feedback of G_2=59.*

only four vibration modes for the characterisation of the structure, a good agreement was obtained, in general, between experimental and simulation results. Based in the same model but using more complex control laws that guarantee optimality and robustness to model uncertainties, the next sections present the simulation results concerning the implementation of a new state feedback controller.

3.4 Linear quadratic regulator

The uncertainty in the definition of the system dynamics, in terms of modelling errors, use of truncated models, modal parameter variations due to operating conditions or environmental degradation, may lead to instability and to a decrease of the system performance if not included in the controller design.

The Linear Quadratic Regulator (LQR) is one of the robust controller algorithms available to determine the optimal matrix gain, G, for a given system. The minimisation of the effects of parameter's uncertainties on the performance of the closed loop system justifies the use of this type of control system's design.

The system is assumed to be linear in the state-space form and the matrices pair, A and B, controllable. The objective is to find a linear state feedback with constant gain

$$u = -Gx \tag{3.15}$$

which minimises a specified performance criteria or "cost function" defined as

$$V = \int_{t_i}^{t_f} (x^T Q x + u^T R u) d\tau \tag{3.16}$$

where V represents the weighted sum of the energy of the state and of the control. Matrices Q and R are, respectively, the state weighting matrix and the control weighting matrix. The lower limit of the integral, t_i, is identified as the present time while the upper limit, t_f, as the final time. This performance criteria has two terms: the first represents the effort of minimising the error while the second the effort of keeping the control input as small as possible [69]. The optimisation problem requires Q to be symmetric positive semi-definite ($Q \geqslant 0$) and R symmetric positive definite ($R > 0$). The former represents the penalty on the deviation of the state x from the origin while the second one the "cost of control". This means that if Q is much larger than R the state is heavily penalised resulting in a very damped system. If, by

the contrary, it is R that is much larger then Q, the control energy is significantly penalised resulting in a design that is liable to generate control signals that can not be achieved by the actuators. This leads to the saturation of the actuator for the maximum signal, feature desired since saturation often produces the fastest possible response. The determination of the optimal values of the matrices Q and R is complex and is generally done by a learning process based on trial and error methods.

In the case that the time interval is infinite and the system has a steady state solution, it is possible to obtain an algebric solution for the optimisation problem. It can be shown that the performance integral can be minimised by solving the *Algebric Riccati Equation* (ARE) in function of J [70]

$$0 = JA + A^T J - JBR^{-1}B^T J + Q \tag{3.17}$$

and the optimum gain in the steady state will be given by

$$G = R^{-1}B^T J \tag{3.18}$$

There are some special cases where the Ricatti equation can be solved analytically, however in almost all applications a numerical solution by iteration is required, which is computationally expensive.

The LQR methodology has many desirable properties. Among them, allows the design of multivariable state feedback which present good stability and sensitivity properties. A major drawback is related with the fact that it assumes the knowledge of the full state vector, x.

3.4.1 Optimal observer design: Kalman-Bucy filter

In the LQR methodology it is assumed that all the states are available for feedback. In practice this is not possible not only because it requires an huge amount of sensors but also because some variables are difficult or impossible to measure. The aim of an observer is to reconstruct the full state vector based on the system model and on the output measurements. The presence of errors and uncertainties during the measurements means that only an estimate, $\widehat{x}(t)$, of $x(t)$ can be obtained and never $x(t)$ itself. A good procedure for obtaining $\widehat{x}(t)$ is to make it an output of a dynamic system excited by the measurement, y, and by the input, u, as shown in Equation (3.19) and Figure 3.26.

$$\dot{\widehat{x}} = \widehat{A}\widehat{x} + \widehat{B}u + Ky \tag{3.19}$$

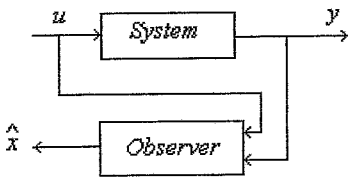

Figure 3.26: *Block-diagram of the system together with the observer*

The inclusion of an observer in the control loop of the system may adversely affect its robustness since, the uncertainties related to the model may contribute to a reduction of the stability margins of the system (gain and phase margins). The problem itself can be addressed in the following way. Given the dynamic process

$$\dot{x} = Ax + Bu + Fv \tag{3.20}$$

with u being a known input, and having observations given by

$$y = Cx + w \tag{3.21}$$

find the optimum observer or state estimator for the state x.

Matrices, $\widehat{A}$, $\widehat{B}$ and K, in Equation (3.19) should be selected such that, the error $e = x - \widehat{x}$ is acceptably small. A differential equation can be obtained for the error using the system's and the observer's dynamics. Specifically,

$$\dot{e} = \dot{x} - \dot{\widehat{x}} = Ax + Bu - \widehat{A}(x - e) - B\widehat{u} - KCx \tag{3.22}$$

$$= \widehat{A}e + (A - KC - \widehat{A})x + (B - \widehat{B})u \tag{3.23}$$

If the error goes to zero asymptotically, independent of x and u, then the correspondent coefficients in last equations must be zero. Therefore,

$$\widehat{A} = A - KC \tag{3.24}$$

$$\widehat{B} = B \tag{3.25}$$

The $\widehat{B}$ matrix is equal to the control matrix of the system and once matrix K is selected, $\widehat{A}$, is completely determined. Introducing these restrictions in Equation (3.19), one can express the dynamics of the full state observer by [69]

$$\dot{\widehat{x}} = A\widehat{x} + Bu + K(y - C\widehat{x}) \tag{3.26}$$

provided that the matrix $[K]$ is optimally chosen. The estimation process is stationary since $[K]$ is independent of time. Matrices $[A]$, $[B]$ and $[C]$ are the matrices of the state-space model of the initial system. The last equation represents the general structure of an observer and is used by the majority of classic observers, namely by the Kalman-Bucy filter and by the deterministic Luenberger observer.

Something worth to note is the fact that system equations for the observer have the same form as the original process, except the additional input $K(y - C\widehat{x})$. The first part of the equation emulates the system while the second part makes use of the information given by the output signals (sensors). If the last term is rewritten

$$r = y - C\widehat{x} = C(x - \widehat{x}) = Ce \tag{3.27}$$

it can be verified that this additional input is the difference between the actual measurement and the estimated measurement. The gain matrix, $[K]$, should be chosen in such a way that the error, e, between these two measurements tends to zero; then the residual, r, will also be zero.

The minimum variance observer is the one that minimises the variance of the measurement error. In the case that the system's input noise, v, and the measurement's noise, w, are assumed to be white noise processes with known spectral density matrices, the minimum variance observer is known as the

Kalman-Bucy filter or the optimum state estimator. Other estimators are available for active control: the Wiener filter, the Luenberger filter [69], etc., however only the Kalman-Bucy filter presents the property of being statistically optimal.

Considering that Kalman filters are governed by the same equations as observers, the gain matrix is the one which makes the covariance matrix of the error smaller. It can be proved that the optimal value designated by $\widehat{K}$, in the case of white and Gaussian noise, is obtained by [70]

$$\widehat{K} = \widehat{P}C^T W^{-1} \tag{3.28}$$

where $\widehat{P}$ is the solution of the following algebric Riccati equation

$$0 = A\widehat{P} + \widehat{P}A^T - \widehat{P}C^T W^{-1} C\widehat{P} + FVF^T \tag{3.29}$$

It is worth to note that the solution is identical to that of the deterministic LQR.

White noise processes are defined as stationary random mathematical idealisations with no correlation between the values of the process at different times. $[V]$ and $[W]$, the correlation matrices of system noise, v, and of the measurement noise, w, are defined, respectively, by

$$V = \begin{bmatrix} E\{v_1(t)v_1(\tau)\} & E\{v_1(t)v_2(\tau)\} & \cdots & E\{v_1(t)v_n(\tau)\} \\ E\{v_2(t)v_1(\tau)\} & \ddots & & \cdots \\ \cdots & \ddots & & \cdots \\ E\{v_n(t)v_1(\tau)\} & \cdots & & E\{v_n(t)v_n(\tau)\} \end{bmatrix} \tag{3.30}$$

$$W = \begin{bmatrix} E\{w_1(t)w_1(\tau)\} & E\{w_1(t)w_2(\tau)\} & \cdots & E\{w_1(t)w_n(\tau)\} \\ E\{w_2(t)w_1(\tau)\} & \ddots & & \cdots \\ \cdots & \ddots & & \cdots \\ E\{w_n(t)w_1(\tau)\} & \cdots & & E\{w_n(t)w_n(\tau)\} \end{bmatrix} \tag{3.31}$$

The symbol $E\{\}$ denotes mathematical expectation and is defined using probability density functions ($pdf[x;t]$) by

$$E\{x(t)x(\tau)\} = \int_{-\infty}^{\infty} x_1 x_2 pdf[x_1, x_2; t, \tau] dx_1 dx_2 \tag{3.32}$$

This methodology is valid only if v and w are zero-mean Gaussian stochastic processes that are independent and non correlated so that

$$E\{v_j(t)\} = 0 \qquad E\{v_j(t)v_k(t)\} = \sigma^2 \delta_{jk}, j, k = 1, 2, ... \tag{3.33}$$

$$E\{w_j(t)\} = 0 \qquad E\{w_j(t)w_k(t)\} = \sigma^2 \delta_{jk}, j, k = 1, 2, ... \tag{3.34}$$

where σ^2 is the variance associated with the noise process.

In practice, a meaningful value, based in the sensor accuracy, can be generally assigned to the measurement disturbance vector, w. The same is not true for the process noise magnitude, v, which normally

takes into account unknown disturbances and imperfections in the system's model. Experimental measurements could be made to determine the input current noise, however modelling errors also affects the system and would need to be quantified to reach a truly optimal estimation. The assumption of white noise is essentially a mathematical artifice that reduces the complexity in solving the resulting optimisation problem [72]. On the other hand the use of white noise to represent process uncertainties may be justified theoretically on the basis of the improvement of the robustness of the resulting control system [70]. In the presence of coloured noise (random disturbance time correlated) the estimator is no longer optimal, resulting in an increase of the complexity and on the size of the model.

3.4.2 Separation principle

In the last sections a control algorithm was derived, based on the fact that all the state variables could be measured. Since, in practice, this is not always true, the variables not accessible for measurement were estimated by the use of an observer. By combining the control law for the full state feedback with the estimated state vector one obtains the complete control system (Figure 3.27).

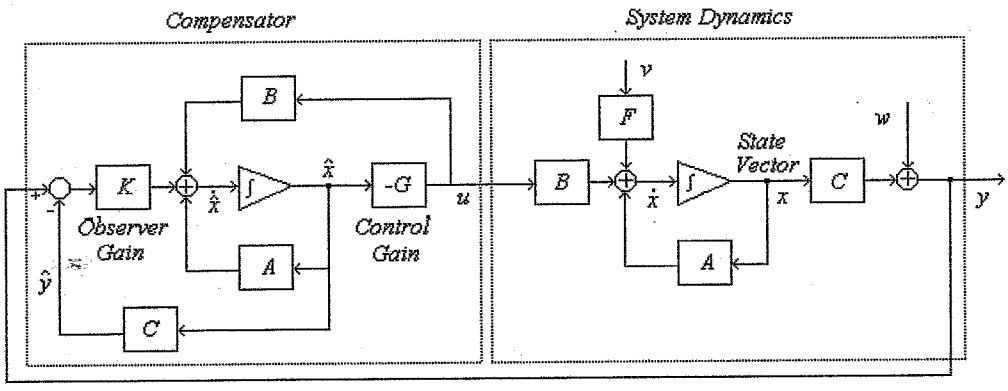

Figure 3.27: *Control system using full state observer [70].*

Figure 3.27 shows the state feedback regulator based on the estimated states obtained from a full state observer. On one side is the system dynamics and the process under control with the control input, u, and the observed output, y. On the other side there is the compensator which input is the observed output, y, of the system and which output is the control input, u, also from the system.

The closed loop equations can be determined considering the system dynamics equations

$$\dot{x} = Ax + Bu + Fv \tag{3.35}$$

together with the observations

$$y = Cx + w \tag{3.36}$$

and the control law defined as

$$u = -G\hat{x} \tag{3.37}$$

being $\hat{x}$ the output of a linear observer

$$\dot{\hat{x}} = A\hat{x} + Bu + \hat{K}(y - C\hat{x}) \tag{3.38}$$

The control gain is first determined by means of the LQR methodology assuming that all state variables are available for measurement followed by the determination of the optimal observer gain assuming a Kalman-Bucy filter. The complete system has $2n$ state variables, being n the order of the initial system. This method is also known by Loop Transfer Recovery/Linear Quadratic Gaussian (LTR/LQG) method. Assuming the reconstruction error, $r = x - \widehat{x}$ as a state variable, instead of the estimated state vector, $\widehat{x}$, the closed loop equations are given by

$$\begin{bmatrix} \dot{x} \\ \dot{r} \end{bmatrix} = \begin{bmatrix} A - BG & BG \\ 0 & A - \widehat{K}C \end{bmatrix} \begin{bmatrix} x \\ r \end{bmatrix} + \begin{bmatrix} F & 0 \\ F & -\widehat{K} \end{bmatrix} \begin{bmatrix} v \\ w \end{bmatrix} \tag{3.39}$$

The eigenvalues of the closed loop system are those of the diagonal blocks $(A-BG)$ and $(A-\widehat{K}C)$. Thus the characteristic roots of the complete system consist in a combination of the system roots and those from the estimator. This means that control and estimation can be designed separately yet used together - *separation principle* [72]. In resume, separation principle states that the controller gains can be calculated assuming that all the states are available for measurement, and, the observer can be designed without regard of the input process, and then the two can be combined to obtain a compensator that guarantees the stability of the closed loop system.

3.4.3 Model reduction

The model obtained from the finite element method possesses typically an high number of degrees of freedom. When projecting a controller one has to opt between a complete model of the system, and consequently a high computational effort, or a simpler model of the system, with a reasonable computational effort. An alternative solution, introduced by L. Meirovitch [73], consists in transforming the finite element model from the cartesian space to the modal space, as described before, decreasing the size of the model and decoupling the equations of motion.

By applying the "Independent Modal Space Control, (IMSC), technique, the behaviour of the structure can be modelled based in the first n dominant low frequency modes, the ones for which the control will be applied. The main drawback of this method is that it ignores the vibration modes greater than n. In practice, there is always the danger that the control signal or the contamination of the sensor output by the residual modes excite the high frequency modes degrading the performance of the system or creating instability. This phenomena, known as *"spill-over instability"*, is potentially critical for residual modes which are observable, controllable and close to the bandwidth of the controller.

The closed loop system equations can be obtained by considering the dynamics of the open loop system (Equations (3.20) and (3.21)) and by substituting u and y by the actuation voltage, V_a, and by the sensor voltage, V_s, respectively.

$$\dot{x_c} = A_c x_c + B_c V_a + F_c v \tag{3.40}$$

$$V_s = C_c x_c + w \tag{3.41}$$

together with the full state observer dynamics

$$\dot{\widehat{x}}_r = A_r \widehat{x}_r + B_r V_a + \widehat{K}(V_s - C_r \widehat{x}_r) \tag{3.42}$$

and the state feedback law

$$V_a = -G\widehat{x}_c \tag{3.43}$$

where the subscript c refers to the complete state vector and the subscript r to the reduced state vector. The order r of the observer can be equal or smaller than the order n of the system. In the case that it is smaller, the observer does not reconstruct the complete state vector from the output variable, y, and the complexity of the observer model is reduced. However the simplicity of the observer structure must be weighted against the higher sensitivity to the sensor noise. If the latter one is significant, the reduced order observer becomes less attractive than the full state observer [69].

The closed loop dynamics can be obtained by combining Equations (3.40), (3.41), (3.42) and (3.43)

$$\begin{bmatrix} \dot{x}_c \\ \dot{\widehat{x}}_r \end{bmatrix} = \begin{bmatrix} A_c & -B_c G \\ \widehat{K} C_c & A_r - B_r G - \widehat{K} C_r \end{bmatrix} \begin{bmatrix} x_c \\ \widehat{x}_r \end{bmatrix} + \begin{bmatrix} F_c & 0 \\ 0 & \widehat{K} \end{bmatrix} \begin{bmatrix} v \\ w \end{bmatrix} \tag{3.44}$$

The above equations are used to determine the poles of the system in closed loop and to design the LQG/LTR controller.

3.4.4 Simulation results

LQG/LTR controller was designed and simulated for the case of a clamped-free composite beam and its performance verified. The structure is made from a $[0_3,90_3,\pm45]_s$ laminate of T300/3501-5 carbon fibre composite. The mechanical properties of the unidirectional material are: E_1=133.6 GPa, E_2=15.3 GPa, G_{12}=12.9 GPa, ν_{12}=0.28, ρ=1530 Kg/m^3. The piezoceramic sensors and actuators (PX5-N from Philips Components) are 0.3 mm thick, 24 mm long and 12 mm wide. The electro-mechanical properties, given by the manufacturer, are presented in Table 3.2.

Table 3.2: *Material properties for the PX5-N piezoceramic material (data from the manufacturer).* $[C^E]$ *is the matrix of elastic coefficients at constant electric field,* $[d]$ *the piezoelectric module matrix,* $[\epsilon^s]$ *the dielectric constants matrix evaluated at constant stress and* ϱ *the material density.*

$C_{11}^E [N/m^2]$	13.11x10^{10}	d_{31} $[m/V]$	-215x10^{-12}
$C_{12}^E [N/m^2]$	7.984x10^{10}	d_{33} $[m/V]$	500x10^{-12}
$C_{13}^E [N/m^2]$	8.439x10^{10}	d_{15} $[m/V]$	515x10^{-12}
$C_{33}^E [N/m^2]$	12.31x10^{10}	$\epsilon_{11}^t/\epsilon_0$	1800
$C_{44}^E [N/m^2]$	2.564x10^{10}	$\epsilon_{33}^t/\epsilon_0$	2100
$C_{66}^E [N/m^2]$	2.564x10^{10}	ϱ $[Kg/m^3]$	7800

Figure 3.28 shows the beam dimensions (293×12×1 mm) together with the localisation of the 6 pairs of piezoelectric elements glued on both sides. Collocated sensors/actuators were considered.

In order to reduce computational effort, only the first 10 vibration modes were used to obtain the state-space model of the structure. The first five natural frequencies are respectively equal to 11.06 Hz, 70.35 Hz, 151.5 Hz, 202.13 Hz and 413.80 Hz. Damping ratios for composite material's are, in general, equal or greater than the ones for metals. A typical and representative [74] damping factor of 0.2% was considered for all the vibration modes and a saturation voltage of ±200 Volt was assumed for the piezoelectric actuators.

The simulation model is based on the mathematical model of the structure and on the one of the controller. The finite element model described in Section 2.2.5 was used to obtain the matrices characterising the system dynamics: the piezoelectric stiffness and the coupled electrical/mechanical stiffness matrices together with the eigenvalue and the normalised eigenvector matrices. A mesh of 13×2 elements was considered. Each piezoelectric patch was divided in two elements making a total of 12 piezoelectric

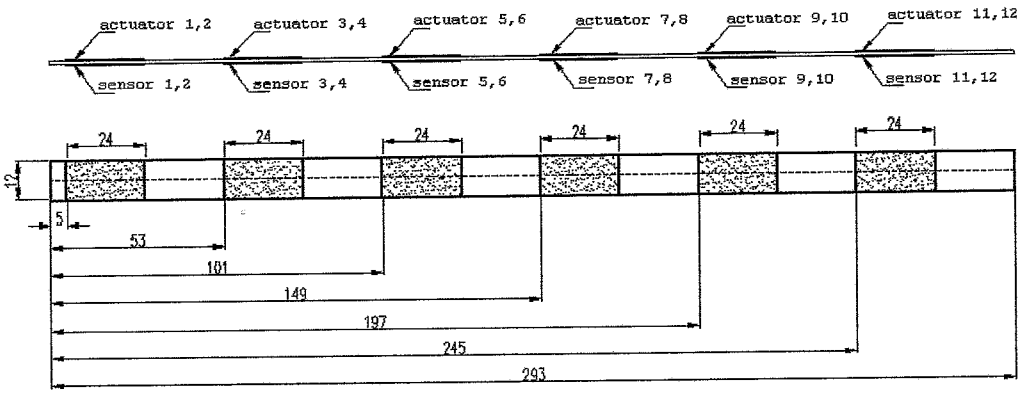

Figure 3.28: *Layout of the 1 mm thick T300/3501-5 carbon fibre composite beam together with 6 pairs of piezoceramic elements. Top and side view. Units in mm.*

sensor elements and 12 piezoelectric actuator elements (longitudinal dotted line in Figure 3.28). This MIMO (multi-input-multi-output) system with 12 input/12 output lead to an LQG/LTR controller with 20 states. The state weighting matrix, Q, and the control weighting matrix, R, were assumed diagonal and were obtained, by trial and error, from a range of values that resulted in a closed loop response meeting the design objectives (Q=8.5×10^3, R=3×10^{-3}). The state-space block diagram used to model the beam structure together with the controller and the observer is shown in Figure 3.29.

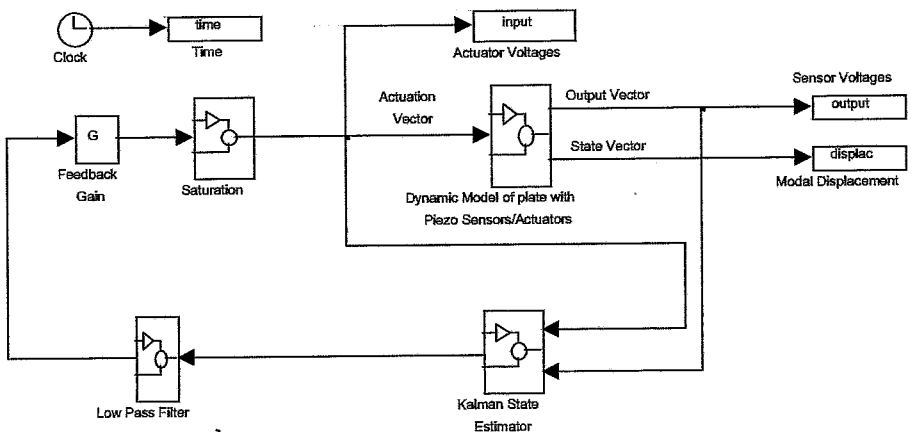

Figure 3.29: *Block diagram of the clamped-free beam structure together with the controller and the observer.*

The block diagram of the whole system is divided in three main blocks: one describing the dynamics of the system, in this case the carbon fibre composite beam, the state estimator and the feedback gain [75]. A low pass filter block (third-order low pass Butterworth filters) was added in order to reduce the effects of spill-over. Figure 3.30 shows the dynamics of the system's block for the case where the state and the measurement disturbance noise was added to the model. The introduction of these two sources of white noise has the objective of testing the robustness of the controller. However the complexity of the system and the computational time are also increased and therefore two different versions of the same controller were designed: a first version without noise disturbances and a second one where both disturbances, system's and measurement's, were included (Figure 3.30).

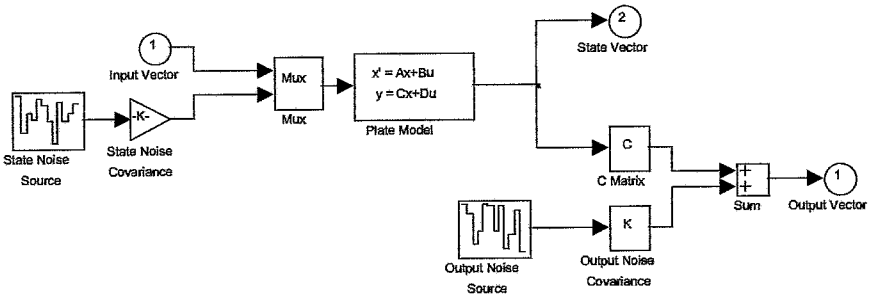

Figure 3.30: *Block diagram of the system's dynamics. Full version including system and measurement noise.*

Active control of a composite structure

In order to demonstrate the different principles and notions presented above, the implementation of a control strategy on a composite beam with piezoelectric elements glued on it (Figure 3.28) will be presented in the next sections. The developed methodology can be easily extended and applied to more complex mechanical systems.

Case 1: Model initial condition

In this first simulation case the first vibration mode is assumed as the initial condition. A modal amplitude of 0.001 was assumed, corresponding in this case to a tip displacement of approximately 18 mm. No disturbance noise is considered in the model and both the system and the observer model have the same order. All the 6 × 2 piezoelectric elements are used in the simulations.

Figure 3.31, Figure 3.32 and Figure 3.33 show, respectively, the tip displacement of the beam, the actuation voltage in actuator number 1 and the sensing voltage in sensor number 1 in open loop and closed loop.

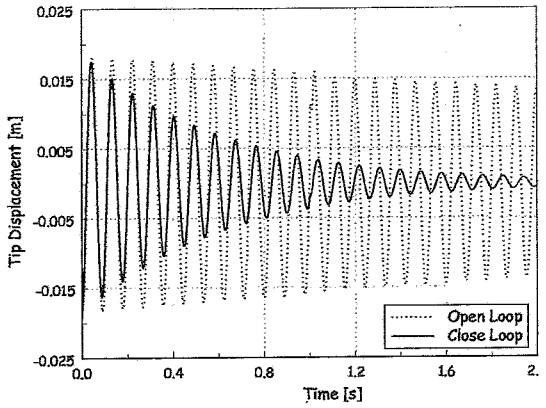

Figure 3.31: *Tip displacement of the beam for mode 1 initial condition in open and closed loop without disturbance noise.*

A clear reduction of the tip amplitude can be observed in Figure 3.31. For example, isolating the first vibration mode from the total response, the correspondent damping ratio in closed loop has increased 108% when compared with the initial one. In Figure 3.32, and as expected, the actuation voltage in open

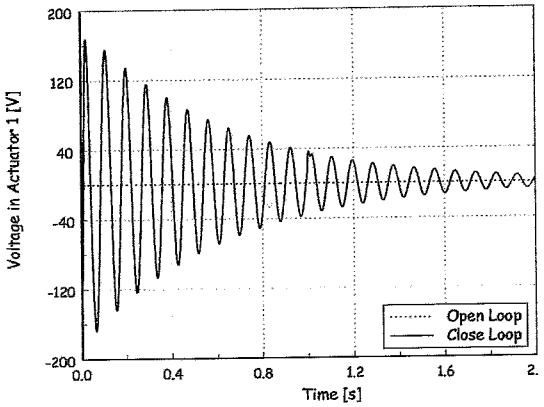

Figure 3.32: *Actuation voltage in actuator number 1 for mode 1 initial condition in open and closed loop without disturbance noise.*

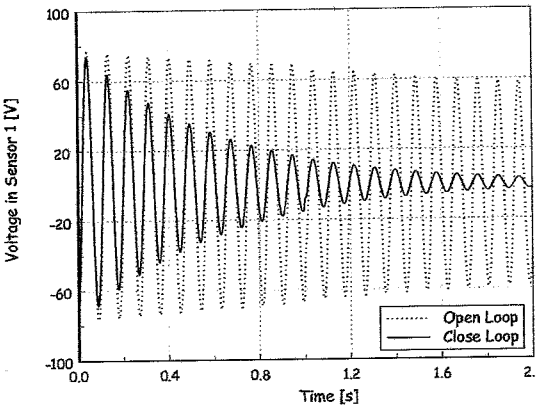

Figure 3.33: *Sensing voltage in sensor number 1 for mode 1 initial condition in open and closed loop without disturbance noise.*

loop is equal to zero since there is no feedback. In closed loop no saturation is attained since the actuation voltage is always below the saturation voltage of the piezoelectric element. In resume, the last figures show that for an initial modal displacement equal to 0.001 of the first vibration mode, the controller is able to successfully damp the vibrations of the beam.

The sensing and the actuation voltage are dependent on the strain field and on the displacement of the structure, and therefore are function of the piezoelectric position in the beam. Figure 3.34 and Figure 3.35 compare, respectively, the actuation and the sensing voltages in two different piezoelectric elements, number 1 and 5, in closed loop.

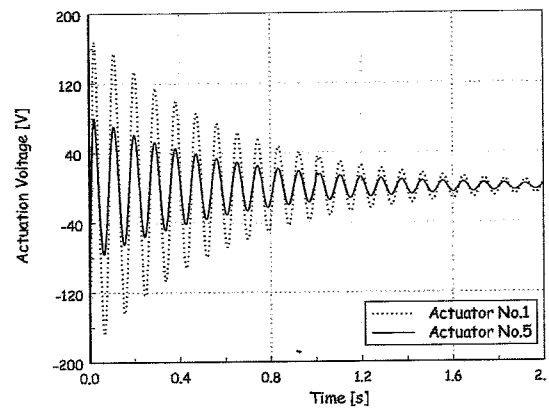

Figure 3.34: *Actuation voltage in actuator number 1 and number 5 for mode 1 initial condition in closed loop without disturbance noise.*

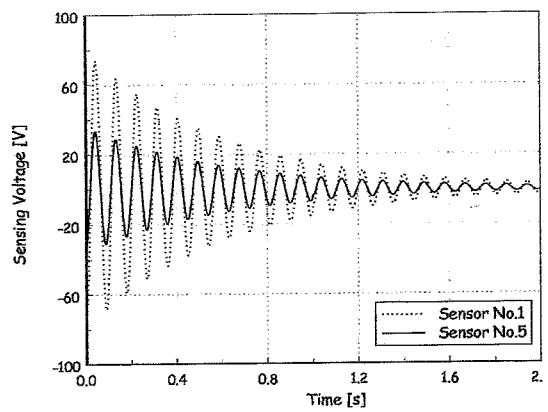

Figure 3.35: *Sensing voltage in sensor number 1 and number 5 for mode 1 initial condition in closed loop without disturbance noise.*

As mentioned, the sensing voltage is proportional to the mechanical effort submitted to the piezoelectric element. Therefore, higher sensing, and, consequently, actuation voltages, are found in piezo number 1 placed near the clamped edge where the strain energy is maximum.

The robustness of the LQG/LTR controller can be tested by varying certain system parameters. The uncertainty in the model definition was simulated by varying the Young Modulus and the density of the carbon fibre laminate. As before, the first mode of vibration with a modal amplitude of 0.001 was used

as the initial condition. Figure 3.36 and Figure 3.37 show, respectively, the tip displacement in open and closed loop of the perturbed system and the comparison, in closed loop, with the original system. In this first case, an increase of +15% of the Young Modulus and a decrease of -15% of the material density was considered.

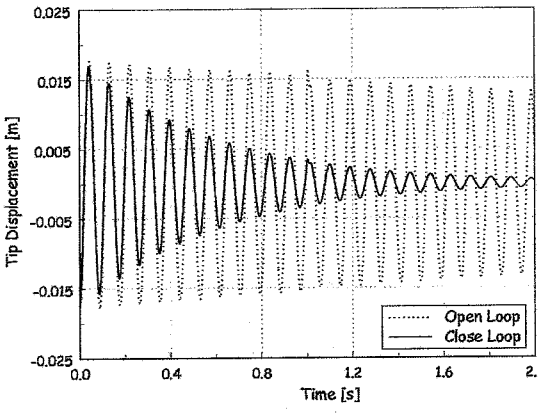

Figure 3.36: *Tip displacement of the beam for mode 1 initial condition in open and closed loop without disturbance noise. Parameter variation: increase natural frequency.*

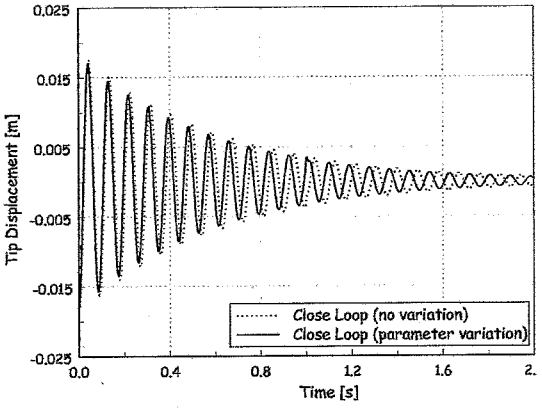

Figure 3.37: *Comparison of the tip displacement of the original beam with the perturbed parameter's beam for mode 1 initial condition in closed loop without disturbance noise. Parameter variation: increase natural frequency.*

The assumed parameter variations in the elastic modulus and in the density of the material lead to an increase of the stiffness of the structure and therefore to an increase of the natural frequencies of the system (in the order of 3%). It can be seen, in the last figures, that the overall response of the perturbed system is quite similar to the one of the original beam.

In the next simulations the inverse situation was considered: a decrease of -15% of the Young Modulus and an increase of +15% of the material density. Figure 3.38 and Figure 3.39 show, respectively, the tip displacement in open and closed loop of the perturbed system and the comparison, in closed loop, with the original system.

The perturbed system (decrease of the Young Modulus and increase of the material's density) is less stiff than the initial one. An average reduction of 3% of the natural frequencies was observed. However, the overall performance was not affected these variations which confirms the existence of a robust controller and validates the simulation model and the control methodology.

Case 1.1: Model initial condition, reduced order observer

Keeping the same initial conditions and the initial material properties a reduced order observer will be considered. In this case a five order reduced observer is assumed while the full state observer previously used was of order ten.

In practice, by reducing the state reconstruction to the missing state variables, the measured state variables are not contaminated by modelling errors. However, and as already mentioned, the reconstruction of the state feedback based only on output measurements may lead, in some cases, to the degradation of the system's performance.

Figure 3.40 and Figure 3.41 show the tip displacement and the sensing voltage in sensor number 1 in the case of a five order observer.

Figure 3.41, shows the output voltage in sensor number 1. The perturbations and the increase of the sensor noise is considerable. This effect, spill-over instability, is due to the excitation of non controlled

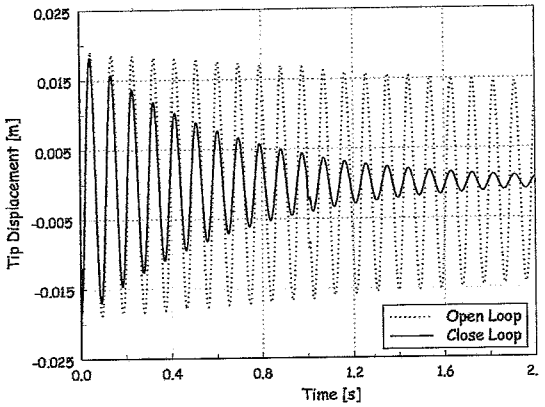

Figure 3.38: *Tip displacement of the beam for mode 1 initial condition in open and closed loop without disturbance noise. Parameter variation: decrease natural frequency.*

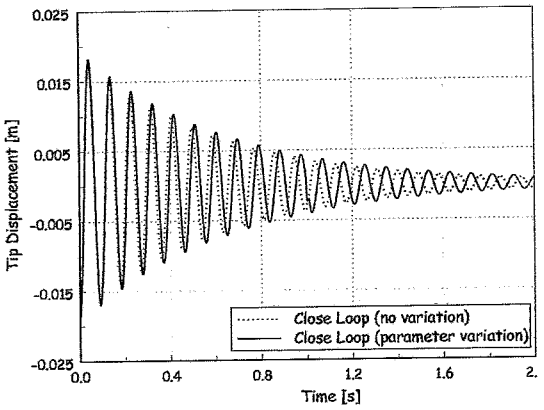

Figure 3.39: *Comparison of the tip displacement of the original beam with the perturbed parameter's beam for mode 1 initial condition in closed loop without disturbance noise. Parameter variation: decrease natural frequency.*

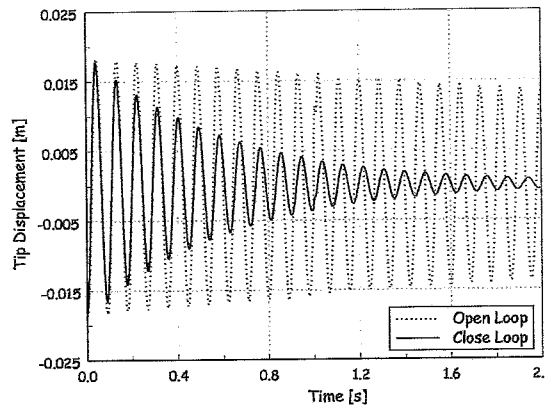

Figure 3.40: *Tip displacement for mode 1 initial condition in closed loop without disturbance noise and with a reduced order observer.*

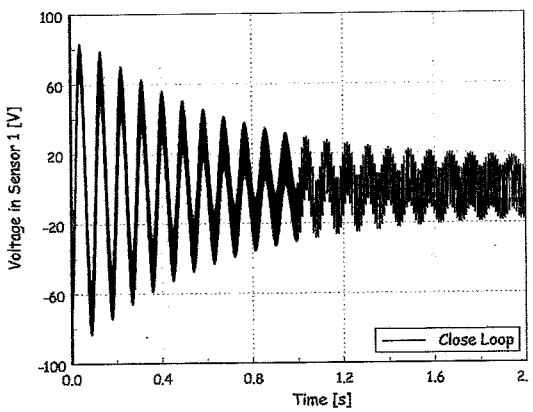

Figure 3.41: *Sensing voltage in sensor number 1 for mode 1 initial condition in closed loop without disturbance noise and with a reduced order observer.*

modes by the control signal. By filtering the signal, before actuating the structure, using low pass filters, these instabilities are avoided as shown in Figure 3.40. In this case, no instability phenomena is visible and if compared with the full order observer no degradation in the system performance is found. This instability phenomena is quite frequent and can be, in some cases, responsible for a serious degradation of the system's performance.

Case 2: impulse load initial condition

All the previous results were obtained considering the initial condition identical to the displacements corresponding to the first vibration mode of the beam. In this section the open loop and the closed loop responses of the beam will be studied for an impulse load of 0.5 N applied in the tip of the beam during 0.005 seconds. A full order observer is considered and no noise disturbances are introduced.

Figure 3.42, Figure 3.43 and Figure 3.44 show, respectively, the tip displacement of the beam, the actuation voltage in actuator number 1 and the sensing voltage in sensor number 1 in open loop and closed loop.

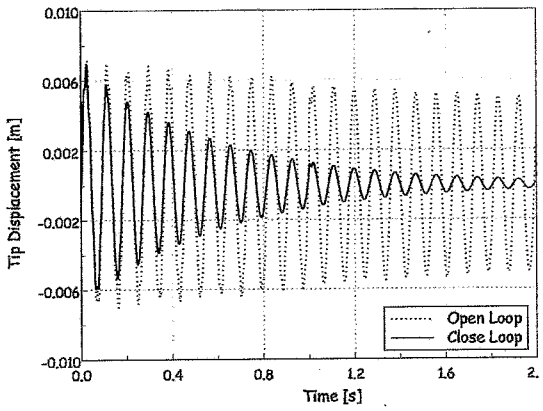

Figure 3.42: *Tip displacement of the beam for an initial load condition in open and closed loop without disturbance noise.*

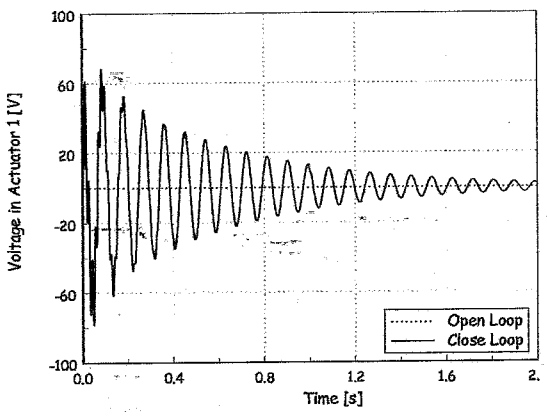

Figure 3.43: *Actuation voltage in actuator number 1 for an initial load condition in open and closed loop without disturbance noise.*

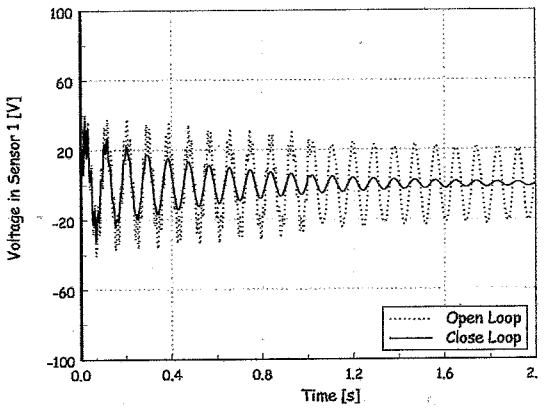

Figure 3.44: *Sensing voltage in sensor number 1 for an initial load condition in open and closed loop without disturbance noise.*

It can be observed that in the first 3 to 4 cycles the controller induces some instabilities in the response of the system. These instabilities may be related with the transient induced by the application of an impulse load. However the controller is able to recuperate and to damp, effectively, the vibrations of the beam. No saturation is observed in the piezoelectric actuators.

A different way to analyse the effect of the control on the system performance is using Frequency Response Functions (FRF). Ranging from 0 to 500 Hz Figure 3.45 shows, in open loop, the driving point FRF H2_2 (response sensor no. 2, input actuator no. 2), the FRF H6_2 (response sensor no. 6, input actuator no. 2) and the FRF H8_2 (response sensor no. 8, input actuator no. 2).

The first five resonant frequency picks at 11.06 Hz, 70.35 Hz, 151.5 Hz, 202.13 Hz and 413.80 Hz can be clearly seen in the picture. The comparison between the FRF H1_2 (response sensor no. 1, input actuator no. 2) and FRF H5_6 (response sensor no. 5, input actuator no. 6), with and without control (dotted line), is shown in Figure 3.46 and Figure 3.47.

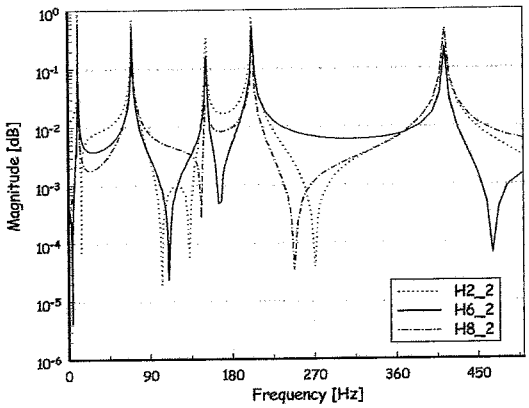

Figure 3.45: *Frequency Response Functions - FRF H2_2, FRF H6_2, FRF H8_2 - in open loop.*

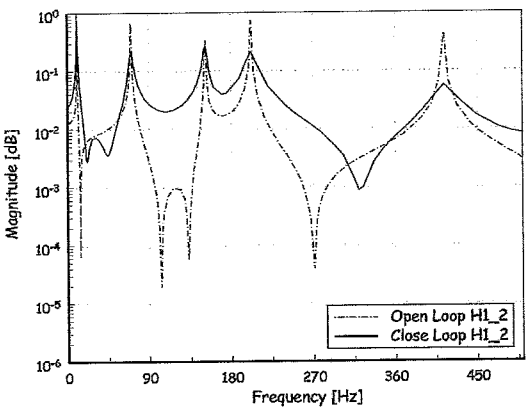

Figure 3.46: *Frequency Response Function, FRF H1_2, in open and closed loop.*

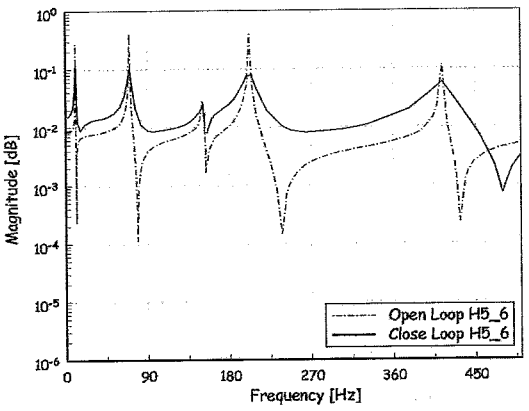

Figure 3.47: *Frequency Response Function, FRF H5_6, in open and closed loop.*

The observation of the last two figures confirm the improvement obtained on the frequency response shape and consequently on the vibration suppression when the controller is activated. The significant amplitude decrease at the level of each peak (natural frequencies) of the FRF between the results with and without control traduce qualitatively the controller performance.

Case 3: controller implementation with noise

The performance and the robustness of the controller in the presence of measurement and state noise was evaluated adding white Gaussian noise in the model (Figure 3.30). Once again a modal displacement of 0.001 of the first vibration mode was taken as the initial condition. A full order observer was considered.

The measurement noise magnitude can be generally taken as the square of the *rms*, of the sensor, given by the manufacturer. In this case was assumed to be equal to 0.01. The determination of the process noise magnitude is generally more inaccurate and complex than the measurement noise magnitude. It was somewhat arbitrarily fixed in 10% of the initial modal deflection of the beam, 0.0001. Figure 3.48 and Figure 3.49 show, respectively, the tip displacement of the beam and the actuation voltage in actuator number 1 in open and closed loop for these noise levels. The response of the system is only shown from 0 to 1 second due to the huge amount of data generated, in this case, by the simulation model.

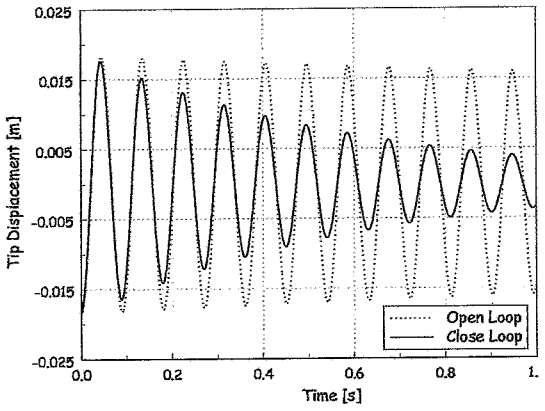

Figure 3.48: *Tip displacement of the beam for mode 1 initial condition in open and closed loop with disturbance noises included.*

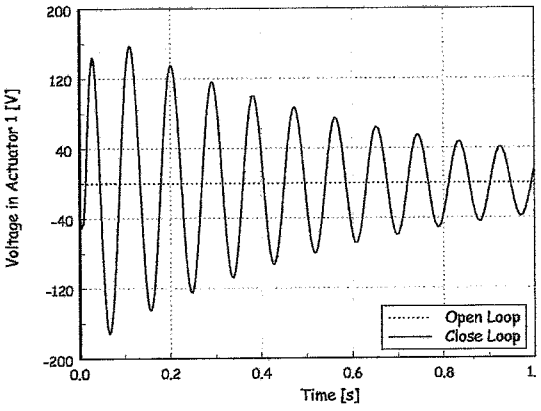

Figure 3.49: *Actuation voltage in actuator number 1 for mode 1 initial condition in open and closed loop with disturbance noises included.*

The last two figures show that the performance of the system is not affected in a visible way by the presence of state and measurement noise (compare with Figure 3.31 and Figure 3.32). Figure 3.50 and Figure 3.51 show, respectively, the sensing voltage in open loop and in closed loop for the same conditions.

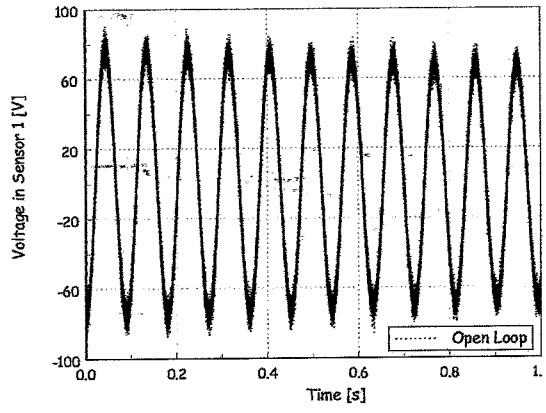

Figure 3.50: *Sensing voltage in sensor number 1 for mode 1 initial condition in open loop with disturbance noises included.*

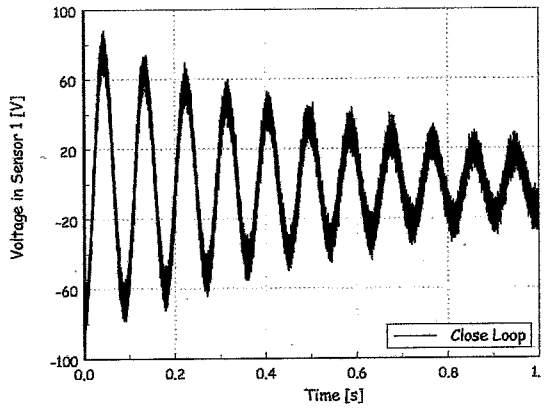

Figure 3.51: *Sensing voltage in sensor number 1 for mode 1 initial condition in closed loop with disturbance noises included.*

The effect of measurement and state disturbances included in the model is visible in the sensor signal. The low pass filter guarantees that these instabilities will not contaminate the actuator signal. On the other hand it was demonstrated that the implemented controller is robust enough to avoid that those disturbances affect the system's performance.

3.5 Conclusions

A model for the vibration control of laminated structures with collocated piezoelectric sensors and actuators was developed. A constant gain/amplitude feedback controllers were designed, and experimental and simulation results were compared for a carbon/epoxy cantilever beam. A good agreement,

between both, validated the mathematical model of the system.

A more powerful and robust controller, LQG/LTR, was also designed based on a reduce-order state space model of the system. The simulated performance of the LQG/LTR controller was studied for different initial conditions and structural parameter variations. Good robustness characteristics were found.

Chapter 4

Optimisation Procedure - Genetic Algorithms

In the very beginning the most common optimisation techniques relied on graphical methods. These methods were in general very simple and straightforward and represented the advantage of showing directly the interval of interest and the stationary points of the function to optimise. However, important limitations were related to the number of variables that were possible to represent and design without loosing the capacity to understand all the information.

As an alternative to graphical methods, numerical optimisation methods were developed in the last four decades. Each variable, representing one dimension, is grouped in a multidimensional vector. The objective or optimisation function, expressing cost, energy, distance, efficiency, investment or any other combination of variables and parameters, obeys to some constraints depending on the relation between variables or on the lower and upper limits of the variables themselves. The inequality constraints define the allowable region in space where the optimal solution should be found. Current literature [76] divides the conventional optimisation search methods in three groups: the algorithms that make use off gradients (calculus-based), the enumerative schemes and random methods.

The algorithms based on gradients assume the continuity of the search space, which in real world problems is seldom the case. Generally, these algorithms make use of the derivatives of the objective function and of the constraints with respect to the problem variables. Calculus-based methods can be divided in two main classes: indirect and direct. Indirect methods seek local extreme by solving the non linear set of equations obtained when the gradient of the objective function is set to zero; direct methods seek local optima by moving in a direction related to the local gradient. For multidimensional problems the relations between variables are complex and generally its not practical and feasible to use the analytical derivatives. In these cases derivatives may be obtained by numerical methods, such as, the finite difference method. However, as the number of variables increases, the computational effort also increases and normally becomes prohibitive. In general, calculus-based methods show lack of robustness over the broad spectrum of optimisation functions and are local in scope.

Enumerative schemes are based in a straightforward idea: within a finite search space, or discritised infinite search space, the algorithm looks at the objective function values at every point in space, one at a time. Although simple and obvious these schemes suffer from lack of efficiency while presenting a massive computational task.

Random search algorithms achieved increasing popularity when the shortcomings of calculus-based and enumerative methods were recognised. By simply performing random walks on the problem space and recording the best optimum values discovered so far, these methods do not use any knowledge from previous results. Yet, random schemes fail the efficiency requirement and, in the long run, can be expected to do no better than enumerative schemes [76].

Randomised techniques must be, however, separated from random methods. These techniques, contrary to the later methods, are not directionless since are able to make use of the knowledge gained from

previous results to guide the search through the parameter space. The result is a powerful search technique able to handle noisy, multimodal, search spaces with relative efficiency. One of the most popular form are genetic algorithms (GA).

In this chapter, and before presenting the applications, the main concepts and the main genetic recombination operators will be presented. The implemented optimisation method will be described together with a short state-of-the-art of structural optimisation using genetic algorithms.

4.1 Evolutionary algorithms

In the 1950's and 1960's evolutionary algorithms started to be studied with the idea that evolution could be used as an optimisation tool for engineering problems. The objective was to evolve a population of candidate solutions to a given problem, using operators inspired by natural genetic variation and natural selection [77].

A variety of evolutionary algorithms have been proposed since then. Rechenberg (1965, 1973) introduced "evolution strategies", an area mostly developed independently from the field of genetic algorithms. In 1966 Fogel, Owens, and Walsh developed "evolutionary programming", a technique in which candidate solutions to given tasks evolved by random mutation and selection of the fittest.

In 1960's John Holland invented the genetic algorithms. In contrast with evolution strategies and evolutionary programming, Holland's main goal was not to design algorithms to solve specific problems but rather to formally study the phenomenon of adaptation as it occurs in nature and to develop ways in which the mechanisms of natural adaptation might be imported into computer systems. Moreover, Holland was the first to attempt to give to computation evolution a theoretical basis [78]. Holland's introduction of a population based algorithm with crossover, mutation and inversion was a major innovation. Fogel, Owens, and Walsh's evolutionary programming used only mutation to provide variation while Rechenberg's evolution strategies started with populations of only two individuals, one being the mutated version of the other. Several individuals and crossover were incorporated much later. In the last years the boundaries between evolution strategies, evolutionary programming, genetic algorithms and other evolutionary approaches have been broken down to some extent and the term "genetic algorithm" is often used to describe something very far from Holland's original concept.

4.2 Genetic algorithms - main concepts

One of the most powerful features of GA are their elegant simplicity. GA can be implemented by a few lines of computer code that perform string copying and partial string exchange plus a random number generator [79]. The main differences between GA and other conventional optimisation and search techniques are essentially the following [80], [81]:

- GA work, in general, with a coding of the parameter set, not with the parameters themselves;
- GA search from a population of points or candidate solutions, not a single point;
- GA use probabilistic transition rules, not deterministic ones, as a result of the use of randomisation techniques;
- GA use the function to be optimised (fitness function), not derivatives or other auxiliary knowledge of that function.

The non existence of closed form gradients to derive and no differentiability or continuity requirements to satisfy make GA very attractive and a powerful alternative over other techniques. When applied to optimisation problems GA present a number of advantages:

- Can handle any kind of objective functions and any kind of constraints (linear or non-linear) defined on discrete, continuous, or mixed search spaces;
- Effective at performing global search. Solution is not dependent on an initial guess or condition;
- Operate on entire populations of candidate solutions in parallel. Therefore, the effect of changing a single variable influences, collectively, other string values;
- Present big flexibility in the implementation of a specific problem;
- Since the search is undertaken from a population of several individuals the susceptibility of the method of focusing mainly on local optima is less important;
- Require little knowledge of the problem itself. Do not require numerical optimisation background.

Due to its stochastic nature, only an estimate of the exact optimum can be find: GA will only by chance find the exact optimum, whereas traditional methods will find it exactly. In this case, the question is to know if the found solution is close enough, which is generally somewhat arbitrary and dependent on the application.

Conceptually, genetic algorithms are iterative procedures which maintain a population of candidate solutions of the problem, the so called *chromosomes*. Each chromosome is constituted by a number of individual structures called *genes*. Each gene is associated with a specific parameter of the search space. Chromosomes are usually constant-length sequences, and traditionally binary numbers; however in practice may be anything including a mix of integers and real numbers, or a mix of numbers and character strings. During each iteration step, *generation*, each solution is evaluated to give some measure of its *fitness*, and, on the basis of those evaluations, a new population of candidate solutions is formed. By applying a selection procedure, *reproduction*, highly fit individuals are more likely to be selected than unfit members. Then, *crossover* and *mutation* operators are applied to this population allowing recombination and exchange of genetic material. The main goal of this iterative process, tailored for vast, complex and multimodal search spaces, is to continually improve the fitness of the best candidate solution, assigned by the objective function, until a pre-defined criteria is reached (see Figure 4.1).

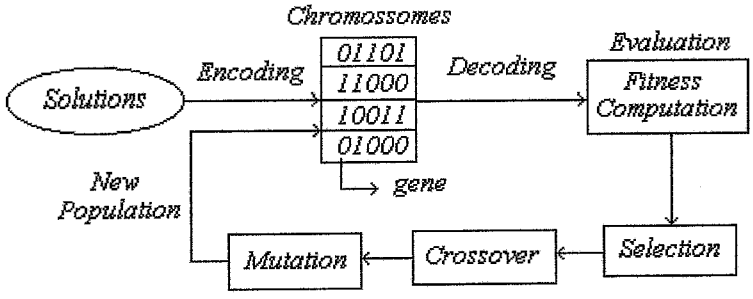

Figure 4.1: *General structure of genetic algorithms.*

The initial population can be chosen at random or can start from an already existing knowledge. In this last case a more rapid convergence will be usually attained. The new solutions are selected by a randomise selection procedure that ensures, at each generation, that the "good" solutions reproduce, while the relatively "bad" ones die. However, and due to the crossover and mutation operators, these "bad" solutions can be again re-evaluated in a later phase of the process.

4.3 Genetic recombination operators

Conventional GA apply to each population set a sequence of operations. The most important, and commonly used, genetic/search operators are reproduction/selection, crossover and mutation.

4.3.1 Reproduction

Reproduction or *selection* is a process in which strings are copied to the new population, according to their objective function values or fitness [76], for use in further reproductive operations. The idea is to allow the more fitted candidate solutions to survive and procreate. It is an individual process where only one string is involved at a time. The selection procedure is responsible for the speed of evolution and is therefore one of the key features for the success of an evolutionary algorithm.

In the case of a binary representation, a decoding to the floating point space must be done before applying the reproduction operator, in order to evaluate each individual by the optimisation function.

The reproduction operator can be implemented in the algorithm in a number of ways (rank-based fitness assignment, stochastic universal sampling, local selection, truncation selection, etc.), of which, the *roulette wheel* and the *tournament selection* procedures are the most commonly used. The *roulette wheel* selection process can be visualised as a biased roulette wheel where each individual is allocated a wheel segment size according to its fitness. A random number is then generated and the individual whose segment spans the random number is selected. The process is repeated until the desired number of individuals is obtained (generally equal to the number of individuals in the population). This procedure belongs to the fitness-proportional selection methods and is based on the probability distribution of the fitness values. The roulette wheel selection can be constructed as follows:

- Evaluate the function to be optimised and determine the fitness values, $eval(v_k)$, for each chromosome, $v_{k=1,\ldots,popsize}$ in the population
- Find the total fitness, F, of the population

$$F = \sum_{k=1}^{popsize} eval(v_k) \tag{4.1}$$

- Calculate the selection probability, p_k, for each chromosome $v_{k=1,\ldots,popsize}$

$$p_k = \frac{eval(v_k)}{F} \tag{4.2}$$

- Calculate the cumulative probability, q_k, for each chromosome $v_{k=1,\ldots,popsize}$

$$q_k = \sum_{j=1}^{k} p_j \tag{4.3}$$

The selection process is based on spinning the roulette wheel *popsize* (population size) times. At each time, a single chromosome is selected in the following way:

- Generate a random number, r, between [0,1];
- If $q_{k-1} < r \leq q_k$ with $(2 \leq k \leq popsize)$ select chromosome v_k; otherwise, if $r \leq q_1$, select the first chromosome v_1.

The *tournament selection* procedure, based also in the idea of ranking, selects randomly in a single iteration, some number k of individuals from the population. The best individual from this group is then selected as a parent for the next generation. The process is repeated until the number of individuals in the breeding population is equal, in size, to the number of candidate solutions in the initial population. A consequence of the process is that the average fitness of the breeding or parent's population will be higher than the fitness values of the preceding generations.

4.3.2 Crossover

Crossover is the main genetic operator under which two (or more) chromosomes, called *parents*, combine portions of their internal representation generating new chromosomes called *offsprings*. Although crossover may take different forms, is generally implemented by choosing one, or more, random cut-point, *crossover point*, and exchanging the segments to the right of this point. Parents and offsprings are generally different from each other. Figure 4.2 shows the crossover operation in a couple of chromosomes, coded in binary, with cut points equal to 2 and 4 respectively.

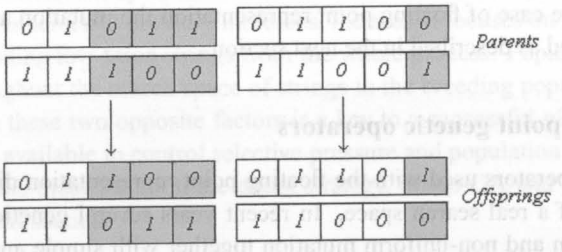

Figure 4.2: *Crossover - genetic algorithm recombination operator. Left chromosomes with a crossover point equal to 2 and right chromosomes with crossover point equal to 4.*

The crossover probability, p_c, associated to this operator, is defined as the ratio of the number of offspring produced in each generation to the population size. A higher crossover probability allows a wide exploration of the solution space and reduces the chances of settling for a false optimum; however if this probability is too high it results in a deeper exploration of unpromising regions of the solution space thus increasing the computation time [82].

4.3.3 Mutation

Mutation is a background operator which produces a random alteration of a gene and restores genetic diversity. In GA this operator provides the genes that were not present in the initial population and replaces the genes lost from the population during the selection process so they can be tried in a new context. In practice, the risk of the search ending at local optimum is decreased. Figure 4.3 shows the mutation operation in one individual of the population, coded in binary, with three chromosomes and 15 genes. The mutated genes are selected randomly in the population total number of genes. In this case genes 7 and 13 were chosen.

The mutation probability, p_m, gives the expected number of mutated genes, and controls the rate at which new genes are introduced in the population for trial. If it is too low, many genes will be never tried out; on the other hand, if it is too high, the ability to learn from the history of the search is lost.

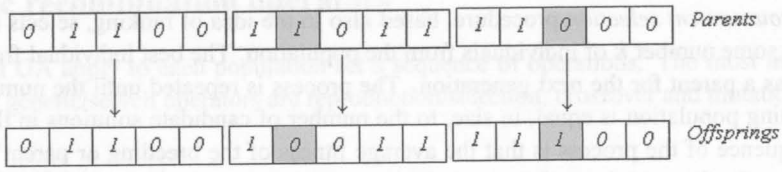

Figure 4.3: *Mutation - genetic algorithm recombination operator. Genes 7 and 13 randomly chosen as the mutation genes.*

4.4 Genetic representation

Traditionally, the binary encoding of the candidate solutions is the representation used in genetic algorithms. In this case, the length of the binary string depends on the required precision of the problem, making this representation not suitable when applied to multidimensional, high-precision numerical problems. An alternative is to use the floating point representation avoiding coding and decoding of the solutions and therefore allowing an easy and efficient implementation combined with an higher degree of precision. In the case of floating point representation the mutation and the crossover operators must be slightly modified as described in the next section.

4.4.1 Floating point genetic operators

The genetic operators used with the floating point representation differ from the classical ones due to the existence of a real search space. In recent years several genetic operators have been proposed [81] [82]. Uniform and non-uniform mutation together with simple and arithmetical crossover will be presented next.

Uniform mutation If $x_i^t = \{v_1, ...v_n\}$ is a chromosome, then, each element v_k has exactly equal chance of undergoing mutation. The result of a single application is a vector $\{v_1, ..., v'_k, ..., v_n\}$ with $1 \leq k \leq n$ and v'_k is a random value from the domain of the corresponding parameter.

Non-uniform mutation Is one of the operators responsible for fine-tune capabilities and is a function of the population age. If $s_v^t = \{v_1, ..., v_n\}$ is a chromosome and the element v_k was selected for this mutation ($v_k \in [l_k, u_k]$), the result is a vector $s_v^{t+1} = \{v_1, ..., v'_k, ..., v_n\}$, with $k \in \{1, ..., n\}$ and

$$v'_k = \begin{cases} v_k + \Delta(t, u_k - v_k) & \text{if a random digit is 0,} \\ v_k - \Delta(t, v_k - l_k) & \text{if a random digit is 1.} \end{cases} \tag{4.4}$$

with

$$\Delta(t, y) = yr(1 - \frac{t}{T})^b \tag{4.5}$$

where t stands for generation number, r is a random number from [0,1], T the maximal generation number and b a system parameter which determines the degree of non-uniformity. The function $\Delta(t, y)$ returns a value in the range $[0, y]$ such that the probability of $\Delta(t, y)$ being close to zero increases as t increases.

Simple crossover This operator is analogous to that of binary implementation. As in the binary implementation we can have more than one cut-point.

Arithmetical crossover Is defined as the weighted average of two vectors. If s_v^t and s_w^t are to be crossed, the resulting offsprings are $s_v^{t+1} = as_w^t + (1-a)s_v^t$ and $s_w^{t+1} = as_v^t + (1-a)s_w^t$. This operator makes use of a parameter a which is either a constant (uniform arithmetical crossover), or a variable depending on the age of the population (non-uniform arithmetical crossover). This operator can be applied either to selected elements of the two vectors or to the whole vector.

4.5 Selective pressure and population diversity

The main parameters controlling the search behaviour are: the *population size*, able to affect both the ultimate performance and the efficiency of GA; the *crossover probability*, that controls, as already mentioned, the frequency at which the crossover operator is applied; the *mutation probability*, which main effect is to increase the population variability and the *selection strategy* [83]. The influence of this parameters on the algorithm's behaviour may be described in terms of two primary factors: selective pressure and population diversity. As selective pressure increases, the search focuses on highly fitted members of the population often excluding low fitted strings from the whole process. Population diversity is related with the distribution throughout the search space of strings in the breeding population. The relation and a correct balance between these two opposite factors is a key to a successful global optimisation search [84]. Several methods are available to control selective pressure and population diversity and to improve genetic search. Three of the most common are elitist strategy, micro GA and scaling mechanisms that will be presented in the next sections.

4.5.1 Elitist model

An *elitist strategy* can be employed to avoid that the best solution in the population disappears due to sampling errors, crossover or mutation. This strategy guarantees that the best performance survives intact to the next generation by comparing the best solutions of two consecutive generations. In the case that the best solution of the previous generation is better that the one from the current generation, the former will replace the worst solution of the current generation. Occasionally, this method may result in a search excessively focused on the best solution found, at the expense of not undertaking a wider search for other potential good solutions [84].

4.5.2 Micro genetic algorithms

One of the available mechanisms to keep diversity are the *micro genetic algorithms*. Krishnakumar (1989) [85] found that a micro-GA avoided better premature convergence to the near optimal region than did a simple GA, for some multimodal problems. A micro-GA starts with a random and very small population. Genetic operators are applied until nominal convergence (all the individuals have their genotypes either identical or very similar) is reached. At this point, a new random population is chosen while keeping the best individual from the previous converged generation and the evolution process restarts [86].

4.5.3 Scaling mechanisms

In proportional selection procedure the selection probability of a chromosome is proportional to its fitness (or optimisation function value). This simple scheme presents some undesirable properties.

Namely, in early generations one may have some super-chromosomes in a population of mediocre solutions that will take over a significant part of the finite population in a few generations, dominating the selection procedure and leading to premature convergence. On the other hand, while selective pressure may be sufficient in early stages of the iterative process, the homogenisation of the individuals of the population towards the end contributes to a decrease of the ability of the algorithm for finding new solutions. In this case the survival of the fittest necessary for improvement becomes a random process. Scaling and ranking mechanisms are proposed to mitigate these problems and to keep appropriate levels of competition throughout the simulation. By scaling up the objective function values the differences between each individual of the population are accentuated while keeping track of the best performers and maintaining an appropriate selective pressure.

The relation between scaled fitness and raw fitness may be constant - static scaling methods - or it can vary according to some factors - dynamic scaling methods. Normally, one divides scaling mechanisms in three categories:

- Linear Scaling
- Sigma Truncation
- Power Law Scaling

For more details on sigma truncation and on power law scaling refer to [76], [82]. Concerning the linear scaling method the relationship between the scaled fitness, f', and the raw fitness, f, is as follows:

$$f' = af + b \tag{4.6}$$

The parameters a and b can be chosen in a number of ways and are normally fixed for the population life and independent of the problem. Normally they are chosen in such a way that the average scaled fitness, f'_{avg}, is equal to the average raw fitness, f_{avg}, and the best fitness, f'_{max}, is increased by a desired multiple of the average raw fitness

$$f'_{avg} = f_{avg} \qquad f'_{max} = C_{mult} \cdot f_{avg} \tag{4.7}$$

For typically small populations (50 to 100 individuals) a C_{mult} of 1.2 to 2.0 has been successfully used [76]. Linear scaling may give negative values that must be dealt with. Several solutions are available to solve this problem: in the presence of negative values the equality between the raw and the scaled fitness averages are still maintained and the minimum raw fitness, f_{min}, is mapped to a scaled fitness of zero ($f'_{min} = 0$).

4.6 Maximisation and minimisation problems

Without any loss of generality one can assume maximisation problems only. If the objective is to minimise a function, f, this is equivalent to maximise a function, g, where

$$min\{f(x)\} = max\{g(x)\} = max\{-f(x)\} \tag{4.8}$$

Normally this does not guarantee the non-negativity of the values in all instances. Thus, with GA the following transformation is commonly used

$$g(x) = \begin{cases} C_{max} - f(x) & \text{, when (f(x) < } C_{max}\text{)} \\ 0 & \text{, otherwise.} \end{cases} \tag{4.9}$$

The coefficient C_{max} can be chosen in a variety of ways: can be just an input coefficient; the largest f value observed so far; the largest f value in the population; the largest f value of the last generations or a variable function of population variance [76].

When the objective is to maximise a function $u(x)$, negative values can be avoided by performing the following transformation

$$f(x) = \begin{cases} u(x) + C_{min} & \text{, when (u(x) + } C_{min}) > 0, \\ 0 & \text{, otherwise.} \end{cases} \tag{4.10}$$

The C_{min} coefficient may be chosen as the absolute value of the worst $u(x)$ values in the current generation or in the last k generations, or as a function of the population variance [76].

4.7 Genetic algorithm's general structure

Genetic algorithms are sufficiently robust to allow several configuration alternatives, however, performance and convergence characteristics may benefit from selecting one configuration over another for a given problem. Various implementation schemes and choices are available. The first consideration concerns the coding of the potential solutions of the problem: binary, floating-point or a mixed of the two can be used. The generation of the initial population: should it be random or not? In the case that the information concerning the region of the search space where the solution is more probable to be found is available, this information should be used to generate the initial population. The objective function, used to evaluate the fitness of each solution and, representing the optimisation problem to be solved should be carefully defined. Finally, an appropriate choice of the genetic operators, as well as, of the different control parameters: number of individuals in the population, crossover and mutation probabilities, maximum number of generations, etc., play an enormous role on the development of an efficient multimodal optimisation algorithm.

4.7.1 Structural optimisation using genetic algorithms

The first applications of structural optimisation using GA were first suggested by Goldberg and Samtani (1986) [87], which considered the optimisation of a 10-bar plane truss. In 1990, Hajela [88] discussed the potential of GA for structural optimisation applications. Encoding, optimal population size, selection, crossover and mutation were discussed together with applications on non convex search spaces. Rao *et. al* (1991) [89] used a genetic algorithm approach for the optimal placement of actuators in a 10-bar truss. The maximum number of actuators was limited to 3 and an optimal linear quadratic regulator was applied to solve the optimal control gain. The dissipation energy of active controller was used as the objective function for maximisation. Schoenauer and Xanthakis (1993) [90] applied to a 10-bar (2D) and to a 25-bar (3D) truss a general method of handling constraints in genetic optimisation.

The problem of using GA to minimise the total weight of a space structure subjected to stress, displacement and dimensional constraints was addressed by Adeli and Cheng (1994) [91]. In 1995, Rajan [92] used GA to determine the size, shape and topology of space structures. The cross sectional area of each member was defined by discrete and continuous values and a penalty function was used for measuring fitness. An history of each chromosome was kept in order to avoid the recalculation of its fitness. The methodology was applied to a 6-node and 14-node truss. Simpson and Hansen (1996) [84] developed a genetic algorithm search technique for the optimisation of the location of vibration control actuators to actively control harmonic interior sound levels in a structure representative of an aircraft fuselage. Coello *et. al* (2000) [93] discussed the suitability of an heuristic technique to solve multi objective optimisation problems. The approach was tested on a 25-bar and on a 200-bar plane truss. Cook and Crossley (2001) [94] presented a genetic algorithm approach to place discrete actuators on an aircraft wing to produce

control moments about all three axes. The method was applied to a simple wing model with 16, 32 and 64 possible actuator locations.

4.7.2 Genetic algorithm's computer code

This section describes the design and implementation of the developed genetic algorithm computer code. Three different implementations had to be tailored to three different optimisation problems. Namely,

- Shape Control I: given a structure and the localisation of the piezoelectric actuators, determinate the optimal actuation voltages needed to apply to each of the actuators in order to induce the structure to deform in a certain pre-defined way;
- Shape Control II: given a structure and a maximum number of piezoelectric actuators that can be used within that structure find the optimal number, the optimal position and the optimal voltages needed to apply to those actuators in order to deform the structure in a certain pre-defined way;
- Vibration Control: given a structure covered with collocated piezoelectric sensors/actuators find the piezoelectric elements that need to be activated, assuming constant gain feedback control, in order to control one of the vibration modes or a combination of several ones.

Table 4.1 describes the main features of each of the three optimisation problems.

Table 4.1: *Description of the main features of the design problems.*

	Shape Control I	Shape Control II	Vibration Control
No. variables	number of piezoelectric actuators	no. of elements in the FE mesh plus maximum no. of piezoelectric actuators	no. of elements in the FE mesh
Problem Representation	real values (actuation voltages)	binary string (0-no piezo / 1-piezo) plus real values for actuation voltages	binary string (0-no active piezo / 1-active piezo)
Problem type	minimisation	minimisation	maximisation
Objective function	error between pre-defined shape and achieved shape	error between pre-defined shape and achieved shape	weighted sum of closed loop damping ratios

The implementation was done in Fortran and MATLAB ®. Several test functions were generated to validate the developed code. Figure 4.4 shows schematically the general layout of the present implementation valid for the three design problems.

The program starts by initialising a random sample of individuals and by reading the control parameters from an external file: population size, maximum number of generations, probabilities of crossover and mutation, number of variables, etc. The coding scheme and the evaluation of the fitness function is dependent on the application as already shown in Table 4.1.

In all the cases, the code makes use of the finite element code described in Section 2.2.5 to model the structure and for calculating mass, stiffness (mechanical and piezoelectric), eigenvectors and eigenvalues matrices. During each cycle, the algorithm undergoes conventional genetic operators. The selection scheme is tournament selection and an elitist strategy was adopted. Concerning the other genetic operators single-point and uniform crossover were implemented together with uniform mutation. An option for the use of micro-GA has been added. At the end of each iteration a small report on the progress of the simulation is performed. The values of the population's fitness mean, standard deviation and best value are written to an output file. The termination test is based on a pre-defined maximum number of generations. The interaction between the three genetic algorithm's implementations and the finite element code is presented in Figure 4.5.

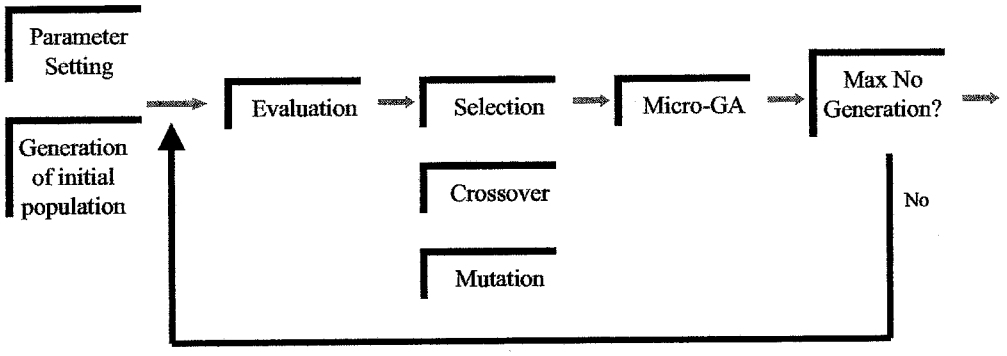

Figure 4.4: *Implementation of GA's code. Main modules.*

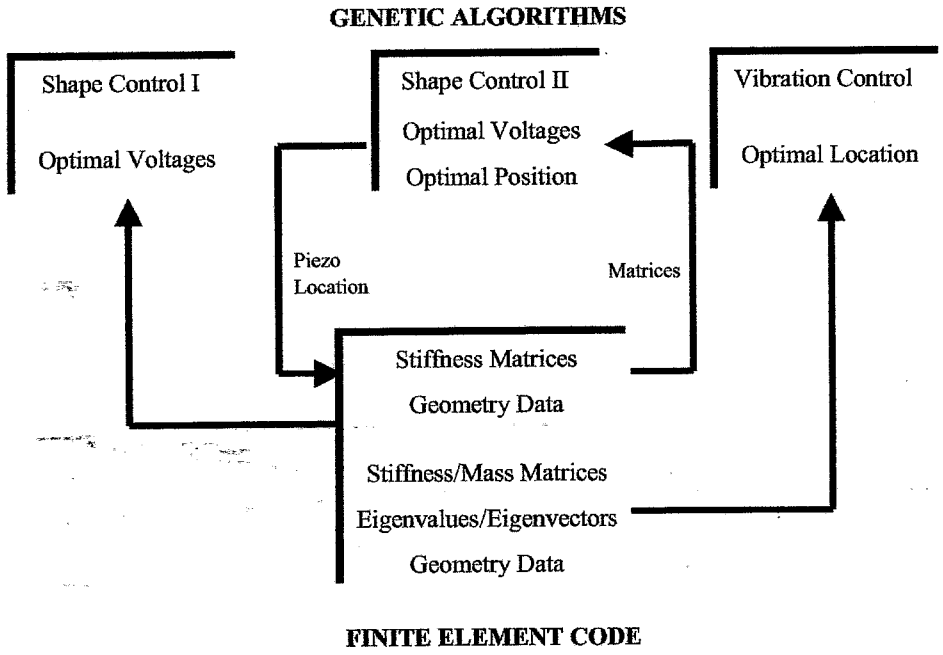

Figure 4.5: *Interaction between the genetic algorithm code and the finite element code.*

The determination of the optimal position of the piezoelectric actuators (Shape Control II) obliges a permanent communication between the genetic algorithm module and the finite element module in order to update the system's matrices, function of the piezoelectric's layout. In the case of the two other designs: determination of the optimal actuation voltages (Shape Control I) and vibration control the calculation of the system's matrices is done only one time at the beginning of the iteration process.

Chapter 5

Shape Control

The use of piezoelectric actuators for shape control and correction of static deformations in mechanical structures is the first main application considered in this work. Genetic Algorithms (GA) were implemented to calculate the optimal actuation voltages that minimise the error between the achieved and the pre-defined shape. The need of an optimisation algorithm able to solve efficiently this problem without imposing a large number of requirements and restrictions lead us to use this algorithms. The model was investigated numerically and experimentally verified for different geometries with different boundary conditions and pre-defined displacement fields. Measurements were carried out using a non-contact capacitive displacement sensor and Electronic Speckle Pattern Interferometry (ESPI). Good agreement was found between simulation results and measured values.

Experimental results consider only beam and plate structures made of isotropic materials, however the developed methodology is general and can be applied to more complex geometries made of orthotropic materials.

5.1 Experimental issues

Piezoelectric actuators/sensors can be either embedded or surface bonded in the structure. With surface mounted piezoelectrics, maintenance and access for inspection is easier while presenting an higher susceptibility to damage because of exposure. Embedded piezoelectrics are inaccessible for inspection, however better protected, and in the case of embedded electronics, the interconnections become easier. Several aspects have to be taken into account when building smart structures. Namely,

- Electrical contact on both sides of the piezo is required. One way to overcome this problem is to drill a hole in the substrate and use non-conducting epoxy. Another way, and in the case of a surface mounted piezo, is to solder to the bottom of the piezo a copper electrode.
- In the case of using structures made of conductive material the piezoelectric element must be insulated from the structure. This can be done by anodising the structure or by gluing between the piezo and the structure a few micron layer of an insulating material.
- For a proper transfer of the induced strain to the main structure, the bonding layer thickness needs to be thin and uniform. Pressure must be applied during curing.
- Before gluing the substrate surface must be prepared. In the case of aluminium substrate, the surface should be slightly roughen and degreased.
- For surface mounted piezoelectric elements, the electrical contact is made by soldering wires to top and bottom surfaces of the piezo. Soldering time should be kept in the order of 3 seconds and soldering iron temperature around 400 °C in the case of nickel electrodes.

For the various experimental set-up used in this work a copper electrode, a 15 μm kapton insulating layer and standard Araldite were used. For non-metallic substrates the kapton layer was not needed. Figure 5.1 shows the details of a piezoelectric element glued to an aluminium substrate.

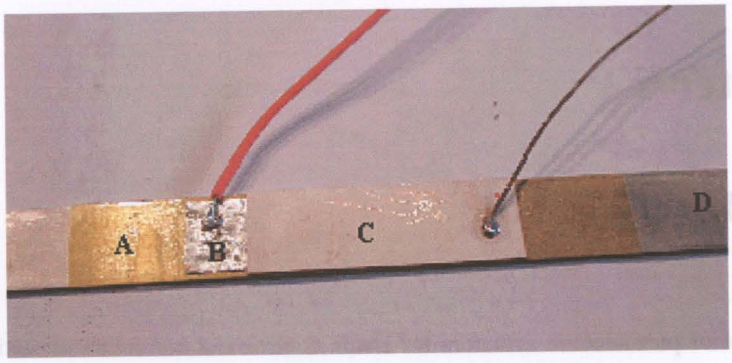

Figure 5.1: *Piezoelectric element glued to an aluminium substrate: A - kapton, B - copper electrode, C - piezoelectric element, D - aluminium beam.*

5.2 Mathematical formulation

Shape control problems can be considered quasi-static if slow time varying disturbances are assumed. In this case the first expression of Equation (2.43), in a free load condition, can be written as

$$[K_{mm}]\{q\} - [K_{em}]\{\phi\} = 0 \tag{5.1}$$

Solving in order to the nodal displacements, $\{q\}$, the displacement field can be easily computed as a function of the stiffness of the structure and of the applied voltages, $\{\phi\}$, by

$$\{q\} = [K_{mm}]^{-1}[K_{em}]\{\phi\} \tag{5.2}$$

The determination of the mechanical stiffness and coupled electrical/mechanical stiffness matrices is based in the Mindlin theory of plates and is calculated with the finite element code presented in Section 2.2.5.

When considering plate elements, the shape of a structure is mainly described by the shape of its mid-plane, which itself, is described by the transverse displacement of the finite element mesh nodes. Therefore, the deviation between the pre-defined displacement field function and the achieved displacement field, can be defined as the sum of the deviations at the n nodal points, and the fitness or objective function, J, is then given by

$$J^2 = \sum_{i=1}^{n} (\gamma_i - q_i)^2 \tag{5.3}$$

where γ_i is the pre-defined displacement at the $i-th$ node and q_i the transverse displacement at the same node. This objective function gives an estimate of the variance of the current displacement values with respect to the pre-defined ones.

The shape control problem, or the correction of static deformations, of a given structure with a given layout of piezoelectric actuators, consists in finding a set of actuator voltages, ϕ_i, that minimises the error function J and satisfies the following constraint

$$\phi_{min} \leq \phi_i \leq \phi_{max} \tag{5.4}$$

where ϕ_i is the actuation voltage of the $i-th$ actuator and ϕ_{min} and ϕ_{max} the lower and upper saturation voltages of the actuators. Equations (5.3) and (5.4) represent the minimisation formulation problem - fitness function and constraints - to be solved by genetic algorithms.

5.3 Applications

The first application consists in finding the best set of actuation voltages, to be applied to six pairs of piezoelectric patches placed on a beam structure, in order to achieve a certain pre-defined displacement field. Two different boundary conditions will be considered. The influence of GA's main parameters: population size, crossover probability and mutation probability in the obtained results and in the convergence rate of the algorithm will then be discussed.

In the next applications, the optimisation procedure will be experimentally verified. Two beam structures, with one and three PZT respectively, and a plate structure with four PZT, will be studied considering different boundary conditions and different pre-defined displacement fields. In the last application the optimisation algorithm will be modified in order to accommodate not only the determination of the optimal actuation voltages but also the best actuator layout for a given pre-defined shape.

5.3.1 Simulation results: composite beam with 6 pairs of PZT

The set-up used in this simulation consists of a carbon fibre composite cantilever beam with six pairs of lead zirconate titanate (PZT) patches symmetrically attached to the locations shown in Figure 5.2 [95].

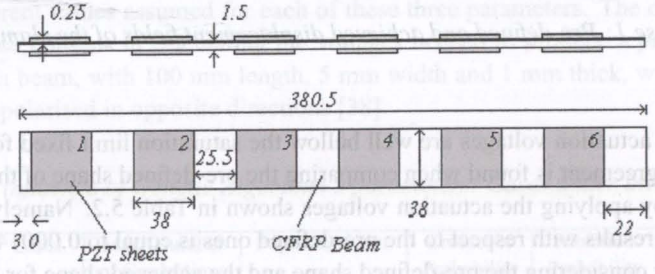

Figure 5.2: *Top and side view of the composite beam with 6 pairs of PZT [mm].*

In this case the variables are the voltages of each of the six piezoelectric patches on one side of the beam, the other six being symmetric. A crossover probability of 0.65, a mutation probability of 0.05, a maximum number of generations equal to 20,000 and a population size of 20 individuals were considered. The pre-defined displacement fields, presented in Table 5.1, were chosen taking into account two different boundary conditions: clamped-free and clamped-clamped. In general and throughout all the simulations the pre-defined displacement fields were chosen arbitrarily. Boundary conditions and magnitude of displacements compatible with the dimensions of the structures were the only two criteria considered.

The pre-defined and the achieved shape for the clamped-free composite beam (Case 1), considering a saturation voltage of ± 200 Volt, is shown in Figure 5.3. The corresponding optimal actuator voltages, obtained by genetic algorithms, for each piezoelectric patch are presented in Table 5.2.

Table 5.1: *Pre-defined displacement fields considered for the composite cantilever beam shown in Figure 5.2 (L is the length of the beam and x the longitudinal co-ordinate).*

	Displacement Field
Case 1	$\gamma(x) = 0.025[1 - cos(\frac{\pi x}{L})]$
Case 2	$\gamma(x) = 0.015[1 - cos(\frac{4\pi x}{L})]$

Table 5.2: *Case 1: Actuation voltages, applied to each pair of piezos, obtained for the clamped-free composite beam considering a saturation voltage of ±200Volt.*

	V_{piezo1} [V]	V_{piezo2} [V]	V_{piezo3} [V]	V_{piezo4} [V]	V_{piezo5} [V]	V_{piezo6} [V]
Case 1	50.7	54.5	23.1	-12.7	-45.9	-53.6

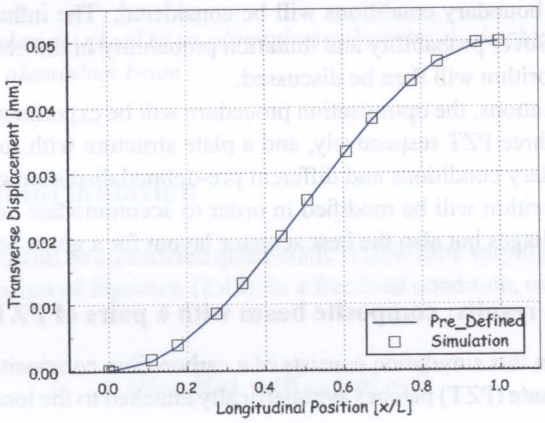

Figure 5.3: *Case 1: Pre-defined and achieved displacement fields of the clamped-free composite beam.*

All the six actuation voltages are well bellow the saturation limit fixed for each piezoelectric patch. An excellent agreement is found when comparing the pre-defined shape of the composite beam with the one obtained by applying the actuation voltages shown in Table 5.2. Namely, the standard deviation of the simulation results with respect to the pre-defined ones is equal to 0.00014 mm.

The results considering the pre-defined shape and the achieved shape for the clamped-clamped composite beam (Case 2) are shown in Figure 5.4. Different saturation voltages for the actuators were assumed: ±200Volt, ±300Volt and ±500Volt. The optimal actuation voltages are shown in Table 5.3.

Table 5.3: *Case 2: Actuation voltages, applied to each pair of piezos, obtained for the clamped-clamped composite beam considering different saturation voltages.*

Voltage Limit [V]	V_{piezo1} [V]	V_{piezo2} [V]	V_{piezo3} [V]	V_{piezo4} [V]	V_{piezo5} [V]	V_{piezo6} [V]
± 200	164.3	-198.7	-40.8	195.1	-199.4	-198.6
± 300	206.7	-299.9	-16.2	298.7	-299.9	-193.1
± 500	282.8	-496.3	94.6	381.2	-450.2	-72.4

It is found that for a limit voltage of ±200 Volt and ±300 Volt the saturation is attained at some

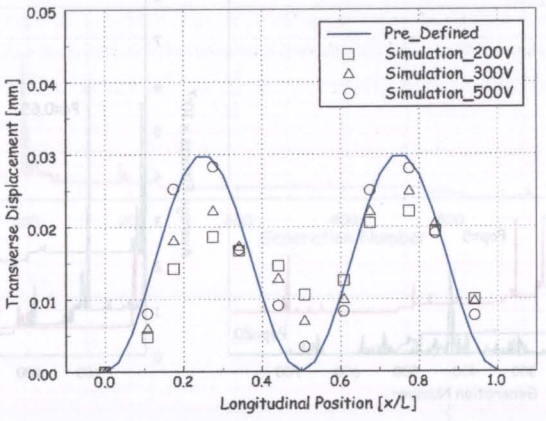

Figure 5.4: *Case 2: Pre-defined and achieved displacement field, for different saturation voltages, of the clamped-clamped composite beam.*

piezoelectric patches and the obtained shape is far from the pre-defined one. Better results are then obtained if higher voltages are allowed in the actuators (e.g. ±500 Volt). Namely, the standard deviation of the simulation results with respect to the pre-defined results is, for a voltage saturation of ±200 Volt, ±300 Volt, ±500 Volt, equal to 0.0065 mm, 0.0047 mm and 0.0028 mm, respectively.

5.3.2 Influence of genetic algorithm's parameters

In this section and before starting the experimental validation of the developed methodology one will try to understand the influence of the population size, the crossover and the mutation probabilities on the convergence of the optimisation algorithm (average fitness and optimal minimum) [96]. Table 5.4 presents the different values assumed for each of these three parameters. The optimisation problem considered in this case consists in calculating the voltages needed to produce a pre-defined shape in a piezoelectric bimorph beam, with 100 mm length, 5 mm width and 1 mm thick, with two PVDF layers bonded together and polarised in opposite directions [38].

Table 5.4: *Influence of Genetic Algorithm's parameters. Cases under investigation.*

Cases	Max. Number of Generations	Population Size	Crossover Probability	Mutation Probability
Case 1	800	5	0.65	0.025
Case 2	800	10	0.65	0.025
Case 3	800	20	0.65	0.025
Case 4	800	10	0.20	0.025
Case 5	800	10	0.90	0.025
Case 6	800	10	0.65	0.05
Case 7	800	10	0.65	0.15

The effect of the population size parameter on the average fitness of each population and on the minimum value of the fitness function obtained after 800 generations is shown in Figure 5.5 and Table 5.5.

A better performance was obtained for a population size of 20 individuals when compared with a population of 10 and 5 individuals. On one hand, the time required to evaluate each group depends on

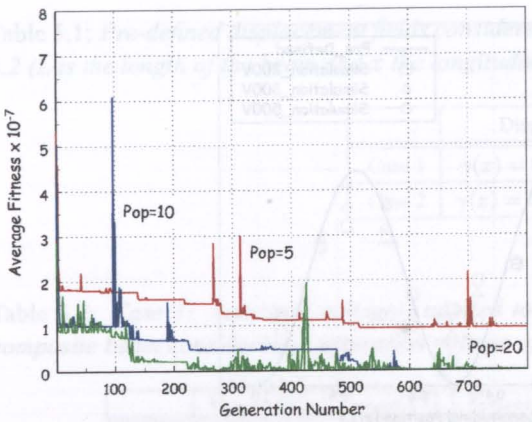

Figure 5.5: *Effect of the population size (pop. size) on the average fitness of the population.*

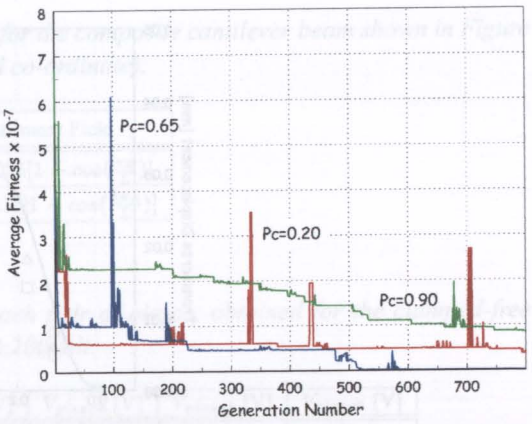

Figure 5.6: *Effect of the crossover probability (p_c) on the average fitness of the population.*

Table 5.5: *Total average fitness and minimum value for different pop. size (p_c=0.65, p_m=0.025).*

Case	1	2	3
Pop. Size	5	10	20
Average	1.28	0.45	0.25
Minimum	0.94	0.014	0.0004

Table 5.6: *Total average fitness and minimum value for different p_c (p_m=0.025, pop. size = 10).*

Case	4	2	5
p_c	0.20	0.65	0.90
Average	0.64	0.45	1.7
Minimum	0.36	0.014	0.84

Table 5.7: *Total average fitness and minimum value for different p_m (p_c=0.65, pop. size = 10).*

Case	2	6	7
p_m	0.025	0.05	0.15
Average	0.45	0.31	0.76
Minimum	0.014	0.002	0.015

the number of individuals, and consequently larger populations impose an higher computational effort. On the other hand a larger population contains more diversity, discouraging premature convergence to sub-optimal solutions. A population of 20 individuals presents the best compromise when compared to a population of 5 and 10 individuals.

The crossover probability was changed between 0.2 and 0.9. Figure 5.6 presents the effect of the crossover probability on the average fitness of the population in each generation and Table 5.6 the total average fitness and the minimum value obtained after the 800 generations. For low crossover probabilities (p_c=0.2) there is the possibility of falling into local minimum and the search may stagnate due to lower exploration rate. If the crossover probability is too high (p_c=0.9) the algorithm spends time searching in unnecessary areas without any benefit on the total average fitness. On the other hand, for higher crossover probabilities, high performance structures may be discarded faster than selection can produce improvements. A crossover probability of 0.65 seems to be a reasonable value for this case.

The mutation probability was changed between 0.025 and 0.15. Figure 5.7 presents the effect of the mutation probability on the average fitness of the population and Table 5.7 the total average fitness and the minimum values attained after the 800 generations.

If the mutation probability is too high, the search becomes random and the next generation will lose the similarity to the parents so that the convergence may suffer (p_m=0.15). On the other hand if the mutation probability is too low, new genes are not tested and the overall convergence may be compromised (p_m=0.025). A mutation probability of 0.05 gives, in this case, the best fitness average and the minimum value of the fitness function.

It is interesting to observe that eventual excursions to non-optimal solutions (the peaks in the plots), in all figures, are rapidly excluded and a fast convergence is obtained.

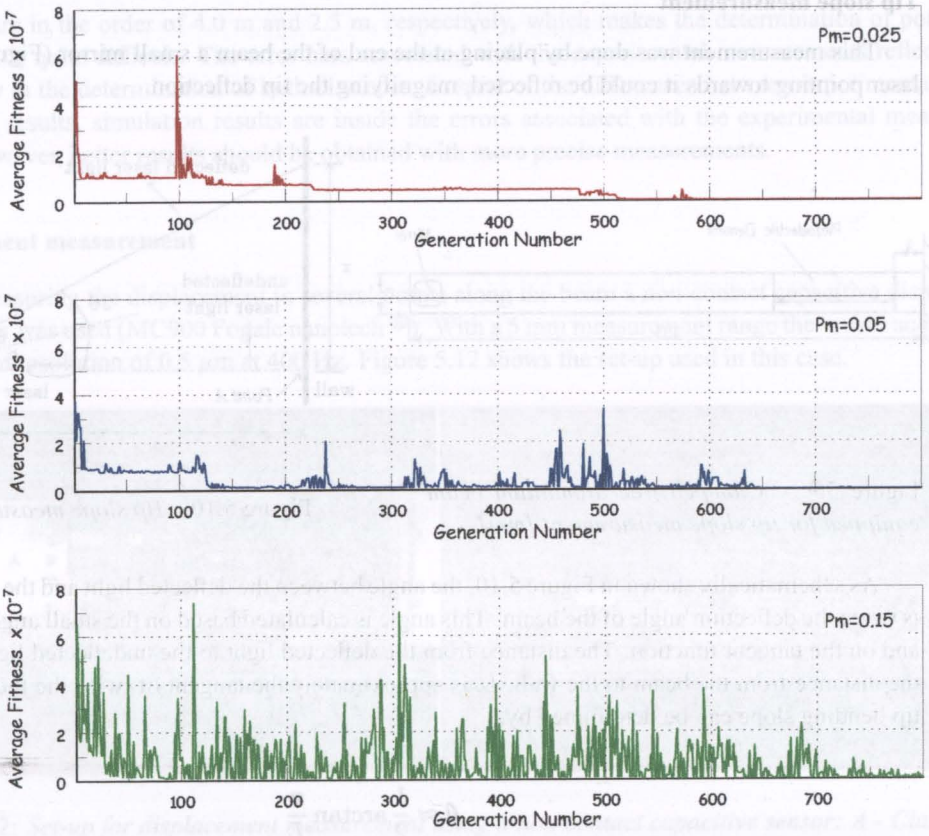

Figure 5.7: *Effect of the mutation probability (p_m) on the average fitness of the population.*

5.3.3 Experimental results: aluminium cantilever beam with 1 PZT

The first experimental set-up comprised an aluminium cantilever beam with one bonded piezoceramic near the clamped edge (see Figure 5.8). The beam was 153 mm long, 12 mm wide and 1 mm thick.

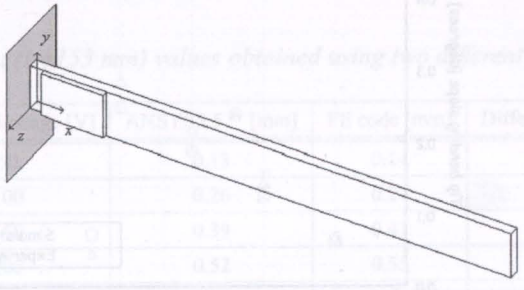

Figure 5.8: *Schematic of the experimental set-up comprising a clamped-free aluminium beam and a piezoceramic element.*

The piezoceramic (P1-91 block) was 0.2 mm thick, 36 mm long and 12 mm wide. Its electromechanical properties were already presented in Section 3.3.

For increasing actuation voltages, applied to the piezoelectric element, the tip slope and the displacement along the beam were measured.

Tip slope measurement

This measurement was done by placing at the end of the beam a small mirror (Figure 5.9), so that a laser pointing towards it could be reflected, magnifying the tip deflection.

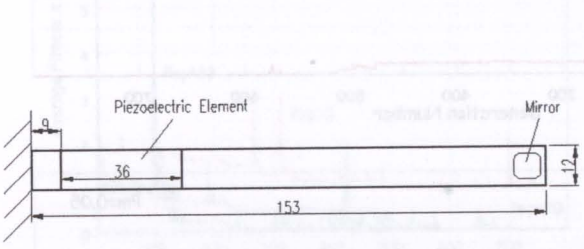

Figure 5.9: *Clamped free aluminium beam equipped for tip slope measurement [mm].*

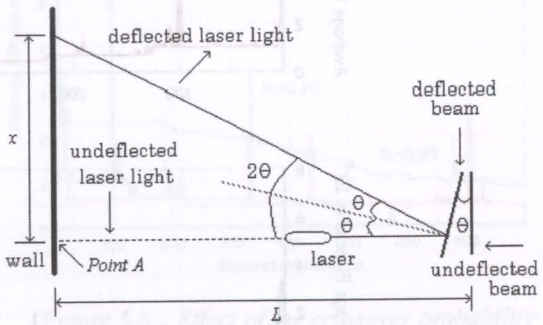

Figure 5.10: *Tip slope measurement scheme.*

As schematically shown in Figure 5.10, the angle between the deflected light and the undeflected light is twice the deflection angle of the beam. This angle is calculated based on the small angle approximation and on the tangent function. The distance from the deflected light to the undeflected light, x, divided by the distance from the beam to the wall, L, is approximately the tangent of twice the theta angle. So, the tip bending slope can be determined by

$$\theta \approx \frac{1}{2} \arctan \frac{x}{L} \tag{5.5}$$

The results obtained for the tip slope measurement function of the applied voltage (50 to 300 Volt) together with the simulation results, obtained with the finite element code described in Section 2.2.5, are presented in Figure 5.11.

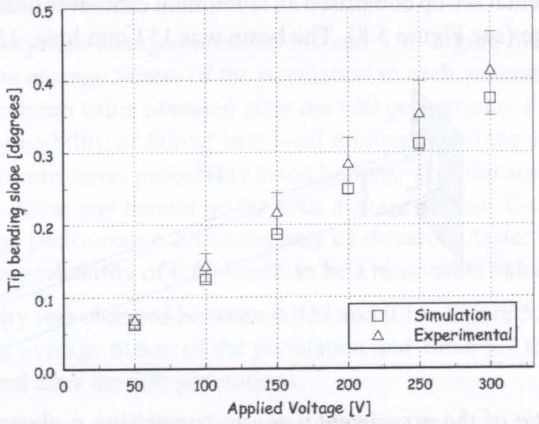

Figure 5.11: *Tip bending slope versus applied voltage. Experimental and simulation results.*

The differences between simulation and experimental results vary between 11-20% and are mainly function of the uncertainty associated with the determination of the distance between the undeflected light beam and the deflected light beam (x) and the distance between the beam and the wall (L). These

distances are in the order of 4.0 m and 2.5 m, respectively, which makes the determination of point A (Figure 5.10) quite difficult. The error bars associated with the experimental measurements reflect the uncertainty in the determination of both distances. In spite of the differences between experimental and simulation results, simulation results are inside the errors associated with the experimental measurements. However, better results should be obtained with more precise measurements.

Displacement measurement

For measuring the displacement in several points along the beam a non-contact capacitive displacement sensor was used (MC900 Fogale nanotech ®). With a 5 mm measurement range the sensor achieves a maximum resolution of 0.5 μm at 400 Hz. Figure 5.12 shows the set-up used in this case.

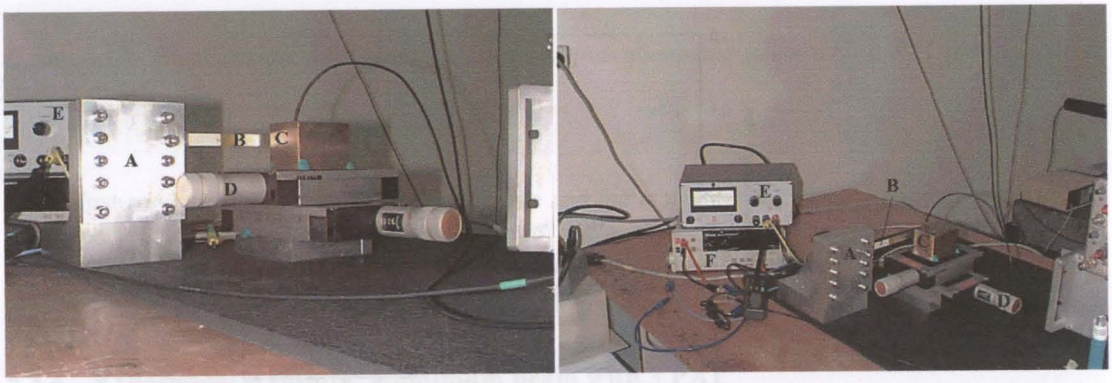

Figure 5.12: *Set-up for displacement measurement using a non-contact capacitive sensor: A - Clamped fixation, B - Aluminium beam with 1 PZT, C - Capacitive sensor, D - 2-Axis micrometer table, E - Power supply, F - Multimeter.*

Simulations were performed using a commercial finite element package (ANSYS55 ®) and the FE code already described (Section 2.2.5). Solid elements were used in the finite element mesh of ANSYS 5.5 ®. Table 5.8 presents the tip displacement values obtained with the two codes for actuation voltages ranging from 50 to 300 Volt.

Table 5.8: *Tip displacement (L=153 mm) values obtained using two different finite element codes [mm].*

Applied Voltage [V]	ANSYS5.5 ® [mm]	FE code [mm]	Difference [%]
50	0.13	0.14	7.7
100	0.26	0.27	3.8
150	0.39	0.41	5.1
200	0.52	0.55	5.8
250	0.65	0.68	4.6
300	0.78	0.82	5.1

The differences found between the two simulation codes are less than 8% and are mainly due to the type of elements - solid elements in ANSYS5.5 ® and plate elements in the FE code - and to the number of elements of the finite element mesh.

The transverse displacement of the aluminium beam was experimentally determined in five longitudinal points, namely at 63 mm (x/L=0.41), 81 mm (x/L=0.53), 117 mm (x/L=0.76), 135 mm (x/L=0.88) and 148 mm (x/L=0.97) (see Figure 5.13).

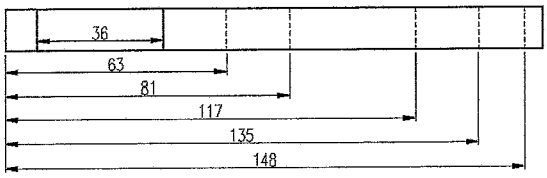

Figure 5.13: *Location of the five longitudinal measurement positions.*

Each measurement point resulted from the average of five measurements. Figure 5.14 shows the applied voltage versus the induced displacement for one of these points x=148 mm. Similar measurements were done for the other four positions. The error bars associated with each measurement were not significant to be represented.

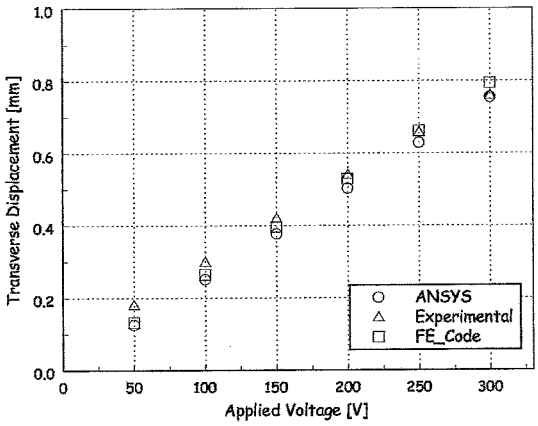

Figure 5.14: *Applied voltage versus induced displacement for x=148 mm. Average experimental values and simulation results.*

Figure 5.15, 5.16 and 5.17 show the simulation and the experimental results concerning the transverse displacement along the beam, for an applied voltage of 100 Volt, 200 Volt and 300 Volt respectively.

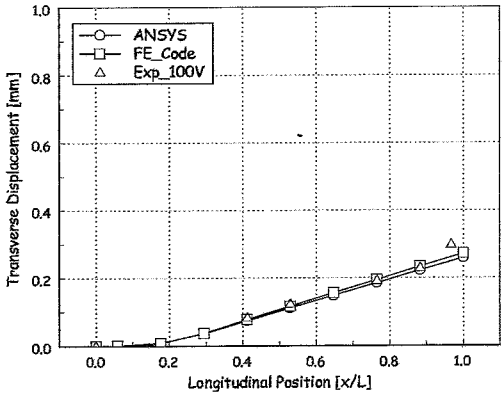

Figure 5.15: *Displacement field along the clamped-free aluminium beam with 1 PZT for an applied voltage of 100 Volt.*

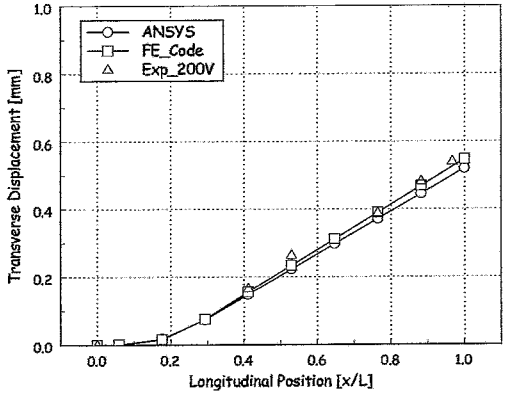

Figure 5.16: *Displacement field along the clamped-free aluminium beam with 1 PZT for an applied voltage of 200 Volt.*

A good agreement can be found between both simulation models and experimental measurements.

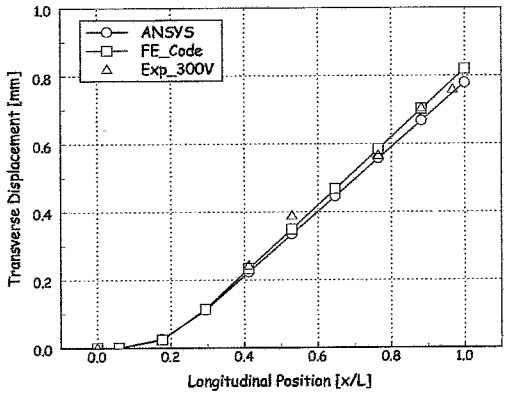

Figure 5.17: *Displacement field along the clamped-free aluminium beam with 1 PZT for an applied voltage of 300 Volt.*

These first results validate the finite element code and the mathematical formulation that will be used in the methodology developed for the shape control and/or correction of static deformations in mechanical structures. It also represents the first step towards the validation of the complete model, including modelisation of the structure plus optimisation algorithm, and to the use of more complex geometries.

5.3.4 Experimental results: aluminium beam with 3 PZT

This second experimental set-up comprises an aluminium beam with three bonded piezoceramics. Figure 5.18 presents schematically the layout of the beam for two different boundary conditions: clamped-free and clamped-clamped. Figure 5.19 shows the experimental set-up for the clamped-clamped beam.

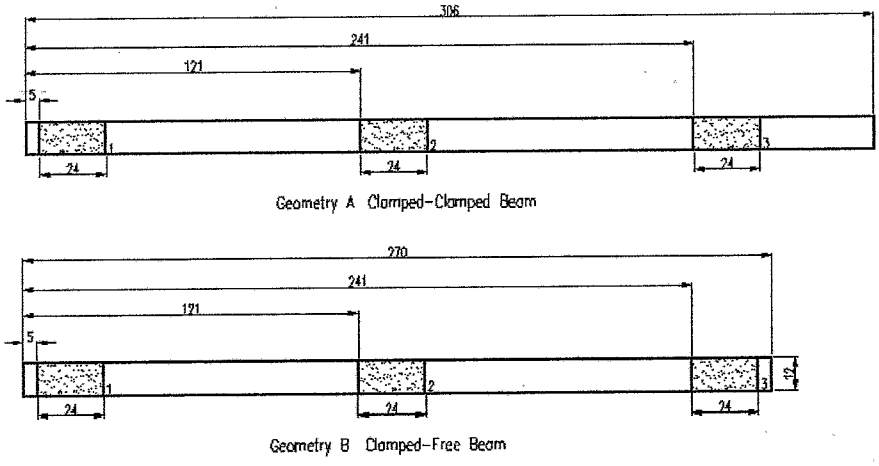

Figure 5.18: *Layout of the aluminium beam, 1.0 mm thick, used in the experiment. Two different boundary conditions are considered: clamped-free and clamped-clamped. Units are in mm.*

The beam, made of aluminium, is 12 mm wide and approximately 1 mm thick. The piezoceramic elements (PX5-N from Philips Components) are 0.3 mm thick, 24 mm long and 12 mm wide. The

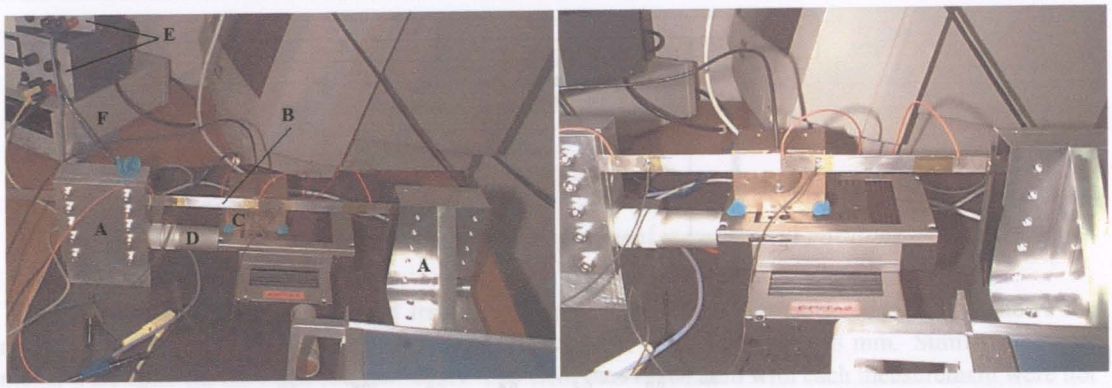

Figure 5.19: *Set-up for the clamped-clamped beam: A - Clamped fixations, B - Aluminium beam with 3 PZT, C - Capacitive sensor, D - 2-Axis micrometer table, E - Power supply, F - Multimeter.*

electro-mechanical properties, given by the manufacturer, have already been presented in Section 3.4.4, Table 3.2. The saturation voltage was set to ±150 Volt.

Validation of the simulation model

Before trying to deform the structure in a certain pre-defined way, the validation and tuning of the simulation model was done by applying increasing voltages (between 0-200 Volt) to each of the three piezoelectric actuators and then simultaneously to all of them. For this particular test, only the clamped-free geometry was studied. The tip displacement for each case, obtained using the non-contact capacitive displacement sensor described before, is respectively shown in Figures 5.20, 5.21, 5.22 and 5.23.

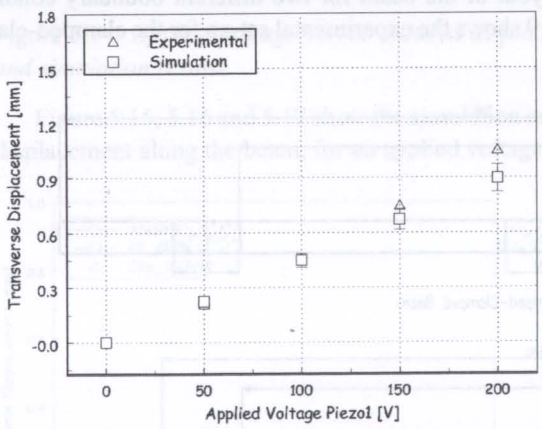

Figure 5.20: *Tip displacement of the clamped-free aluminium beam obtained for different actuation voltages applied to the first piezoelectric element.*

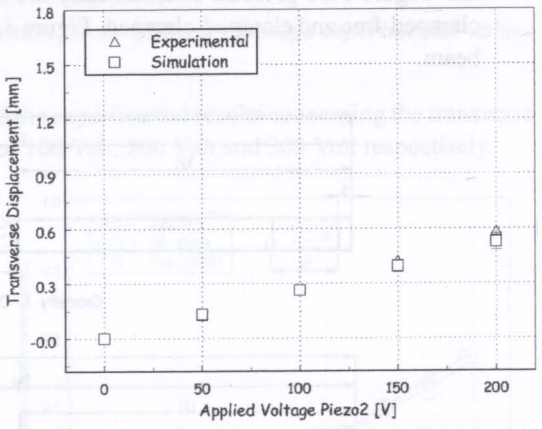

Figure 5.21: *Tip displacement of the clamped-free aluminium beam obtained for different actuation voltages applied to the second piezoelectric element.*

In general an excellent agreement between the simulation model and the experimental measurements is obtained for voltages below or equal to 100 Volt. It seems that for higher voltages there is a small loss of linearity in the response of the piezoelectric elements. This effect is less significant in the case of the second element, as well as, when the actuation voltage is applied simultaneously to all the piezoelectric elements.

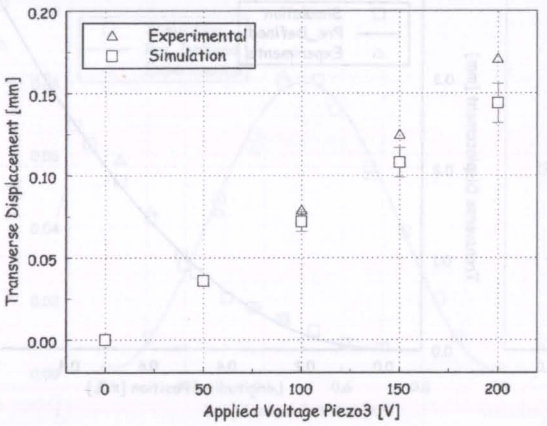

Figure 5.22: *Tip displacement of the clamped-free aluminium beam obtained for different actuation voltages applied to the third piezoelectric element.*

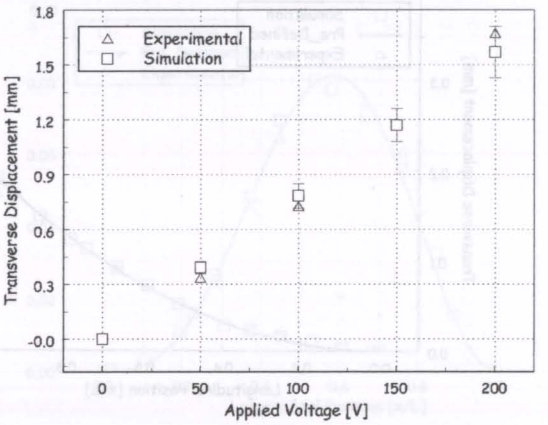

Figure 5.23: *Tip displacement of the clamped-free aluminium beam obtained for different actuation voltages applied simultaneously to all piezoelectric elements.*

The error bar of the simulation results represents the uncertainty existent in the determination of the mechanical properties of the aluminium and of the piezoelectric material. In order to reduce random errors, each experimental measurement is the averaged result of five measurements. The error associated with it is too small to be represented.

After the validation of the finite element model together with the tuning of the material properties, the next sections present the results concerning the deformation of the beam in a pre-defined way for the two different boundary conditions: clamped-free and clamped-clamped.

Clamped-free aluminium beam

Considering the clamped-free geometry two different displacement fields were considered. The actuation voltages applied to each of the three piezoelectric elements in order to match the pre-defined displacement fields were calculated by the implemented genetic algorithm code described in Section 4.7.2. A population size of 25 individuals, a probability of crossover equal to 0.85, a probability of mutation equal to 0.15 and a maximum number of generations of 15,000 were considered in the calculations. Table 5.9 shows the pre-defined displacement fields and the actuation voltages obtained by the optimisation algorithm.

Table 5.9: *Pre-defined displacement fields and actuation voltages obtained, by genetic algorithms, for the clamped-free aluminium beam. L is the length of the beam and x the longitudinal co-ordinate.*

	Displacement Field	$V_{piezo1}[V]$	V_{piezo2} [V]	V_{piezo3} [V]
Case 1	$\gamma(x) = 0.0002(\frac{x}{L})^2$	17	36	26
Case 2	$\gamma(x) = 0.0004(\frac{x}{L})^2$	34	72	51

As expected, the optimal actuation voltages obtained for Case 2 are twice the ones obtained for Case 1 since the displacement fields differ only by a factor of two. Figures 5.24 and 5.25 show the comparison between the two pre-defined displacement fields shown in Table 5.9, experimental measurements and simulation results.

The χ^2 between the pre-defined results and the simulation ones and between the pre-defined results

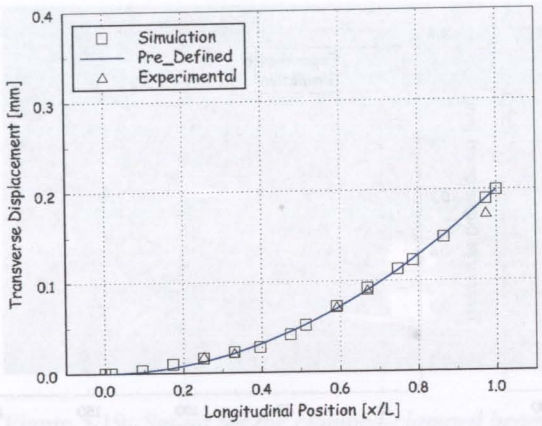

Figure 5.24: *Case 1 (clamped-free): Pre-defined displacement field, simulations and experimental measurements when the actuation voltages obtained by GA are applied to the 3 piezoelectric elements.*

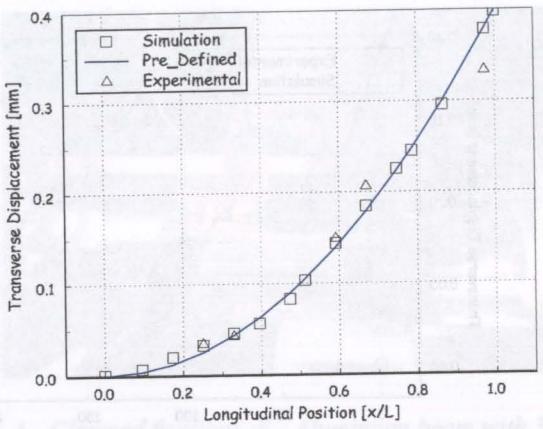

Figure 5.25: *Case 2 (clamped-free): Pre-defined displacement field, simulations and experimental measurements when the actuation voltages obtained by GA are applied to the 3 piezoelectric elements.*

and the experimental ones was calculated. For Case 1 values of 0.0021 mm and 0.0073 mm were obtained while for Case 2 one obtains 0.0042 mm and 0.024 mm, respectively. For both cases, experimental results are more dispersed from pre-defined values than simulation results. For Case 1, this dispersion in the experimental results is compatible with the error associated with each measurement. In general, a very good agreement is obtained.

Clamped-clamped aluminium beam

The same aluminium beam was now clamped on both sides. Table 5.10 shows the two pre-defined displacement fields, considered for this case, and the actuation voltages obtained by the optimisation algorithm. The genetic algorithm parameters were kept unchanged.

Table 5.10: *Pre-defined displacement fields and actuation voltages obtained, by genetic algorithms, for the clamped-clamped aluminium beam.*

	Displacement Field	$V_{piezo1}[V]$	V_{piezo2} [V]	V_{piezo3} [V]
Case 1	$\gamma(x) = 0.00004(1 - cos(\frac{2\pi x}{L}))$	-53	80	-56
Case 2	$\gamma(x) = 0.000075(1 - cos(\frac{2\pi x}{L}))(\frac{x}{L})$	17	74	-121

Figures 5.26 and 5.27 show the comparison between the two pre-defined displacement fields, simulation results and experimental measurements.

For the first case, the desired shape is achieved with relatively small voltages, with piezoelectric elements 1 and 3 presenting similar voltage values: -53 Volt and -56 Volt respectively. For the second case, which corresponds to a non symmetry shape, the voltage level is higher in the piezoelectric element number 3, -121 Volt, and opposite in sign to the one of piezoelectric element number 1, +17 Volt.

The standard deviation between the pre-defined results and the simulation ones and between the pre-defined results and the experimental ones was calculated. For Case 1 values of 0.0018 mm and 0.0041 mm were obtained while for Case 2 one obtains 0.0024 mm and 0.0033 mm, respectively. As for the case of the clamped-free beam, experimental results are more dispersed from pre-defined values

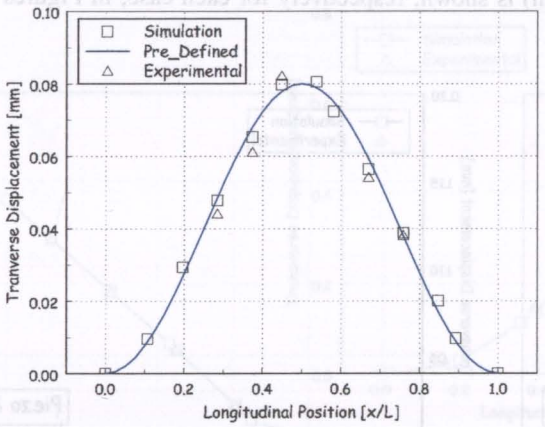

Figure 5.26: *Case 1 (clamped-clamped): Predefined displacement field, simulations and experimental measurements when the actuation voltages obtained by GA are applied to the 3 piezoelectric elements.*

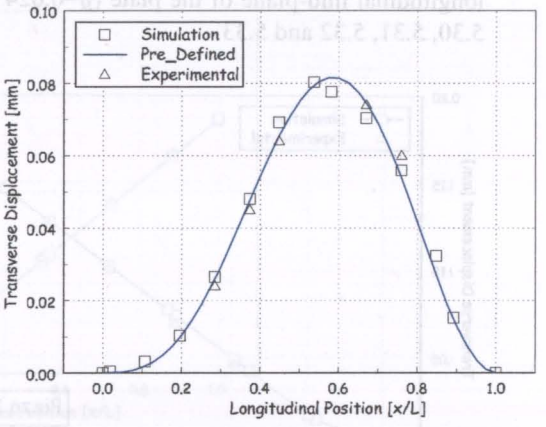

Figure 5.27: *Case 2 (clamped-clamped): Predefined displacement field, simulations and experimental measurements when the actuation voltages obtained by GA are applied to the 3 piezoelectric elements.*

than simulation results. However, this dispersion in the experimental results is compatible with the error associated with each measurement and in general a very good agreement is obtained for both cases.

These two cases validates both the finite element code being used, as well as, the optimisation algorithm.

5.3.5 Experimental results: aluminium plate with 4 PZT

The shape control in two directions, longitudinal and transversal, will be experimentally verified using a plate structure. Measurements, otherwise stated, were performed using the same non-contact capacitive displacement sensor as before. The experimental set-up comprises an aluminium plate, 48 mm wide, 153 mm long and 0.5 mm thick, with four bonded piezoceramics. Figure 5.28 presents the layout.

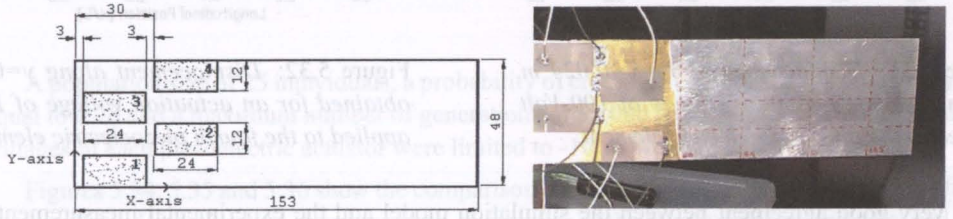

Figure 5.28: *Aluminium plate used in the experiment. Units are in mm.*

The piezoceramic elements (PX5-N from Philips Components) are 0.3 mm thick, 24 mm long and 12 mm wide. Only a clamped-free boundary condition will be considered.

Validation of the simulation model

The validation and tuning of the simulation model was done by applying 100 Volt to each of the four piezoelectric actuators and then simultaneously to all of them. The displacement obtained along the

longitudinal mid-plane of the plate (y=0.024 m) is shown, respectively for each case, in Figures 5.29, 5.30, 5.31, 5.32 and 5.33.

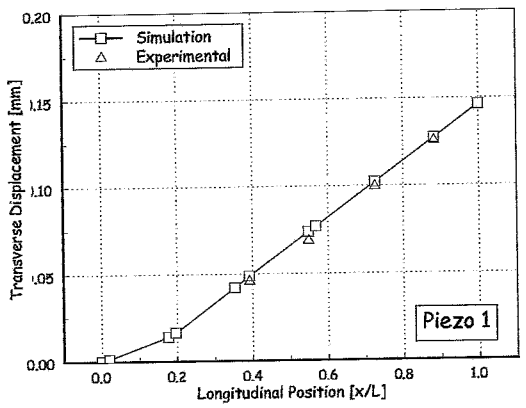

Figure 5.29: *Displacement along y=0.024 m obtained for an actuation voltage of 100 Volt applied to the first piezoelectric element.*

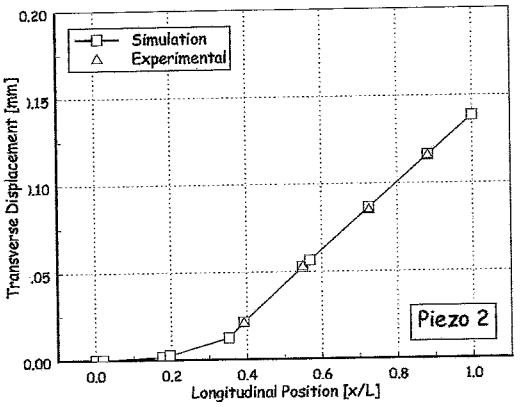

Figure 5.30: *Displacement along y=0.024 m obtained for an actuation voltage of 100 Volt applied to the second piezoelectric element.*

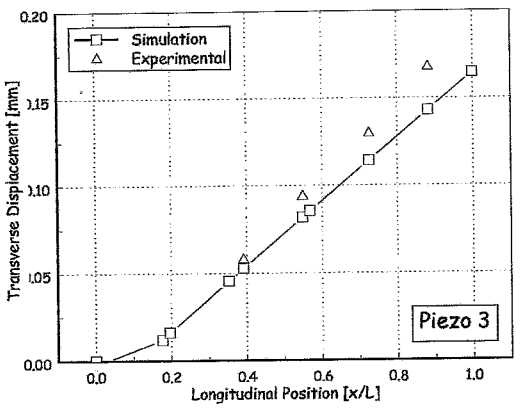

Figure 5.31: *Displacement along y=0.024 m obtained for an actuation voltage of 100 Volt applied to the third piezoelectric element.*

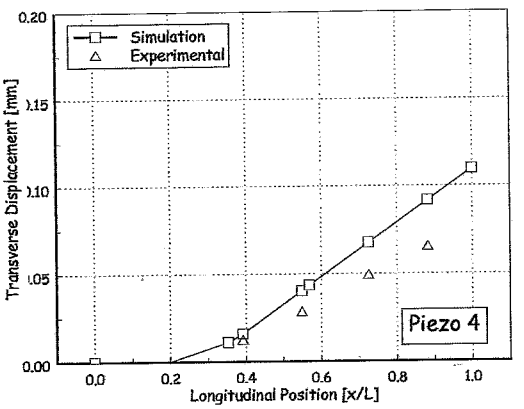

Figure 5.32: *Displacement along y=0.024 m obtained for an actuation voltage of 100 Volt applied to the fourth piezoelectric element.*

A very good agreement between the simulation model and the experimental measurements is obtained, except for the piezoelectric elements 3 and 4. These two elements present a different behaviour when compared to the simulations. While the piezoelectric element number 3 over estimate the predictions, piezoelectric element number 4 sub estimate them. Namely, for piezoelectric element number 3 and for an actuation voltage of 100 Volt, an average error of +16% is obtained between the experimental and simulated transversal displacement, while for piezoelectric element number 4 this value is in the order of -27%.

However, when working simultaneously the piezoelectric elements compensate for each other (Figure 5.33) and the agreement between simulation and experimental results is excellent. Each experimental measurement is the average result of five measurements and once again the error associated with it was too small to be represented.

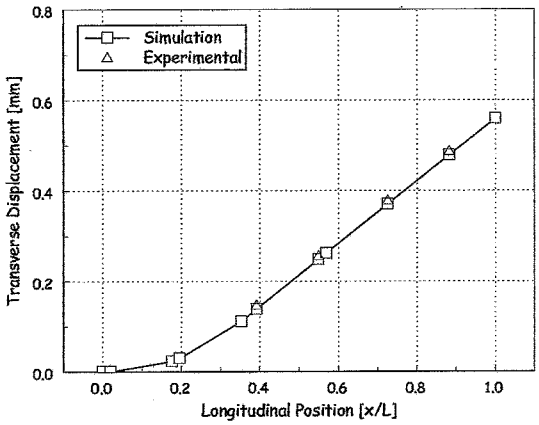

Figure 5.33: *Displacement along y=0.024 m obtained for an actuation voltage of 100 Volt applied simultaneously to all four piezoelectric elements.*

Clamped-free aluminium plate

Considering the same aluminium plate, Table 5.11 shows the considered pre-defined shape and the actuation voltages, obtained by genetic algorithms, needed to apply to each of the four piezoelectric elements in order to achieve that same shape. The plate is intended to have a combined movement of bending and torsion.

Table 5.11: *Pre-defined displacement field and actuation voltages obtained for the clamped-free aluminium plate.*

Displacement Field	$V_{piezo1}[V]$	V_{piezo2} [V]	V_{piezo3} [V]	V_{piezo4} [V]
$\gamma(x,y) = 0.0076x^2 + 0.0035xy + 0.00075x$	-68	-100	196	200

A population size of 25 individuals, a probability of crossover equal to 0.75, a probability of mutation equal to 0.20 and a maximum number of generations of 50,000 were considered in the calculations. The voltages in each piezoelectric actuator were limited to -100 Volt and +200 Volt.

Figures 5.34, 5.35 and 5.36 show the comparison between the pre-defined displacement field, simulation results and experimental measurements, as function of the longitudinal co-ordinate, and respectively at sections y=12 mm, y=24 mm and y=36 mm.

Figures 5.37, 5.38, 5.39 and 5.40 show the comparison between the pre-defined displacement field, simulation results and experimental measurements at sections x=60 mm, x=84 mm, x=111 mm and x=135 mm, as function of the transversal y co-ordinate.

For both, longitudinal and transversal measurements, experimental data follows much better simulation results then pre-defined ones. This means that the simulation model can be considered realistic and accurate. On the other hand, and since the saturation voltage was attained in piezoelectric number 2, 3 and 4, our geometry may be too rigid, the layout of the piezoelectric actuators is not the best or the number of piezoelectric patches are not enough to induce the structure to deform in the correct and pre-defined way.

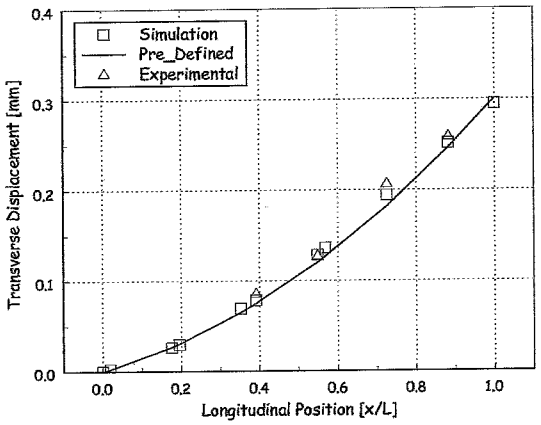

Figure 5.34: *Pre-defined displacement field, simulations and experimental measurements (y=12 mm).*

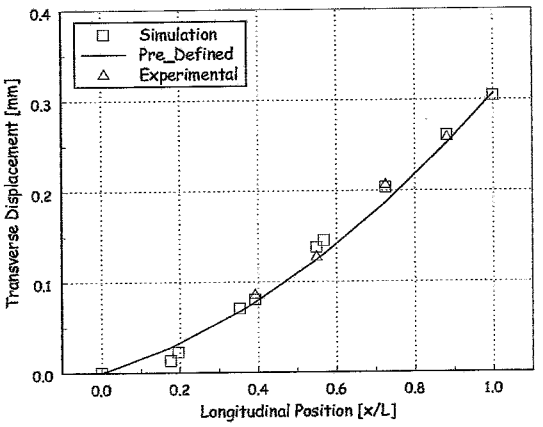

Figure 5.35: *Pre-defined displacement field, simulations and experimental measurements (y=24 mm).*

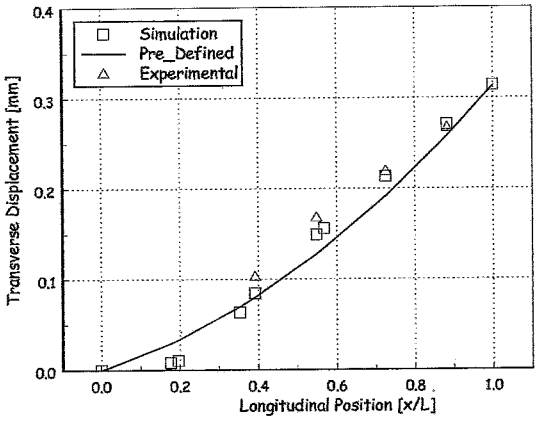

Figure 5.36: *Pre-defined displacement field, simulations and experimental measurements (y=36 mm).*

Fittings to experimental and simulation data

Fittings to the experimental and simulation data, obtained along y=12 mm, y=24 mm and y=36 mm, were performed in order to understand how well the measured shape of the plate is close to the pre-defined one. Along a longitudinal section (y equal to constant) the pre-defined shape shown in Table 5.11 takes the form $y = ax^2 + bx$ with $a = 0.1791$, b dependent on the y co-ordinate and $x \in [0, 1]$.

The coefficients a and b obtained after the polynomial fit of the simulation and experimental data, along y=0.012 m, y=0.024 m and y=0.036 m, are shown in Table 5.12 while Figures 5.41, 5.42 and 5.43 show the pre-defined shape and the polynomial fittings to the simulation and experimental data. Remark that, during the fitting of the data, a zero derivative of the curve near the clamped edge was not imposed.

One can observe that, except for the experimental curve along y=36 mm, the fitting to the simulation and experimental data follows, approximately, the same parabolic shape as the pre-defined displacement field. In the case of y=36 mm the obtained fit is mediocre and is almost linear, mainly due to the transverse displacement value obtained at point $\frac{x}{L}$=0.55.

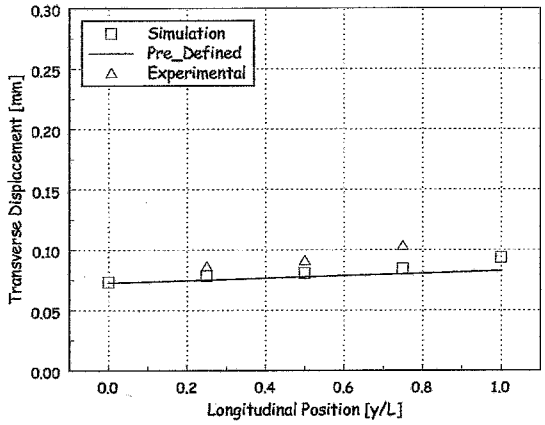

Figure 5.37: *Pre-defined displacement field, simulations and experimental measurements (x=60 mm).*

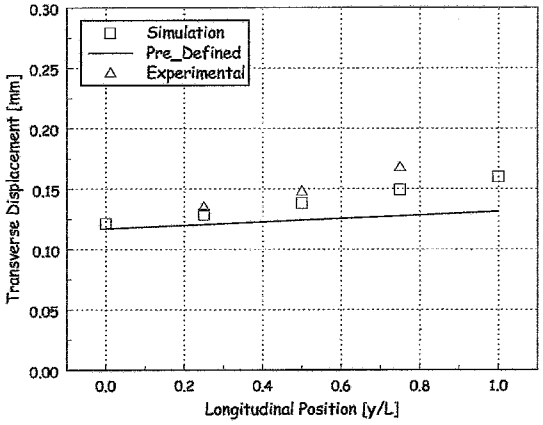

Figure 5.38: *Pre-defined displacement field, simulations and experimental measurements (x=84 mm).*

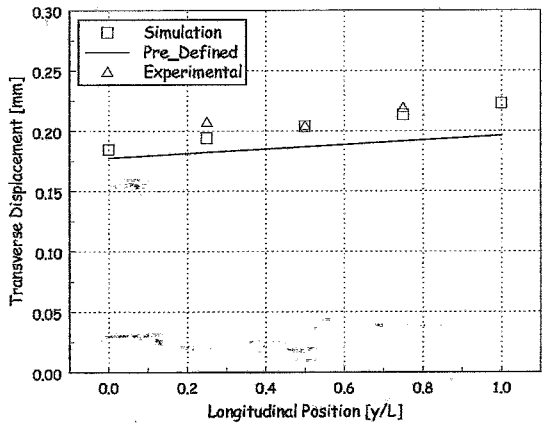

Figure 5.39: *Pre-defined displacement field, simulations and experimental measurements (x=111 mm).*

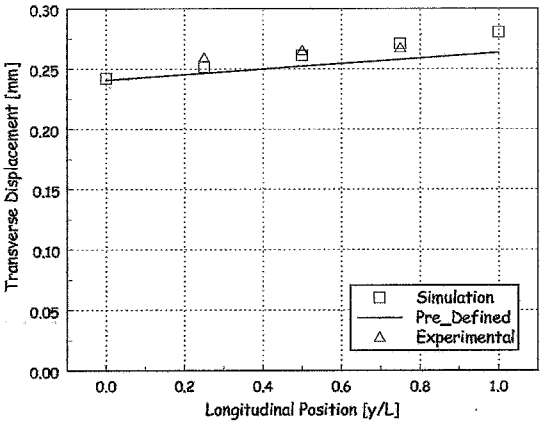

Figure 5.40: *Pre-defined displacement field, simulations and experimental measurements (x=135 mm).*

5.3.6 Electronic speckle pattern interferometry: aluminium plate

Deformations in the micron range and over an area are easily and accurately detected with optical methods like the Electronic Speckle Pattern Interferometry [97]. This technique, capable of providing three-dimensional displacements and dynamic response characteristics of surfaces, has been applied in a variety of applications including non-destructive evaluation and testing of structures and materials for fatigue and heat damage, on-line inspection of electronic devices, and as an instrument for a variety of medical diagnostic applications. The schematic representation of the ESPI system is shown in Figure 5.44.

The basic system, relies on phase recording of light wave fronts reflected by an object, and includes a CCD camera, micro lenses, a fibber coupled to a laser, an imaging card and an application software. After passing through a shutter, the laser beam is splitted, and reflected by a lens, converging into the object. The CCD camera simultaneously receives the wave front diffused by the object and the reference beam coming directly from the beam splitter following the laser. Speckles are interference images created in a pattern consistent with the surface being illuminated. By subtracting these images from various

Table 5.12: *Pre-defined shape with the polynomial fitting of the simulation and experimental data obtained along y at the points y=12 mm, y=24 mm and y=36 mm.*

	y=12 mm			y=24 mm			y=36 mm		
	a	b	χ^2	a	b	χ^2	a	b	χ^2
Pre-Defined	0.1791	0.1214	1.0	0.1791	0.1278	1.0	0.1791	0.1343	1.0
Simulation	0.1527	0.1477	0.9985	0.1665	0.1471	0.9929	0.1831	0.1442	0.9839
Experimental	0.1619	0.1552	0.9967	0.1196	0.1954	0.9991	0.0423	0.2684	0.9965

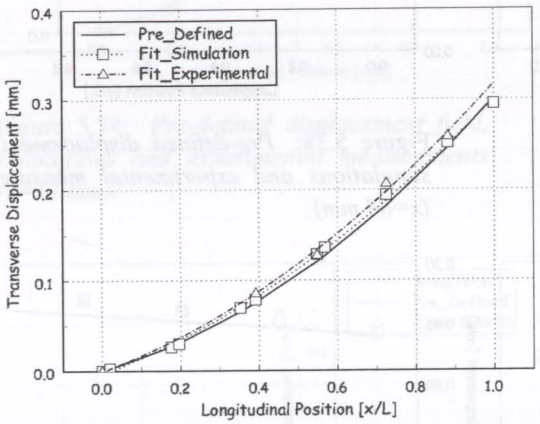

Figure 5.41: *Pre-defined shape, and the polynomial fittings to the simulation and experimental data (y=12 mm).*

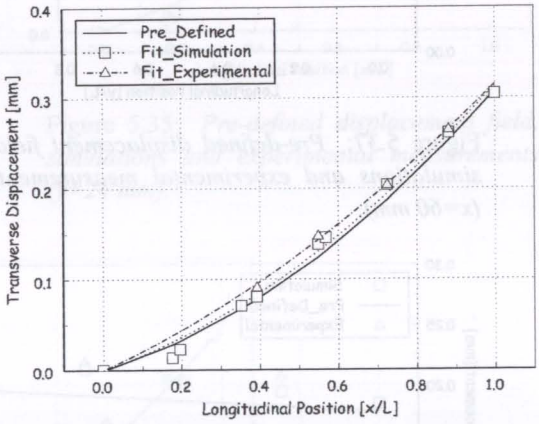

Figure 5.42: *Pre-defined shape, and the polynomial fittings to the simulation and experimental data (y=24 mm).*

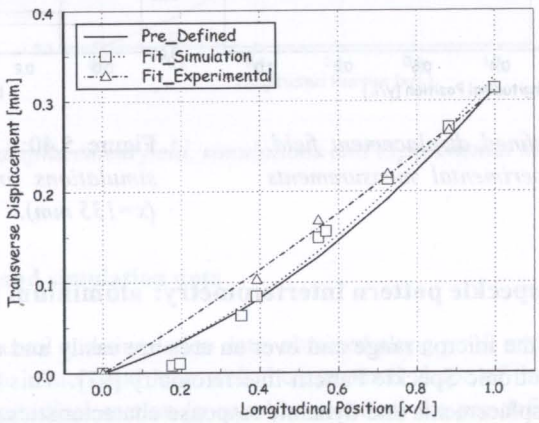

Figure 5.43: *Pre-defined shape, and the polynomial fittings to the simulation and experimental data (y=36 mm).*

phases of testing, interference fringes are formed. The number of fringes and their widths are a measure for the displacements of the illuminated area and after being computer filtered enable the creation of high-resolution contour maps of the shape of the object.

The deformation of a plate in two pre-defined directions according to the actuation voltages obtained

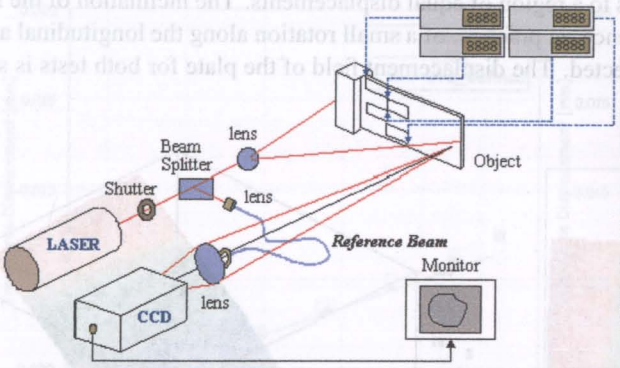

Figure 5.44: *Schematic representation of Electronic Speckle Pattern Interferometry (ESPI).*

Figure 5.45: *Set-up for measuring displacements in an aluminium plate using ESPI.*

by genetic algorithms, will be experimentally verified using this method. The experimental set-up (Figure 5.45) comprises the same clamped free aluminium plate used in Section 5.3.5. Table 5.13 shows the considered pre-defined shape and the actuation voltages, obtained by genetic algorithms, needed to apply to each of the four piezoelectric elements in order to achieve that same shape. The plate is intended to have a combined movement of bending and torsion.

Table 5.13: *Pre-defined displacement field [m] and optimal actuation voltages obtained by GA [V].*

	Displacement Field	V_{piezo1}	V_{piezo2}	V_{piezo3}	V_{piezo4}
Case 1	$\gamma(x,y) = (1.91x^2 + 0.88xy + 0.19x)10^{-4}$	-1.7	-2.5	4.9	5.0
Case 2	$\gamma(x,y) = (3.83x^2 + 1.76xy + 0.38x)10^{-4}$	-3.4	-5.0	9.8	10.0

Both pre-defined fields are identical in shape to the one defined in Table 5.11, and differing between each other by a factor of two. As expected, and since the geometry is the same, the obtained actuation voltages follow the same proportion as the one existante between the corresponding pre-defined displacements. The voltages in each piezoelectric actuator were limited to -10 Volt and +20 Volt. A finite element mesh of 4 × 10 elements was considered. A population size of 25 individuals, a probability of crossover equal to 0.75, a probability of mutation equal to 0.20 and a maximum number of generations of 50,000 were considered in the calculations. The actuation voltages applied to each piezoelectric element, with a precision of ± 0.1 Volt, generated stable deformations during time. Figure 5.46 and Figure 5.47 show the phase map of the raw fringe pattern captured for Case 1 and Case 2, respectively.

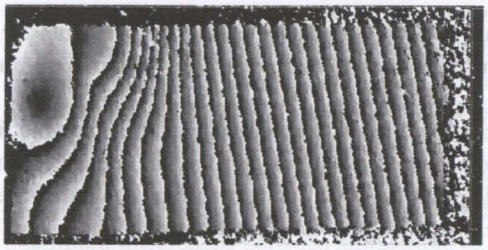

Figure 5.46: *Case 1: Phase map resulting from the captured raw fringe pattern.*

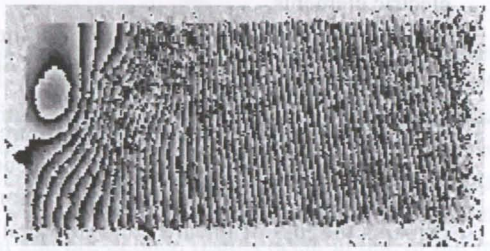

Figure 5.47: *Case 2: Phase map resulting from the captured raw fringe pattern.*

It is worthwhile to mention that the interferometer is sensitive to displacements normal to the plate's

surface and that each fringe corresponds to a region of equal displacements. The inclination of the fringe pattern in both figures implies the existence, in practice, of a small rotation along the longitudinal axis of the plate (torsion effect) as already expected. The displacement field of the plate for both tests is shown in Figure 5.48 and Figure 5.49.

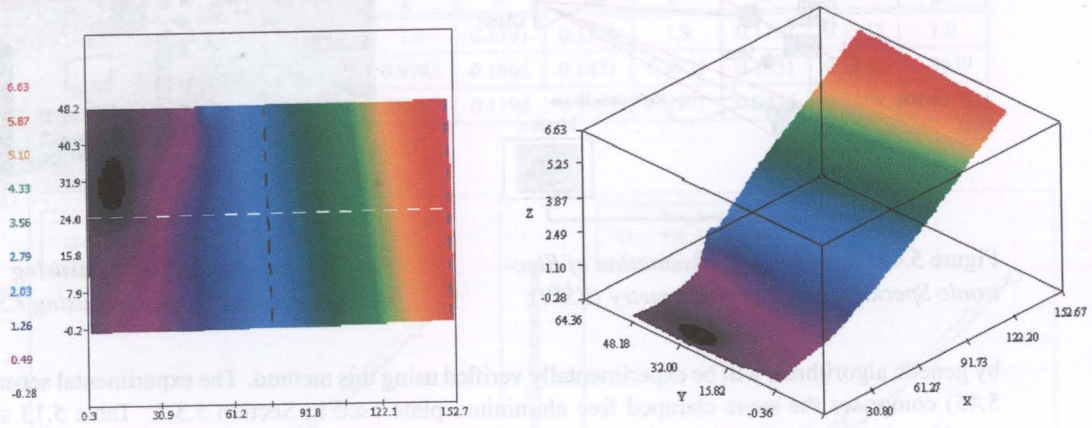

Figure 5.48: *Case 1: Representation of the displacement field.*

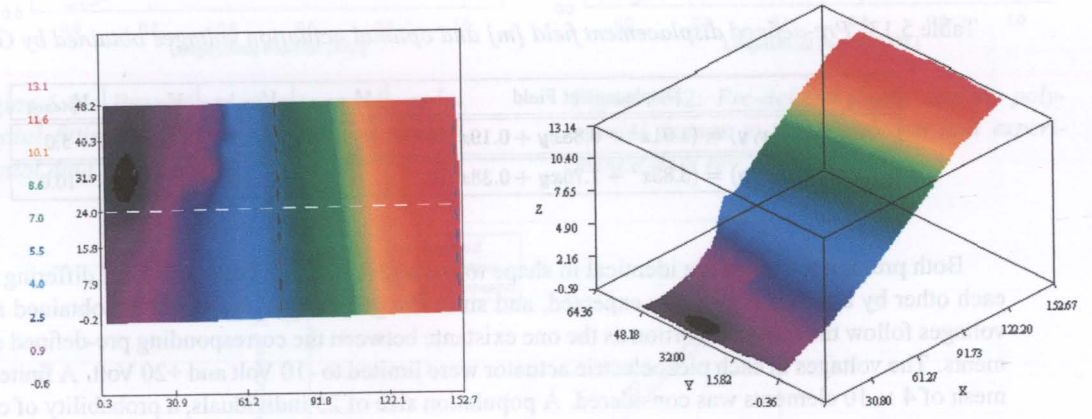

Figure 5.49: *Case 2: Representation of the displacement field.*

In both figures is visible a localised modification of the displacement field in the region of the piezoelectric elements.

The pre-defined displacement field, the simulation results and experimental measurements are compared for Case 1 and Case 2, in Figure 5.50 and Figure 5.51, as function of the longitudinal co-ordinate at points $y = 24$ mm.

It was observed that for Case 2, Figure 5.51, in the region near the free edge of the plate, the fringes present an area where their space frequency is too close from the upper limit of the measurements for that reference. This introduces some errors in the determination of the displacements for that area and explains the loss of linearity and information of the displacements in the extremity of the plate. Using the available information of the displacement field along the middle longitudinal axis of the plate the tip displacement was extrapolated for this case. A value of 14.43 μm was obtained representing a difference of 3% from the simulated value and a difference of 4.1% from the pre-defined one (Figure 5.52). In general, and for both cases an excellent agreement is found between the pre-defined shape, the simulation

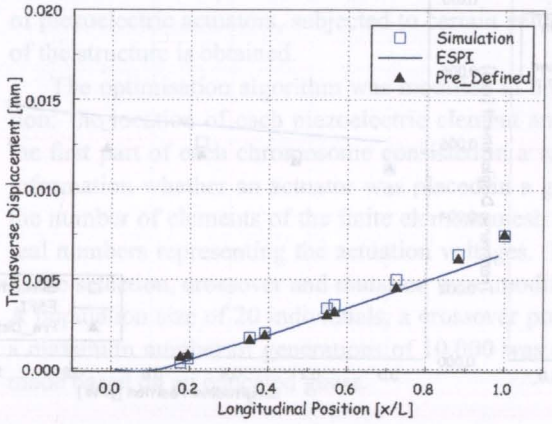

Figure 5.50: *Case 1: Pre-defined shape, simulation results and the experimental measurements for y=24 mm.*

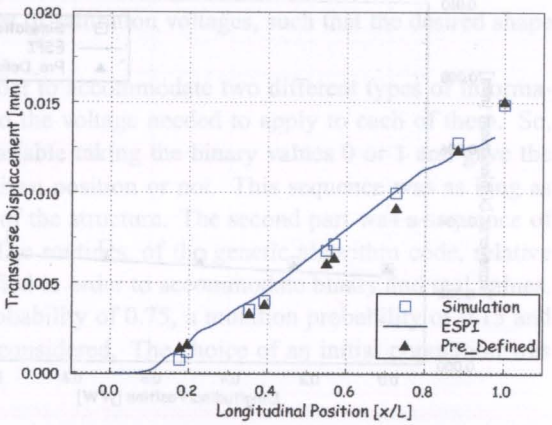

Figure 5.51: *Case 2: Pre-defined shape, simulation results and the experimental measurements for y=24 mm.*

results and the experimental measurements obtained with ESPI along the longitudinal co-ordinate.

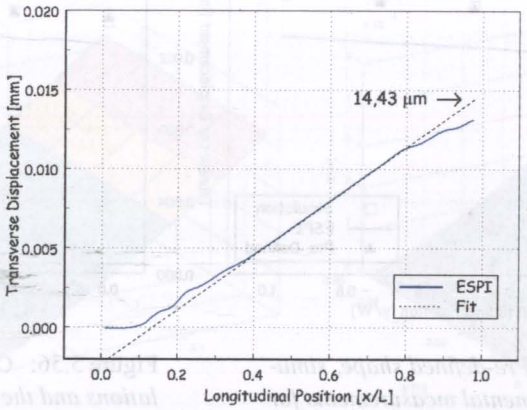

Figure 5.52: *Case 2: Fit of the experimental measurements obtained with ESPI.*

The pre-defined displacement field, the simulation results and experimental measurements are compared in Figure 5.53, Figure 5.54 and Figure 5.55, Figure 5.56 as function of the transversal coordinate along x = 77 mm and x = 153 mm, respectively.

For Case 1, Figure 5.53, it can be shown that the maximum error between the simulation results and the pre-defined curve, along x = 77 mm, is equal to 15% at one of the extremities of the plate (y/W=1.0), while between the experimental results and the pre-defined ones this value equals 3%. The comparison for Case 2, Figure 5.54, is less satisfactory. Please note the constant offset along the width between measurements and the pre-defined curve. Previous errors attain, once again at the extremity of the plate and for both cases, a value of the order of 15%. For Case 1, Figure 5.55, it is still verified that the maximum differences between simulation, experimental and pre-defined results occur at one of the free edges of the plate (y/W=1.0). Namely, a maximum error of 14% is found between the experimental results and pre-defined ones, while between simulation results and pre-defined ones this value drops to 3%. For Case 2, Figure 5.56, the experimental measurements made along x = 153 mm present a loss of linearity. This fact, as already explained, is related to the introduction of considerably high

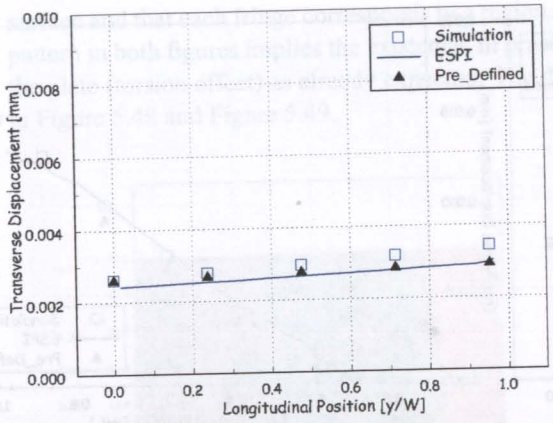

Figure 5.53: *Case 1: Pre-defined shape, simulations and the experimental measurements for x=77 mm.*

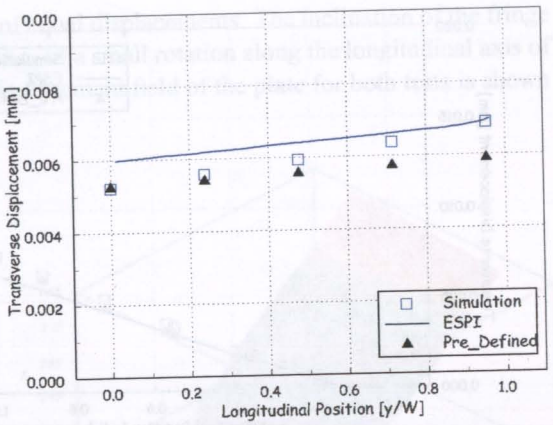

Figure 5.54: *Case 2: Pre-defined shape, simulations and the experimental measurements for x=77 mm.*

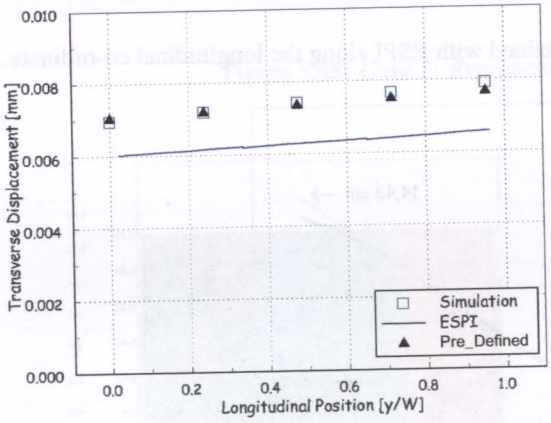

Figure 5.55: *Case 1: Pre-defined shape, simulations and the experimental measurements for x=153 mm.*

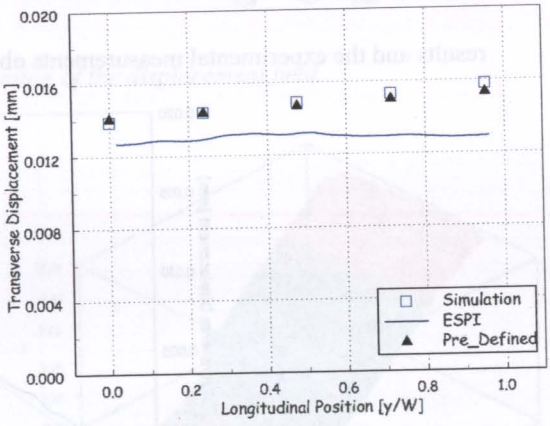

Figure 5.56: *Case 2: Pre-defined shape, simulations and the experimental measurements for x=153 mm.*

measurement's errors that invalidate any comparison. On the other hand, the maximum error between the simulation results and the pre-defined curve is equal to 3% and an excellent agreement is obtained.

Maximum errors of 15% were obtained between simulation results and the pre-defined curve and between experimental results and the pre-defined ones. Still, this method confirms, once again, the effectiveness of the developped methodology and the use of genetic algorithms to determine the optimal actuation voltages.

5.3.7 Simulation results: optimal layout of piezoelectric actuators

The procedure developed so far assumed a specific layout of actuators and determined the optimal actuation voltages with respect to that layout. However the optimisation of the actuator location for achieving a desired shape can be advantageous in order to minimise the error in the deflection.

The extension of the genetic algorithm optimisation code in order to include the best actuator location with respect to the fitness function was done. The optimisation problem consists now in finding a set of actuation voltages and the position, within the finite element mesh of the structure, of a limited number

of piezoelectric actuators, subjected to certain values of saturation voltages, such that the desired shape of the structure is obtained.

The optimisation algorithm was modified in order to accommodate two different types of information: the location of each piezoelectric element and the voltage needed to apply to each of them. So, the first part of each chromosome consisted in a variable taking the binary values 0 or 1 and gave the information whether an actuator was placed in a given position or not. This sequence was as long as the number of elements of the finite element mesh of the structure. The second part was a sequence of real numbers representing the actuation voltages. The routines, of the genetic algorithm code, relative to the selection, crossover and mutation were modified in order to accommodate binary and real values. A population size of 20 individuals, a crossover probability of 0.75, a mutation probability of 0.15 and a maximum number of generations of 10,000 was considered. The choice of an initial population was made based on an educated guess.

Clamped-free aluminium plate

This simulation aims at finding the location and the voltages of a fixed number of piezoelectric patches, glued in the clamped-free aluminium plate, in order to deform it according to the functions shown in Figures 5.57 and 5.58.

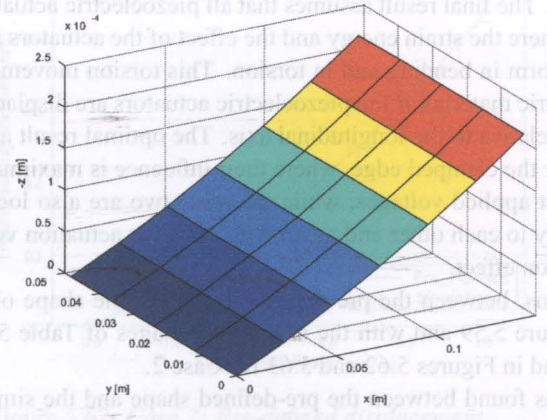

Figure 5.57: *Case 1: Pre-defined displacement field assumed for the clamped-free aluminium plate* $\gamma(x) = 0.0012x + 0.003x^2$.

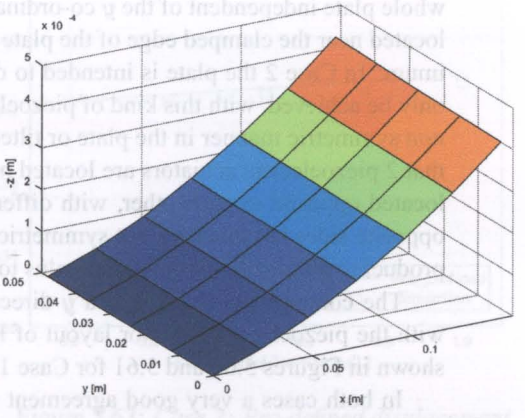

Figure 5.58: *Case 2: Pre-defined displacement field assumed for the clamped-free aluminium plate* $\gamma(x, y) = 0.0015x + 0.01x^2 + 0.002xy$.

An aluminium plate, 144 mm long, 48 mm wide and 0.5 mm thick, together with a maximum number of piezoelectric elements (PX5-N from Philips Components) limited to 4 with 24 mm long, 12 mm wide and 0.3 mm thick was considered. The saturation voltages were arbitrarly limited to -100 Volt and +200 Volt.

The finite element model of the plate consisted in 24 elements (6 longitudinally and 4 transversally). Each chromosome had a length of 28 variables; 24 binary values corresponding to a piezoelectric (1) or non piezoelectric (0) element and 4 real values corresponding to the actuation voltages.

Figure 5.59 shows the results of the optimisation procedure concerning the location of the piezoelectric elements for Case 1 and Case 2 and Table 5.14 the corresponding optimal actuation voltages.

Since there was no penalty, in the fitness function, for the increase of the weight due to the piezoelectric actuators the final optimal result, for both cases, assumes that all the four piezoelectric actuators are contributing to induce deformations in the structure. Case 1 consists in a bending movement of the

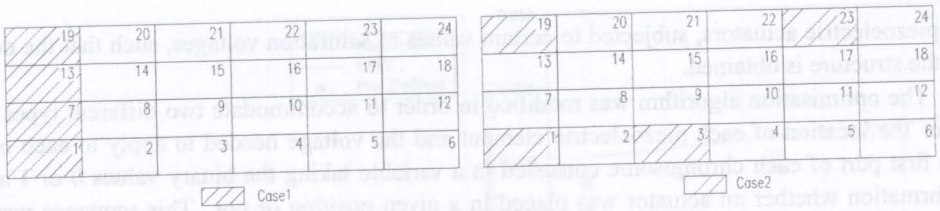

Figure 5.59: *Optimal location of the four piezoelectric actuators in order to achieve the pre-defined shape of Case 1 and Case 2.*

Table 5.14: *Results concerning the optimal placement of the piezoelectric actuators, within the aluminium plate, and the corresponding actuation voltages obtained by genetic algorithms.*

	Piezoelectric Elements	$V_{piezo1}[V]$	V_{piezo2} [V]	V_{piezo3} [V]	V_{piezo4} [V]
Case 1	1 ; 7 ; 13 ; 19	57.5	45.9	43.4	52.9
Case 2	1 ; 3 ; 19 ; 23	88.2	25.7	120.5	82.0

whole plate independent of the y co-ordinate. The final result assumes that all piezoelectric actuators are located near the clamped edge of the plate where the strain energy and the effect of the actuators is maximum. In Case 2 the plate is intended to deform in bending and in torsion. This torsion movement can only be achieved, with this kind of piezoelectric material, if the piezoelectric actuators are displaced in a non symmetric manner in the plate or tilted relative to the longitudinal axis. The optimal result assumes that 2 piezoelectric actuators are located near the clamped edge, where their influence is maximum, and located opposite to each other, with different applied voltages, while the other two are also located in opposite sides but this time not symmetrically to each other and again with different actuation voltages, producing all together this bending plus torsion effect.

The comparison, along x and y directions, between the pre-defined shape and the shape obtained with the piezoelectric actuator layout of Figure 5.59 and with the actuation voltages of Table 5.14 are shown in Figures 5.60 and 5.61 for Case 1 and in Figures 5.62 and 5.63 for Case 2.

In both cases a very good agreement was found between the pre-defined shape and the simulation results concerning the optimal location of the piezoelectric elements and the optimal actuation voltages. As expected, Case 1 corresponds to pure bending movement with no torsion. For Case 2 (Figure 5.63) the torsion effect is visible and a difference less than 1% is found between the slope of the simulation results (α=0.0118) and the pre-defined ones (α=0.0117). Contrary to the case presented in Section 5.3.5 concerning the experimental results of an aluminium plate with 4 piezoelectric actuators glued on it in an non optimal manner, there are no significant discrepancies between pre-defined and simulation results.

5.4 Conclusions

A systematic and general methodology, using a finite element code and genetic algorithms, for the shape control and/or correction of static deformations of adaptive structures, was proposed and experimentally verified. Throughout the presented results only glued piezoelectric elements are considered, however the developed methodology also supports embedded ones.

Shape control was applied to beams and plate structures with different boundary conditions. A good agreement was found between simulation and experimental results. The square root of the error between the nodal pre-defined displacement and the achieved displacement was considered as the objective function. The use of genetic algorithms was successfully demonstrated and the influence of its control

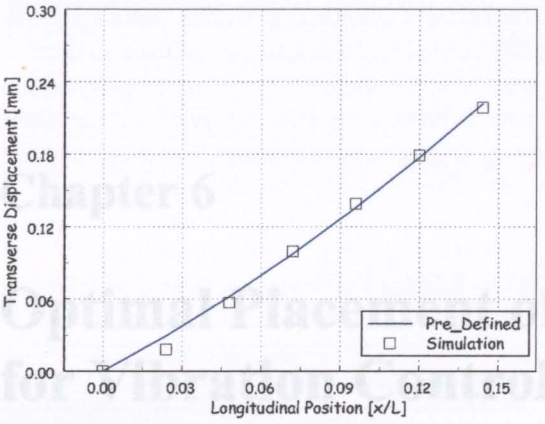

Figure 5.60: *Case 1: Pre-defined displacement field and simulation results concerning the optimal placement of 4 piezoelectric actuators in a clamped-free aluminium plate (y=0.024 m).*

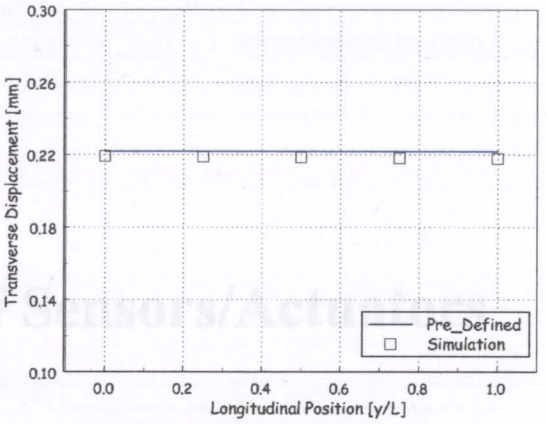

Figure 5.61: *Case 1: Pre-defined displacement field and simulation results concerning the optimal placement of 4 piezoelectric actuators in a clamped-free aluminium plate (x=0.144 m).*

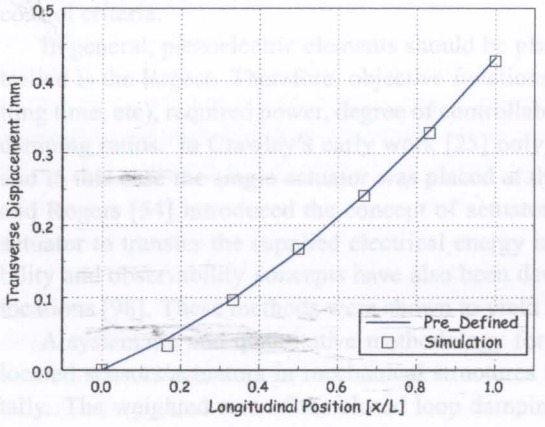

Figure 5.62: *Case 2: Pre-defined displacement field and simulation results concerning the optimal placement of 4 piezoelectric actuators in a clamped-free aluminium plate (y=0.024m).*

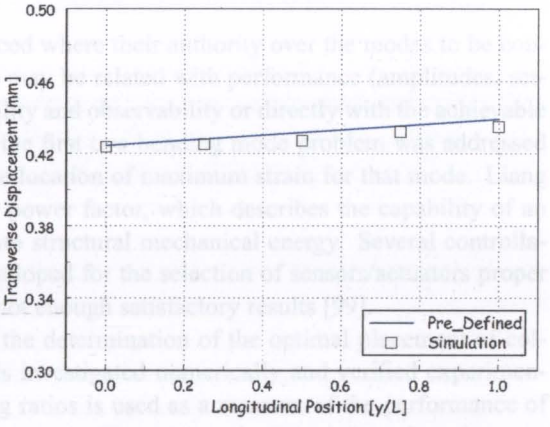

Figure 5.63: *Case 2: Pre-defined displacement field and simulation results concerning the optimal placement of 4 piezoelectric actuators in a clamped-free aluminium plate (x=0.144 m).*

parameters: population size, crossover probability and mutation probability, in the final performance and convergence of the algorithm was discussed.

With the aim of decreasing the errors between the pre-defined shape and the obtained shape of a structure the optimisation algorithm was modified in order to consider not only the determination of optimal voltages but also to optimise the best location of the piezoelectric actuators. The coding scheme proposed for this case, while useful for problems with a low number of potential actuator locations, in this case 24, may be rejected and become too heavy when considering a large number of possible actuator locations. For that case, the implemented algorithm can be easily extended and strings of integer numbers, with a size equal to the maximum number of actuators to be positioned, can be considered for representing the location of each actuator in the finite element mesh of the structure. The practicality and the effectiveness of using genetic algorithms to determine the optimal location and the optimal actuation voltages was demonstrated and the adopted methodology validated.

Chapter 6

Optimal Placement of Sensors/Actuators for Vibration Control

The number and the location of piezoelectric actuators and sensors is a critical problem in the robust functioning of active vibration control systems. The determination of the proper location of actuators and sensors is mainly formulated as a multivariable optimisation problem based either on structural or control criteria.

In general, piezoelectric elements should be placed where their authority over the modes to be controlled is the largest. Therefore, objective functions may be related with performance (amplitudes, settling time, etc), required power, degree of controllability and observability or directly with the achievable damping ratios. In Crawley's early work [25] only the first two bending mode problem was addressed and in this case the single actuator was placed at the location of maximum strain for that mode. Liang and Rogers [54] introduced the concept of actuator power factor, which describes the capability of an actuator to transfer the supplied electrical energy into structural mechanical energy. Several controllability and observability concepts have also been developed for the selection of sensors/actuators proper locations [98]. These methods were shown to yield not enough satisfactory results [99].

A systematic and quantitative methodology for the determination of the optimal placement of collocated sensors/actuators in mechanical structures is investigated numerically and verified experimentally. The weighted sum of the closed loop damping ratios is used as a measure of the performance of the system and constant gain feedback control is assumed. The proposed methodology, based on genetic algorithms and on the finite element method, is quite flexible since it allows the optimisation of the piezoelectric placement considering one single vibration mode or a combination of several modes. Collocated sensors and actuators were adopted. This collocation enhances robustness and stability in feedback resulting in an easier controller design.

After presenting the mathematical formulation involved, some results will be compared with data presented in literature. Simulations are then performed on beam and plate structures, subjected to different boundary conditions, and the obtained results are compared with the strain energy fraction distribution. The validation of the developed methodology is finally completed with some experimental tests.

6.1 Mathematical formulation

The equations of motion describing the behaviour of a mechanical structure with piezoelectric elements glued or embedded in it have already been derived. In the case of collocated sensors/actuators and in the absence of external forces, the reduced modal equation of motion, can be rewritten as (Equation 2.65)

$$\ddot{\{\eta\}} + [2\xi\omega]\dot{\{\eta\}} + [\omega^2]\{\eta\} - [\Psi]^T[K_{me^a}]\{\phi^a\} = 0 \tag{6.1}$$

As shown in Section 3.2, the correspondent first order state-space system equations equivalent to the previous expression are

$$\begin{aligned} \dot{x} &= [A]x + [B]u \\ y &= [C]x \end{aligned} \tag{6.2}$$

with

$$x = \begin{bmatrix} \dot{\eta} \\ \eta \end{bmatrix} \qquad u = \begin{bmatrix} \phi^a \\ 0 \end{bmatrix} \tag{6.3}$$

and

$$A = \begin{bmatrix} -[2\xi\omega] & -[\omega^2] \\ [I] & 0 \end{bmatrix} \qquad B = \begin{bmatrix} [\Psi]^T[K_{me^a}] \\ 0 \end{bmatrix} \qquad C = [0 \quad -[K_{e^se^s}]^{-1}[K_{me^s}]^T[\Psi]] \tag{6.4}$$

If constant gain linear feedback control is assumed, the constant gain matrix, G, is related to the output system vector and to the input vector by $u = -Gy$. The determination of the optimal gain and of the optimal location of the piezoelectric actuators can be done simultaneous or separately. Namely, the optimal gain can be calculated using the feedback of the state vector of the system and the linear quadratic regulator methodology presented before. Methods for the optimal placement are relatively recent and yield from "cut and try" optimisation techniques or intuitive placement techniques to more sophisticated and systematic optimisation methods [100]. The methodology developed here, excepted when stated otherwise, assumes a non-optimal constant gain, introduced as an input in the optimisation algorithm, and only the issue of the optimal placement of the piezoelectric elements is addressed.

The system dynamics, in closed loop, can de derived by introducing in Equation 6.2 the feedback control law

$$\dot{x} = ([A] - [B][G][C])x \tag{6.5}$$

The feedback of the strain rate in the structure sensed by the sensor to the actuator induces an increase of the damping. Therefore, in closed loop, the system's damping is composed by the structure's inherent damping and by the active damping due to the control input. The total modal damping ratios are obtained from

$$\xi_i = \frac{-Re(\lambda_i)}{\sqrt{Re^2(\lambda_i) + Im^2(\lambda_i)}} \tag{6.6}$$

where λ_i is the solution of the following complex problem

$$(\lambda[I] - [A]_{cl})\vec{x} = 0 \tag{6.7}$$

with $[A]_{cl}$ being the system's dynamics matrix in closed loop defined by $[A]_{cl} = ([A] - [B][G][C])$.

The system's performance for a given controller and for a given layout of the piezoelectric elements is measured using the rate of decay of the amplitude of the system's response. Mathematically the problem can be stated as maximise the weighted sum of the closed loop damping ratios by using the following expression

$$maximise \sum_{i=1}^{n} c_i\xi_i \tag{6.8}$$

where c_i are the weighting factors for each of the n relevant modes of the response under consideration.

The problem is formulated in such a way that there is a discrete and finite set of possible locations within the structure where the sensors and actuators can be placed. These already pre-defined positions are coincident with the finite element mesh used to discritise the system's equations. By fixing the feedback gain, the maximum number of piezoelectric elements, the structure's geometry and the possible locations of the piezoelectric elements within the structure, genetic algorithms are used to find the best layout which leads to the highest damping ratios. This optimisation, as already mentioned, can be done for a certain vibration mode or for a combination of several. As the number of actuators increases, the possible combinations of actuator's location also increase and consequently more computational effort is required in order to choose the best locations. One of the major advantages of the purposed methodology and of the use of genetic algorithms is its ease of programming and the ability to deal with such problems. The design and the implementation of the genetic algorithm computer code was already described in Section 4.7.2.

6.2 Model validation

The first validation of the modelisation is done by comparing the obtained simulations with results available in literature [101]. A square laminated composite plate with 400 mm side, 0.8 mm thick and 4 layers of T300/976 unidirectional graphite/epoxy composite is considered. The symmetric angle-ply laminate, with a sequence of [-30°,30°,30°,-30°], has an elasticity modulus of E_1=150 GPa, E_2=9 GPa and a density of 1600 Kg/m^3. A 0.1 mm thick layer of PZT G-1195N, with an Young Modulus of 63 GPa, a density of 7600 Kg/m^3 and piezoelectric constants equal to $d_{31} = d_{32} = -166$ pm/V, is symmetrically bonded on the upper and on the lower surface of the plate. It is assumed that the upper piezoelectric elements act as sensors while the lower elements as actuators. The plate, discretised into 8×8 identical elements, is simply supported on the 4 sides.

The results, presented in [101], concerning the vibration's suppression and the influence of sensor/actuator's location on the plate's response are compared with the ones obtained by the present methodology. A first crosscheck between the two models is done in Table 6.1 that presents the values for the first six natural frequencies of the composite plate.

Table 6.1: *Comparison of the first six natural frequencies of the composite plate obtained in literature [101] and by the present model.*

Mode Nr.	Literature [101] [Hz]	Current Model [Hz]	Error [%]
1	174.0	169.4	2.6
2	383.5	401.1	4.6
3	464.9	478.5	2.9
4	658.8	726.6	10.3
5	754.2	840.2	11.4
6	936.1	1073.4	14.7

An excellent agreement is verified between the values presented in literature and the ones obtained with the present model. Namely, an error less than 5% was achieved for the first three natural frequencies while never passing 15% for the first six natural frequencies.

The influence of the location of collocated sensor/actuator pairs (100×100 mm) on the response of the composite plate was investigated for 4 different configurations (Figure 6.1).

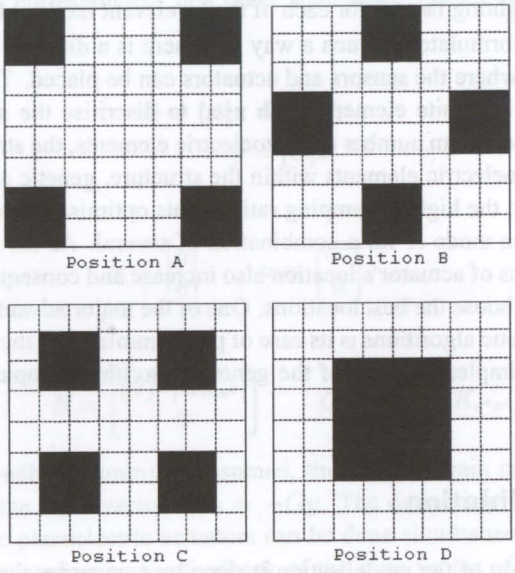

Figure 6.1: *Location of the collocated sensor/actuator pairs for the different configurations [101].*

A simple control methodology - constant gain feedback equal to 10 - was used in the analysis and it was assumed that the plate was vibrating freely due to an initial imposed middle node displacement (1.8 mm). Only the first six vibration modes were considered in the state-space model and an initial damping ratio of 0.8% was assumed for all the modes. Figure 6.2 shows the first six vibration modes of the composite plate.

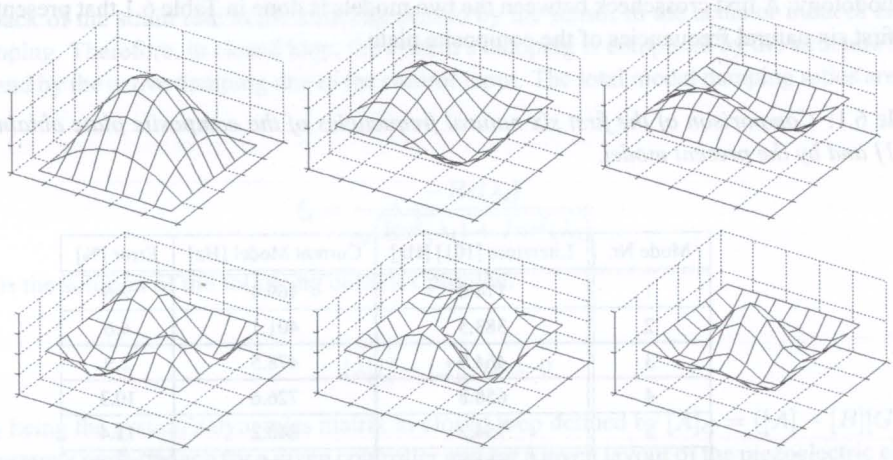

Figure 6.2: *First six vibration modes of the square composite plate.*

The response in time of the middle node of the plate for each of the 4 configurations was calculated using MATLAB & SIMULINK ® and is presented in Figure 6.3 to 6.6.

As expected, the influence on the suppression of the system's vibrations is more effective when all the piezoelectric sensor/actuator pairs are located in the centre of the plate (Position D, Figure 6.1). The

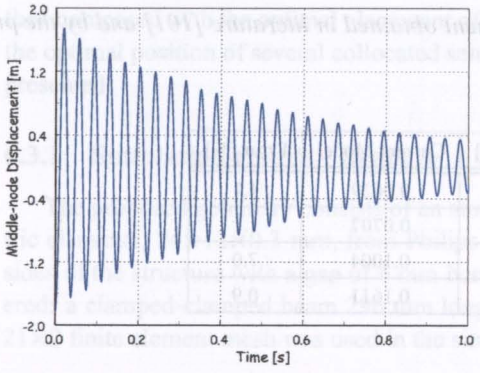

Figure 6.3: *Middle node displacement field for Position A.*

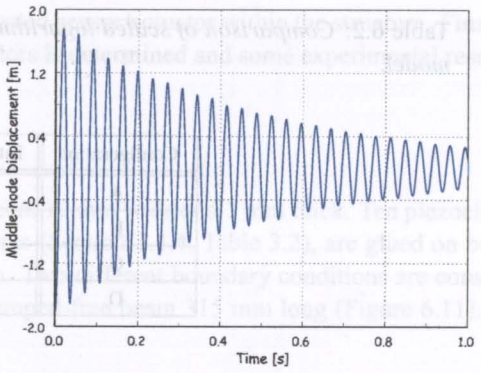

Figure 6.4: *Middle node displacement field for Position B.*

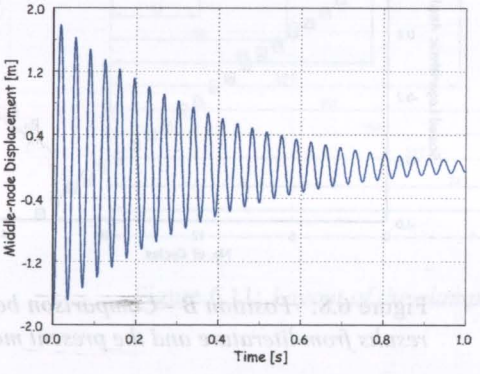

Figure 6.5: *Middle node displacement field for Position C.*

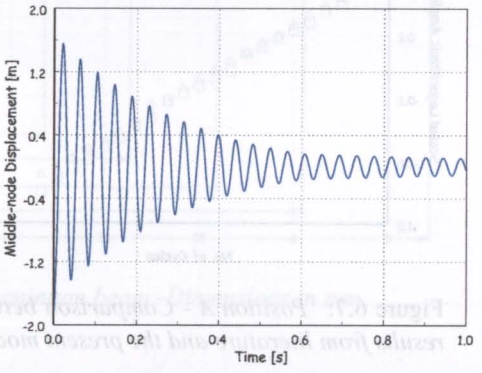

Figure 6.6: *Middle node displacement field for Position D.*

strain energy attains a minimum near the simply supported edges of the plate for almost all the modes. Therefore, the effectiveness of the actuators in this region is quite low (Positions A and B). On the other hand, the main contribution for the system's response is given by the first vibration mode, for which the modal strain energy is maximum at the centre of the square composite plate explaining the higher performance of the controller when the sensor/actuator pairs are located in this region.

The semi-logarithmic amplitude of the system's response function of the number of cycles, for each of the four configurations, obtained using the results in literature [101] and the present model, is represented in Figure 6.7 to Figure 6.10. The amplitude values were scaled for ease of comparison. The slope of each line is proportional to the logarithmic decrement. Table 6.2 shows the values of the slope obtained in the literature and by simulations using linear interpolation.

In spite of using different control methodologies both models give similar results concerning the scaled logarithmic decrement. Namely, an error less than 7% was obtained for all the 4 configurations. The results presented so far validate the modelisation of the structure in state-space and the feedback control methodology.

6.3 Applications

The use of genetic algorithms for the determination of the optimal location of collocated piezoelectric sensors/actuators for free vibration control of simple mechanical structures is demonstrated. In the present approach each individual in the population represents a given location of the active piezoelectric

Table 6.2: *Comparison of scaled logarithmic decrement obtained in literature [101] and by the present model.*

Configuration	Literature [101]	Current Model	Error [%]
A	0.0604	0.0629	4.1
B	0.0715	0.0707	1.1
C	0.0938	0.1004	7.0
D	0.1596	0.1611	0.9

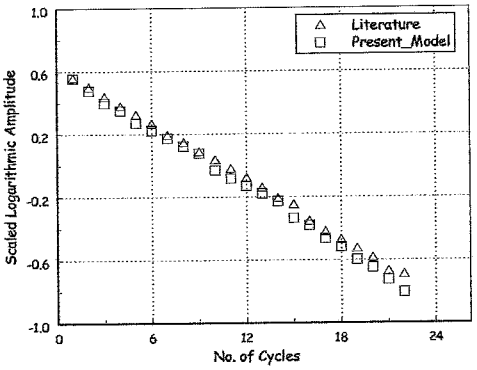

Figure 6.7: *Position A - Comparison between results from literature and the present model.*

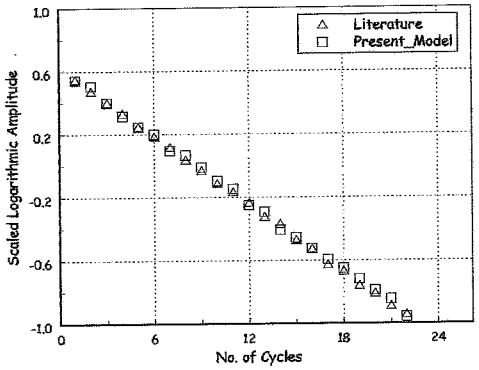

Figure 6.8: *Position B - Comparison between results from literature and the present model.*

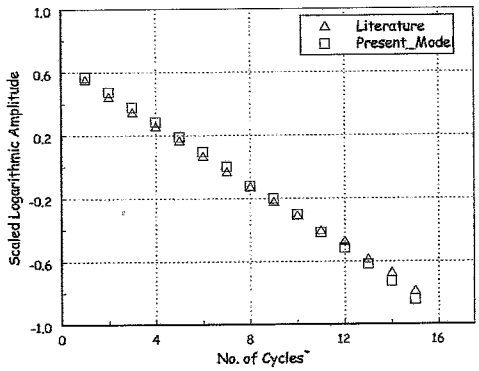

Figure 6.9: *Position C - Comparison between results from literature and the present model.*

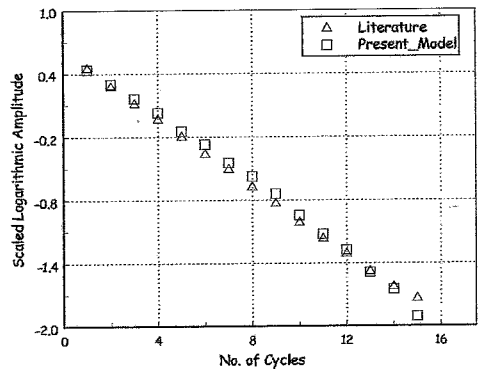

Figure 6.10: *Position D - Comparison between results from literature and the present model.*

elements within the structure. Each chromosome consists in sequences of 0's, non active collocated sensor/actuator, and 1's, active collocated sensor/actuator, with the length equal to the number of elements of the finite element mesh used in the model. A constant gain feedback control, unless otherwise stated, was considered in the simulations.

Next sections will present the optimal placement of sensors/actuators in several beam and plate structures, subjected to different boundary conditions, using the strain energy method and the weighted sum of the closed loop damping ratios. A comparison between the strain energy percentage distribution for the first vibration modes obtained using two different finite element codes is made. These results are

then compared with the optimal placement of one collocated sensor/actuator within the structure. Finally the optimal position of several collocated sensors/actuators is determined and some experimental results presented.

6.3.1 Simulation results - Beam A

The proposed geometry consists of an aluminium beam 12 mm wide and 1 mm thick. Ten piezoelectric elements, 24×12×0.3 mm, from Philips Components (Section 3.4.4, Table 3.2), are glued on both sides of the structure with a gap of 6 mm between them. Two different boundary conditions are considered: a clamped-clamped beam 296 mm long and a clamped-free beam 315 mm long (Figure 6.11). A 21×2 finite element mesh was used in the simulations.

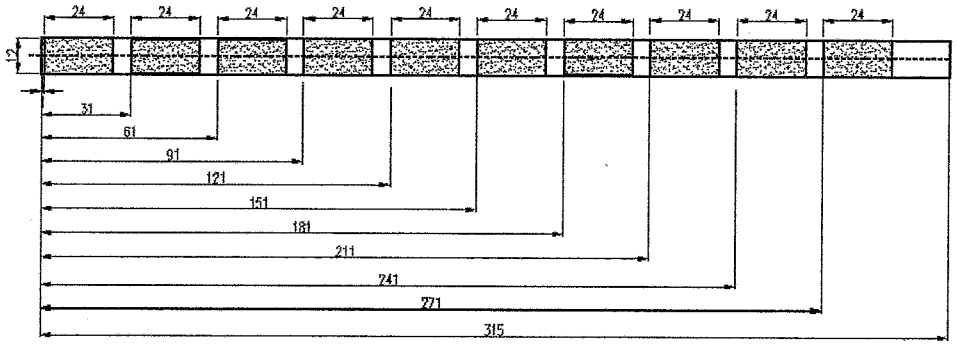

Figure 6.11: *Layout of the clamped-free aluminium beam. Dimensions in mm.*

Strain energy percentage distribution

The strain energy distribution, in the aluminium beam, for each of the first four bending modes was calculated. The results, obtained using the finite element code described in Section 2.2.5 and a commercial finite element software, ANSYS 5.7.®, are shown in Figures 6.12 and 6.13 for the clamped-clamped and for the clamped-free beam, respectively. The beam was modelled in ANSYS ® using a structural shell element, SHELL99, with 8 nodes and six degrees of freedom per node. The line in bold referenced as "Piezo" connects the strain energy values correspondent to only the piezoelectric elements of the finite element mesh.

For both boundary conditions an excellent agreement is found between both finite element codes. The non-smooth shape of the strain energy along the beam is the result of the discontinuity of the thickness and of the different material properties due to the presence of the piezoelectric elements. However, the distribution of the strain energy in the piezoelectric elements is qualitatively equal to the one of a constant thick beam (curve "Piezo").

Strain energy versus closed loop damping ratio

The results relative to the strain energy distribution presented hereafter are the ones obtained with the finite element code based in the Mindlin theory of plates (Section 2.2.5), except if otherwise stated. The next figures show, for each mode and for the 2 different boundary conditions, the comparison between the strain energy percentage distribution in the piezoelectric elements and the variation of the closed loop damping ratios obtained when each of the ten collocated sensor/actuator (24×12 mm) along the beam is made active. A constant gain feedback was used ($G = 3.0$). The results, presented in Figures 6.14 and 6.15 were scaled between 0 and 1 for ease of understanding and comparison.

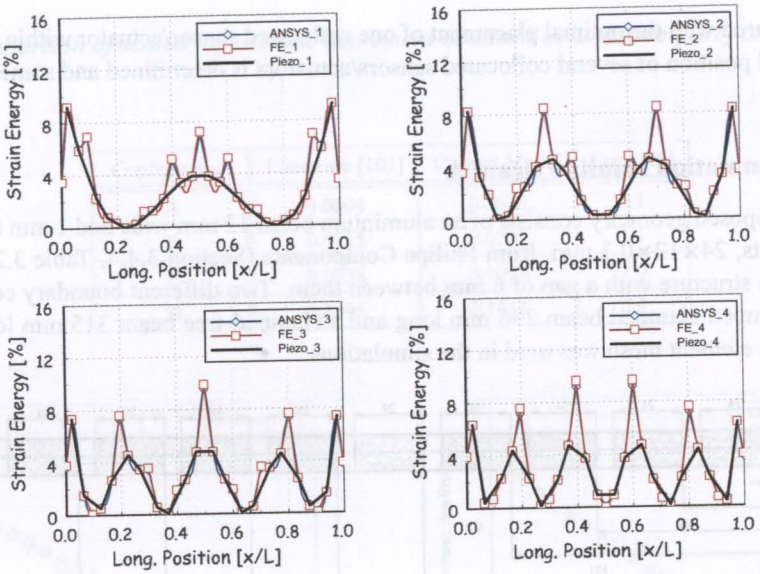

Figure 6.12: *Beam A - Strain energy percentage distribution for the clamped-clamped beam.*

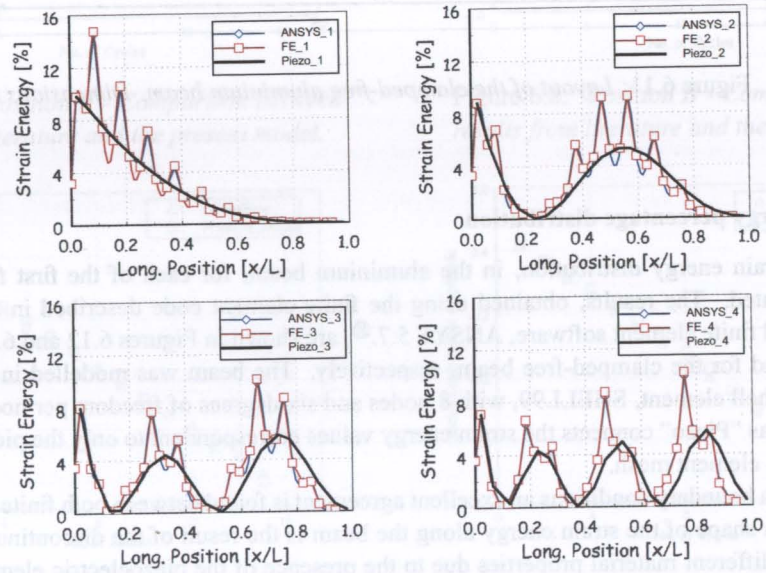

Figure 6.13: *Beam A - Strain energy percentage distribution for the clamped-free beam.*

As expected, the strain energy distribution in the piezoelectric elements is qualitatively similar to the distribution of the damping ratios obtained when one piezoelectric sensor/actuator of the beam is made active. The control is thus more effective when the piezoelectric patches actuate exactly in the locations of maximum strain. The existing differences in the fourth mode for the clamped-clamped boundary condition, and in general, are related to the smaller number of piezoelectric elements (10), when compared to the number of elements of the finite element mesh, used to calculate the strain energy distribution in these same elements.

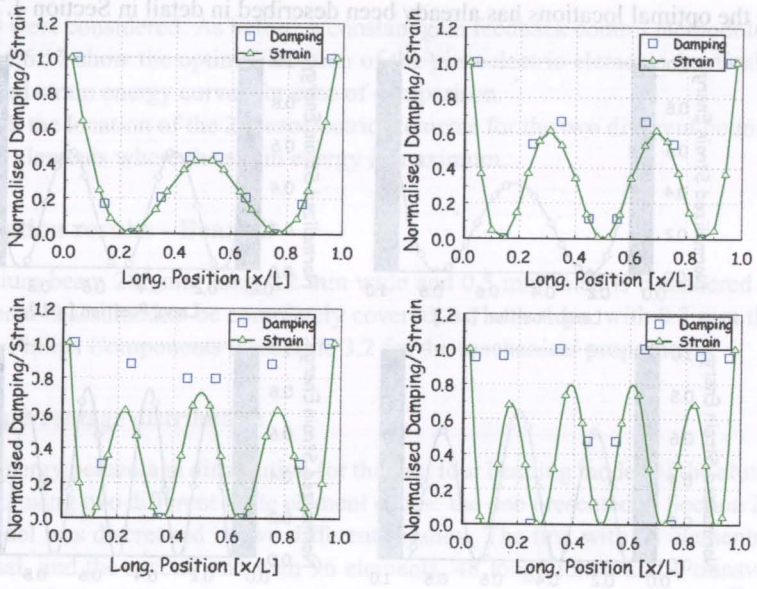

Figure 6.14: *Beam A (clamped-clamped) - Normalised strain energy versus closed loop damping ratio for one collocated sensor/actuator.*

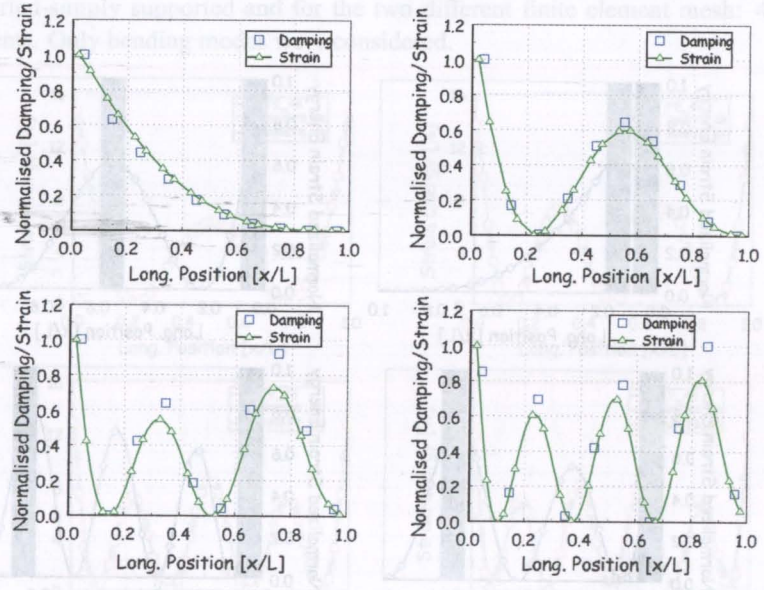

Figure 6.15: *Beam A (clamped-free) - Normalised strain energy versus closed loop damping ratio for one collocated sensor/actuator.*

Optimal placement of two collocated sensor/actuator

This section presents the results concerning the optimal placement of two collocated sensors/actuators in the beam geometry previously described (Figure 6.11) for the 2 different boundary conditions: clamped-clamped and clamped-free.

The design and the implementation of the optimisation procedure, based in genetic algorithms, for

determining the optimal locations has already been described in detail in Section 4.7.2.

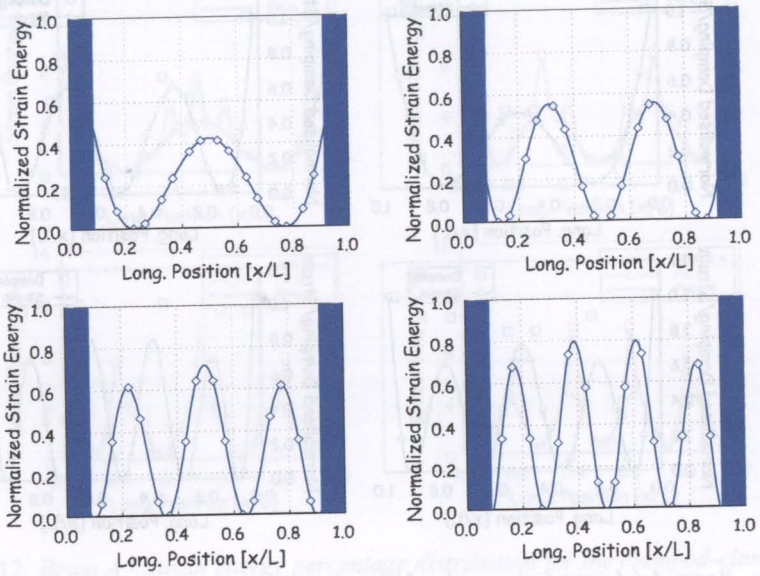

Figure 6.16: *Beam A (clamped-clamped) - Strain energy percentage and optimal location of 2 collocated sensor/actuator for the first 4 bending modes.*

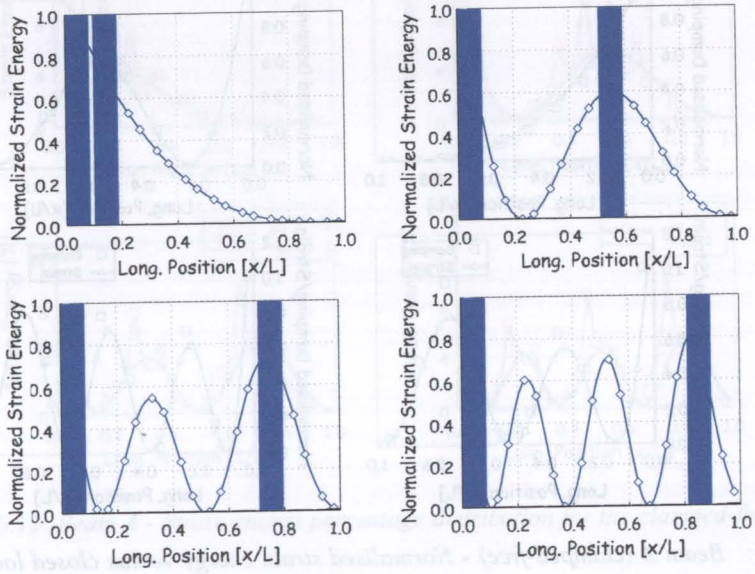

Figure 6.17: *Beam A (clamped-free) - Strain energy percentage and optimal location of 2 collocated sensor/actuator for the first 4 bending modes.*

The objective is to determine the optimal placement of 2 (24×12 mm) collocated piezoelectric sensors/actuators, between the 10 possible locations of piezoelectric elements within the aluminium beam, such that the closed loop damping ratio for a certain mode is maximum. A population of 15 individuals, a crossover probability equal to 0.60, a mutation probability of 0.25 and a maximum number of genera-

tions of 10,000 were considered. As before, a constant gain feedback control methodology was assumed. Figure 6.16 and 6.17 show the optimal location of the piezoelectric elements (vertical columns) on top of the normalised strain energy curves for ease of comparison.

As expected, the location of the 2 piezoelectric elements for the two different boundary conditions is coincident with elements where the strain energy is maximum.

6.3.2 Simulation results - Beam B

An aluminium beam 288 mm long, 12 mm wide and 0.5 mm thick is considered in the next simulations. The beam is assumed to be completely covered, on both sides, with 0.3 mm thick piezoelectric elements, from Philips Components (see Table 3.2 for the mechanical properties).

Strain energy percentage distribution

The strain energy percentage distribution for the first four bending modes of the aluminium beam was again calculated using two different finite element codes: the one presented in Section 2.2.5 and ANSYS 5.7 ®. The model was discretised in two different meshes. The first with 48 elements, 24 longitudinal and 2 transversal, and the second one with 96 elements, 48 longitudinal and 2 transversal. The beam, covered in all its length with the piezoelectric elements, was modelled in ANSYS ® using a structural shell element, SHELL99, from the element's library. Figure Figure 6.18, Figure 6.19 and Figure 6.20 show the results concerning the strain energy percentage distribution along the length, obtained with both finite element codes, for three different boundary conditions: clamped-clamped, clamped-free and simply supported-simply supported and for the two different finite element mesh: 48 (24×2) and 96 (48×2) elements. Only bending modes were considered.

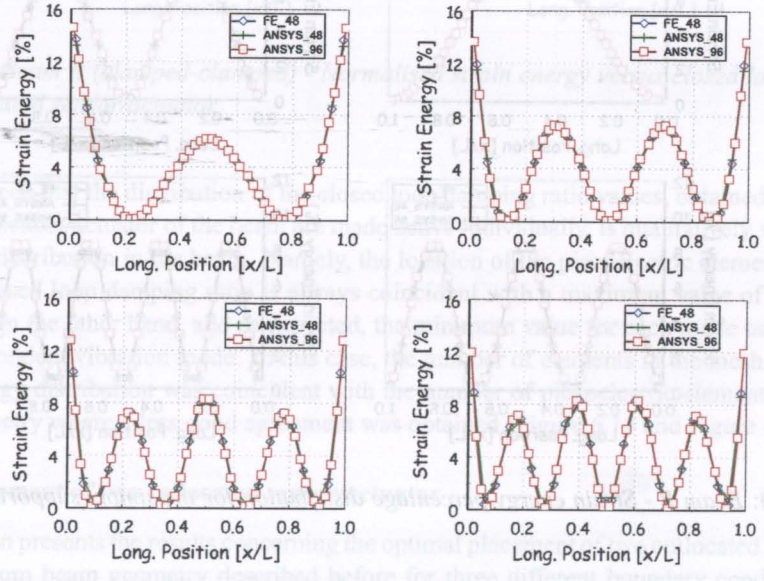

Figure 6.18: *Beam B - Strain energy percentage distribution for the clamped-clamped beam.*

For all the three different boundary conditions an excellent agreement is found between the two finite element codes and between the two different mesh. The strain energy is proportional to the second derivative of the displacement field. Therefore, and as expected, near the simply-supported edges the strain energy percentage is minimum for all the modes while for the clamped geometry this percentage attains its maximum value in elements near to the clamped edge.

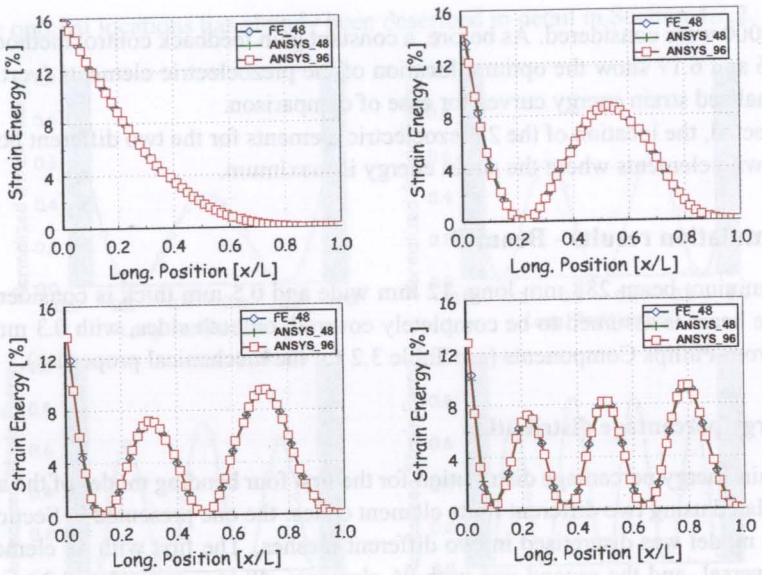

Figure 6.19: *Beam B - Strain energy percentage distribution for the clamped-free beam.*

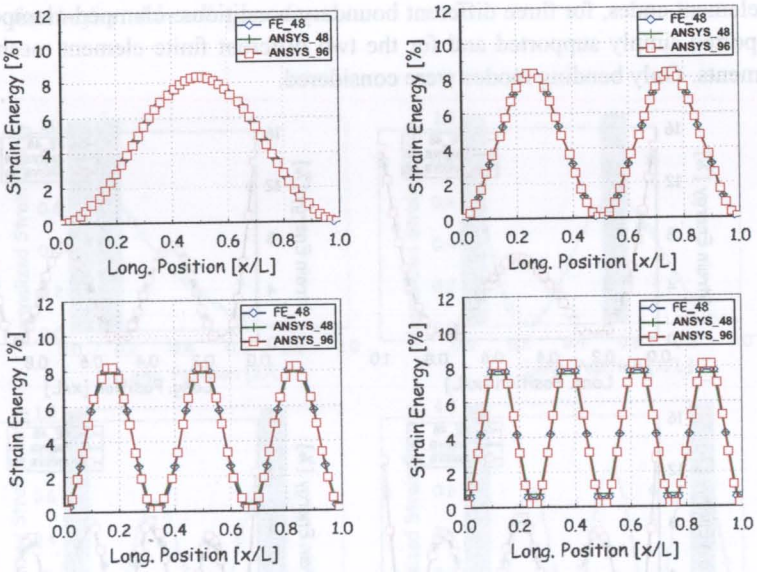

Figure 6.20: *Beam B - Strain energy percentage distribution for the simply supported-simply supported beam.*

Strain energy versus closed loop damping ratio

In this section the strain energy percentage of each mode, and for the 3 different boundary conditions, is compared with the closed loop damping ratio distribution obtained when one collocated sensor/actuator (12×12 mm) along the 24 longitudinal elements of the aluminium beam is made active. Only the 48's (24×2) elements mesh will be used in the simulations. The state-space model was defined considering twenty vibration modes, and an initial damping of ξ_i=[0.003, 0.0008, 0.0005, 0.0003, 0.0003, ..., 0.0003]

was, respectively, assumed for each of the vibration modes. The damping factors were chosen with the same order of magnitude as the ones experimentally determined in Section 3.3.

Again, a constant gain feedback control was used: the sensor voltage, multiplied by a constant gain, in this case 3.0, was feed-backed to the actuator. The results, shown in Figure 6.21, Figure 6.22 and Figure 6.23, corresponding to the strain energy percentage and to the damping ratio for each of the first four bending modes and for the three different boundary conditions, were scaled between 0 and 1 for ease of understanding and comparison.

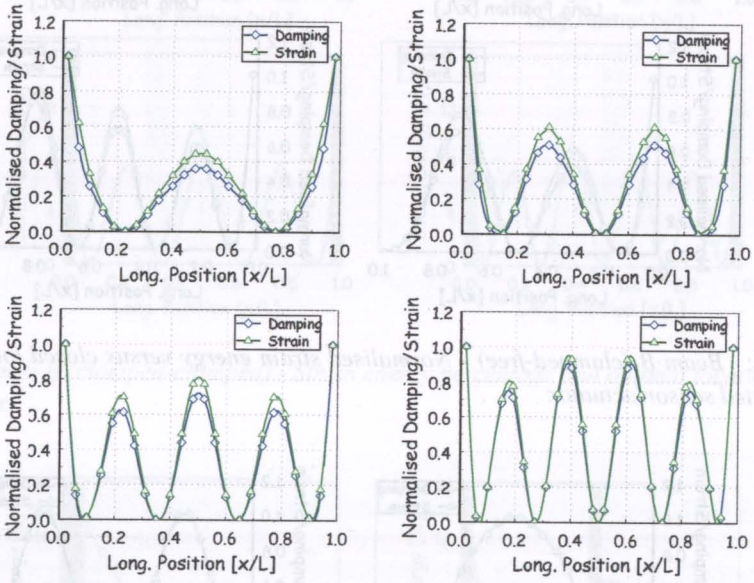

Figure 6.21: *Beam B (clamped-clamped) - Normalised strain energy versus closed loop damping ratio for one collocated sensor/actuator.*

It can be seen that the distribution of the closed loop damping ratio values, obtained when each of the 24 collocated sensor/actuator of the beam are made active individually, is qualitatively very similar to the strain energy distribution in the beam. Namely, the location of the piezoelectric element which presents the highest closed loop damping ratio is always coincident with a maximum value of the strain energy distribution. On the other hand, and as expected, the minimum value for each mode occurs at the nodes of the correspondent vibration mode. In this case, the number of elements in the mesh used to calculate the strain energy distribution was coincident with the number of piezoelectric elements, contrary to the Beam A geometry where a less good agreement was obtained (Figure 6.14 and Figure 6.15).

Optimal placement of two collocated sensor/actuator

This section presents the results concerning the optimal placement of two collocated sensors/actuators in the aluminium beam geometry described before for three different boundary conditions: clamped-clamped, clamped-free and simply supported - simply supported. The 24×2 elements mesh was used in the calculations. The aim is to find the optimal placement of 2 (12×12 mm) collocated piezoelectric sensors/actuators along the 24 elements of the aluminium beam such that the closed loop damping ratio for a certain mode is maximum.

Genetic algorithms were used as the optimisation method. A population of 15 individuals, a crossover probability equal to 0.60, a mutation probability of 0.25 and a maximum number of generations of 1,000 were considered. Concerning the control methodology, a constant gain feedback control with an arbitrarly chosen gain of 3.0 was assumed. As before, all the calculations considered that the aluminium

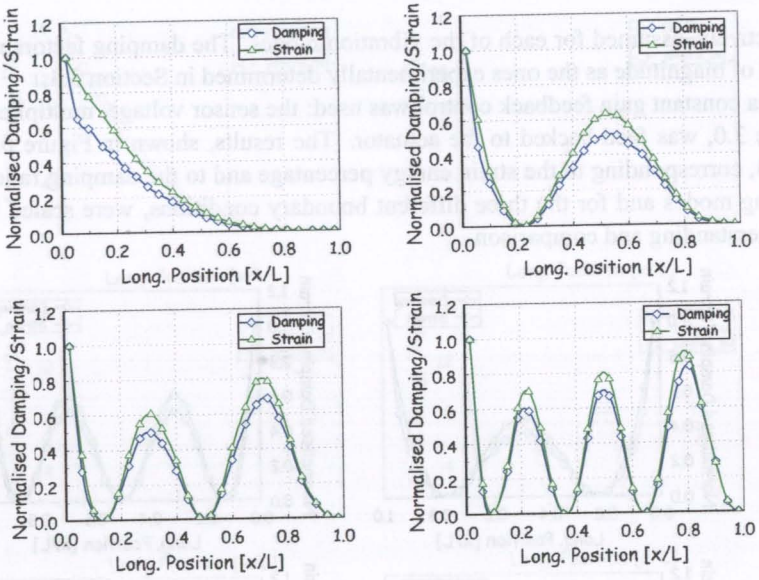

Figure 6.22: *Beam B (clamped-free) - Normalised strain energy versus closed loop damping ratio for one collocated sensor/actuator.*

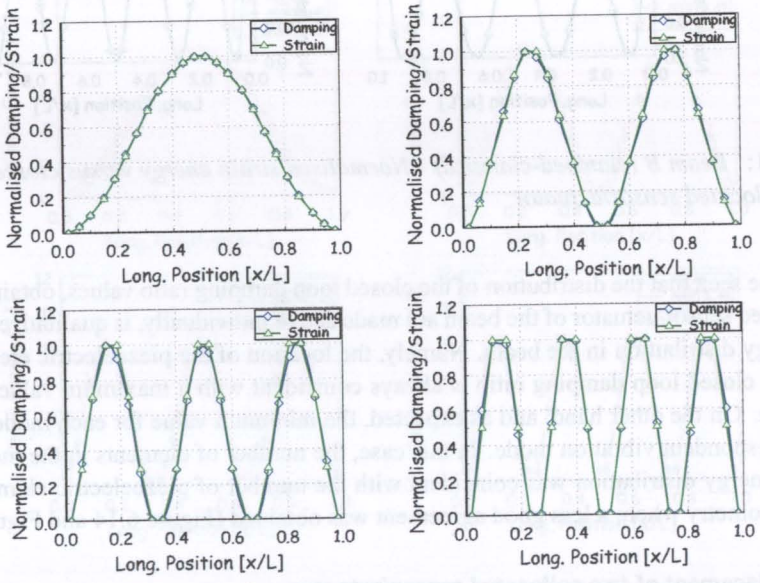

Figure 6.23: *Beam B (simply supported-simply supported) - Normalised strain energy versus closed loop damping ratio for one collocated sensor/actuator.*

beam was covered in both sides by piezoelectric elements. The optimal location of the two collocated sensor/actuator is represented by a column, for ease of comparison, in Figure 6.24, Figure 6.25 and Figure 6.26 for the different boundary conditions.

In general, the location of the 2 piezoelectric elements for the three different boundary conditions is coincident with elements where the strain energy is maximum. The only exception is observed for the

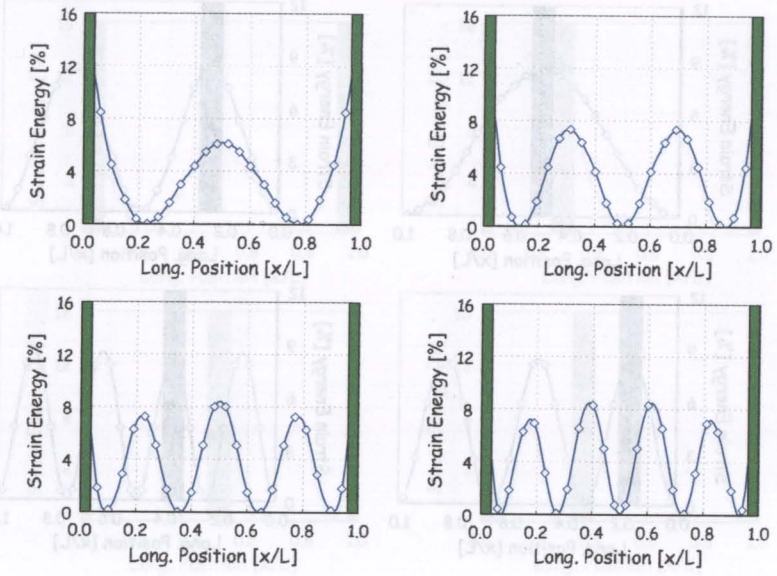

Figure 6.24: *Beam B (clamped-clamped) - Strain energy percentage and optimal location of 2 collocated sensor/actuator.*

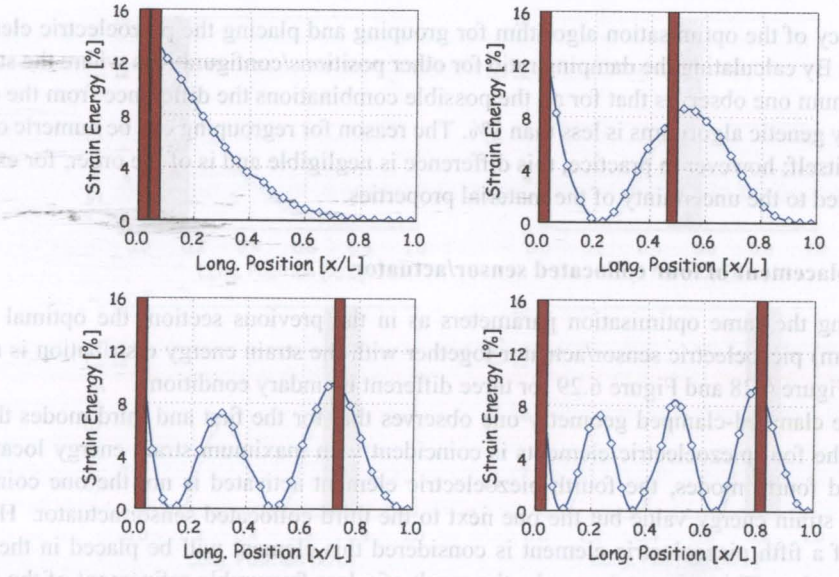

Figure 6.25: *Beam B (clamped-free) - Strain energy percentage and optimal location of 2 collocated sensor/actuator.*

second bending mode of the clamped-free beam, where the second piezo is placed next to an element of maximum strain energy percentage (see Figure 6.25). This may be due to a non optimum refinement of the finite element mesh of the structure and therefore to lack of precision in the determination of the strain energy and in the positioning of the collocated sensors/actuators. This aspect will be investigated further in the next section. For the simply supported-simply supported geometry, Figure 6.26, the location of the 2 piezoelectric elements coincide with elements where the strain energy is maximum. However, there

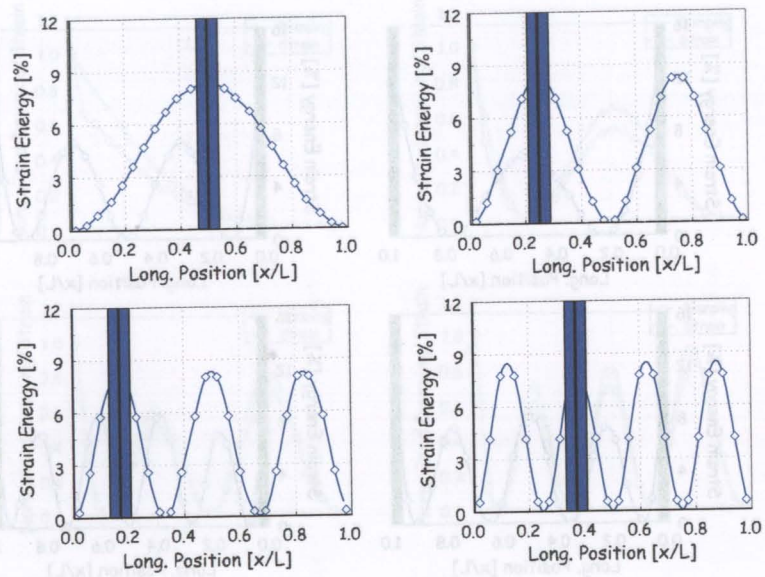

Figure 6.26: *Beam B (simply supported-simply supported) - Strain energy percentage and optimal location of 2 collocated sensor/actuator.*

is a tendency of the optimisation algorithm for grouping and placing the piezoelectric elements next to each other. By calculating the damping ratio for other positions/configurations where the strain energy is also maximum one observes that for all the possible combinations the difference from the optimal value obtained by genetic algorithms is less than 1%. The reason for regrouping can be numeric or related with the model itself; however in practice, this difference is negligible and is of the order, for example, of the errors related to the uncertainty of the material properties.

Optimal placement of four collocated sensor/actuator

Keeping the same optimisation parameters as in the previous section, the optimal location of 4 (12×12 mm) piezoelectric sensor/actuator together with the strain energy distribution is shown in Figure 6.27, Figure 6.28 and Figure 6.29 for three different boundary conditions.

For the clamped-clamped geometry one observes that for the first and third modes the optimal location of the four piezoelectric elements is coincident with maximum strain energy locations. For the second and fourth modes, the fourth piezoelectric element activated is not the one coincident with a maximum strain energy value but the one next to the third collocated sensor/actuator. However, if the location of a fifth piezoelectric element is considered this element will be placed in the strain energy maximum value. This mismatch may be the result of a less favourable refinement of the mesh for even modes. For the clamped-free geometry the optimal location of the four collocated sensor/actuator for controlling the first three bending modes is coincident with maximum strain energy value's location. For the fourth bending mode there is once again a mismatch between both methods, which, however is corrected with the location of a fifth piezoelectric element, placed this time in a location of maximum strain energy as it was verified for the clamped-clamped geometry. As before, the difference between these two configurations - the one coincident with points of maximum strain energy and the other with the tendency for grouping the collocated sensor/actuator - is negligible in practice and is around 0.95%. For the simply supported-simply supported boundary condition the tendency for grouping the collocated sensor/actuator in the locations of maximum strain rather than disperse then is still observed.

In general, the number of elements in the finite element mesh play an important role in the obtained

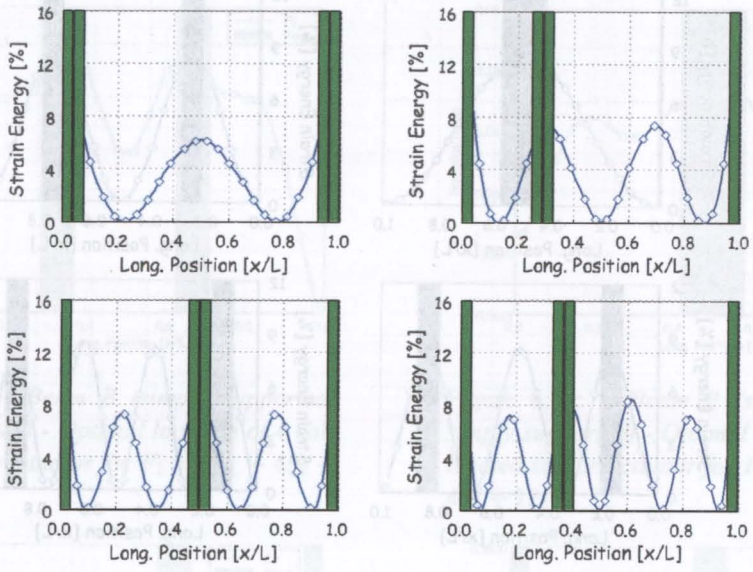

Figure 6.27: *Beam B (clamped-clamped) - Strain energy percentage and optimal location of 4 collocated sensor/actuator.*

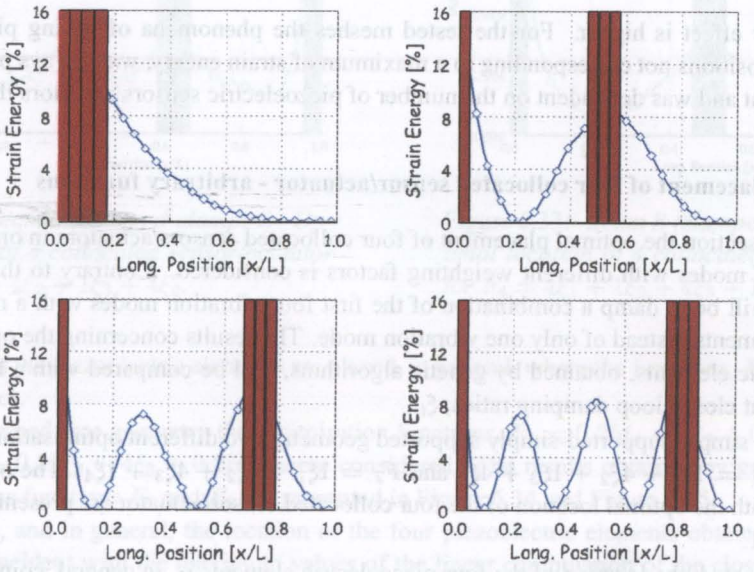

Figure 6.28: *Beam B (clamped-free) - Strain energy percentage and optimal location of 4 collocated sensor/actuator.*

results. Namely, the strain energy is calculated per element (integration in the element's volume), and therefore it is not a continuous interpolation as it is being represented. On the other hand, the location of each piezo is also discrete and dependent on the mesh and on the position of the elements. Several different finite element meshes with different refinements were tested. The dimensions of the element within each mesh were constant otherwise, a new factor in the placement of the piezoelectric elements would have been introduced: piezos would preferably been put in elements with higher dimensions,

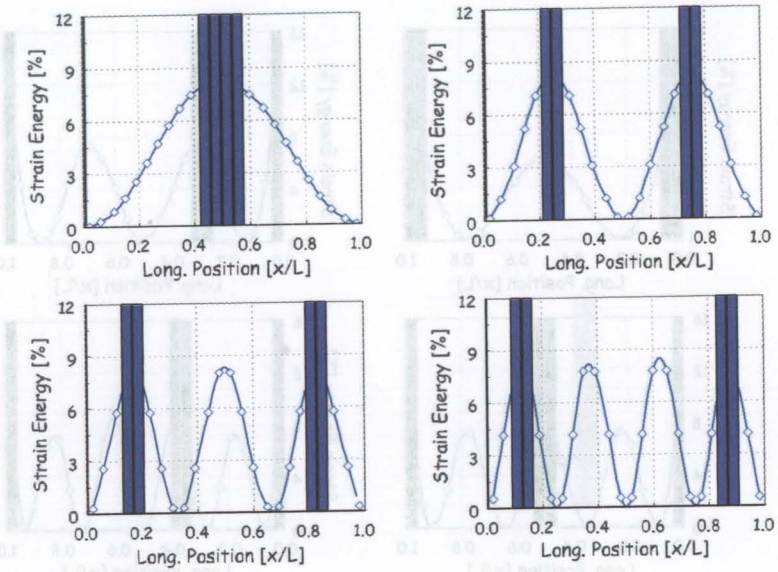

Figure 6.29: *Beam B (simply supported-simply supported) - Strain energy percentage and optimal location of 4 collocated sensor/actuator.*

where their effect is higher. For the tested meshes the phenomena of having piezoelectric elements placed in positions not corresponding to a maximum of strain energy, was always present in a smaller or larger extent and was dependent on the number of piezoelectric sensors/actuators that were activated.

Optimal placement of four collocated sensor/actuator - arbitrary functions

In this section the optimal placement of four collocated sensors/actuators in order to control a combination of modes with different weighting factors is considered. Contrary to the previous cases, the objective will be to damp a combination of the first four vibration modes with a maximum of 4 piezoelectric elements instead of only one vibration mode. The results concerning the optimal location of the piezoelectric elements, obtained by genetic algorithms, will be compared with a linear combination of the different closed loop damping ratios, ξ_i.

For the simply supported-simply supported geometry two different optimisation functions were considered: $F_1 = 1\xi_1 + 4\xi_2 + 1\xi_3 + 4\xi_4$ and $F_2 = 1\xi_1 + 1\xi_2 + 4\xi_3 + 1\xi_4$. The optimisation functions together with the optimal location of the four collocated sensor/actuator are presented in Figure 6.30 and Figure 6.31.

As expected, the location of the four piezoelectric elements is, in general, coincident with the maximum values of each optimisation function. Since the feedback gain is constant during the optimisation process, as well as, the matrices characterising the structure, the linear combination of the closed loop damping ratios can be computed and compared with the genetic algorithms results. In the case of F_1, where a higher weight is given to even modes, the piezoelectric elements are placed away from the centre of the beam where even vibration modes have nodes and away from the edges where the strain energy attains a minimum. For F_2, where an higher weight is given to the third vibration mode (odd mode), all the piezoelectric elements were placed in the centre of the beam where their effect is bigger.

For the clamped-clamped geometry, two different optimisation functions were considered: $F_3 = 1\xi_1 + 4\xi_2 + 1\xi_3 + 4\xi_4$ and $F_4 = 4\xi_1 + 1\xi_2 + 4\xi_3 + 1\xi_4$. The optimal location of the four piezoelectric elements together with each optimisation function are presented in in Figure 6.32 and Figure 6.33.

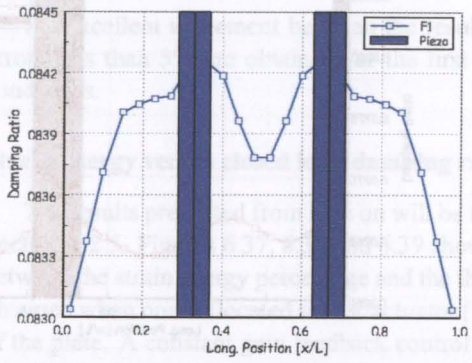

Figure 6.30: *Beam B (simply supported-simply supported) - Optimal location of 4 collocated sensor/actuator for* $F_1 = 1\xi_1 + 4\xi_2 + 1\xi_3 + 4\xi_4$.

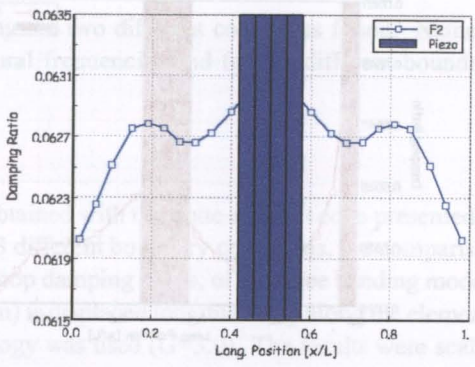

Figure 6.31: *Beam B (simply supported-simply supported) - Optimal location of 4 collocated sensor/actuator for* $F_2 = 1\xi_1 + 1\xi_2 + 4\xi_3 + 1\xi_4$.

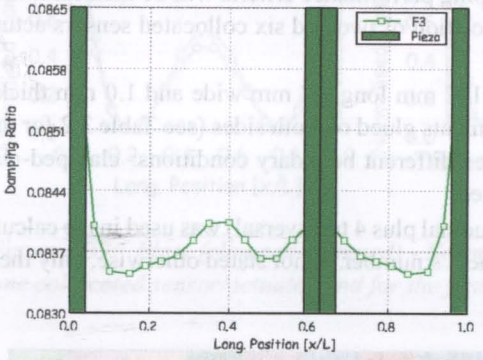

Figure 6.32: *Beam B (clamped-clamped) - Optimal location of 4 collocated sensor/actuator for* $F_3 = 1\xi_1 + 4\xi_2 + 1\xi_3 + 4\xi_4$.

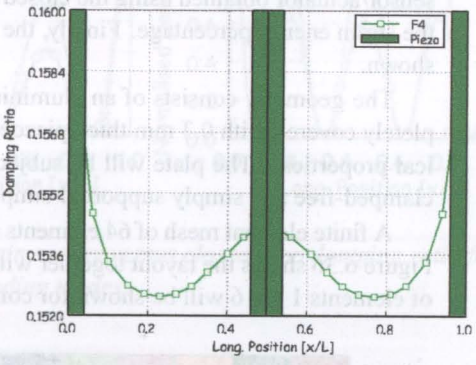

Figure 6.33: *Beam B (clamped-clamped) - Optimal location of 4 collocated sensor/actuator for* $F_4 = 4\xi_1 + 1\xi_2 + 4\xi_3 + 1\xi_4$.

As expected the piezoelectric elements are placed, in general, where the functions, F_3 and F_4, present maximum values.

For the clamped-free geometry the optimisation functions, $F_5 = 0.25\xi_1 + 4\xi_2 + 0.25\xi_3 + 4\xi_4$ and $F_6 = 0.25\xi_1 + 0.25\xi_2 + 4\xi_3 + 0.25\xi_4$, were considered. The results obtained by genetic algorithms together with the functions F_5 and F_6 are presented in Figure 6.34 and Figure 6.35.

Once again, and in general, the location of the four piezoelectric elements obtained by genetic algorithms is coincident with the maximum values of the linear combination of the closed loop damping ratios. For all the three boundary conditions, the optimal location coincides with the anti-nodes of the modes with higher weights.

6.3.3 Simulation results - Plate

The optimal placement of collocated sensors/actuators on a rectangular plate using the strain energy method and genetic algorithms together with the weighted sum of the closed loop damping ratios is considered in this section. In the first part, and as previously done for a beam structure, a comparison is made between the strain energy percentage of each of the first four bending modes obtained using two different finite element codes. The code presented in Section 2.2.5 and ANSYS 5.7.® will be used in order to validate the current model. The results concerning the optimal placement of one collocated

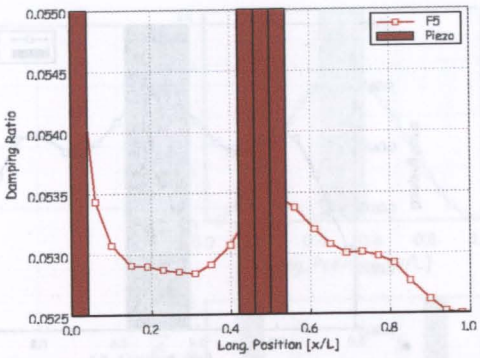

Figure 6.34: *Beam B (clamped-free) - Optimal location of 4 collocated sensor/actuator for* $F_5 = 1\xi_1 + 4\xi_2 + 1\xi_3 + 4\xi_4$.

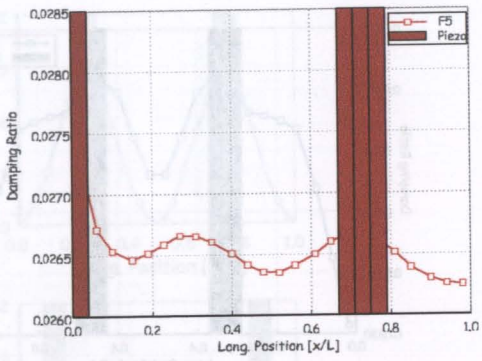

Figure 6.35: *Beam B (clamped-free) - Optimal location of 4 collocated sensor/actuator for* $F_6 = 4\xi_1 + 1\xi_2 + 4\xi_3 + 1\xi_4$.

sensor/actuator obtained using the closed loop damping performance criteria will be then compared with the strain energy percentage. Finally, the optimal position of two and six collocated sensors/actuators is shown.

The geometry consists of an aluminium plate, 192 mm long, 48 mm wide and 1.0 mm thick, completely covered with 0.3 mm thick piezoelectric elements glued on both sides (see Table 3.2 for mechanical properties). The plate will be subjected to three different boundary conditions: clamped-clamped, clamped-free and simply supported-simply supported.

A finite element mesh of 64 elements (16 longitudinal plus 4 transversal) was used in the calculations. Figure 6.36 shows the layout together with the element's number. If not stated otherwise, only the results of elements 1 to 16 will be shown for comparison.

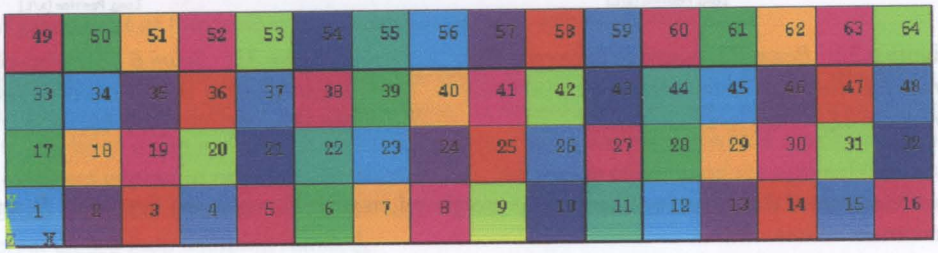

Figure 6.36: *Plate's finite element mesh.*

Table 6.3 shows the natural frequencies corresponding to the first three bending modes obtained with the two finite element codes and for the three boundary conditions.

Table 6.3: *Comparison of the natural frequencies for the three bending modes.*

	Clamped-Clamped		Clamped-Free		Simply Supported-Simply Supported	
	Freq. FE/ANSYS [Hz]	Error [%]	Freq. FE/ANSYS [Hz]	Error [%]	Freq. FE/ANSYS [Hz]	Error [%]
1	177.21/177.24	0.02	27.53/27.63	0.36	77.52/76.64	1.15
2	498.5/487.63	2.18	173.98/172.47	0.87	314.65/308.24	2.08
3	1007.7/956.28	5.10	495.78/482.84	2.61	725.39/697.1	4.06

An excellent agreement between the results given by the two different codes was found. Namely, errors less than 5% are obtained for the first three natural frequencies and for the different boundary conditions.

Strain energy versus closed loop damping ratio

The results presented from here on will be the ones obtained with the finite element code presented in Section 2.2.5. Figures 6.37, 6.38 and 6.39 show, for the 3 different boundary conditions, the comparison between the strain energy percentage and the the closed loop damping ratios, of the three bending modes, obtained when one collocated sensor/actuator (12×12 mm) is displaced longitudinally along the elements of the plate. A constant gain feedback control methodology was used (G=3.0). The results were scaled between 0 and 1 for ease of understanding and comparison.

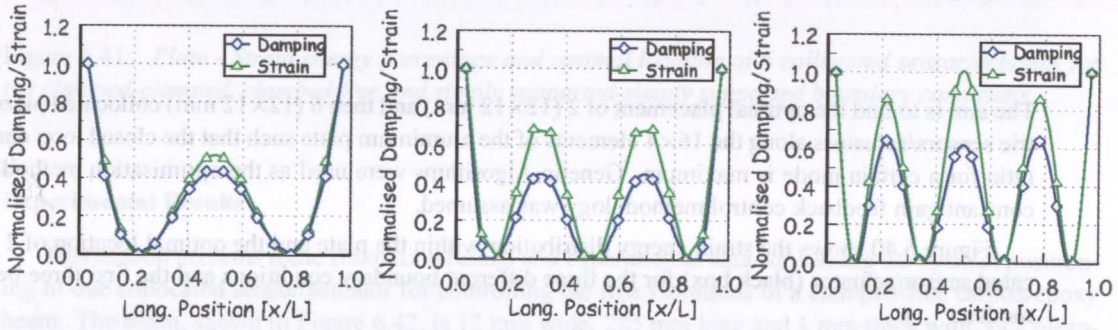

Figure 6.37: *Plate (clamped-clamped) - Normalised strain energy versus closed loop damping ratio for one collocated sensor/actuator and for the first three bending modes.*

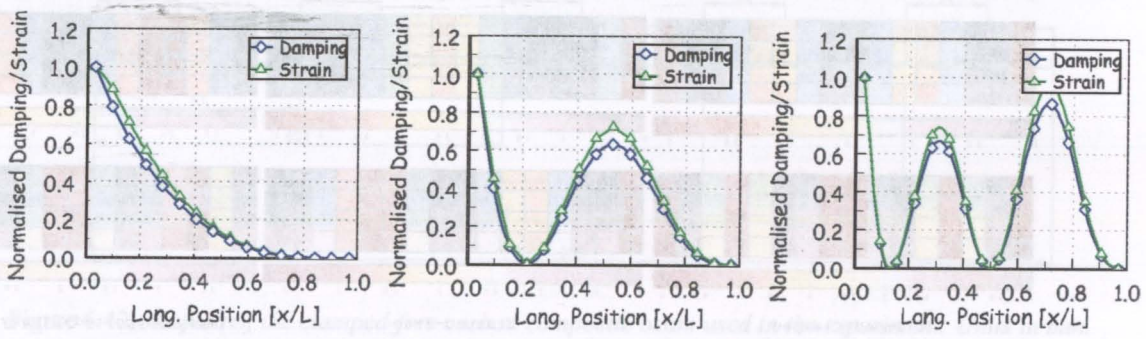

Figure 6.38: *Plate (clamped-free) - Normalised strain energy versus closed loop damping ratio for one collocated sensor/actuator and for the first three bending modes.*

Qualitatively, and as already verified for the beam structure, the strain energy and the distribution of the closed loop damping ratio along the plate elements is very similar for all the considered modes and boundary conditions.

Optimal placement of two/six collocated sensor/actuator

This section presents the results concerning the optimal placement of two and six collocated sensors/actuators in the plate geometry described in Figure 6.36 for the three different boundary conditions.

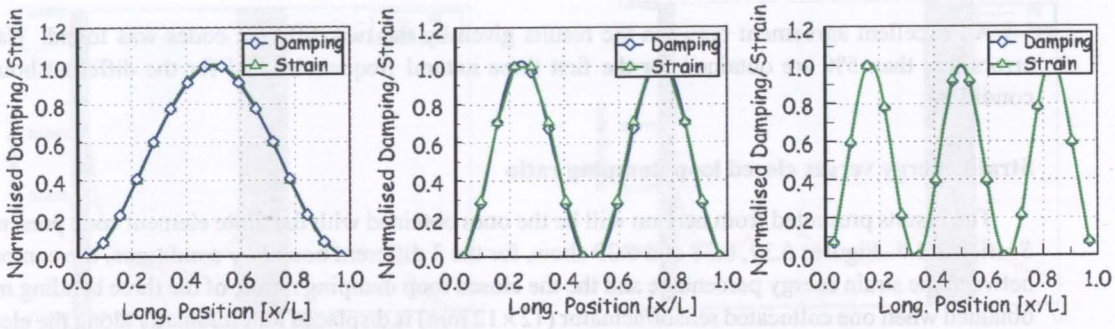

Figure 6.39: *Plate (simply supported-simply supported) - Normalised strain energy versus closed loop damping ratio for one collocated sensor/actuator and for the first three bending modes.*

The aim is to find the optimal placement of 2 (12×12 mm) and then 6 (12×12 mm) collocated piezoelectric sensors/actuators along the 16×4 elements of the aluminium plate such that the closed loop damping ratio for a certain mode is maximum. Genetic Algorithms were used as the optimisation method and a constant gain feedback control methodology was assumed.

Figure 6.40 shows the strain energy distribution within the plate and the optimal location of 2 collocated sensor/actuator (black box) for the three different boundary conditions and the first three bending modes.

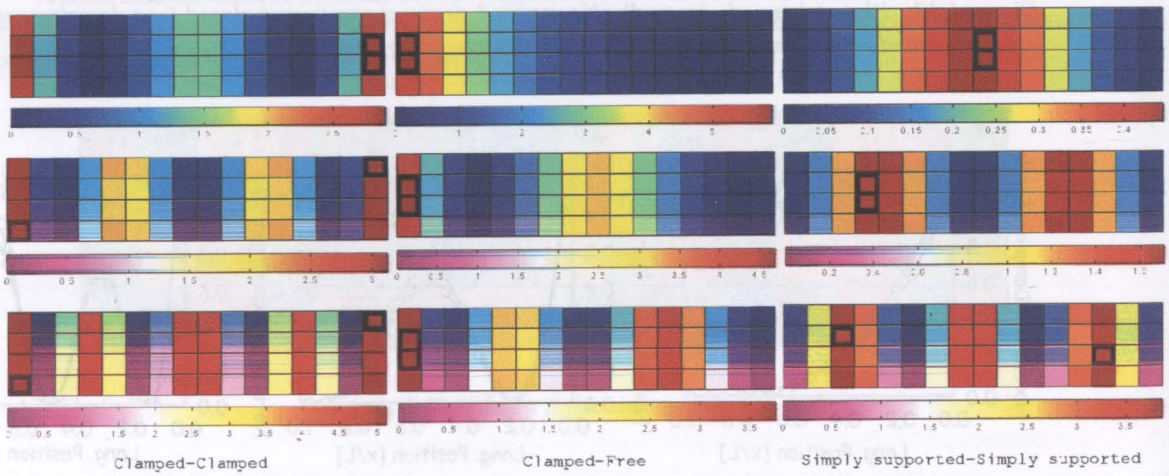

Figure 6.40: *Plate - Strain energy percentage and optimal location of 2 collocated sensor/actuator for the clamped-clamped, clamped-free and simply supported-simply supported boundary conditions.*

In general the location of the 2 piezoelectric elements for the three different boundary conditions and for the bending modes coincides with elements where the strain energy is maximum. Figure 6.41 shows the strain energy distribution within the plate and the optimal location of 6 collocated sensor/actuator for the three different boundary conditions and the first three bending modes.

Again, an excellent agreement is obtained and in general the piezoelectric active elements are coincident with strain energy maximum values.

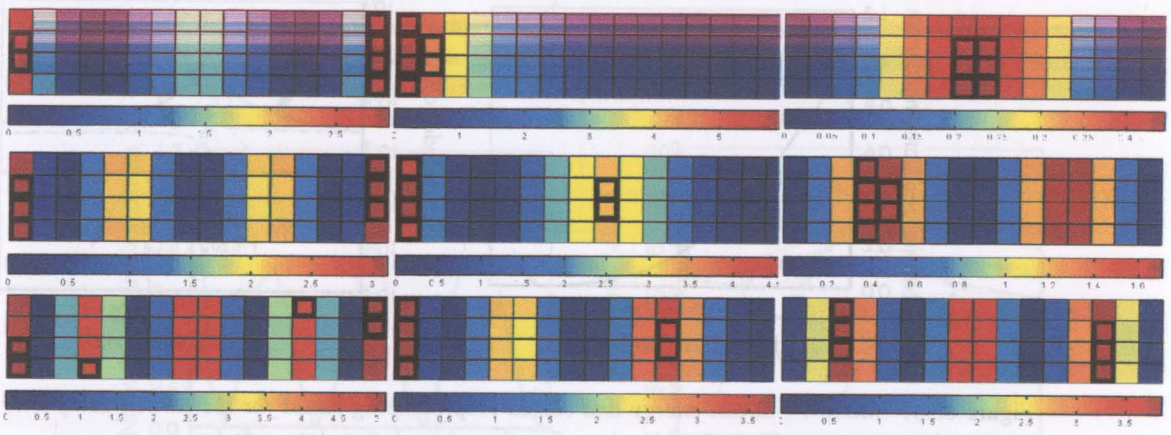

Figure 6.41: *Plate - Strain energy percentage and optimal location of 6 collocated sensor/actuator for the clamped-clamped, clamped-free and simply supported-simply supported boundary conditions.*

Experimental Results

This section presents some simulation results and experimental data concerning the optimal positioning of one collocated sensor/actuator for controlling the free vibrations of a clamped-free carbon/epoxy beam. The beam, shown in Figure 6.42, is 12 mm wide, 285 mm long and 1 mm thick with 5×2 piezoelectric elements from Philips Components, 0.3 mm thick, 24 mm long and 12 mm wide, glued on both sides.

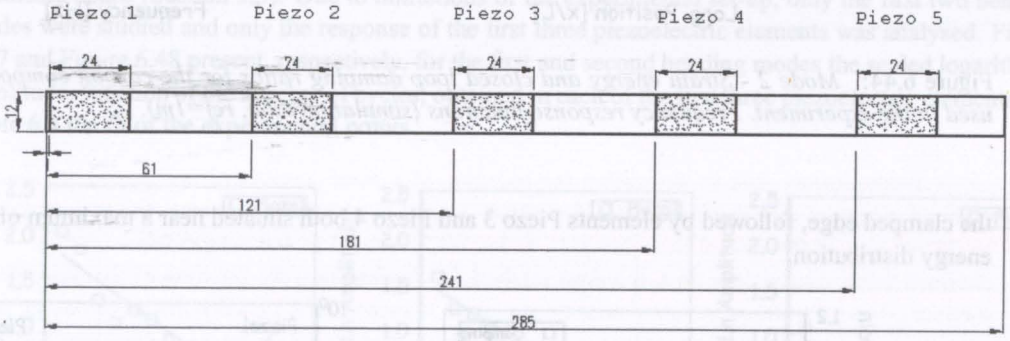

Figure 6.42: *Layout of the clamped-free carbon composite beam used in the experiment. Units in mm.*

Figure 6.43, 6.44, 6.45 and 6.46 show, respectively, for the first four bending modes, the strain energy distribution along the beam and the closed loop damping ratio obtained when a piezoelectric element is made active, together with the structure's correspondent frequency response function (FRF). Piezoelectric element number 4 was used as the excitation element. A linear quadratic regulator control methodology was used in the simulations (see Section 3.4) and an initial damping of 0.002 was assumed for all the modes.

As expected, for the first vibration mode, Figure 6.43, the effect of the collocated sensor/actuator on the damping of the vibrations is higher near the clamped edge and minimum near the tip, as shown by the frequency response function.

The most effective location for damping the second vibration mode, Figure 6.44, is once again near

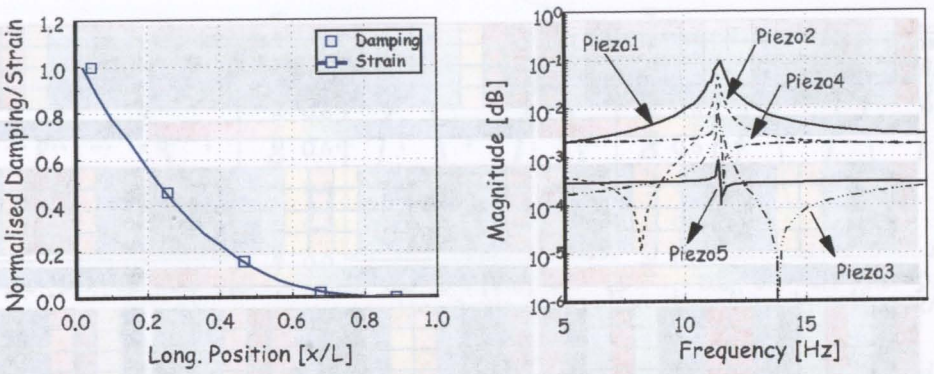

Figure 6.43: *Mode 1 - Strain energy and closed loop damping ratios for the carbon composite beam used in the experiment. Frequency response functions (simulation data, ref=1m).*

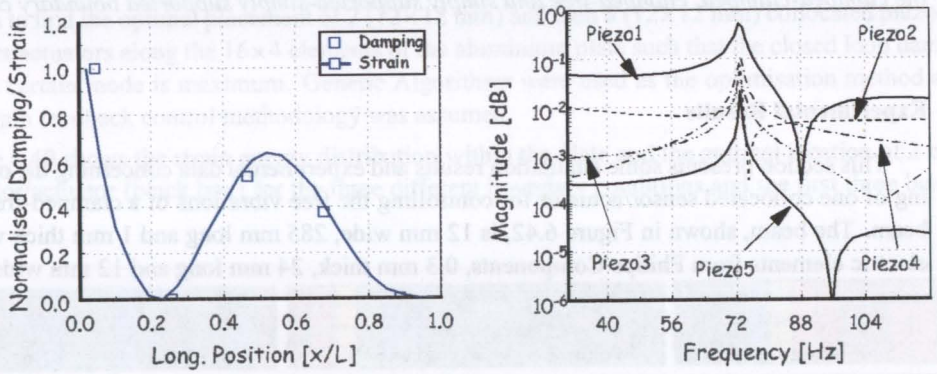

Figure 6.44: *Mode 2 - Strain energy and closed loop damping ratios for the carbon composite beam used in the experiment. Frequency response functions (simulation data, ref=1m).*

the clamped edge, followed by elements Piezo 3 and Piezo 4 both situated near a maximum of the strain energy distribution.

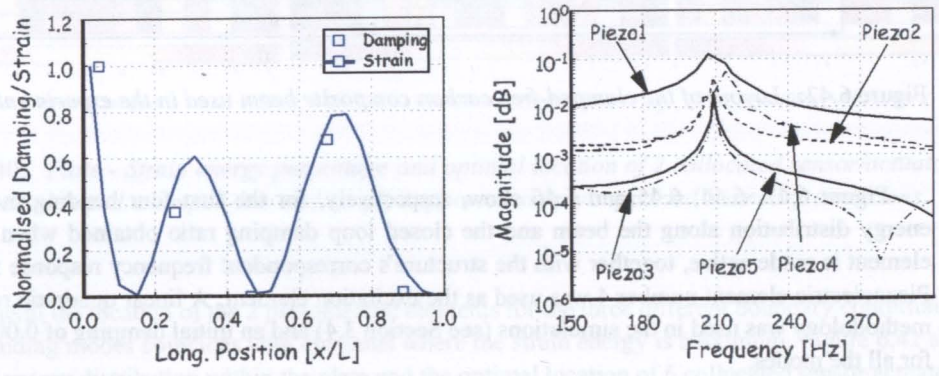

Figure 6.45: *Mode 3 - Strain energy and closed loop damping ratios for the carbon composite beam used in the experiment. Frequency response functions (simulation data, ref=1m).*

The effect of the collocated sensor/actuator for the third vibration mode, Figure 6.45, is maximum near the clamped edge followed by the element referenced as Piezo 4; while for Piezo 3 and Piezo 5, located near a node, the effect is minimum.

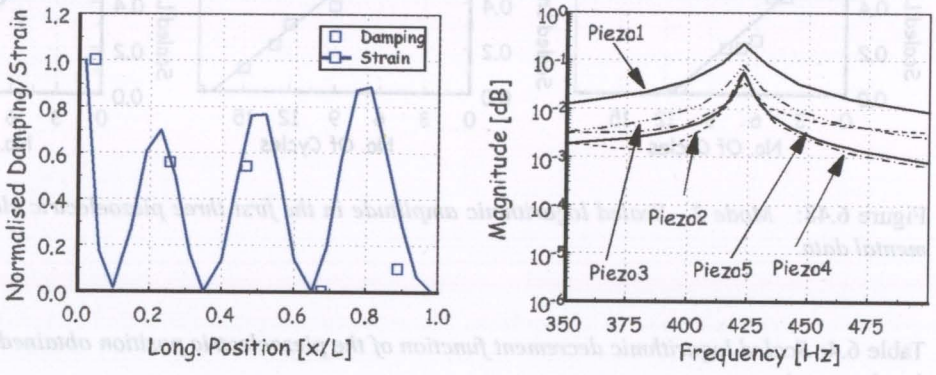

Figure 6.46: *Mode 4 - Strain energy and closed loop damping ratios for the carbon composite beam used in the experiment. Frequency response functions (simulation data, ref=1m).*

For the fourth vibration mode, Figure 6.46, the most effective location is again near the clamped edge, followed by Piezo 2 and Piezo 3 with very similar performances.

The simulations and the results presented above will be confirmed experimentally. A constant gain feedback control was considered in the experimental tests and the set-up consisted in a voltage amplifier with a constant gain of 11.5 and a low pass filter. The data acquisition was done with a National Instruments board (Section 3.3). Due to limitations of the experimental set-up, only the first two bending modes were studied and only the response of the first three piezoelectric elements was analysed. Figure 6.47 and Figure 6.48 present, respectively, for the first and second bending modes the scaled logarithmic amplitude, function of the number of cycles, obtained in each of the first three piezoelectric elements and Table 6.4 the fit of the experimental points.

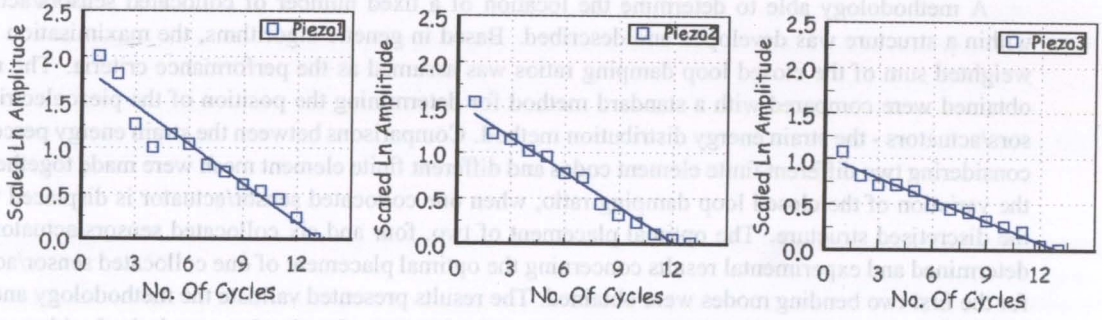

Figure 6.47: *Mode 1 - Scaled logarithmic amplitude in the first three piezoelectric elements. Experimental data.*

As expected the experimental data confirms that for the first vibration mode the effectiveness of the collocated sensor/actuator decrease with the distance to the clamped edge while for the second vibration mode this effectiveness is maximum near the clamped edge and increasing again at the position of the third piezoelectric element. As a result of the limitations of the control methodology and of the experimental set-up (amplifier voltage limited to $\pm$ 150 Volt) no more experimental data was generated.

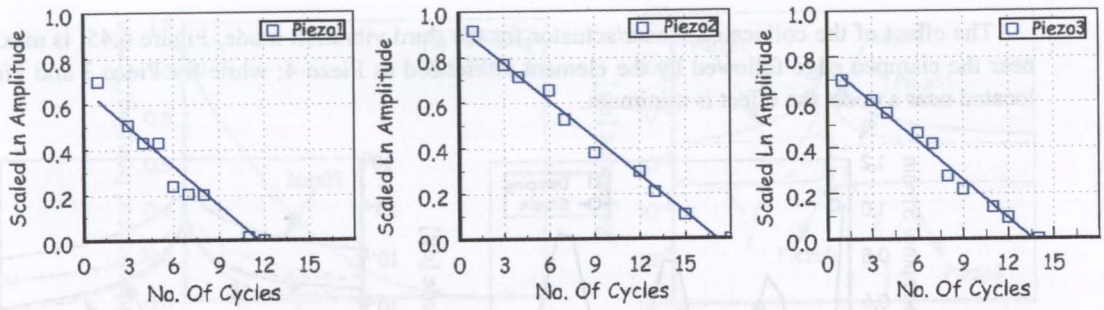

Figure 6.48: *Mode 2 - Scaled logarithmic amplitude in the first three piezoelectric elements. Experimental data.*

Table 6.4: *Scaled logarithmic decrement function of the piezoelectric position obtained for the first two bending modes.*

Piezo No.	x/L [%]	Mode 1	Mode 2
1	4.5	0.143	0.0579
2	25.6	0.123	0.0546
3	46.7	0.079	0.0567

However, the experimental results available fully confirm the simulations and the results obtained with the developed methodology.

6.4 Conclusions

A methodology able to determine the location of a fixed number of collocated sensors/actuators within a structure was developed and described. Based in genetic algorithms, the maximisation of the weighted sum of the closed loop damping ratios was assumed as the performance criteria. The results obtained were compared with a standard method for determining the position of the piezoelectric sensors/actuators - the strain energy distribution method. Comparisons between the strain energy percentage considering two different finite element codes and different finite element mesh were made together with the variation of the closed loop damping ratio, when one collocated sensor/actuator is displaced within the discretised structure. The optimal placement of two, four and six collocated sensors/actuators was determined and experimental results concerning the optimal placement of one collocated sensor/actuator for the first two bending modes were obtained. The results presented validate the methodology and were all obtained assuming that the structure is covered with piezoelectric elements in both sides and that the control is achieved by activating individually each piezoelectric element. In practice this means that the matrices modelling the structure are constant during the optimisation process. In case that the geometry, comprising structure and piezoelectric elements, is not defined before the optimisation process starts and/or the structure is not completely covered with piezoelectric elements the present methodology is still valid but the iteration process is much longer since at each step the system's matrices must be recalculated.

No strong mathematical justification was found for the observed general tendency of the optimisation algorithm to place piezoelectric elements near to already existing ones, when there are other locations

with the same strain energy. When the strain energy value is the same in several locations, a collocated sensor/actuator with a higher dimension is more effective than two smaller ones, each with half of the dimensions, placed apart from each other. In practice the difference between configurations is negligible and lower than 1%. This fact may be related with numerical errors of the simulation model.

Chapter 7

Aplications

In this chapter both methodologies, shape control developed in Chapter 5 and optimal placement of collocated sensors/actuators for vibration control presented in Chapter 6, are applied to a 2.5 meter sandwich disc known as alignment wheel. After describing the structure, the experimental results obtained concerning the dynamic characterisation of the full-scale prototype are presented, followed by shape control simulations and determination of optimal placement of collocated sensors/actuators for vibration control.

7.1 Introduction and context

The European Laboratory for Particle Physics (CERN), Geneva, foresees in 2005 the construction of two large purpose high-energy physics experiments - CMS and ATLAS - at the Large Hadron Collider (LHC) presently in preparation. The main scope of the Compact Muon Solenoid Experiment (CMS) is the investigation of the most fundamental properties of matter and the identification and precise measurement of muons, electrons and photons. The inner detector, Tracker, plays a major role in all physics searches and their performance depends upon the intrinsic detector characteristics, on the stability of the supporting structures and on the overall position monitoring and alignment system. On the other hand, the performance of the Position Monitoring System (PMS) for the Tracker is strongly related with the stability and performance of two composite structures known as alignment wheels [102]. Each alignment wheel, with 2.5 m diameter, is a sandwich structure with 2 mm thick skins of standard carbon fibre composite and 16 mm core of aramid honeycomb. It is a fundamental piece of the alignment system and presents stability requirements in the order of some tens of micron. The structure provides 18 connections for the various elements of the PMS and 3 for the fixations to the detector. It is divided in two halves due to operational purposes. The full scale prototype mechanical drawing is shown in Figure 7.1.

In situ, the structure sits in the centre of several sub-detectors, which will selectively filter and possibly amplify vibrations at specific frequencies. Seismic vibrations and vibrations from ventilation systems, pumps for cryogenics, vacuum and cooling, can only be realistic quantified by performing measurements on the final structures. The results concerning the dynamic testing of the alignment wheel prototype, and presented in the next section, are an essential part in the study of the propagation of vibrations in the structure, in the quantification of the vibration risk and in accessing the need of passive and/or active control [3].

7.2 Modal testing

The modal testing of the alignment wheel involved the determination of frequency response functions, natural frequencies, damping factors and mode shapes; together with the validation and update of the finite element model.

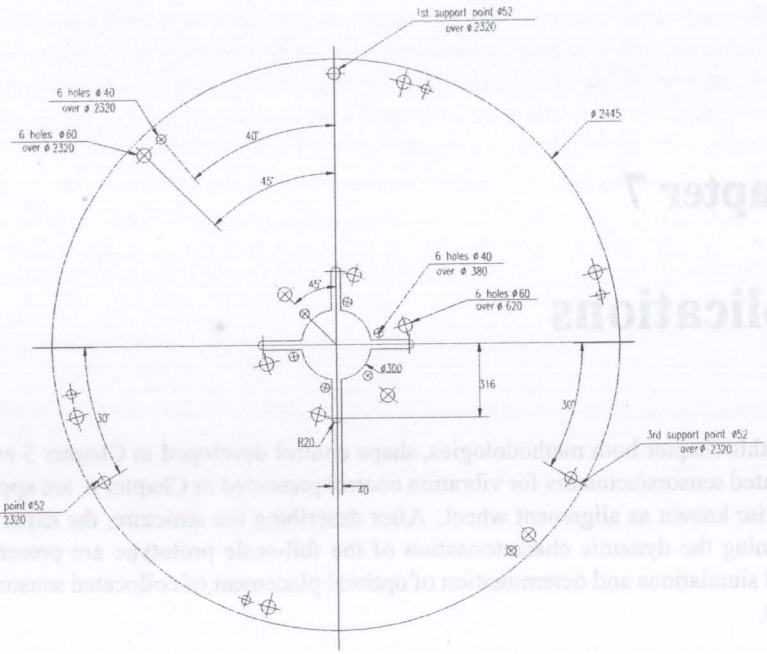

Figure 7.1: *Mechanical drawing of the full scale prototype of the alignment wheel. X and Y (vertical) axis are in-plane directions; Z-axis is out-of-plane.*

In order to approximate the free boundary condition the structure was suspended from 2 fixation points by steel flexible cables. By choosing a free support instead of a grounded support, the structure was isolated from parasite excitations and the modelisation in itself was facilitated [67]. On the other hand, with this kind of support, the structure is constrained in in-plane motion but free in the normal direction with rigid mode behaviour. A single-point excitation was adopted. The schematic layout of the experimental set-up is shown in Figure 7.2.

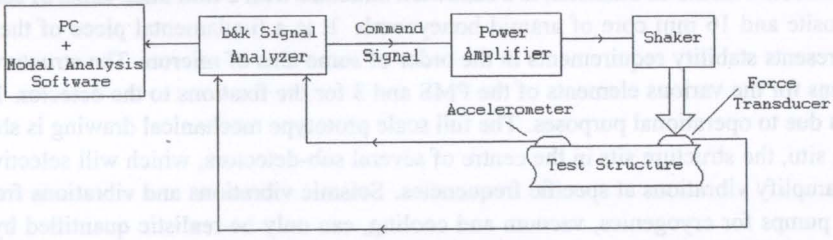

Figure 7.2: *Schematic layout of the experimental set-up used in the modal testing.*

An electromagnetic shaker provides the excitation signal to the system through a piezoelectric force transducer and the response is measured by an accelerometer attached to it by a thin layer of bees wax. The use of a shaker guarantees a good signal-to-noise ratio and an accurate control of the applied force. Four steel cables, attached to a frame, support the shaker (Figure 7.3). This procedure ensures that the reaction force imposed on the shaker (opposite to the one applied to the structure) is not transmitted to the test structure. The connection between both is done by means of a steel stinger. This attachment has high

axial stiffness but low transverse stiffness giving good directional control of the excitation (Figure 7.4). A spectrum analyser is used to measure the force and the response signals needed to build the frequency response functions (FRFs) of the system. The excitation force is broadband and is generated by a signal generator that sends the signal to a power amplifier driving the electrodynamic vibration exciter. The waveform generator is built-in the analyser. The excitation is random and continuous in time [103]. The FRFs obtained during the analysis are stored in a computer running the modal analysis identification software package: CADA-PC from LMS. The measurement of the structure's response to the excitation spectrum were performed on a uniformly distributed measuring mesh of 128 points.

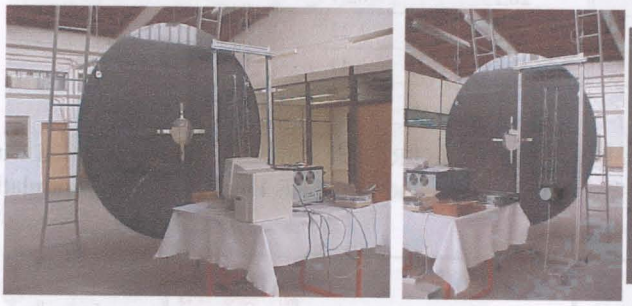

Figure 7.3: *Experimental set-up for testing the alignment wheel prototype.*

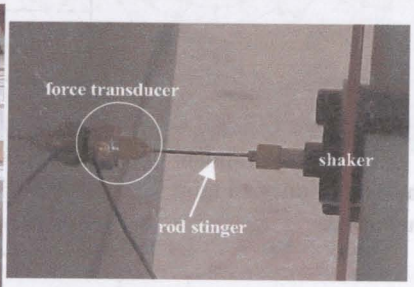

Figure 7.4: *Detailed system excitation.*

7.2.1 Experimental results

The experimental measurements are performed in the frequency bandwidth 0-100 Hz with a frequency resolution of 0.125 Hz. Each FRF results from a frequency domain averaging of 25 samples, used to reduce the influence of random errors. To avoid the leakage errors an Hanning window is applied to weight the excitation and the response data. Modal parameters are extracted from the 128 measured FRFs by a modal analysis identification package. For modal parameter estimation, a multi degree technique is used. It uses a time domain algorithm to identify poles (frequency and damping values) by the so-called Least Squares Complex Exponential (LSCE) method. In a second phase, residues are identified with the Least Squares Frequency Domain (LSFD) technique. Ranging from 0 to 100 Hz, Figure 7.5 and Figure 7.6 show 3 measured FRFs: the driving point FRF $H_{84:84}$ (response node 84, excitation node 84), the FRF $H_{11:84}$ (response node 11, excitation node 84) and the FRF $H_{119:84}$ (response node 119, excitation node 84) overlapped with the Modal Indicator Function (MIF) and the Sum function of the measured FRFs, respectively [103]. The other FRFs can be found in [104].

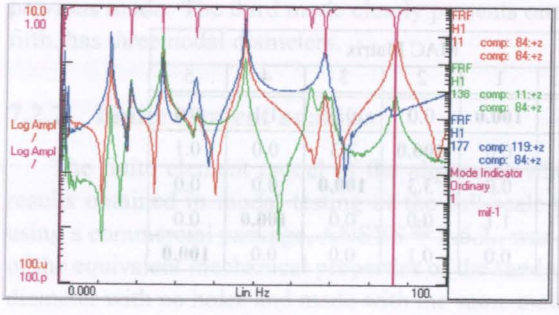

Figure 7.5: *Measured frequency response functions and MIF function.*

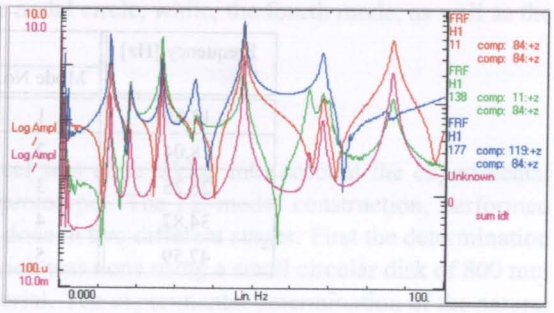

Figure 7.6: *Measured frequency response functions and SUM function.*

The Modal Indicator Function, built upon the set of the measured FRFs, is used to show the location

of each mode. The presence of 5 modes in the analysis bandwidth of 6-69 Hz were identified. Table 7.1 shows the experimental modal analysis parameters.

Table 7.1: *Modal parameters obtained with the LMS CADA-PC software.*

Mode Nr.	Frequency [Hz]	Damping [%]
1	12.80	0.69
2	18.04	1.29
3	26.25	0.39
4	34.87	1.22
5	47.59	0.44

In order to validate the modal model identified, some FRFs are synthesised and compared with the measured ones. Figure 7.7 shows the measured and synthesised FRF $H_{11:84}$. A good correlation is achieved.

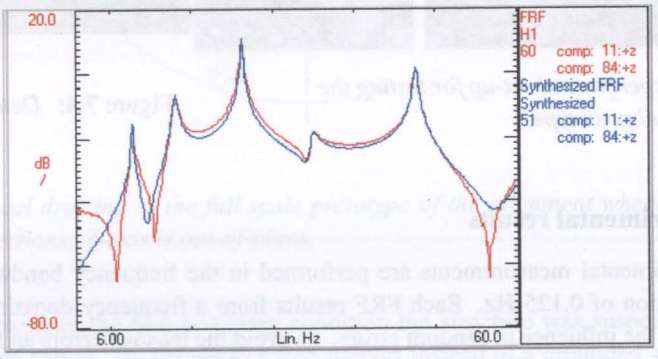

Figure 7.7: *Measured and synthesised FRF $H_{11:84}$.*

The validation of the model is completed using the Modal Assurance Criterion (MAC). This criterion correlates a mode shape for one pole against the mode shape of all the others poles. If the model is valid, little or no correlation between modes should be found as confirmed in Table 7.2, showing the MAC matrix.

Table 7.2: *Modal assurance matrix obtained with the LMS CADA-PC software.*

Frequency [Hz]	MAC Matrix					
	Mode No.	1	2	3	4	5
12.80	1	**100.0**	0.0	0.0	1.1	0.0
18.04	2	0.0	**100.0**	3.3	0.0	0.1
26.25	3	0.0	3.3	**100.0**	0.0	0.0
34.87	4	1.1	0.0	0.0	**100.0**	0.0
47.59	5	0.0	0.1	0.0	0.0	**100.0**

The biggest off-diagonal term of the MAC Matrix is 3.3%, thus, there is no correlation between mode shapes and a good analysis is assured. Displacement amplitudes at each node of the measurement mesh for the first five experimental mode shapes are presented in Figure 7.8 to Figure 7.12.

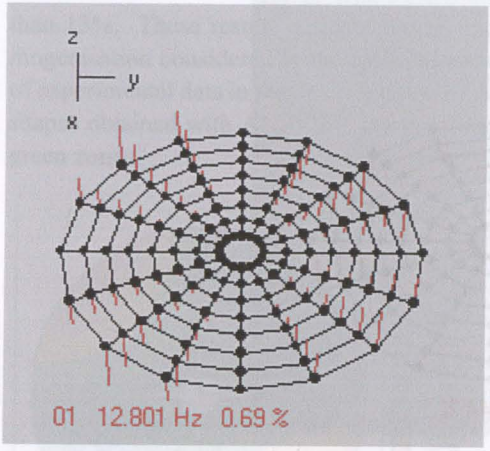

Figure 7.8: *First mode shape (12.80 Hz) obtained by modal testing.*

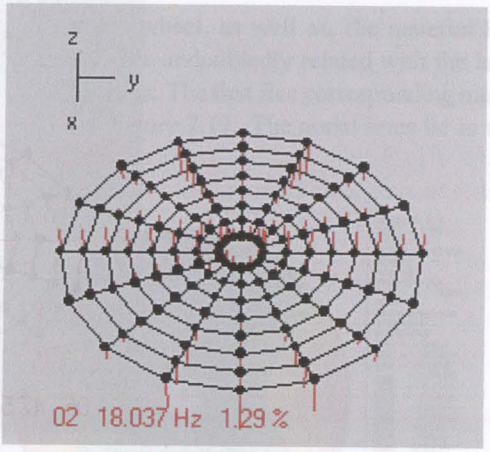

Figure 7.9: *Second mode shape (18.04 Hz) obtained by modal testing.*

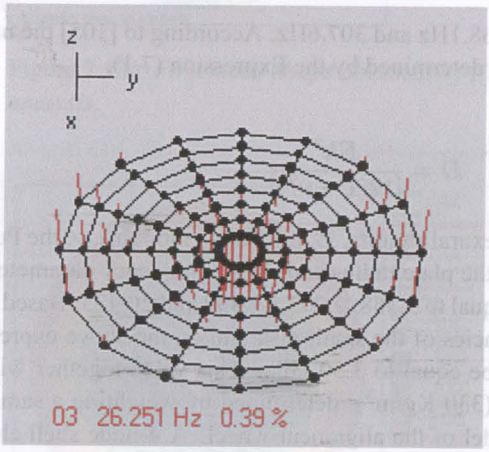

Figure 7.10: *Third mode shape (26.25 Hz) obtained by modal testing.*

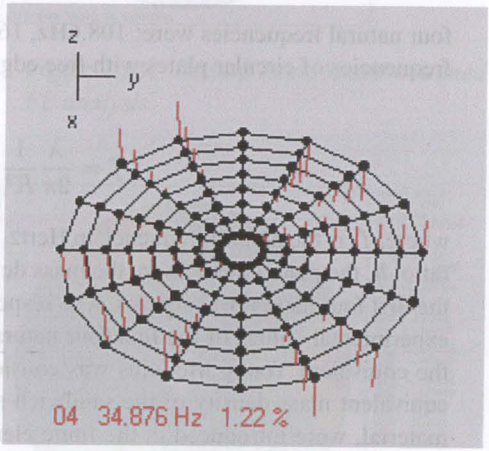

Figure 7.11: *Fourth mode shape (34.87 Hz) obtained by modal testing.*

The first mode shows the existence of two perpendicular nodal diameters. The second mode shape, very similar to the first one, presents again two nodal diameters rotated with respect to the ones of the previous mode. The third mode clearly presents one nodal circle, while, the fourth mode, as well as the fifth, has three nodal diameters.

7.2.2 Finite element analysis

The finite element model of the alignment wheel was done taking into account the experimental results obtained in modal testing of the full-scale prototype. The FE model construction, performed using a commercial package, ANSYS ® 5.6.2., was done in two different stages. First the determination of the equivalent mechanical properties of the sandwich was done using a small circular disk of 800 mm diameter with no holes and made with the same material. The experimental determination of the natural modes of this disk, using the same procedure described above, and the comparison with the theoretical ones enabled the calculation of the equivalent Young Modulus of the sandwich structure. This result was then introduced in the alignment wheel finite element model and the cross check with the experimental results was performed. The 800 mm diameter disk was tested in a free boundary condition. The first

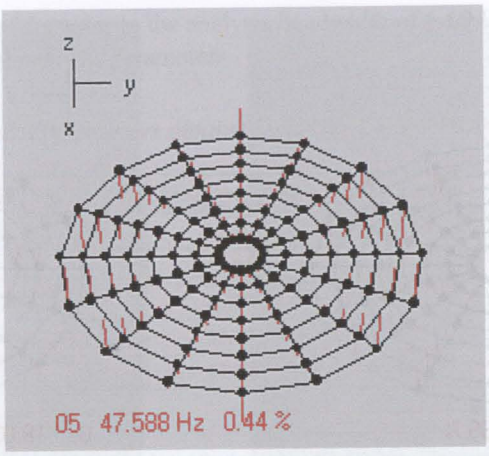

Figure 7.12: *Fifth mode shape (47.59 Hz) obtained by modal testing.*

four natural frequencies were: 108.6Hz, 164.6Hz, 268.1Hz and 307.6Hz. According to [105] the natural frequencies of circular plates with free edges can be determined by the Expression (7.1).

$$f = \frac{\lambda}{2\pi}\frac{1}{R^2}\sqrt{\frac{D}{\rho h}} \quad , \quad D = \frac{Eh^3}{[12(1-\nu^2)]} \tag{7.1}$$

where, f, is the natural frequency in Hertz, D, the flexural rigidity, E, the Young modulus, ν, the Poisson ratio, h, the plate thickness, ρ, the mass density, R, the plate radius and, λ, the frequency parameter. For the first four natural frequencies, λ, is respectively equal to 5.358, 9.003, 12.439 and 20.475. Based in the experimental values of the first four natural frequencies of the small disk and on the above expression, the equivalent Young Modulus was considered to be equal to 3.50 GPa. This value together with the equivalent mass density of the sandwich structure (330 Kg/m^3), determined by weighting a sample of material, were introduced in the finite element model of the alignment wheel. A 4-node shell element with 6 degrees of freedom per node and with both membrane and bending capabilities was chosen for the model (element SHELL63 from ANSYS ® element's library).

Table 7.3 shows the first five natural frequencies obtained experimentally and by finite element calculation, together with the error percentage.

Table 7.3: *First five natural frequencies of the alignment wheel structure obtained experimentally and by finite element analysis.*

Mode Nr.	Experimental Freq. [Hz]	FE Freq. [Hz]	Error [%]
1	12.80	11.23	12.3
2	18.04	16.33	9.5
3	26.25	27.01	2.9
4	34.87	39.23	12.8
5	47.59	47.26	0.7

One can observe that in spite of having determined the mechanical properties of the sandwich material in a indirect way the difference between experimental and simulation natural frequencies is lower

than 13%. These results validate the FE model of the alignment wheel, as well as, the material homogenisation considered in the calculations. The obtained errors are undoubtedly related with the lack of experimental data in the determination of the mechanical properties. The first five corresponding mode shapes obtained with ANSYS ® are presented in Figure 7.13 to Figure 7.17. The nodal lines lie in the green zones.

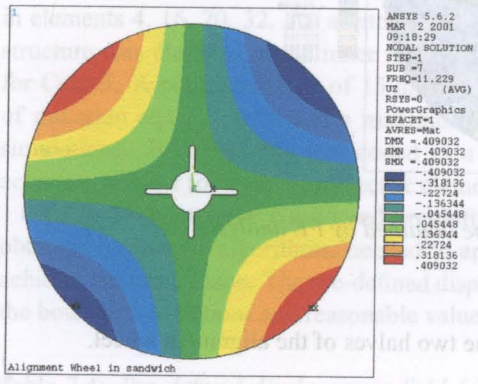

Figure 7.13: *First mode shape obtained by FE analysis.*

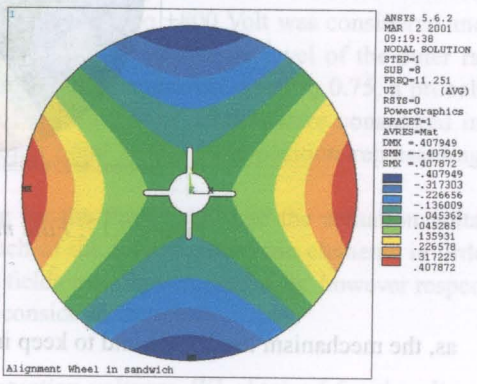

Figure 7.14: *Second mode shape obtained by FE analysis.*

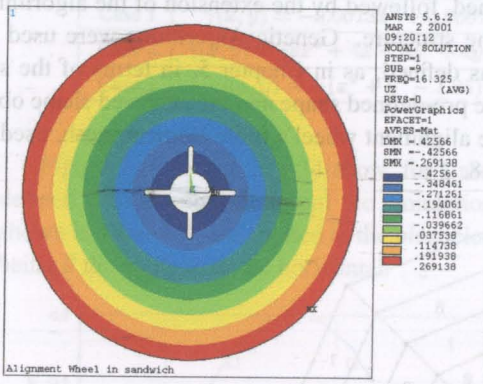

Figure 7.15: *Third mode shape obtained by FE analysis.*

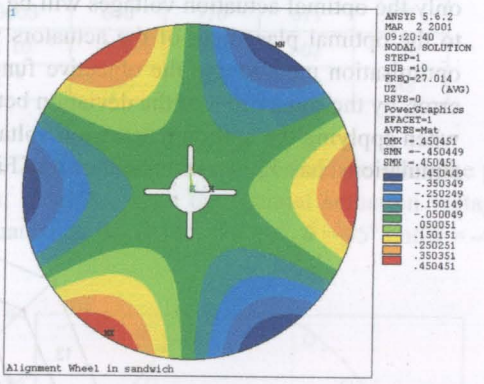

Figure 7.16: *Fourth mode shape obtained by FE analysis.*

The same number of nodal circles and nodal diameters, obtained for each of the first five modes, is found experimentally and by finite element analysis. The FE model assumes the material as perfectly homogeneous and does not take into account the joint between the two halves of the structure, the embedded aluminium inserts and the edge sealing material of the sandwich structure - adhesive in the exterior diameter and aluminium parts in the interior diameter. Due to these facts, there is a non-direct correspondence between the mode shapes and the frequencies obtained experimentally and by simulation. This means, for example, that in the case of the first and of the second mode shapes, both with two nodal diameters rotated with respect to each other, the finite element model associates two similar frequencies (11.23 Hz and 11.25 Hz) and not distinct ones as observed experimentally. This fact is again observed for the fourth and fifth modes (27.01 Hz and 27.01 Hz), both with 3 nodal diameters. Once again, the FE model cannot distinguish between the two cases. However the relevant fact is that the same natural frequencies and the same mode shapes found experimentally are again found by simulation. Therefore, in spite of the assumptions made in the FE model, these results validate the FE model in itself, as well

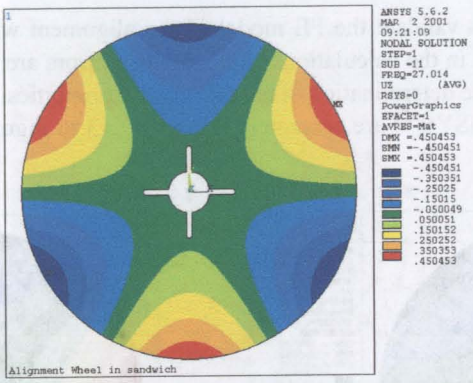

Figure 7.17: *Fifth mode shape obtained by FE analysis.*

as, the mechanism used to fix and to keep in place the two halves of the alignment wheel.

7.3 Shape control of the alignment wheel

This section presents the results concerning the shape control of the alignment disk. In a first analysis, only the optimal actuation voltages will be determined, followed by the extension of the algorithm also to the optimal placement of the actuators within the structure. Genetic Algorithms were used as the optimisation method and the objective function was defined, as in Chapter 5, in terms of the surface error, by the square root of the deviation between the pre-defined shape and the achieved shape obtained when applying the optimum actuation voltages. The alignment wheel's finite element mesh, used in the simulations, has 32 elements as shown in Figure 7.18.

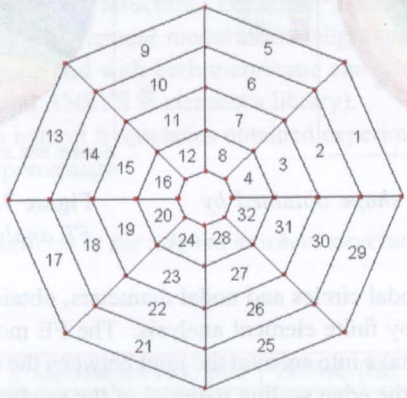

Figure 7.18: *Finite element mesh of the alignment wheel used in the simulations.*

7.3.1 Simulation results: optimal voltages

This first set of simulations consists in determining the optimal actuation voltages needed to apply to four piezoelectric elements, already glued to the alignment wheel, in order to deform it in a certain

pre-defined way. The electro-mechanical properties of the piezoceramic elements (PX5-N from Philips Components) were already shown (Table 3.2).

The first simulation case, Case 1, assumes that the 4 piezoelectric actuators were glued, on both sides of the structure, at the level of the inner radius in elements 4, 12, 20, 28. For the second case, Case 2, the 4 piezoelectric actuators were located at the level of the outer radius in elements 1, 9, 17, 25 of the finite element mesh, while for the third and last case, Case 3, the piezoelectric actuators were located in elements 4, 16, 20, 32. An arbitrary saturation voltage of -600 to +800 Volt was considered and the structure was clamped at the inner radius for Case 1 and Case 2; and at the level of the outer radius for Case 3. A population size of 15 individuals, a probability of crossover equal to 0.75, a probability of mutation equal to 0.20 and a maximum number of generations of 20,000 were considered in the simulations. Each variable was coded as a four floating point string, each position representing the actuation voltage for each piezoelectric element.

Table 7.4 shows the considered pre-defined shape for the three cases and the actuation voltages, obtained by genetic algorithms, needed to apply to each of the four piezoelectric elements in order to achieve that same shape. The pre-defined displacement fields were chosen arbitrarily, however respecting the boundary conditions and reasonable values for the considered structure.

Table 7.4: *Pre-defined displacement field [m] and actuation voltages [V] obtained for the alignment wheel clamped at the level of the inner radius for Case 1 and Case2 and at the outer radius for Case 3.*

	Displacement Field	V_{piezo1}	V_{piezo2}	V_{piezo3}	V_{piezo4}
Case 1	$\gamma(x,y) = -0.0013x^2 + 0.0007y^2 - 0.00003$	670	-76	671	-77
Case 2	$\gamma(x,y) = (8x^3 + 4x + 5y^3 + 4y + x^2y) \times 10^{-3}$	-600	230	602	-230
Case 3	$\gamma(x,y) = -(x^2 + y^2 - 1.25)/1.5 \times 10^{-3}$	580	600	569	588

Figure 7.19 to Figure 7.24 show, for Case 1, Case 2 and Case 3, the comparison between the pre-defined displacement field and the simulation results, obtained when the optimal actuation voltages, shown in Table 7.4, are applied to the piezoelectric actuators, along $\theta = 0°$, $\theta = 90°$, $\theta = 45°$ and $\theta = -45°$, being θ the angle with the horizontal.

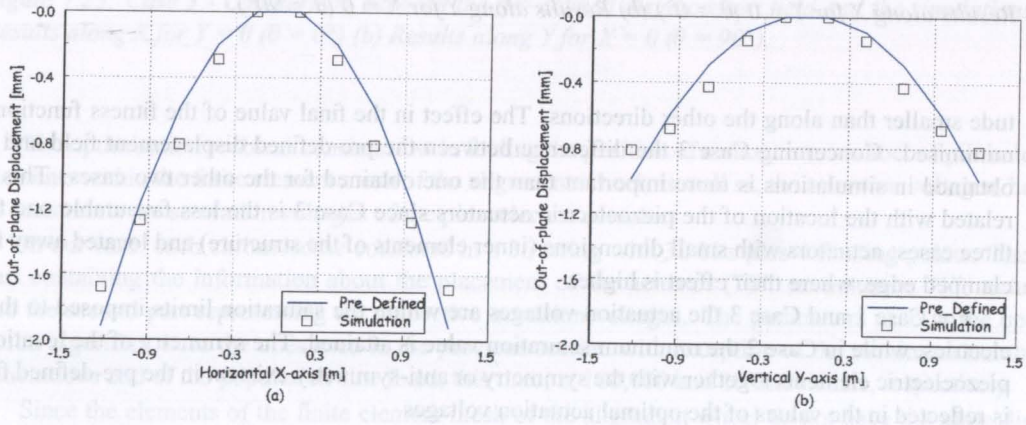

Figure 7.19: *Case 1 - Comparison between the pre-defined displacement field and the simulations. (a) Results along X for Y = 0 (θ = 0°) (b) Results along Y for X = 0 (θ = 90°).*

For Case 1 and Case 2, simulation results follow pre-defined results very well. The main variations are verified in Case 2 along θ = -45°, however in this case, displacements are one order of magni-

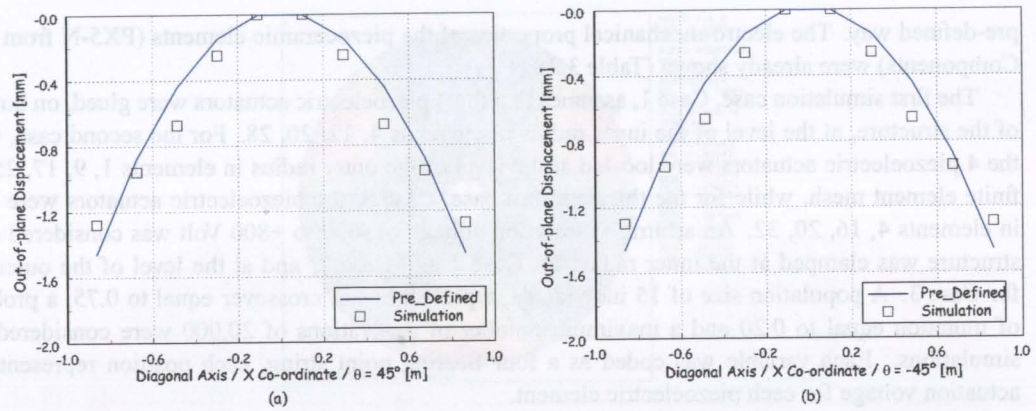

Figure 7.20: *Case 1 - Comparison between the pre-defined displacement field and the simulations. (a) Results along a diagonal θ = 45° (b) Results along a diagonal θ = -45°.*

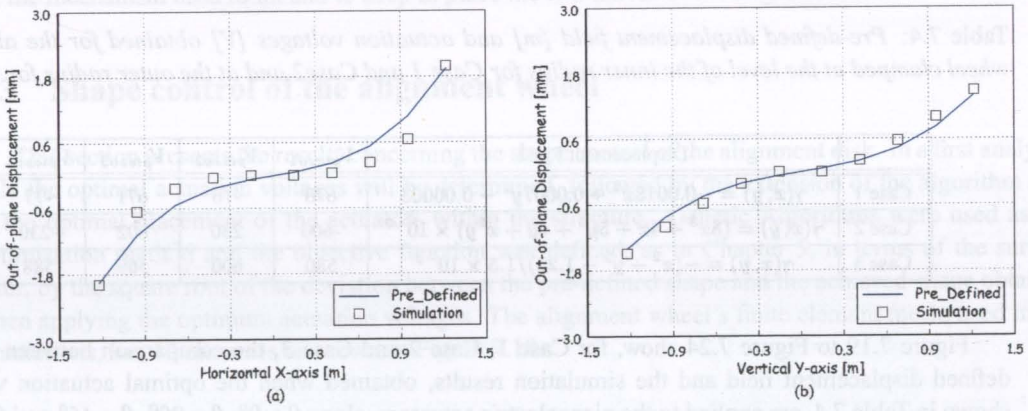

Figure 7.21: *Case 2 - Comparison between the pre-defined displacement field and the simulations. (a) Results along X for Y = 0 (θ = 0°) (b) Results along Y for X = 0 (θ = 90°).*

tude smaller than along the other directions. The effect in the final value of the fitness function is thus minimised. Concerning Case 3 the difference between the pre-defined displacement field and the one obtained in simulations is more important than the one obtained for the other two cases. This may be related with the location of the piezoelectric actuators since Case 3 is the less favourable one from the three cases: actuators with small dimensions (inner elements of the structure) and located away from the clamped edge, where their effect is higher.

For Case 1 and Case 3 the actuation voltages are within the saturation limits imposed to the piezoelectrics, while in Case 2 the minimum saturation value is attained. The symmetry of the location of the piezoelectric elements together with the symmetry or anti-symmetry existent in the pre-defined functions is reflected in the values of the optimal actuation voltages.

7.3.2 Simulation results: optimal voltages and optimal placement

A more interesting approach is to determine not only the optimal voltages but also the optimal placement of the actuators within the structure. As in Section 5.3.7, the optimisation algorithm was changed in order to accommodate this new feature.

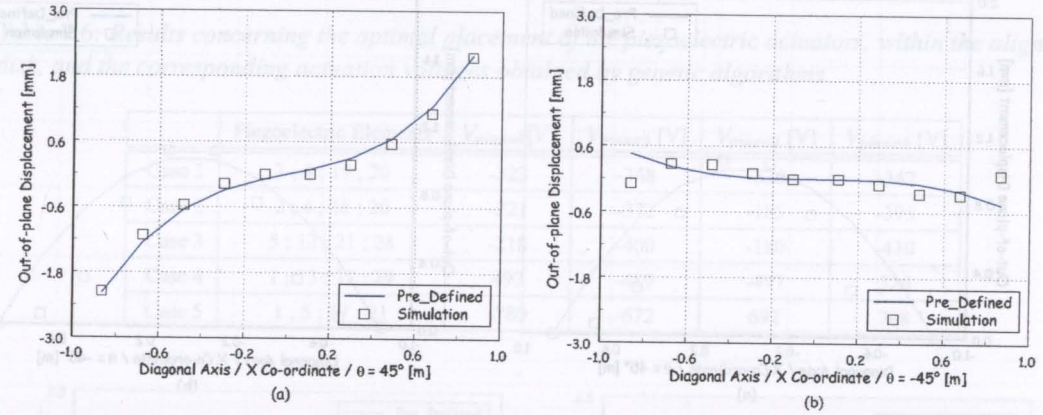

Figure 7.22: *Case 2 - Comparison between the pre-defined displacement field and the simulations. (a) Results along a diagonal θ = 45° (b) Results along a diagonal θ = -45°.*

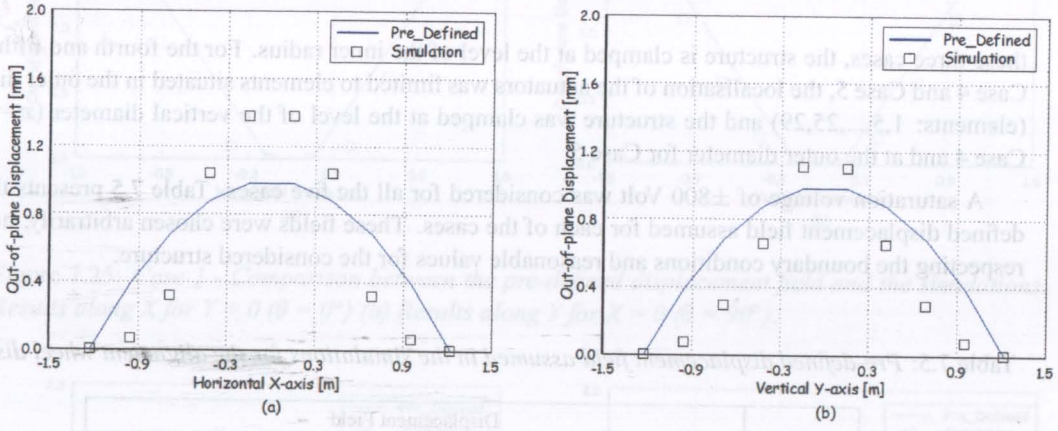

Figure 7.23: *Case 3 - Comparison between the pre-defined displacement field and the simulations. (a) Results along X for Y = 0 (θ = 0°) (b) Results along Y for X = 0 (θ = 90°).*

The optimisation problem consists now in finding the position of a maximum number of piezoelectric elements within the finite element mesh of the alignment wheel, as well as, the actuation voltages, having as constraints the saturation voltages of the piezoelectric actuators.

In our case, each chromosome consisted in a 36 string with 32-bits plus 4 floating points. The first part containing the information about the placement of the actuator ("0": no actuator, "1": actuator) and the second part representing the respective actuation voltages. The parameters used in the optimisation algorithm were the ones used in the previous section with exception of the maximum number of generations and of the population size fixed, this time, at 100,000 and 10 individuals, respectively.

Since the elements of the finite element mesh of the alignment wheel do not have the same dimensions, the localization of the piezoelectric actuators was constrained. Namely, five different cases were considered in the simulations. In the first case, Case 1, the localisation of the actuators is limited to elements situated in the first (elements: 4,8,12,16,20,24,28,32) and in the second (elements: 3,7,...,27,31) inner diameters. The second case, Case 2, the localisation of the actuators is limited to elements situated in the first (4,8,...,28,32) and in the third (2,6,...,26,30) inner diameters. For the third case, Case 3, elements are limited to the innermost (4,8,...,28,32) and outermost (1,5,...,25,29) diameters. For all

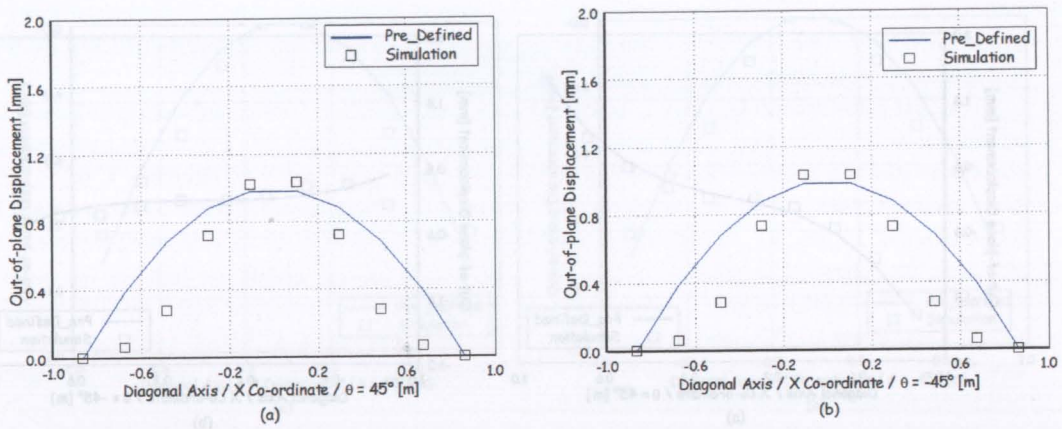

Figure 7.24: *Case 3 - Comparison between the pre-defined displacement field and the simulations. (a) Results along a diagonal $\theta = 45°$ (b) Results along a diagonal $\theta = -45°$.*

these three cases, the structure is clamped at the level of the inner radius. For the fourth and fifth cases, Case 4 and Case 5, the localisation of the actuators was limited to elements situated in the outer diameter (elements: 1,5,...,25,29) and the structure was clamped at the level of the vertical diameter ($x = 0$) for Case 4 and at the outer diameter for Case 5.

A saturation voltage of ± 800 Volt was considered for all the five cases. Table 7.5 presents the pre-defined displacement field assumed for each of the cases. These fields were chosen arbitrarily, however respecting the boundary conditions and reasonable values for the considered structure.

Table 7.5: *Pre-defined displacement field assumed in the simulations for the alignment wheel disk [m].*

	Displacement Field
Case 1	$\gamma(x,y) = \sqrt{2.5 \times 10^{-6}x^2 + 2.5 \times 10^{-6}y^2}$ - 0.000024
Case 2, 3	$\gamma(x,y) = \sin(2.5 \times 10^{-6}x^2 + 1.8 \times 10^{-6}y^2 - 1.2 \times 10^{-6}xy) \times 500$
Case 4	$\gamma(x,y) = -0.0013x^3 + 0.0002x - 0.0018xy^2$
Case 5	$\gamma(x,y) = (-1.2x^3 - 1.2y^3 + 1.8x + 1.8y - 1.2x^2y - 1.2xy^2$

Table 7.6 shows the location of the piezoelectric elements for the five cases together with the corresponding optimal actuation voltages.

The comparison between the pre-defined displacement field and the simulation results, for each of the five cases, is presented in Figure 7.25 to Figure 7.32.

Since there was no penalization concerning the increase of weight due to the piezoelectric elements or concerning the number of actuators used, the final results, for all the cases, assume that all the four piezoelectric actuators are contributing to induce deformations in the structure and thus the actuation voltages are all different from zero. The agreement between the pre-defined displacement fields and the simulations is excellent for Cases 2, 3, 4 and 5. In Case 1 the actuation voltages are all within the saturation limits; however the structure presents some difficulty in deforming according to the pre-defined shape. This is due not to a non-efficient optimisation algorithm but rather to the structure's high stiffness unable to comply with the pre-defined linear displacement field and the boundary condition.

Table 7.6: *Results concerning the optimal placement of the piezoelectric actuators, within the alignment disk, and the corresponding actuation voltages obtained by genetic algorithms.*

	Piezoelectric Elements	$V_{piezo1}[V]$	V_{piezo2} [V]	V_{piezo3} [V]	V_{piezo4} [V]
Case 1	3 ; 4 ; 19 ; 20	-323	-348	-320	-347
Case 2	2 ; 4 ; 18 ; 20	-221	-372	-185	-395
Case 3	5 ; 12 ; 21 ; 28	-218	-400	-180	-410
Case 4	1 ; 13 ; 17 ; 29	497	-489	-497	526
Case 5	1 ; 5 ; 17 ; 21	-780	-672	692	788

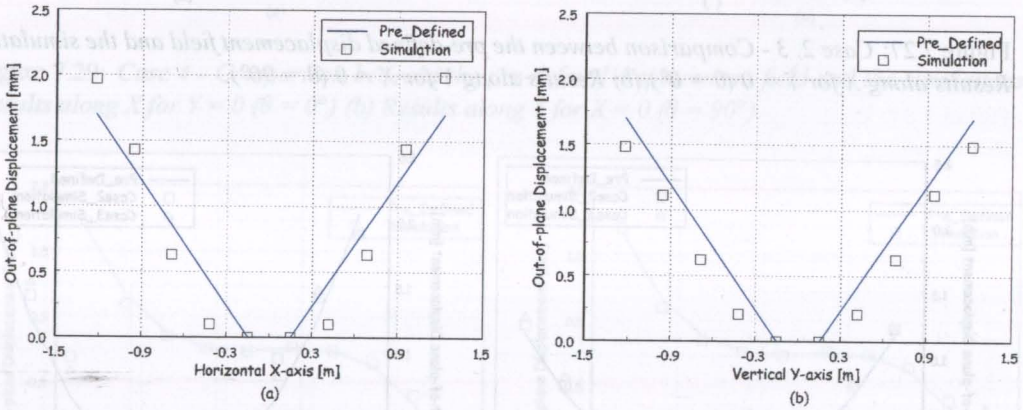

Figure 7.25: *Case 1 - Comparison between the pre-defined displacement field and the simulations. (a) Results along X for Y = 0 (θ = 0°) (b) Results along Y for X = 0 (θ = 90°).*

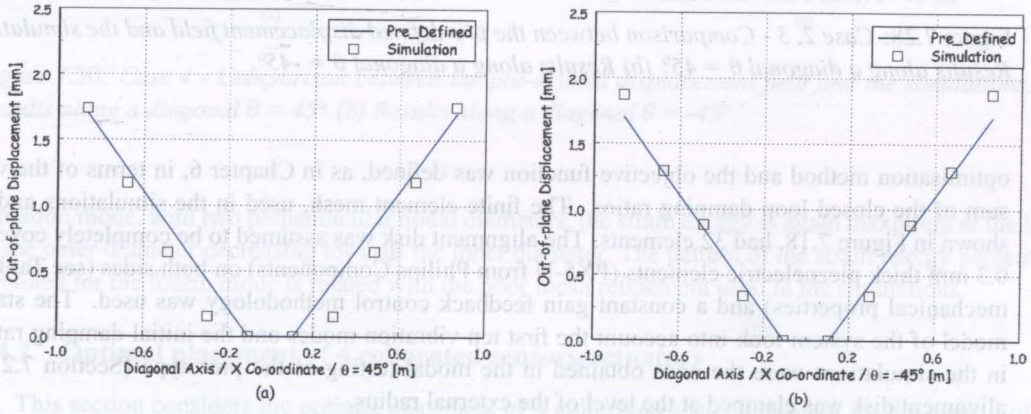

Figure 7.26: *Case 1 - Comparison between the pre-defined displacement field and the simulations. (a) Results along a diagonal θ = 45° (b) Results along a diagonal θ = -45°.*

7.4 Optimal placement of sensors/actuators in the alignment wheel for vibration control

This section presents the results concerning the optimal placement, in the alignment disk, of collocated sensors/actuators in order to damp the free vibrations. Genetic Algorithms were used as the

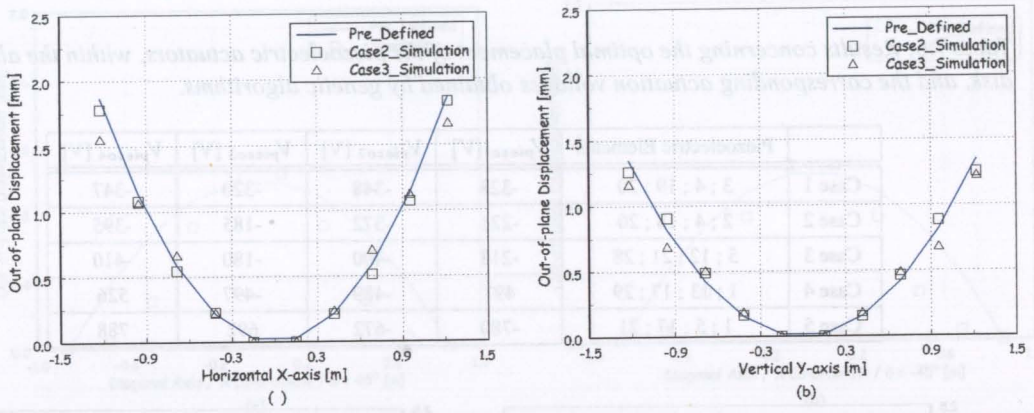

Figure 7.27: *Case 2, 3 - Comparison between the pre-defined displacement field and the simulations. (a) Results along X for Y = 0 (θ = 0°) (b) Results along Y for X = 0 (θ = 90°).*

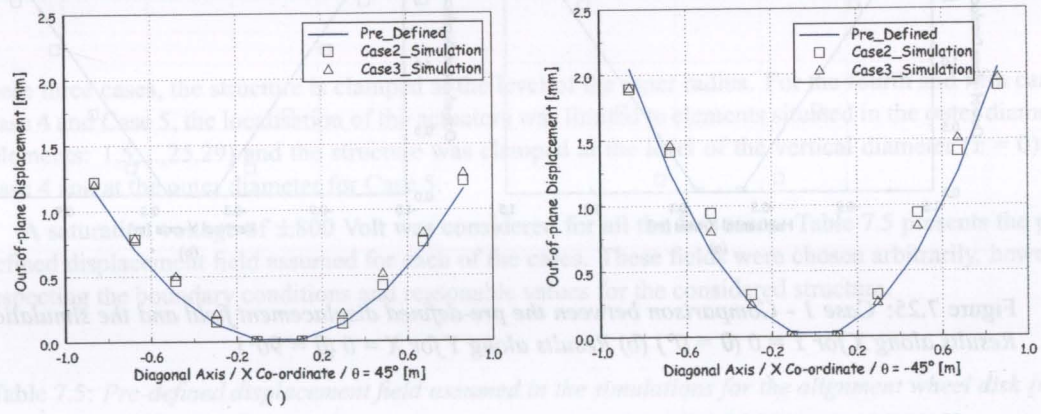

Figure 7.28: *Case 2, 3 - Comparison between the pre-defined displacement field and the simulations. (a) Results along a diagonal θ = 45° (b) Results along a diagonal θ = -45°.*

optimisation method and the objective function was defined, as in Chapter 6, in terms of the weighted sum of the closed loop damping ratios. The finite element mesh, used in the simulations and already shown in Figure 7.18, had 32 elements. The alignment disk was assumed to be completely covered with 0.3 mm thick piezoelectric elements (PX5-N from Philips Components) on both sides (see Table 3.2 for mechanical properties) and a constant gain feedback control methodology was used. The state-space model of the system took into account the first ten vibration modes and the initial damping ratios used in the simulations were the ones obtained in the modal testing of the prototype (Section 7.2.1). The alignment disk was clamped at the level of the external radius.

7.4.1 Simulation results

Before presenting the different cases considered in the simulations, Figure 7.33 and Figure 7.34 show, respectively, the first four bending vibration modes, of the alignment disk clamped at the outer radius, and the correspondent strain energy distribution obtained with the 32 element's mesh.

For the first mode, with one nodal circle, the strain energy is maximum at the level of the outer diameter. In the case of second and third modes, both presenting one nodal diameter, the strain energy is maximum near the clamped edge rotated 90 degrees with respect to the nodal line. For the fourth

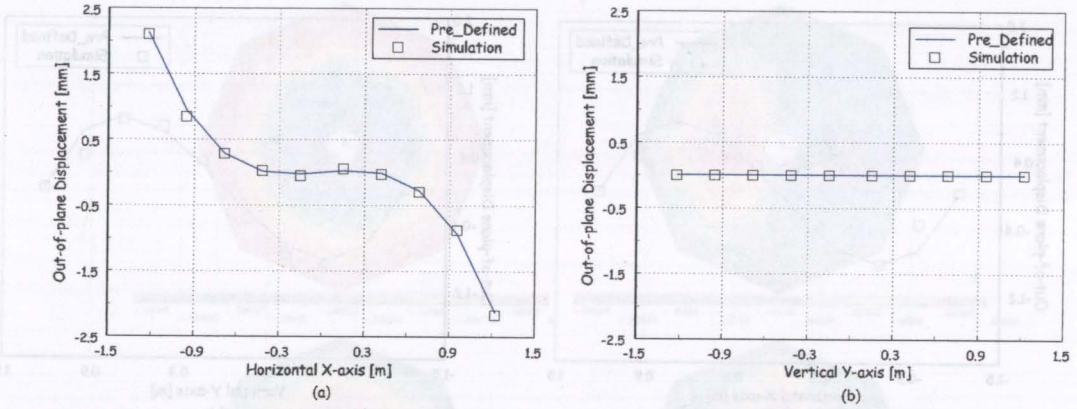

Figure 7.29: *Case 4 - Comparison between the pre-defined displacement field and the simulations. (a) Results along X for Y = 0 (θ = 0°) (b) Results along Y for X = 0 (θ = 90°).*

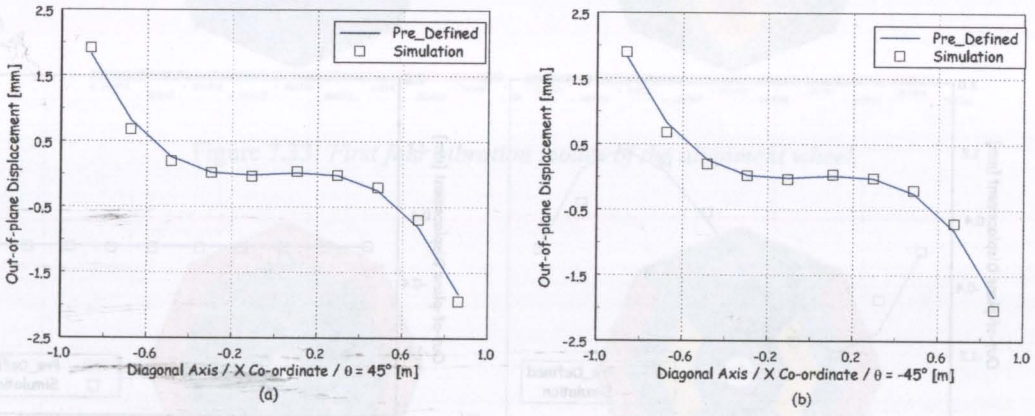

Figure 7.30: *Case 4 - Comparison between the pre-defined displacement field and the simulations. (a) Results along a diagonal θ = 45° (b) Results along a diagonal θ = -45°.*

vibration mode, with two perpendicular nodal diameters, the strain energy is again maximum at the level of the outer diameter decreasing towards the inner diameter. The pattern of the strain energy percentage obtained for the fourth mode is related with the poor mesh refinement used in the simulations.

7.4.2 Optimal placement of 4 collocated sensors/actuators

This section considers the optimal placement of 4 collocated sensor/actuators for the control of the first four bending vibration modes, individually or a combination between them. A population size of 15 individuals, a probability of crossover equal to 0.75, a probability of mutation equal to 0.20 and a maximum number of generations equal to 20,000 were considered in the simulations. Each chromosome consisted in 32 bits, equal to the number of elements of the finite element mesh, representing if a certain collocated sensor/actuator was being made active or not. The location constraints, dependent on each simulation case, reduced, however, the number of variables used in practice.

The first simulation case, Case 1, assumes that the 4 piezoelectric elements are situated at the level of the outer diameter (elements: 1,5,...,25,29). Results concerning the optimal placement of the 4 collocated sensor/actuators for controlling the first four vibration modes independently are presented in Table 7.7

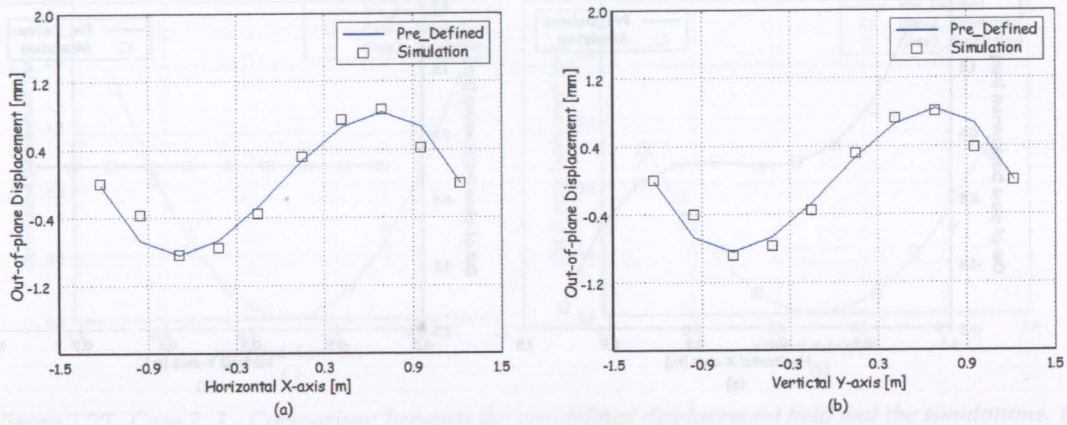

Figure 7.31: *Case 5 - Comparison between the pre-defined displacement field and the simulations. (a) Results along X for Y = 0 (θ = 0°) (b) Results along Y for X = 0 (θ = 90°).*

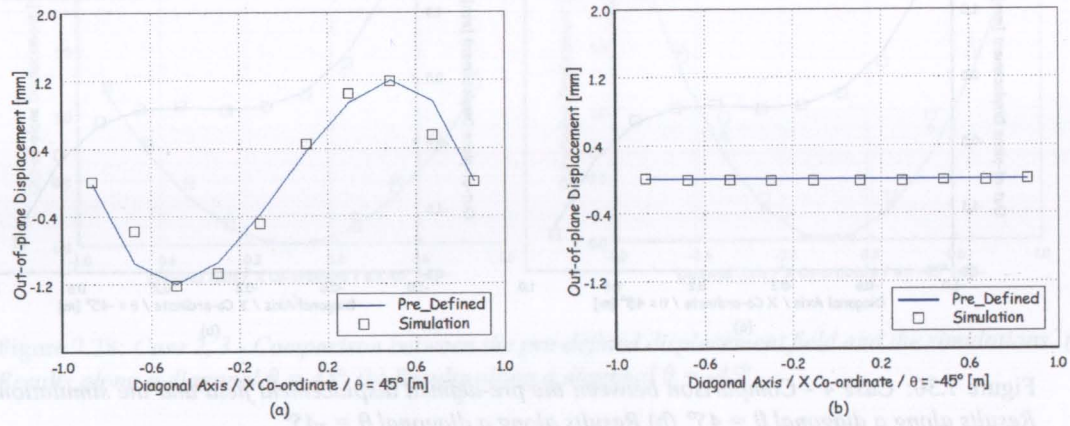

Figure 7.32: *Case 5 - Comparison between the pre-defined displacement field and the simulations. (a) Results along a diagonal θ = 45° (b) Results along a diagonal θ = -45°.*

and in Figure 7.35.

For the first and fourth modes, where all the elements at the level of the external radius present the same strain energy, the algorithm places the 4 collocated sensors/actuators all together for the first mode and without any particular pattern in the fourth mode. In the second and third modes the piezos are placed in the four elements of maximum strain energy.

For the second case, Case 2, the 4 piezoelectric actuators were located at the level of the third diameter (elements: 3, 7,... , 27, 31). Results concerning the optimal placement are presented in Table 7.8 and in Figure 7.36. Similar conclusions to Case 1 can be drawn for this case, with exception of the fourth piezo in the third mode that is not placed in an element with the maximum value of strain energy, but next to it.

In the third case, Case 3, two piezoelectric elements are placed at the level of the outer diameter and 2 other elements at the level of the third one. Results for the optimal location are presented in Table

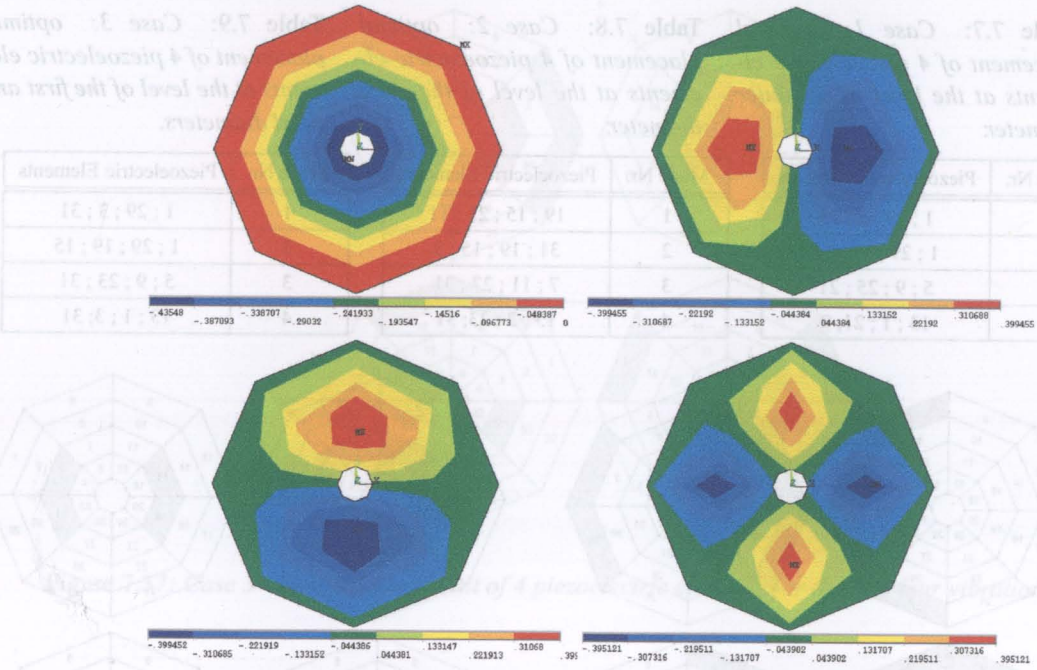

Figure 7.33: *First four vibration modes of the alignment wheel.*

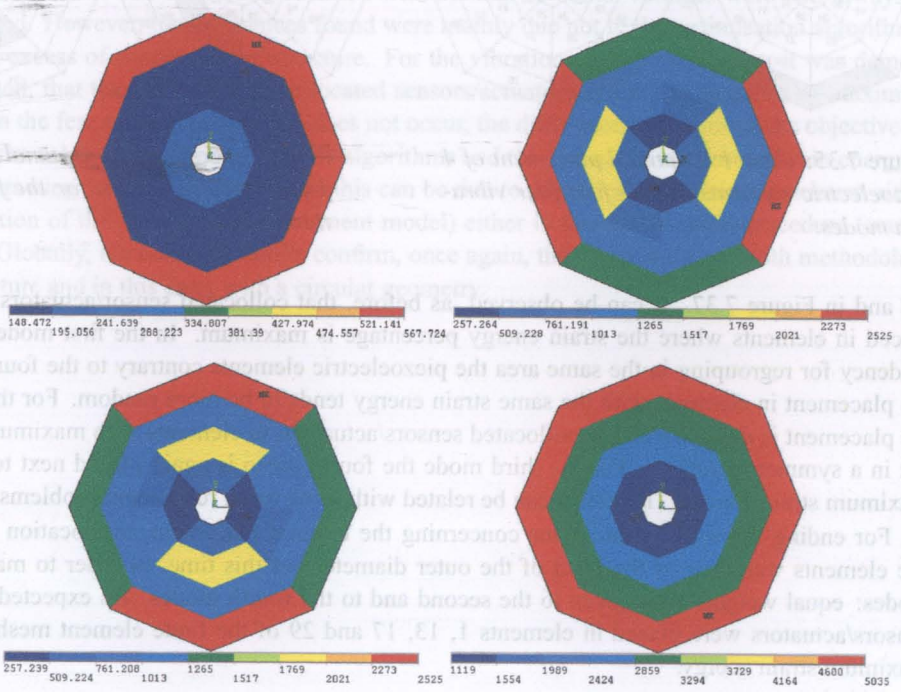

Figure 7.34: *Strain energy of the first four bending vibration modes of the alignment wheel clamped at the outer radius.*

Table 7.7: *Case 1: optimal placement of 4 piezoelectric elements at the level of the outer diameter.*

Mode Nr.	Piezoelectric Elements
1	1 ; 29 ; 5 ; 25
2	1 ; 29 ; 17 ; 13
3	5 ; 9 ; 25 ; 21
4	13 ; 1 ; 21; 9

Table 7.8: *Case 2: optimal placement of 4 piezoelectric elements at the level of the third diameter.*

Mode Nr.	Piezoelectric Elements
1	19 ; 15 ; 23 ; 11
2	31 ; 19 ; 15 ; 3
3	7 ; 11 ; 27 ; 31
4	15 ; 7 ; 23; 31

Table 7.9: *Case 3: optimal placement of 4 piezoelectric elements at the level of the first and third diameters.*

Mode Nr.	Piezoelectric Elements
1	1 ; 29 ; 3 ; 31
2	1 ; 29 ; 19 ; 15
3	5 ; 9 ; 23 ; 31
4	13 ; 1 ; 3; 31

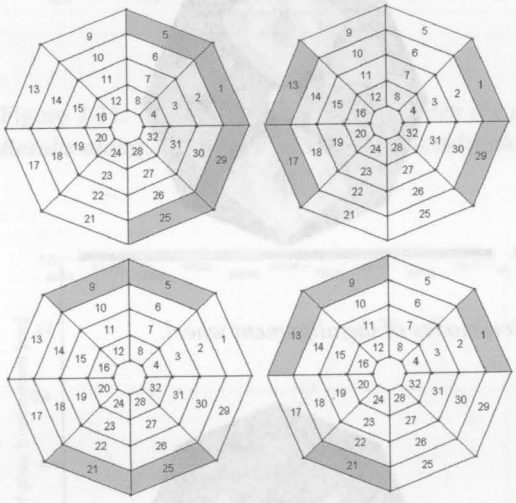

Figure 7.35: *Case 1 - Optimal placement of 4 piezoelectric elements for the first four vibration modes.*

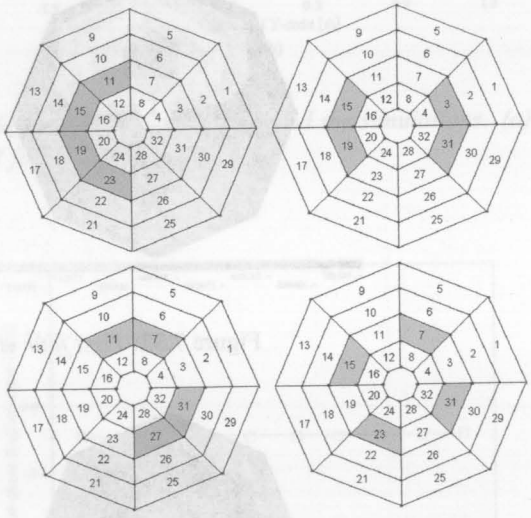

Figure 7.36: *Case 2 - Optimal placement of 4 piezoelectric elements for the first four vibration modes.*

7.9 and in Figure 7.37. It can be observed, as before, that collocated sensor/actuators continue to be placed in elements where the strain energy percentage is maximum. In the first mode there is still a tendency for regrouping in the same area the piezoelectric elements contrary to the fourth mode where the placement in elements with the same strain energy tends to be more random. For the second mode the placement is done, for all the collocated sensors/actuators, in elements with maximum strain energy but in a symmetric pattern. For the third mode the fourth piezo is again placed next to an element of maximum strain energy. This effect can be related with some mesh refinement problems.

For ending the set of simulations concerning the optimal placement, the location of 4 piezoelectric elements was done at the level of the outer diameter but this time, in order to maximise the odd modes: equal weights were given to the second and to the fourth modes. As expected, the collocated sensors/actuators were placed in elements 1, 13, 17 and 29 of the finite element mesh, the ones with maximum strain energy.

7.5 Conclusions

The methodologies developed in the previous chapters concerning the optimal placement of piezoelectric elements for shape and vibration control were applied to a real structure: the alignment disk of

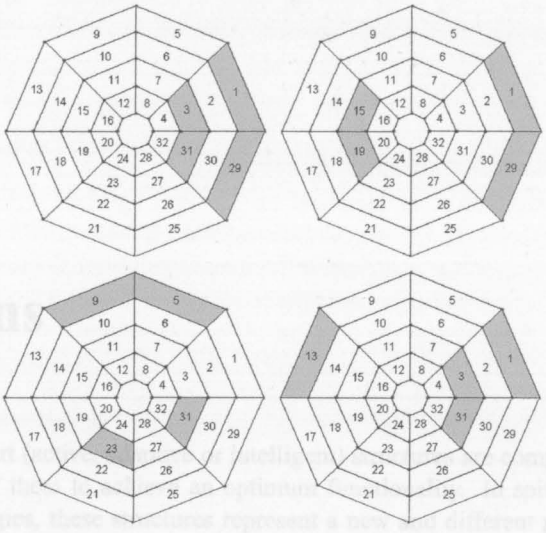

Figure 7.37: *Case 3 - Optimal placement of 4 piezoelectric elements for the first four vibration modes.*

the CMS detector. The finite element model of this 2.5 m sandwich disc was defined based on the modal testing of a prototype. Concerning the shape control application, the agreement between pre-defined displacement fields and the results obtained with optimal actuation voltages were not, always, as good as expected. However, the differences found were mainly due not to the optimisation algorithm in itself but to an excess of rigidity of the structure. For the vibration control application it was demonstrated, as expected, that the placement of collocated sensors/actuators is done at locations of maximum strain energy. In the few exceptions that this does not occur, the differences, in terms of the objective function, between the solution obtained by genetic algorithms and the one of the maximum strain energy is negligible in practice. As already mentioned this can be due to numerical uncertainties existent either in the modelisation of the structure (finite element model) either in the optimisation procedure (truncation of values). Globally, the obtained results confirm, once again, the applicability of both methodologies to a real structure and in this case, with a circular geometry.

Chapter 8

Conclusions

As already seen, smart (active, adaptive or intelligent) structures are complex systems with inherent characteristics that allow them to achieve an optimum functionality. In spite of not always involving recent material technologies, these structures represent a new and different project philosophy that integrates a network of actuators, sensors and control methodologies in a unique and global system, able to respond efficiently to environmental changes. Needs for different and efficient methodologies able to deal with multidisciplinary and complex systems, such as smart structures motivate and support the current work.

The modelisation of mechanical structures with integrated piezoelectric elements was done in Chapter 2 using standard techniques such as the finite element method. The equations governing the static and dynamic characteristics of orthotropic plates with piezoelectric elements glued or embedded in it, were determined using the Hamilton's principle and Mindlin's plate theory. All the formulation was based in linear piezoelectricity.

For both shape and vibration control of mechanical structures, the location of sensors and actuators is one of the most important factors affecting the performance of the system. The large set of candidate solutions, results in a substantially large number of combinations that must be evaluated, and consequently the need of an effective and robust optimisation method. Chapter 4 introduced the main concepts of genetic algorithms and genetic operators. The general structure of the optimisation method and the particularities related to each problem type: shape control and optimal location of collocated sensors/actuators for free vibration control were presented. In both applications, the developed methodologies, based on genetic algorithms, reduce the computational effort in large scale problems and eliminate a large number of restrictions common to most optimisation methods. Namely, any kind of objective functions and any kind of constraints (linear or non-linear) defined on discrete, continuous, or mixed search spaces can be easily integrated; the implementation of a specific problem is highly flexible; the susceptibility of the method of focusing on local optimum is reduced and little knowledge of the problem itself is required.

The first application is discussed in Chapter 5: the use of piezoelectric actuators for correcting and/or modifying the shape of mechanical structures. Both the determination of the optimal voltages, as well as, the determination of the optimal position of the actuators were addressed. Throughout the presented results only glued piezoelectric elements were considered, however the developed methodology also supports embedded ones. The square root of the error between the nodal pre-defined displacement and the achieved displacement was considered as the objective function. The use of genetic algorithms was successfully demonstrated and the influence of its control parameters: population size, crossover probability and mutation probability, in the final performance and convergence of the algorithm was discussed. The coding scheme proposed for the determination of both the optimal actuation voltages and the optimal location, while useful for problems with a low number of potential actuator locations, may be rejected and become too heavy when considering a large number of possible actuator locations. For that case, the implemented algorithm can be easily extended and strings of integer numbers, with a size equal to the maximum number of actuators to be positioned, can be considered for representing the

location of each actuator in the finite element mesh of the structure. Several beam and plate structures with different boundary conditions were studied. Experimental results obtained using simple set-ups and sophisticated optical methods (ESPI - Electronic Speckle Pattern Interferometry) were compared with simulations enabling the validation of the whole methodology. The practicality and the effectiveness of using genetic algorithms to determine the optimal location and the optimal actuation voltages was demonstrated and the adopted methodology validated.

Chapter 6 introduced the second application: the use of genetic algorithms to determine the optimal location, within a discretised domain of the structure, of collocated sensors/actuators for free vibration control. Based in genetic algorithms, the maximisation of the weighted sum of the closed loop damping ratios was assumed as the performance criteria. The results obtained were compared with a standard method for determining the position of the piezoelectric sensors/actuators - the strain energy distribution method. Comparisons between the strain energy percentage considering two different finite element codes and different finite element mesh were made, together with the variation of the closed loop damping ratio, when one collocated sensor/actuator is displaced within the discretised structure. The optimal placement of two, four and six collocated sensors/actuators was determined and experimental results concerning the optimal placement of one collocated sensor/actuator for the first two bending modes were obtained. The results presented validate the methodology and were all obtained assuming that the structure is covered with piezoelectric elements in both sides and that the control is achieved by activating individually each piezoelectric element. In practice this means that the matrices modelling the structure are constant during the optimisation process. In case that the geometry, comprising structure and piezoelectric elements, is not defined before the optimisation process starts and/or the structure is not completely covered with piezoelectric elements the present methodology is still valid but the iteration process is much longer since at each step the system's matrices must be recalculated. No strong mathematical justification was found for the observed tendency of the optimisation algorithm to place piezoelectric elements near to already existing ones, when there are other locations with the same strain energy. When the strain energy value is the same in several locations, a collocated sensor/actuator with a higher dimension is generally more effective than two smaller ones, each with half of the dimensions, placed apart from each other. In practice the difference between configurations is negligible and lower than 1%. This fact may be related with numerical errors of the simulation model. For this application a constant gain feedback controller was designed. However a more robust technique, like the linear quadratic regulator, can also be used. The state-space model of a mechanical structure was validated in Chapter 3. Namely, experimental results using constant amplitude/gain feedback control were presented. A LQG/LTR, was also designed based on a reduce-order state space model of the system and its performance was studied for different initial conditions and structural parameter variations. Good robustness characteristics were found.

The methodologies developed in the previous chapters concerning the optimal placement of piezoelectric elements for shape and vibration control were applied to a real structure (Chapter 7): the mechanical support of the alignment system of the CMS detector. The finite element model of this 2.5 m sandwich disc was defined based on the modal testing of a prototype. Concerning the shape control application, the agreement between pre-defined displacement fields and the results obtained with optimal actuation voltages were not, always, as good as expected. However, the differences found were mainly due not to the optimisation algorithm in itself but to an excess of rigidity of the structure. For the vibration control application it was demonstrated, as expected, that the placement of collocated sensors/actuators is done at locations of maximum strain energy. In the few exceptions that this does not occur, the differences, in terms of the objective function, between the solution obtained by genetic algorithms and the one of the maximum strain energy is negligible in practice. As already mentioned this can be due to numerical uncertainties existent either in the modelisation of the structure (finite element model) either in the optimisation procedure (truncation of values). Globally, the obtained results confirm, once again, the applicability of both methodologies to a real structure and in this case, with a circular geometry.

For both applications, key points of the modelisation and of the global methodology were experi-

mentally verified and the extension to real applications was straightforward. Future developments can cover the following areas.

- Modelisation: use of layerwise theories, more adequate to the modelisation of thick laminates but representing higher computational efforts due to an increase of the number of the degrees of freedom. Extension of the finite element library to shell elements;
- Sensors/actuators: the developed mathematical model considers only piezoelectric sensors and actuators. The current methodology can be extended to other types of sensors. Namely to fibre optics sensors, easily integrated during the manufacturing process of composite materials;
- Experimental: more experimental tests, related to the optimal placement for free vibration control application, could have been done: a different structure, different boundary conditions and different control algorithm;
- Control Algorithms: experimentally, the only control methodology used was a constant amplitude/gain feedback. The use of more efficient and robust control techniques able to act on several modes and respond to random excitations should be developed;
- Genetic Algorithms: the representation of the coding of a solution can dramatically change the performance of the optimisation algorithm. Namely, instead of using a string with a length equal to the number of elements in the finite element mesh to represent if a certain element has a piezoelectric layer on it ("1") or not ("0"), the use of a string of length equal to the actuators to be placed will be more efficient. The present algorithm could also be enhanced by using a scaling mechanism;
- Neural Networks: neural networks controllers can adapt and train themselves to changing parameters in order to control effectively structural vibrations and thus eliminate the need for the time consuming robust control design. While conventional controllers require a good knowledge about the mathematical model of the controlled system, most neural network controllers do not need such requirements and can handle complex systems efficiently.

Bibliography

[1] S. da Mota Silva, H. Dumontet, C. Hauviller, P. Kanoute, and R. Ribeiro, "Hygro-thermal transient analysis for highly stable structures," in *Twelfth International Conference on Composite Materials ICCM-12*, T. Massard, ed., *CD-ROM edition* **Durability and Ageing**, pp. 139–145, Paris, July 1999.

[2] S. da Mota Silva, R. Ribeiro, and C. Hauviller, "High precision and stable structures for particle detectors," in *SPIE's 6th Annual International Symposium on Smart Structures and Materials*, vol. 3668 - Part Two, pp. 1017–1025, Newport Beach, CA, March 1999.

[3] R. Ribeiro, S. da Mota Silva, J. Rodrigues, and M. Vaz, "Genetic algorithms for optimal design and control of adaptive structures," in *SPIE's 7th Annual International Symposium on Smart Structures and Materials, to be published*, Newport Beach, CA, March 2000.

[4] M. Gandhi and B. Thompson, *Smart materials and structures*, Chapman & Hall, 1992.

[5] G. Akhras, "Smart materials and smart structures for the future," *Canadian Military Journal* **1(3)**, 2000.

[6] G. Akhras, "Advanced composites for smart structures," in *Twelfth International Conference on Composite Materials, ICCM-12*, Paris, 5-9th July 1999.

[7] *http://me.wpi.edu/ cirrus/Publications/SmartMaterials/SmartMaterialExtension.html*, Smart Materials and Structures, November, 1999.

[8] A. Suleman and V. Venkayya, *Flutter control of an adaptive laminated composite panel with piezoelectric layers*, Wright Laboratory WL-TR-94-0000, August 1994.

[9] *http://www.physikinstrumente.com/produkte.html*, November, 1999.

[10] W. Buehler and R. Wiley, *Nickel-Base alloys*, U.S. Patent 3,174,851, 1965.

[11] I. Chopra and N. Wereley, "Smart structures: theory and applications," in *SPIE's 7th Annual International Symposium on Smart Structures and Materials*, vol. SC19 Short Course Notes, Newport Beach, California, March 2000.

[12] C. Rogers, J. Jia, and C. Liang, "Behavior of shape memory alloy composite plates. part i and ii," in *30th SDM Conference*, Mobile, AL, 1989.

[13] C. Rogers, J. Jia, and D. Barker, "Dynamic control concepts using shape memory alloy reinforced plates," in *Smart materials, structures, and mathematical issues*, I. Lancaster, PA: Technomic Publishing Co., ed., 1989.

[14] B. Wada, J. Fanson, and E. Crwaley, "Adaptive structures," *Journal of Intelligent Materials Systems and Structures* **1**, pp. 157–174, April 1990.

[15] A. Ealey and J. Wellman, "Fundamentals of deformable mirror design and analysis," in *Precision engineering and optomechanics*, B. Nicquevert and G. C. Hauviller, CERN, eds., *Society of Photo-Optical Instrumentation Engineers* , pp. 66–84, 1989.

[16] S. Murray, R. Hayashi, M. Marioni, S. Allen, and R. O'Handley, "Magnetic and mechanical properties of the fenicoti and nimnga magnetic shape memory alloys," in *SPIE's 6th Annual International Symposium on Smart Structures and Materials*, vol. 3675, pp. 204–211, Newport Beach, California, March 1999.

[17] C. Miller, T. Li, J. Miller, F. Bao, and K. Hsu, *Multiplexed fiber gratings enhance mechanical sensing*, Edition of Laser Focus World, 1998.

[18] A. Bronowicki, "Active structures for vibration and shape control," in *SPIE's 6th Annual International Symposium on Smart Structures and Materials*, vol. Short Course Notes, Newport Beach, California, March 1999.

[19] E. S. Agency, *Structural Materials Handbook. Vol.2 - New Advanced Materials*, ESA PSS-03-203 Issue 1, 1994.

[20] *http://civil.colorado.edu/courseware/structlabs/tstraingage.html*, Strain Gages, November, 1999.

[21] J. Fraden, *Handbook of modern sensors. Physics, designs and applications*, 1996.

[22] H. Strehlow and H. Rapp, "Smart materials for helicopter active control," *AGARD Conference Proceedings AGARD-CP-531, Paper 5* , 1993.

[23] F. Nitzsche and E. Breitbach, "A study of the feasibility of using adaptive structures in the attenuation of vibration characteristics of rotary wings," in *Proceedings of the IAAA 33rd Structures, Structural Dynamics and Materials Conference*, Dallas, 1992.

[24] I. Chopra, "State-of-the-art of smart structures and integrated systems," in *SPIE Far East Pacific Rim Symposium on Smart Materials, Structures and MEM*, India, 1996.

[25] E. Crawley and J. Luis, "Use of piezoelectric actuators as elements of intelligent structures," *AIAA Journal* **25(10)**, pp. 1373–1385, 1987.

[26] C. Lee, "Theory of laminated piezoelectric plates for the design of distributed sensors/actuators. part i: Governing equations and reciprocal relationships," *Journal Acoust. Soc. Am.* **87(3)**, pp. 1144–1158, 1990.

[27] V. Correia, C. M. Soares, and C. M. Soares, "A numerical model for the optimal design of composite laminated structures with piezoelectric laminae," in *SPIE's 6th Annual International Symposium on Smart Structures and Materials*, vol. 3667, pp. 427–437, Newport Beach, California, March 1999.

[28] C. Shakeri, C. Bordonaro, M. Noori, and R. Champagne, "Experimental study of thunder: A new generation of piezoelectric actuators," in *SPIE's 6th Annual International Symposium on Smart Structures and Materials*, M. Wuttig, ed., *SPIE* **3675**, pp. 63–71, Newport Beach, California, March 1999.

[29] R. Kellog and A. Flatau, "Blocked force investigation of a terfenol-d transducer," in *SPIE's 6th Annual International Symposium on Smart Structures and Materials*, vol. 3668, pp. 184–195, Newport Beach, California, March 1999.

[30] *http://www.isiscanada.com/programs/sensing/field.htm*, Fibre Optic Sensor Technology, September, 2002.

[31] A. Kalamkarov, D. MacDonald, S. Fitzgerald, and A. Georgiades, "On fabrication and mechanical performance of smart composites incorporating fiber optics sensors," in *Thirteenth International Conference on Composite Materials, ICCM-13*, Beijing, 2001.

[32] H. Strock, M. Pascucci, M. Parish, A. Bent, and T. Shrout, "Active pzt fibers, a commercial production process," in *SPIE's 6th Annual International Symposium on Smart Structures and Materials*, vol. 3675, pp. 22–31, Newport Beach, California, March 1999.

[33] M. Surgeon and M. Wevers, "Quantifying the damage state of quasi-isotropic cfrp with embedded optical fibres during fatigue testing using acoustic emission and microfocus radiography," *The e-Journal of Nondestructive Testing* **3. No.9**, 1998.

[34] D. Warkentin and E. Crawley, "Embedded electronics for intelligent structures," in *AIAA/AHS/ASME/ASC 32nd Structures, Structural Dynamics and Materials*, vol. AIAA-91-1084-CP, pp. 1322–1331, 1991.

[35] S. Mall and J. Coleman, "Monotonic and fatigue loading behavior of quasi-isotropic graphite/epoxy laminate embedded with piezoelectric sensor," *Smart Materials and Structures* **7, No.6**, pp. 822–832, December, 1998.

[36] S. Mall and T. Hsu, "Electromechanical fatigue behavior of graphite/epoxy laminate embedded with piezoelectric actuator," in *SPIE's 6th Annual International Symposium on Smart Structures and Materials*, vol. 3668, pp. 770–778, Newport Beach, California, March 1999.

[37] T. Bailey and H. Jr, "Distributed piezoelectric polymer active vibration control of a cantilever beam," *AIAA Journal of Guidance and Control* **8(5)**, pp. 605–611, 1985.

[38] H. Tzou and C. Tseng, "Distributed piezoelectric sensor/actuator design for dynamic measurement/control of distributed parameter systems: a piezoelectric finite element approach," *Journal of Sound and Vibration* **138(1)**, pp. 17–34, 1990.

[39] D. Koconis, L. Kollar, and G. Springer, "Shape control of composite plates and shells with embedded actuators i. voltages specified," *Journal of Composite Materials* **28(5)**, pp. 415–458, 1994.

[40] D. Koconis, L. Kollar, and G. Springer, "Shape control of composite plates and shells with embedded actuators ii. desired shape specified," *Journal of Composite Materials* **28(3)**, pp. 262–285, 1994.

[41] J. Onoda and Y. Hanawa, "Optimal locations of actuators for statistical static shape control of large space structures: a comparison of approaches," in *Proc. 31st AIAA/ASME/ASCE/AHS/ASC Structures, Structural Dynamics and Materials Conference*, pp. 2788–2795, Washington DC, April 1992.

[42] K. Chandrashekhara and S. Varadarajan, "Adaptive shape control of composite beams with piezoelectric actuators," *Journal of Intelligent Materials and Structures* **8**, pp. 112–124, February 1997.

[43] S. da Mota Silva, R. Ribeiro, J. D. Rodrigues, and M. Vaz, "Shape control of structures with pzt actuators using genetic algorithms," in *Thirteenth International Conference on Composite Materials, ICCM-13*, Beijing, 2001.

[44] T. Meressi and B. Paden, "Buckling control of a flexible beam using piezoelectric actuators," *Journal of Guidance Control and Dynamics* **16**, pp. 977–980, 1993.

[45] S. Thompson and J. Loughlan, "The active buckling control of some composite column strips using piezoceramic actuators," *Composite Structures* **32**, pp. 59–67, 1995.

[46] S. Pai and C. Chamis, "Probabilistic structural analysis of adaptive/smart/intelligent space structures," *Journal of Intelligent Materials and Structures* **3**, pp. 600–616, 1992.

[47] M. Gonçalves, *Modelação e optimização de estruturas adaptativas electromecânicas*, Tese de Mestrado, Instituto Superior Técnico, July 1997.

[48] E. Waterman, D. Kaptein, and S. Sarin, "Fokker's activities in cabin noise control for propeller aircraft," in *SAE Paper 891080, General aviation aircraft meeting and expo*, 1989.

[49] S. Elliot, P. Nelson, I. Stothers, and C. Boucher, "In-flight experiments on the active control of propeller induced cabin noise," *Journal of sound and vibration* **140(2)**, pp. 219–238, 1990.

[50] T. Brama, *The structural optimization system OPTSYS: current status and applications in integrated design analysis and optimization of aircraft structures*, Bath U.K., AGARD-R-784, 1991.

[51] F. Sun, Z. Chaudry, C. Liang, and C. Rogers, "Truss structure integrity identification using pzt sensor-actuator," *Journal of Intelligent Materials and Structures* **6**, pp. 134–139, 1995.

[52] C. Keilers and F. Chang, "Identifying delamination in composite beams using built-in piezoelectrics: Part i - experimental analysis," *Journal of Intelligent Materials and Structures* **6**, pp. 649–663, 1995.

[53] C. Keilers and F. Chang, "Identifying delamination in composite beams using built-in piezoelectrics: Part ii - an identification method," *Journal of Intelligent Materials and Structures* **6**, pp. 664–672, 1995.

[54] C. Liang, F. Sun, and C. Rogers, "Determination of design of optimal actuator location and configuration based on actuator power factor," *Journal of Intelligent Materials and Structures* **8**, pp. 344–352, April 1997.

[55] A. Chattopadhyay and C. Seeley, "A multiobjective design optimization procedure for control of structures using piezoelectric materials," *Journal of Intelligent Materials and Structures* **5**, pp. 403–411, May 1994.

[56] M. Athans, "A tutorial on the lqg/ltr method," in *American control conference*, vol. 2, pp. 1289–1296, 1986.

[57] K. Chandrashekhara, P. Smyser, and A.Agarwal, "Dynamic modelling and neural control of composite shells using piezoelectric devices," *Journal of intelligent materials and structures* **9**, pp. 29–43, January 1998.

[58] C. Chen, "Active vibration control using the modified independent modal space control (mimsc) and neural networks as state estimators," *Journal of Intelligent Materials and Structures* **5**, pp. 550–558, 1994.

[59] K. Narendra and K. Parathasarthi, "Identification and control of dynamical systems using neural networks," in *IEEE transactions on neural networks*, vol. 1, pp. 4–27, 1990.

[60] M. Collet, *Controle actif des structures par couches piezo-electriques*, These de doctorate. Ecole Centrale de Lyon, Juin 1996.

[61] *Quartz & Silice. Product Catalogue*, 1998.

[62] *Sensor technology limited. Product Catalogue*, 1995.

[63] H. Tiersten, *Linear piezoelectric plate vibrations*, Plenum Press, 1969.

[64] J. Reddy, *Mechanics of laminated composite plates - Theory and analysis*, CRC Press, 1997.

[65] A. Suleman and V. Venkayya, "A simple finite element formulation for a laminated composite plate with piezoelectric layers," *Journal of Intelligent Materials and Structures* **6**, pp. 776–782, November 1995.

[66] K. Chandrashekhara and A. N. Agarwal, "Active vibration control of laminated composite plates using piezoelectric devices: a finite element approach," *Journal of Intelligent Materials and Structures* **4**, pp. 496–508, October 1993.

[67] D.J.Ewins, *Modal testing: theory and practice*, Research Studies Press Ltd., John Wiley & Sons, 1984.

[68] K. Bathe, *Finite element procedures in engineering analysis*, Prentice-Hall, Inc., 1982.

[69] A. Preumont, *Vibration control of active structures*, Kluwer academic publishers, 1997.

[70] B. Friedland, *Control System Design: An introduction to state-space methods*, McGraw-Hill, Inc., 1986.

[71] S. Rao, *Mechanical vibrations*, Addison-Wesley Publishing Company, 3rd Edition, 1995.

[72] G. Franklin, J. Powell, and M. Workman, *Digital control of dynamic systems*, Addison-Wesley Publishing Company, 2nd Edition, 1990.

[73] L. Meirovitch and H. Baruh, "The implementation of modal filters for control of structures," *Journal of Guidance and Control* **8(6)**, pp. 707–716, 1985.

[74] C. Fredo, P. Andren, and T. Falk, "Mechanical damping simulation in msc.nastran," in *Nordic MSC User's Conference*, Gothenburg, 1999.

[75] A. Costa and M. Freire, *Implementação de um controlador LTR/LQG para a supressão de vibracões numa placa compósita e estudo dos efeitos aeroelásticos*, Trabalho final de curso. Instituto Superior Técnico, Lisboa, Portugal, 1997.

[76] D. E. Goldberg, *Genetic algorithms in search, optimization, and machine learning*, Addison-Wesley Publishing Company, Inc., 1989.

[77] M. Mitchell, *An Introduction to Genetic Algorithms*, The MIT Press, 1996.

[78] J. H. Holland, *Adaptation in natural and artificial systems*, University of Michigan Press, Second Edition, 1992.

[79] R. Baker, *Genetic algorithms in search and optimization*, Financial Engineering News, 1998.

[80] K. Krishnakumar and D. Goldberg, "Control system optimization using genetic algorithms," *Journal of guidance, control and dynamics* **15(3)**, pp. 735–740, 1992.

[81] Z. Michalewicz, *Genetic algorithms + data structures = evolution programs*, Springer, 1996.

[82] M. Gen and R. Cheng, *Genetic algorithms and engineering design*, John Wiley & Sons Inc., 1997.

[83] J. J. Grefenstette, "Optimization of control parameters for genetic algorithms," in *IEEE transactions on systems, man and cybernetics*, vol. SMC-16 (1), pp. 122–128, January/February 1986.

[84] M. Simpson and C. Hansen, "Use of genetic algorithms to optimize vibration actuator placement for active control of harmonic interior noise in a cylinder with floor structure," *Noise Control Engineering Journal* **44(4)**, 1996.

[85] K. Krishnakumar, "Micro-genetic algorithms for stationary and non-stationary function optimization," in *Intelligent control and adaptive systems*, SPIE, ed., pp. 289–296, 1989.

[86] D. Carroll, "Genetic algorithms and optimizing chemical oxygen-iodine lasers," in *Developments in theoretical and applied mechanics*, T. U. of Alabama, ed., vol. XVIII, pp. 411–424, 1996.

[87] D. Goldberg and M. Samtani, "Engineering applications via genetic algorithm," in *Ninth Conference on Electronic Computation*, ASCE, ed., pp. 471–482, New York, 1986.

[88] P. Hajela and C. Shih, "Multiobjective optimum design in mixed integer and discrete design variable problems," *AIAA Journal* **28(4)**, pp. 670–675, April, 1990.

[89] S. Rao, T. Pan, and V. Venkayya, "Optimal placement of actuators in actively controlled structures using genetic algorithms," *AIAA Journal* **29(6)**, pp. 942–943, June, 1991.

[90] M. Schoenauer and S. Xanthakis, "Constrained ga optimization," in *Fifth International Conference on Genetic Algorithms*, M. K. Publishers, ed., pp. 573–580, July, 1993.

[91] H. Adeli and N. Cheng, "Integrated genetic algorithm for optimization of space structures," *Journal Aerospace Engineering* **6(4)**, pp. 104–118, January 1994.

[92] S. Rajan, "Sizing, shape, and topology design optimization of trusses using genetic algorithms," *Journal of structural Engineering* **121(10)**, pp. 1480–1487, October, 1995.

[93] C. Coello, A. Carlos, and A. Christiansen, "Multiobjective optimization of trusses using genetic algorithms," *Computers and structures* **75**, pp. 647–660, April, 2000.

[94] A. Cook and W. Crossley, "Investigation of genetic algorithm approaches for smart actuator placement for aircraft manoeuvring," *AIAA Journal* **2001-0924**, pp. 1–11, 2001.

[95] J. Hollkamp, "Multimodal passive vibration suppression with piezoelectric materials and resonant shunts," *Journal of Intelligent Materials and Structures* **5(1)**, pp. 49–57, 1994.

[96] M. Kwak and T.-S. Shin, "Real-time automatic tuning of vibration controllers for smart structures by genetic algorithm," in *SPIE's 6th Annual International Symposium on Smart Structures and Materials*, vol. 3667, pp. 679–690, Newport Beach, California, March 1999.

[97] J. S. Gomes, J. Monteiro, and M. Vaz, "Ndi of interfaces in coating systems using digital interferometry," *Mechanics of Materials* **32**, pp. 837–843, 2000.

[98] A. Amdan and A. Nayfeh, "Measures of modal controllability and observability for first and second order linear systems," *Journal of Guidance, Control and Dynamics* **12(3)**, pp. 421–428, 1989.

[99] J. Choi, U. Park, and S. Lee, "Measures of modal controllability and observability in balanced coordinates for optimal placement of sensors/actuators: a flexible structure application," in *SPIE's 7th Annual International Symposium on Smart Structures and Materials*, vol. 3984, pp. 425–436, Newport Beach, California, March 2000.

[100] S. Padula and R. Kincaid, *Optimization strategies for sensor and actuator placement*, NASA/TM-1999-209126, April, 1999.

[101] G. Liu, X. Peng, and K. Lam, "Vibration control simulation of laminated composite plates with integrated piezoelectrics," *Journal of Sound And Vibration* **220(5)**, pp. 827–846, 1999.

[102] R. Alemany, S. da Mota Silva, R. Ribeiro, and H. V. *et al*, "Technical feasibility studies for the cms tracker position monitoring system," *CERN CMS NOTE - 2001/006* , February 2001.

[103] J. Rodrigues and S. da Mota Silva, "Experimental modal analysis of the alignment disk of the cms tracking system," *INEGI, Project CERN/P/FIS/1192/98* , July, 2000.

[104] J. Rodrigues and C. Vasques, "Experimental modal analysis of the alignment disk of the cms tracking system. analysis ii," *INEGI, Project CERN/P/FIS/1192/98* , January, 2001.

[105] K. Liew, C. Wang, Y. Xiang, and S. Kitipornchai, *Vibration of Mindlin Plates*, Elsevier, 1998.